Novel Induction Machines for Electric Vehicle Application

Mallampalli Srinivas

A thesis submitted for the degree of Doctor of Philosophy

Department of Electronic and Electrical Engineering

The University of Sheffield

Mappin Street, Sheffield, S1 3JD, UK

September 2020

Abstract

This thesis investigates the use of electronic pole-changing winding induction machines for an automotive starter-generator application. Induction machines offer the benefits of a low cost, rugged construction and high overload capability. A starter-generator requires the machine to have a high torque capability at low speeds for engine cranking operations and a wide-speed flux weakening region for providing a torque boost and for extending the region of regeneration. Induction machines that are designed for a fixed pole number that can meet both of these requirements have a large frame size and this results in poor torque density.

Electronic pole-changing windings utilise the inverter to change the number of poles. The machine is wound for the higher number of poles and the number of poles is reduced to half by reversing the direction of current in specific coils of the phase windings. To avoid cancellation of MMF and the associated copper losses, state of the art, three-phase, electronic pole-changing windings for induction machines use windings with a 120^o phase belt. However, 120^o phase belt windings have a fundamental winding factor below 0.85 and this results in poor torque density. When the number of poles is reduced, the winding factor degrades further. In this thesis, six-phase, electronic pole-changing windings to extend the flux weakening region of operation is investigated. Six-phase pole-changing windings can be wound with a 60^o phase belt without the disadvantage of MMF cancellation and still retain the ability to perform the pole-changing operation. The fundamental winding factor with a 60^o phase belt is improved by 15% and this proportionately increases the torque capability when operating with the higher number of poles, below the base speed. For operation with the higher number of poles, the six-phase pole-changing winding is symmetric, with a 60^o phase separation between the phases. When the number of poles is halved, the resulting machine is an asymmetric six-phase machine with a 30^o spatial separation between the phases. The enables the injection of 3^{rd} harmonic currents to produce additional torque within the limits imposed by the inverter current and the DC bus voltage. The optimal 3^{rd} harmonic current to maximise torque capability and its impact on the torque ripple is determined for the pole-changing winding induction machine. The performance of the three-phase and the proposed six-phase pole-changing winding machines are simulated using finite element analysis and the results are validated using experimental data on a prototype machine.

Finally, using vector space decomposition, the dynamic *dq*-model for a six-phase pole-changing winding is developed. The transient performance of the three-phase and six-phase pole-changing winding are compared under scalar control and indirect rotor field-oriented control.

Acknowledgements

I would like to express my deepest gratitude to my supervisor Prof. Zi-Qiang Zhu for this opportunity to collaborate with and learn from him. His continuous support, honest feedback, guidance and invaluable discussions through the course of this work made it possible and much better.

My experience at Sheffield was made richer through discussions with the cohorts of the Electrical Machines and Drives group at the University of Sheffield. In particular, thanks to Dr Cai Shun for the absorbing technical discussions. Special thanks are due to Iain Urquhart whose willingness to always lend an ear far exceeded the patience, time and compassion expected of a colleague and friend. The hours spent in the department and the lab on developing this thesis were possible with the warmth and technical support of the entire staff of the Electrical Machines and Drives group. Specifically, I would like to acknowledge the assistance provided by the late Lawrence Obodo and Thomas Templeman in setting up my experiments.

I would like to thank Dr Jean-Claude Mipo and Dr Sophie Personnaz from Valeo Powertrain Systems, Paris, France for the financial and technical support that made this dissertation possible.

Finally, thanks are due to my entire family for putting up with my idiosyncrasies that were inevitable through this long journey.

Contents

List of Symbols

Symbol	Definitions	Units
a	Number of parallel paths	
A_{co}	Conductor area	m^2
A_{slot}	Area of slot	m^2
$a_{strands}$	Number of stands per conductors	
B_{cs}	Yoke flux density	T
B_g	Average air gap flux density	T
b_{os}	Stator slot opening width	m
b_{s1}	Stator slot top width	m
b_{s2}	Stator slot bottom width	m
B_{tr}	Rotor tooth flux densities	T
B_{ts}	Stator tooth flux densities	T
b_{ts}	Stator tooth width	m
B_{yr}	Rotor yoke flux densities	T
B_{ys}	Stator yoke flux densities	T
d_{co}	Conductor diameter	m
D_{er}	Diameter of end-ring	m
D_{out}	Stator outer diameter	m
D_{sh}	Shaft diameter	m

D_{is}	Bore diameter	m
e_m	Induced EMF	V
F_{1m}	Magnetising MMF	AT
F_{mcr}	MMF drop across the rotor back irons	AT
F_{mcs}	MMF drop across the stator back irons	AT
F_{mtr}	MMF drop across the rotor tooth	AT
F_{mts}	MMF drop across the stator tooth	AT
F_{rotor}	Rotor tooth MMF	AT
F_{stator}	Stator tooth MMF	AT
g	Air gap length	m
$g_{effective}$	Effective air-gap	m
h_{cr}	Height of rotor yoke	m
h_{cs}	Stator yoke density	m
h_{os}	Stator slot opening height	m
h_s	Slot height	m
h_s	Stator slot height	m
H_{tr}	Rotor tooth field strength	A/m
H_{ts}	Stator tooth field strength	A/m
h_w	Slot wedge height	m
i_a	Armature winding current	A
I_{bar}	Rotor bar current density	A/mm^2

i_{dr}^{e}	Rotor d-axis current in the rotating reference frame	A
i_{ds}^{e}	Stator d-axis current in the rotating reference frame	A
I_{phase}	Phase current	A
i_{qr}^{e}	Rotor q-axis current in the rotating reference frame	A
i_{qs}^{e}	Stator q-axis current in the rotating reference frame	A
I_{ring}	Rotor end-ring current density	A
I_{smax}	Stator current limit	A
J	Rotor inertia	$kg\ m^{-2}$
J_r	rotor current density	A/mm^2
J_s	Stator current density	A/mm^2
K_C	Carter's coefficient	
K_{fill}	Slot fill factor	
K_{st}	Saturation factor	
K_{stack}	Stacking factor	
k_T	Motor torque constant	Nm/A
k_w	Total winding factor	
k_{wrp}	Rotor winding factor for the fundamental,	
k_{wrv}	Rotor winding factor for the v^{th} harmonic	
k_{wsp}	Stator winding factor for the fundamental	
k_{wsv}	Stator winding factor for the v^{th} harmonic	

L_{dR}	Differential leakage inductance	H
L_{end}	Length of the end winding	m
L_{eR}	End-ring leakage inductance	H
l_{er}	Length of the end ring section	m
L_l	Leakage inductance	H
L_s	Stator self-inductance	H
L_s^t	Stator transient inductance	H
L_{slR}	Stator slot leakage inductance	H
L_{stk}	Stack length	m
m	Number of phases	
N_R	Number of rotor slots	
N_S	Number of stator slots	
n_s	Number of conductors per slot	
p	Number of pole pairs	
P	Number of poles	
P_{cuR}	Rotor copper loss	W
p_w	Number of poles for which the stator is wound	
q	Slots per pole per phase	
R_R	Rotor bar resistance	W
R_s	Stator phase resistance	ohms
T_e	Electromagnetic torque	Nm

T_L	Load torque	Nm
T_{max}	Breakdown torque	Nm
v_{dr}^{e}	Rotor d-axis voltage in the rotating reference frame	V
v_{ds}^{e}	Stator d-axis voltage in the rotating reference frame	V
v_{qr}^{e}	Rotor q-axis voltage in the rotating reference frame	V
v_{qs}^{e}	Stator q-axis voltage in the rotating reference frame	V
V_{smax}	Maximum allowable voltage limit	V
W	Number of series turns per phase	
$w_{tr_{min}}$	Minimum rotor minimum tooth width	m
$w_{ts_{min}}$	Minimum stator minimum tooth width	m
X_m	Magnetising reactance	ohms
X_s	Stator leakage reactance	ohms
y	Coil pitch in the number of slots	
α_i	Flux density shape factor	
ζ	Coil axis	
Θ_s	Stator winding MMF	AT
λ	Stator active stack length to bore diameter ratio	
λ_{slR}	Stator slot leakage coefficient	
λ_{dR}	Differential leakage coefficient	
λ_{eR}	End winding leakage coefficient	
μ_o	Permeability of free space	H/m

v	Harmonic order	
τ	Coil pitch for a full pitch winding in the number of slots	
τ_r	Rotor time constant	s
$\hat{\phi}_m$	Maximum value of the air gap flux over a full-pitch winding	Wb
ψ_{dr}^e	Rotor d-axis flux in the rotating reference frame	Wb
ψ_{ds}^e	Stator d-axis flux in the rotating reference frame	Wb
ψ_f	Flux-linkage due to PM	Wb
$\hat{\psi}_m$	Flux linkage of a single-phase	Wb
ψ_{qr}^e	Rotor q-axis flux in the rotating reference frame	Wb
ψ_{qs}^e	Stator q-axis flux in the rotating reference frame	Wb
ω	Excitation electrical frequency	$rad\ s^{-1}$
ω_r	Rotor speed	$rad\ s^{-1}$
ω_e	Synchronous frequency	$rad\ s^{-1}$

Chapter 1

General Introduction

1.1 Introduction

The electrification factor, defined as the percentage of the on-board electric power to a vehicle's total power, has been consistently increasing since the advent of the use of automobiles. An increase in the electrification factor is inversely proportional to the emissions of the automobile. Early attempts to increase this involved replacing hydraulic power steering systems with electric steering, motor drive air-conditioning compressors as opposed to belt-driven compressors, and replacing mechanical pumps with electric pumps. All of these are non-propulsion loads and their electrification improves the electrification factor in increments of 15-20%. Electrification of the propulsion loads produces the highest improvement of the electrification factor in the order of 50-70% with fully electric vehicles (EVs) having a near 100% electrification factor. EVs offer the best solution to meet the increasingly stringent emission norms, which are only set to require further reduction of emissions in the years to come [EMA14]. Lack of charging infrastructure, relatively poor battery power densities, the years and capital spent on internal combustion (IC) engine research and development prevent the immediate and widespread adoption of EVs. In the interim, hybrid EVs (HEV) offer a path to meeting emission norms while maximizing the efficiency potential of IC engines. Different levels of hybridized vehicles are in production. In conventional automobiles, there are two separate machines. One of the machines is a high torque machine for cranking the engine, known as the starter, and the other for charging the on-board battery when the engine is operating at higher speeds, known as the alternator. As the electric loads become higher, the alternator rating increases and this presents an opportunity to combine these machines into a single starter-generator machine. Vehicles equipped with such machines are called micro hybrids. 12V micro-hybrid EVs incorporate a starter-generator with start-stop functionality, limited regeneration, and low fuel consumption reduction potential. 48V architectures offer a higher level of hybridization with a larger starter-generator machine that can provide start-stop functionality, regeneration over a wide engine speed range, and a moderate torque boost capability thus offering significant fuel saving [SCH17]. These mild-hybrid vehicles offer a good short term opportunity to meet emissions targets with modest fuel saving. This thesis explores the potential application of the induction machines for starter-generator applications for mild-hybrid vehicles. The thesis particularly addresses the contradicting and simultaneous requirement of high torque capability in the low-speed region and a

wide flux weakening range of operation by the use of electronic pole changing windings to double the flux weakening region of operation while preserving the other benefits afforded by the induction machines by employing 6-phase windings. Additional improvement in the torque capability by the 3rd harmonic current injection is shown.

In Section 1.2 different degrees of hybridization are discussed and the various machines and methods to meet the demands of mild hybrid electric vehicles are discussed in the sections that follow.

1.2 Hybrid Electric Vehicle System

One way to classify hybrid electric vehicles is by the extent to which electrical machines play a role in the propulsion or drive train of the vehicle. A pictorial representation of such a classification is depicted in Fig. 1.1. The various locations of machines, vis-à-vis the internal combustion engine, used in hybrid vehicles architectures, are shown in Fig. 1.2. Typically, in propulsion systems, the engine or turbine is designed for the peak load demand. This demand for peak load, however, occurs only during a short period in operation and the system then runs inefficiently during other times. This is because the engine is directly coupled to the thrust transferring device like the wheels of an automobile. Hybrid propulsion systems combine an electrical machine and an engine or turbine in such a way that each of them is running at their most optimum conditions. To enable this, hybrid propulsion systems have more than one source of energy, such as a flywheel, fuel cells, engines, etc. on board the moving system [EMA08]. Broadly, there are two main categories of hybridization, series hybrid and parallel hybrid vehicles. Distinguishing the two classes of hybrid vehicles are the roles played by the electric motor and the internal combustion engine in propulsion. The classification of different hybrid systems is described in the next few sections.

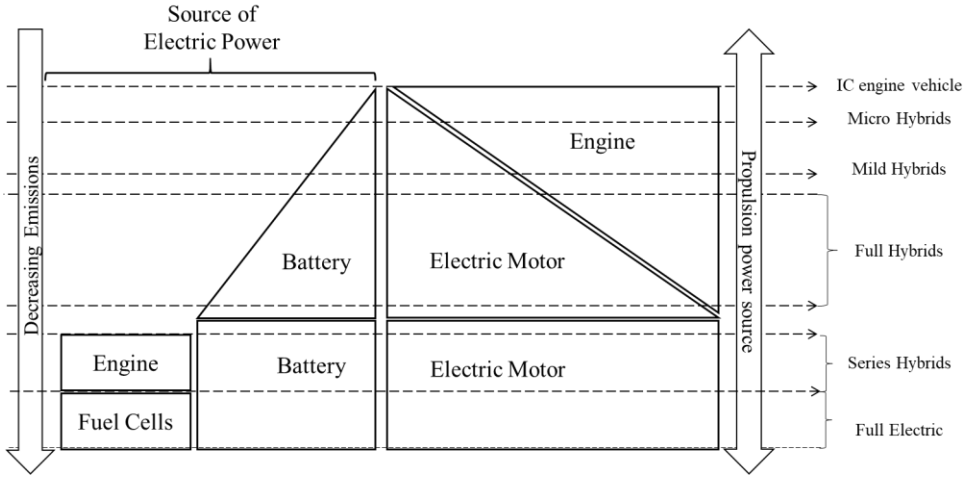

Fig. 1.1 Vehicle Classification by degree of hybridization [GAN10].

1.2.1 Series Hybrid Vehicles

The series hybrid vehicles use the electrical motor as the prime mover coupled to the transmission and the internal combustion (IC) engine as the power generation equipment, the IC engine, and the motor is decoupled by the energy storage system that is placed between them. This affords complete flexibility to run the IC engine and the electric motor transmission at their peak efficiency levels to maximise the overall system efficiency. For instance, in such an architecture the vehicle may operate as a pure electric vehicle with the electric motor drawing power only from the battery for propulsion during slow speeds with the IC engine remaining idle. However, during acceleration, the IC engine may be operated at its peak efficient point to compensate for the power being drawn from the battery and also recharge the battery if surplus power is produced. The motor can also be used as a generator to recharge the battery during deceleration through regenerative braking. The functioning of the IC engine over a narrow speed and high-efficiency regime eliminates the need for a clutch and multi-speed transmission and this improves the fuel economy in comparison to a conventional vehicle.

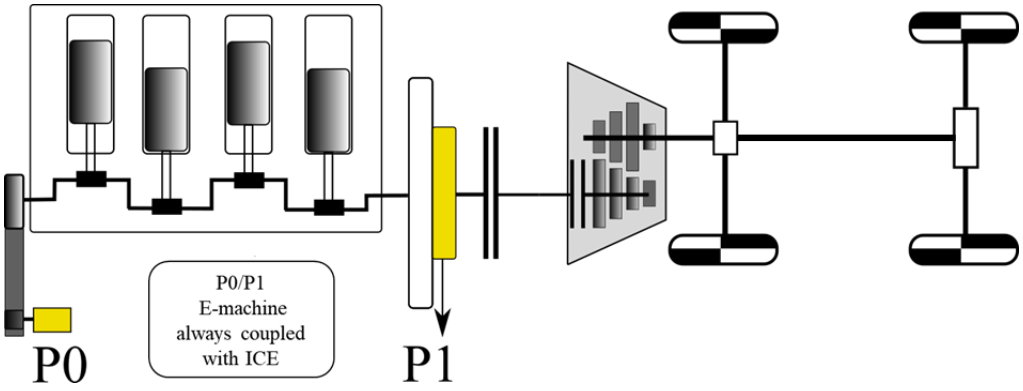

(a) P0 and P1 architecture

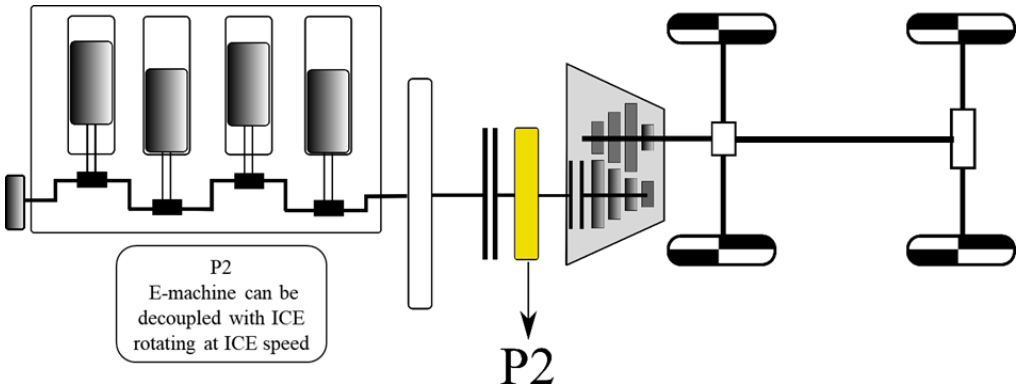

(b) P2 architecture

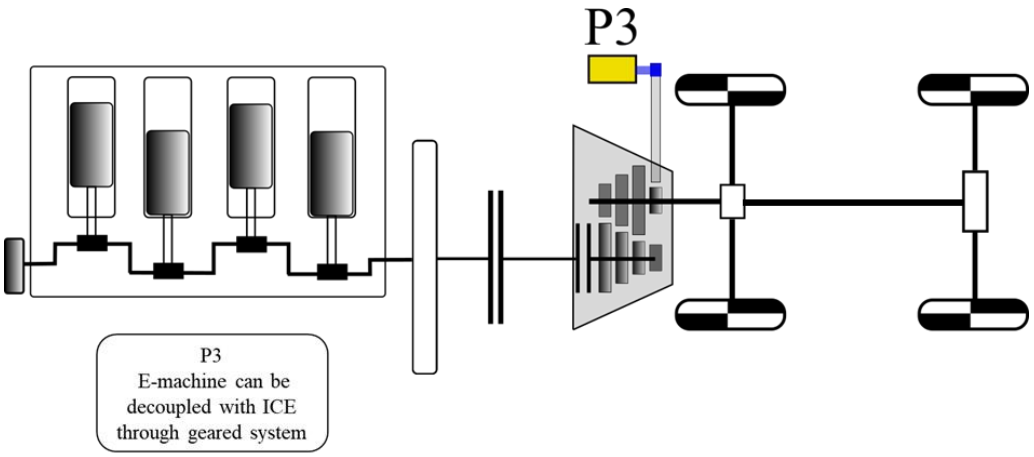

(c) P3 architecture

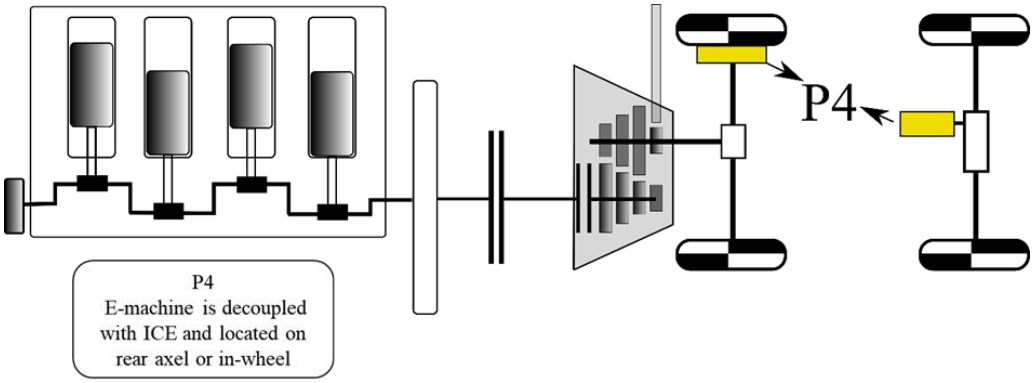

(d) P4 architecture

Fig. 1.2 Various machines in Hybrid vehicles [LEE18].

1.2.2 Parallel Hybrid Vehicles

In parallel hybrid systems, as shown in Fig. 1.1, the extent of the IC engine's contribution to propulsion results in different kinds of parallel hybrid vehicles. The full hybrid vehicle has both the IC engine and the electric motor capable of producing the full power requirements for propulsion independently. This architecture results in the elimination of the generator that was previously coupled to the IC engine in the series hybrid system for energy conversion. It does, however, necessitate a transmission system between the IC engine and the wheels. The electric motor or the IC engine may be selectively used for propulsion based on the peak efficiency point and the load demand. The reduction in conversion stages improves the overall efficiency of the system.

In mild hybrid systems, the electric motor is used supplementary to the IC engine and rather than producing total power required for the propulsion of the vehicle. The electric motor can provide what is known as a boost torque for augmenting the IC engine during high load conditions. In addition, the electric motor is also used as a starter/generator for frequent cranking of the IC engine

In micro-hybrid systems, the electric motor provides no propulsion power at all. Instead, while the IC engine provides all the power needed for propulsion the electric motor is used as a starter/generator for frequent cranking of the IC engine as well as for powering auxiliary loads [GAN10].

As is apparent each of these systems has its unique advantages and disadvantages. The choice amongst the various architectures appears to be as much an exercise in the economy as it is in ease of engineering and availability of technology.

1.2.3 Mild Hybrid Vehicles

In the series hybrid or the full hybrid vehicles, the fuel efficiency gained is superior to the mild or micro-hybrid. The amount of disruption needed relative to the conventional IC engine vehicle is also the most in these architectures compared to a mild or micro-hybrid. Micro hybrid systems are already widely used today with the Lundell generator being the machine of choice in many systems. The mild-hybrid system, on the other hand, allows for the least disruption of the vehicle architecture for the maximum benefit. As reported in [GAN10], mild hybrid systems have shown fuel economy benefits in the range of 15% to 25%. The mild-hybrid system can be arranged in one of two possible arrangements defined by the method of coupling the electric machine to the IC engine. As seen in Fig. 1.2(a), the electric machine could be linked to the IC engine with a belt/chain/gear drive mechanism, also called the Belt-Integrated Starter-generator (B-ISG) or be arranged in a way that allows for it to be decoupled from the IC engine via a clutch mechanism also called the Crankshaft-integrated starter-generator(C-ISG). The B-ISG are the machines in the P0 or P1 location in Fig. 1.2(a). The machine P2 is the C-ISG as shown in Fig. 1.2(b). The basic application of the C-ISG is in mild hybrids, where the rotor is directly fitted on the crankshaft in place of the flywheel. This drive unit achieves its full hybrid functionality (starting, electrical propulsion, regeneration and boost) in combination with a mechanically integrated combined clutch and damper between the combustion engine and the electric motor. With its high torque, this electrical drive can not only start-up heavy combustion engines at cold-start but also restarts the combustion engine very quickly and conveniently during electric driving. While the vehicle is being driven electrically and regenerating, an additional clutch disconnects the combustion engine and the powertrain is provided with torque from the electric motor exclusively. The machines used for B-ISG or C-ISG applications share the feature of having a large diameter to length ratio compared to conventional machines due to the restriction of the axial space available in the location near the engine where the machines are to be accommodated.

1.3 Electrical Machines Topologies for Starter-generator Applications

The starter-generator machine, as the name suggests, needs to able to start the IC engine as well as generate the power from the IC engine during other times. Within the motoring mode of operation of the IC engine, the starter-generator machine has the dual functions of providing torque required for cranking of the engine and also to provide torque assist to the IC engine at high speeds. The torque-speed range over the motoring mode of the starter-generator machine is shown in Fig. 1.3. The peak torque is required for a small range of low speeds. The operation region of the starter-generator machine is however over a large range of speed meaning that the machine needs to be designed with a wide flux weakening region. The start-stop feature of mild hybrid vehicles requires that the starter-generator machine must be able to frequently crank the engine even in cold temperatures when the cranking torque is higher. The quick starting and cold starting requirements will establish the values for the peak motoring torque and the maximum motoring torque curve for the electric machine. The peak torque value is determined by the time to crank the engine to the idling speed. This is in the range of 250 to 400 milliseconds depending on the application [WAL04]. The torque values for performing launch assist or torque boost are engine-specific. The machine also needs to generate power for battery charging during regenerative braking at high-speeds or while cruising on the highway. The machine is also used to regulate the state of charge of the battery. As seen in Fig. 1.4, the starter-generator machine needs to have fairly high efficiency at higher speed ranges in generating mode. Apart from the function of a starter and generator, the machine also needs to provide power to auxiliary loads like water pumps, air conditioning etc. This results in the traditional 12V battery system unable to supply the necessary power at reasonable current. The automotive industry is adopting a 48V system that ensures that the voltage level is still below the permissible safe voltage limit of 60V while ensuring that the current levels result in a reasonable wire gage. Lower current levels keep the power cable cross-sections low and thus less expensive. The upper limit of 60V, including voltage spikes, is based on the safe operating voltage below which additional, expensive insulation systems for electrical shock protection are not required. This ensures the cost of implementing a sub-60V system remains reasonable. Staying in the 48V region means the system design can be done as a 12V system would be given that the wires are rated for 60V. However, additional precautions for short circuit faults need to be taken into account [MAL04].

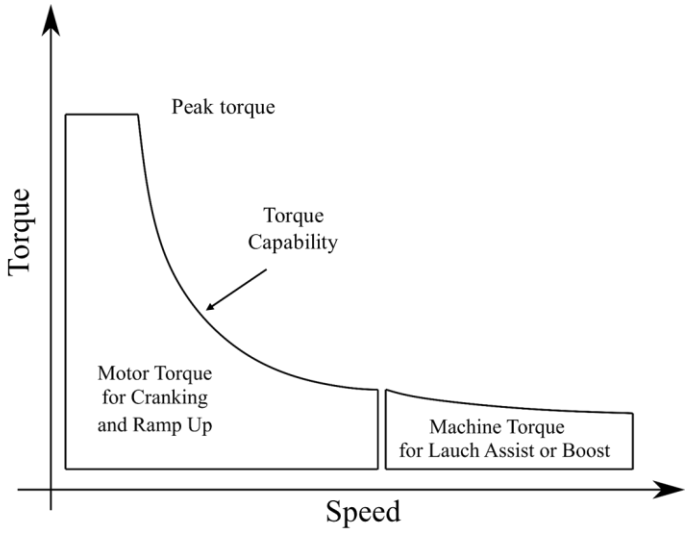

Fig. 1.3 Motoring requirements [WAL04].

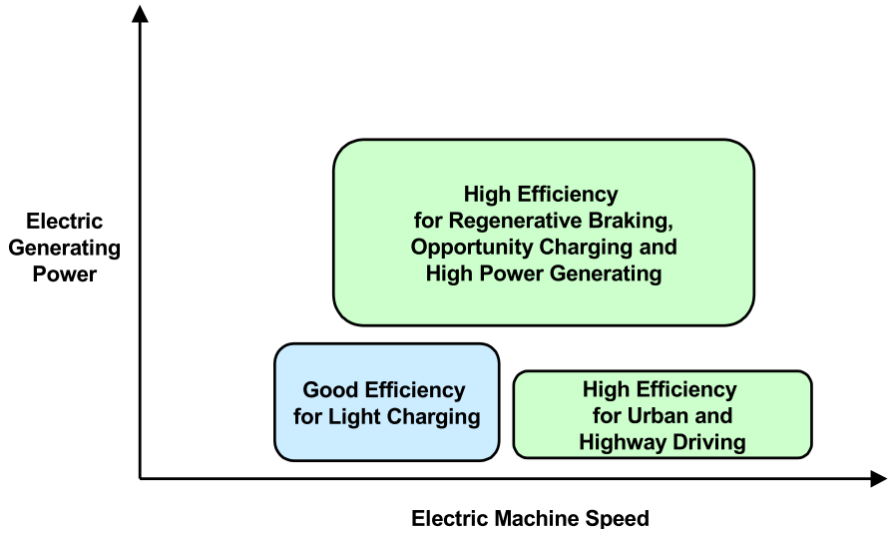

Fig. 1.4 Generating requirements [WAL04].

In summary, the challenges for the starter-generator machine design include:

1. High torque/power density
2. Low voltage, high power design resulting in a high current design
3. Wide speed flux weakening region, 5-6 times base speed
4. Good thermal performance in high ambient of 105ºC
5. High torque at low speed for cold cranking

Different machine topologies have been considered in literature for starter-generator applications [CAI04] [CAI06]. The most commonly investigated machines are claw pole machines, PM synchronous machines, switched reluctance machines (SRM) and induction machines. Their relative merits for this application are compared in this section.

1.3.1 Claw Pole Machine

Claw pole synchronous machines are well established as Lundell alternators in conventional IC engine vehicles. The claw pole machine is a wound rotor machine which gets its name from the rotor structure composed of two interlocking claw-like structures as shown in Fig. 1.5.

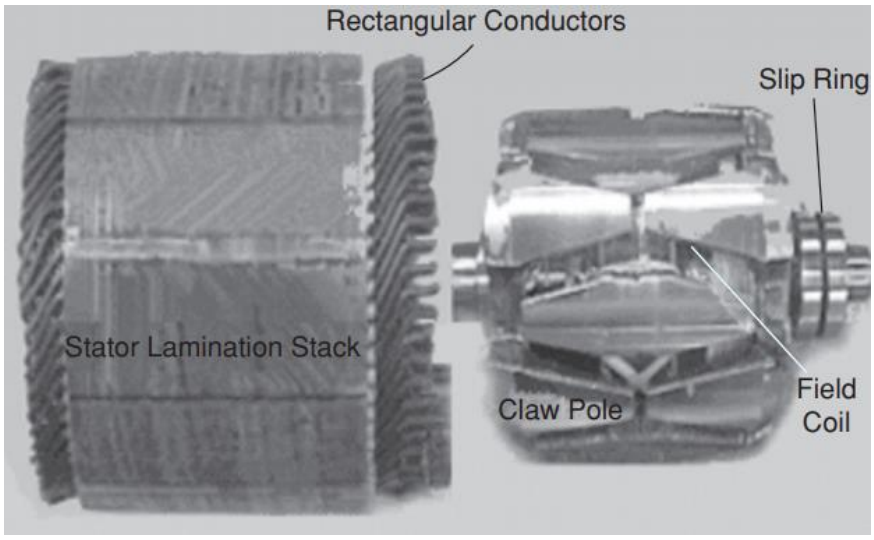

Fig. 1.5 Parts of a claw pole machine [CAI06].

The rotor winding is housed between the claw poles and fed via slip rings. DC current in the field windings produces axial fields that flow axially through the rotor core and cross the air gap radially to link with the stator windings. The stator is housed with conventional windings. The rotor structure results in high leakage inductance and this limits the power to which this machine can be rated. The leakage can be reduced with the use of permanent magnets housed between the two claw poles and with dual-field coils. Claw pole machines have high flux weakening regions due to the ability to control the flux. However, at higher speeds, the spatial harmonics in the MMF cause eddy current losses on the rotor surface which is usually solid [CAI06].

1.3.2 Permanent Magnet Synchronous Machines

While a claw pole machine is also a synchronous machine, the PM synchronous machines have high efficiency due to the absence of field windings to produce the working flux. Additionally, with PM machines, the stator can be wound with fractional slot or tooth wound windings which reduces the overall axial length of the machine. Surface eddy current losses remain an issue at high speeds especially when fractional slot stator windings are used. While the efficiency is the highest amongst other machines at low-speed high torque operation, in the flux weakening region, large currents in *d*-axis are required to reduce the flux and this results in high stator copper losses and a higher risk of demagnetization as well as poor fault tolerance during failure of control.

Depending on the structure of the rotor, PM machines are classified as surface mount machines (SPM) or as interior permanent magnet machines (IPM). In the former, the magnets are mounted on the rotor surface and in the latter embedded into the rotor laminations as shown in the rotor cross-sections of Fig. 1.6(a) and Fig. 1.6(b) respectively. SPM machines are limited in the application to ISG or BSG applications due to their limited flux weakening range of operation. This is due to the voltage limit of 48V for this application. Solutions to get around this limitation involve the use of a DC-DC converter to boost the DC bus voltage at high speeds. The magnets also have a mechanical limitation at high speeds.

IPM machines have buried magnets lending the rotor better mechanical strength at high speeds. The location of the magnets within the rotor lamination also produces additional reluctance torque that adds to the torque created by the permanent magnets. This results in a high torque density and high-efficiency machine with a wide speed flux weakening region [RIC07] [KAM13] [PEL12] [SCR05]. However, the magnets within the rotor structure require large *d*-axis currents to demagnetise resulting in poor efficiency in the flux weakening region.

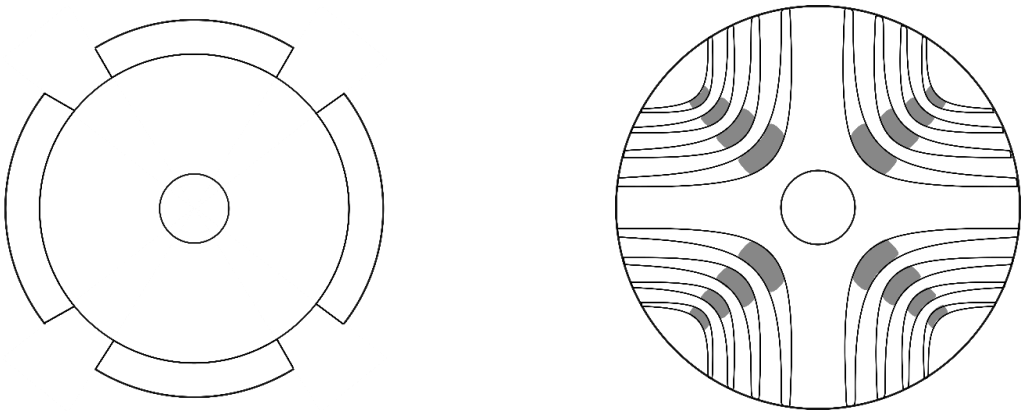

(a) Surface mount rotor structure. (b) Interior permanent magnet structure.

Fig. 1.6 Rotor structures of permanent magnet machines.

1.3.3 Switched Reluctance Machine

A typical cross-section of a switched reluctance machine (SRM) is shown in Fig. 1.7. The rotor structure of the machine is robust and is suitable for high-speed operation. The SRM is however known to be prone to high torque ripple and acoustic noise. Methods to limit the noise and torque ripple by suitable current shaping and harmonic injection are being investigated [ZHU17] [FEN19]. SRMs also require small air gaps for achieving high torque density. In starter-generator applications, additional vibrations from the engine shaft require a larger air gap that compromises

the torque density of the machine. The efficiency of the SRM is comparable to that of an induction machine. A bulk of the losses like the case of an induction machine are due to the stator copper loses.

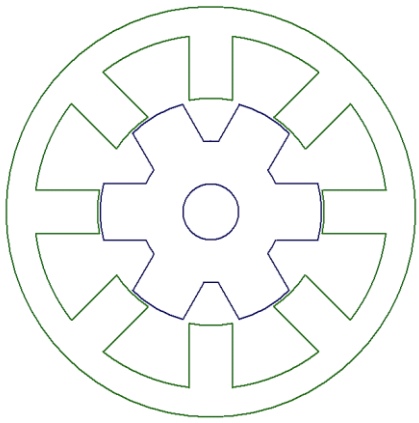

Fig. 1.7 Switched reluctance motor cross-section.

1.3.4 Induction Machine

Induction machines can have wound rotors where the rotor currents can be controlled externally via brush and slip ring arrangements. This is a limitation for operation at high speeds and is not preferred. Alternatively, cast aluminium or copper rotors with shorted bars can be used.

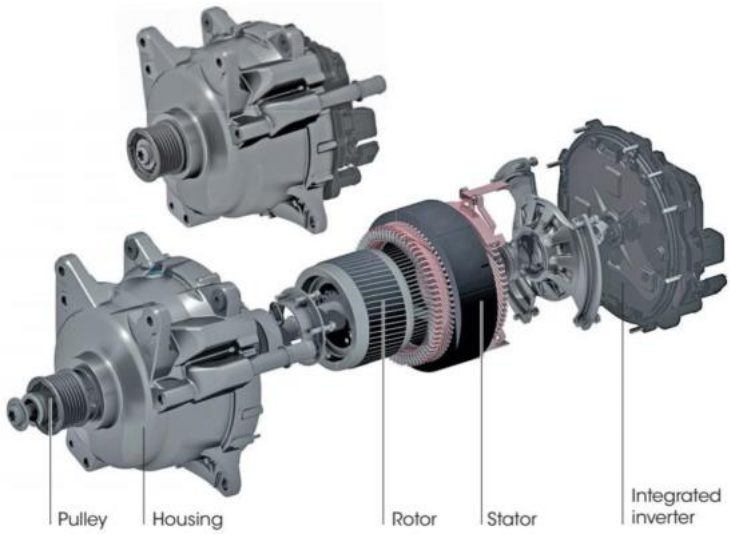

Fig. 1.8 Exploded view of induction machine used in a Continental BSG product [WEB16].

This results in a low cost and mechanically robust rotor. Induction machines have high overload capability which makes them a suitable candidate for BSG applications where high starting torque is required during cranking for overcoming the engine breakaway torque. At such high torques, the slip is high and this results in poor power factor and high stator losses. However, this operation is only intermittent and of short durations of 300ms. Operation on the envelope of the

torque-speed curve is usually for short term duty. After the engine is cranked, the operation of the induction machine is within the torque-speed envelope. The flux weakening range of induction machines is limited to 3-5 times the corner speed and this limits the amount of power that can be generated at high-speed operation. Additionally, at the high-speed operation, the magnetising current is very low relative to the q-axis or the torque component of the current resulting in difficulties and instability of control [CHE02].

1.3.5 Comparison of Various Machines for Starter-Generator Applications

A qualitative comparison of the machines discussed is shown in TABLE 1-1. While the SPM machine cannot meet the wide speed operating range required in starter-generator applications, it is included in the comparison for completeness.

TABLE 1-1 QUALITATIVE COMPARISON OF MACHINES FOR STARTER-GENERATOR APPLICATIONS

Parameter	Claw pole machine	SPM machine	IPM machine	SRM	Induction machine
Efficiency	Low	High	Very high	Low	Low
Torque density	Low	High	High	Low	High
Flux weakening range	High	Low	High	High	High
Robustness	Low	Low	High	High	High
Cost	Low	Very high	Very high	Low	Low
Cranking Overload capability	High	Low	Low	Very low	Very high
NVH	Low	Low	Low	Very high	Medium

The permanent magnet machines have the highest efficiency and torque density amongst all the machines The SPM is the worst performer when compared across the wide speed operating range, all other machines being comparable. The induction machine and the SRM have the most robust rotor structures followed by the IPM. Both the claw pole machine (due to slip-rings) and the SPM (due to surface magnets) have poor rotor structural integrity. The permanent magnet machines are the most expensive of all the machines due to the use of rare earth material. The induction machine stands out in overload capability with no magnets present there is no risk of demagnetisation and overload torque can be produced as long as there is a current capability of the

inverter for short duties. SRM while comparable to induction machines in all respects have the highest noise and vibration issue and coupled with the vibration of the engine make it an unattractive option. The low cost, low noise, high overload capability and ruggedness of the induction machine make it suitable for this application. The flux weakening range of operation is still limited and in this thesis that aspect is addressed by the use of pole changing windings to double the flux weakening region of operation while preserving the other benefits afforded by the induction machine.

1.4. Induction Machines for Starter-generator Applications

Induction machines are more than 130 years old with the first wound field induction machine patented in 1888 [TES88] and a subsequent patent on the squirrel cage induction motor filed in 1897 [LAM97]. Since then, numerous papers have been published to investigate and improve the performance of various aspects of the induction machine. The literature can be divided into the categories shown in TABLE 1-2 with references addressing these topics shown alongside. While the list of references is by no means exhaustive, it provides recent work in these categories, relating to research on induction machines. In this thesis, the focus is on the application of induction machines for starter-generator applications and a literature review of induction machine designs specific to this application is discussed in the following sections. As discussed in Section 1.3, the major requirement of the starter-generator machine is to provide high torque at low speed and a wide speed operating region for torque boost and regeneration. Due to the location of the starter-generator next to the engine, the axial length of the machine is also of importance. The categorisation of the literature review on induction machines for applications is shown in Fig. 1.9. The overall axial length of the machine is affected by the active stack length (which is optimised for torque) and the overhang length. This aspect is addressed by studying the use of bar conductors with hairpin windings and tooth wound fractional slot concentrated windings in Section 1.4.1 and Section 1.4.2. To achieve a wide speed flux weakening region for this application, the rotor slot shape can be optimised to improve the breakdown torque and the flux weakening region to a limited extent. A summary is provided in Section 1.4.4. The stator windings with a variable pole number provide the best method of wide speed flux weakening operation while retaining peak torque capability. Five different methods to vary the number of poles to obtain a wide speed flux weakening region are discussed in Section 1.4.5.

TABLE 1-2 CLASSIFICATION OF LITERATURE ON INDUCTION MACHINES

CATEGORIES	REFERENCES
Comparison studies	[ZHU07], [PEL12], [GUA14a], [DOR12]
Impact of slot/pole combinations	[YEP16], [KRO31], [BES09], [MOR13], [DAJ13]
Novel winding and geometrical structures	[HAO17a], [HAO17b], [NEE95], [PAT14], [CHO01], [SPA13], [EAS08], [SUN16]; [ABD11]; [KON16]; [KIR07]; [PER12]; [ZHA00], [CAV14] [MAG12] [ZHA00] [NEE95] [LIW05] [AKI94] [JUN15] [WAN05] [BOJ16] [BOJ16a]
Parameter determination and physical phenomena	[GUN16a], [GUN16b], [ZHU15], [PER12], [XIA08]
Modelling and analysis (modelling methodologies, optimization studies, analytical formulations)	[BIA97], [CAI14], [ARN15], [TIE05], [DOR15], [MEN14], [KIM98], [GUA14b], [CHO01], [XIA08], [NEE95], [BRA16]; [DOR12], [REF08]
Impact of drive cycles on performance (efficiency map improvement, impact of drive cycles)	[CPT16], [CAI13], [GUN16c], [HER09], [BIA98],[CAV16], [CAV16a], [BOJ14], [CHE01]
Impact of inverter and control methodologies (impact of inverter topology, control system,)	[AOU14], [LOR90], [OSA96], [WAL93], [WAL94], [BUY11]

1.4.1 Fractional Slot Concentrated Winding Induction Machines

Permanent magnet topologies with tooth wound stators are well known. Tooth wound machines have the advantage of shorter end winding lengths and more cost-effective and have lower losses due to reduced stator resistance. Higher-order harmonics are usually used to produce useful torque while the sub-harmonics cause eddy current losses on the surface of the magnets when these winding are used with permanent magnet stators. With induction machines, however, the subharmonics create significant torque ripple and high eddy current losses in the rotor bars (which have much higher conductivity than permanent magnets).

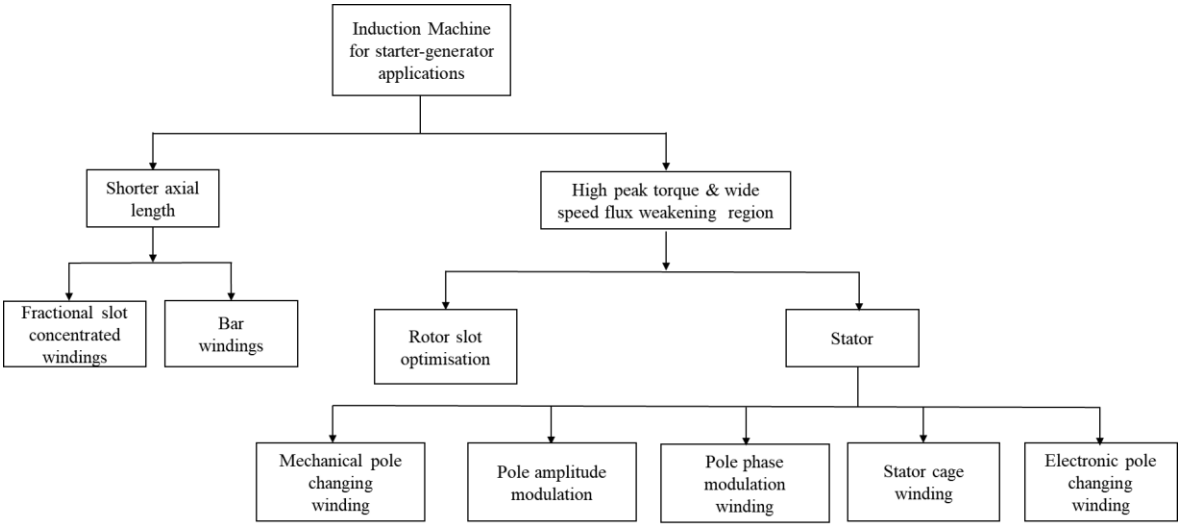

Fig. 1.9 Categories of literature review of induction machines for starter-generator applications.

As such, when tooth windings are used in induction machines, great care must be taken in the design of the windings to eliminate the harmonics that do not contribute to torque production while preserving the benefits of tooth windings.

TABLE 1-3 CONFIGURATIONS OF FRACTIONAL SLOT CONCENTRATED WINDINGS OF INDUCTION MOTOR

Method	References	Advantages	Disadvantages
Conventional FSCW	[REF08], [GUN14], [BAC15]	Low cost, short end windings	High MMF harmonics, parasitic torque, high rotor eddy losses
Wound-rotor FSCW	[EAS08], [BIA12]	Ability to select working harmonics and reject all parasitic harmonics	Wound rotor requires slip-rings and reduces reliability and ruggedness
Phase shifted stator windings with different turns per coil	[DAJ11], [DAJ13], [PAT14]	Sub harmonics can be eliminated with uneven tooth width. Higher-order harmonics amplitudes are reduced	Complex stator winding in the slots. End winding region connections are complex and lead to a longer overall length
Dual stator slot layers and multilayer windings	[SUN15], [DAJ16]	Shorter stack length, subharmonics are eliminated	Higher-order harmonics still present. High slot leakage, poor winding factor and low magnetising inductance result in higher losses.
Multiphase modular induction machine	[ABD12]	Higher-order harmonics can be eliminated by suitable rotor design, fault tolerance	30% poorer power density, low winding factor
Stator cage winding	[DAJ14], [PAT15], [PAT16], [PAT16a], [SPA16], [GER15]	Very low space harmonics, cheap construction, programmable pole and phase number	A large number of high current PE devices required. High AC losses in the stator winding when operating at higher frequencies

Methods of reducing the MMF harmonics of FSCWs for induction machines from literature, their relative advantages and disadvantages are summarised in TABLE 1-3.When conventional FSCWs similar to those used in permanent magnet machines are used, the MMF harmonics cause high torque ripple and rotor losses [REF08], [GUN14], [BAC15]. A wound-rotor induction machine that is wound for the same number of poles as the order of the working MMF harmonic of the FSCW induction machine can eliminate all the losses and torque ripples created from the sub-harmonics and the higher-order harmonics. However, this requires a slip ring rotor or a shorted wound-rotor induction machine which reduces the ruggedness of the induction machine as well as reducing the rotor slot fill factor compared to what could be achieved with a cage rotor [BIA12]. This method, however, lends itself well to linear induction machines where the end effects due to the finite length of the stator create significant torque ripple and eddy current losses when copper or aluminium sheets are used as the translator [EAS08]. The procedure to eliminate the harmonics from the MMF spectrum of FSCWs involves the cancellation of the undesirable harmonics using two or more sets of windings, multi-layer stator windings, multi-phase machines or a combination of these, as seen from TABLE 1-3. This process can be explained using the widely used 12-slot 10-pole FSCW. A two-layer layout of the 12/10 winding is shown in Fig. 1.10.

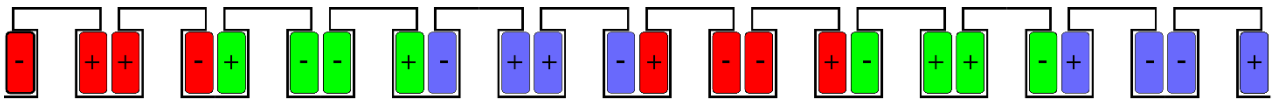

Fig. 1.10 Three-phase winding layout of a 12-slot 10 pole FSCW machine

The MMF waveform and the harmonic spectrum of this winding layout are shown in Fig. 1.11(a) and Fig. 1.11(b), respectively. If this winding is used in its present form with a squirrel cage rotor, the dominant harmonics will produce torque and depending on the speed of the rotor there will be significantly high torque ripple and rotor eddy current losses. To attenuate the harmonics (in this case the 7^{th} harmonic is cancelled since the fundamental is the 5^{th} harmonic for a 10-pole machine) two sets of identical windings spatially shifted by an angle α_w result in the cancellation of the MMF harmonics. This is shown in Fig. 1.12. The reduction of the MMF harmonics, while maintaining the amplitude of the fundamental is achieved by the reduction of the winding factor of the harmonics that are being attenuated. The variation of the winding factor of the first 3 harmonics with a varying shift between the windings is shown in Fig. 1.13. The combination of these two windings into one stator is shown in Fig. 1.14.

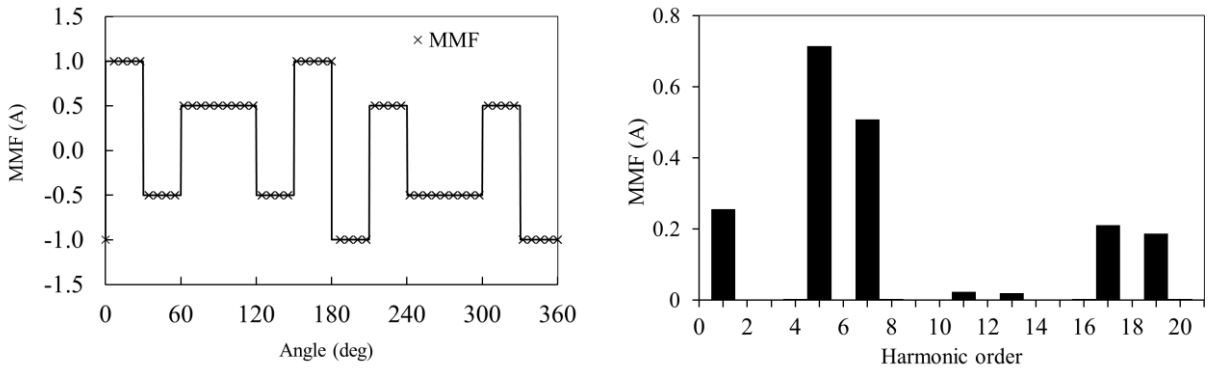

(a) MMF waveform (b) Harmonic spectrum

Fig. 1.11 MMF waveform and spectrum of the 12/10 winding layout.

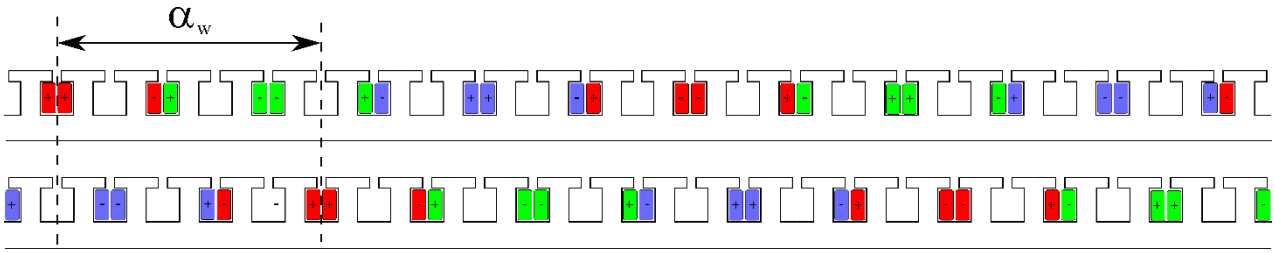

Fig. 1.12 Winding layout of 24-slot 10-pole stator winding with a spatial shift of α_w

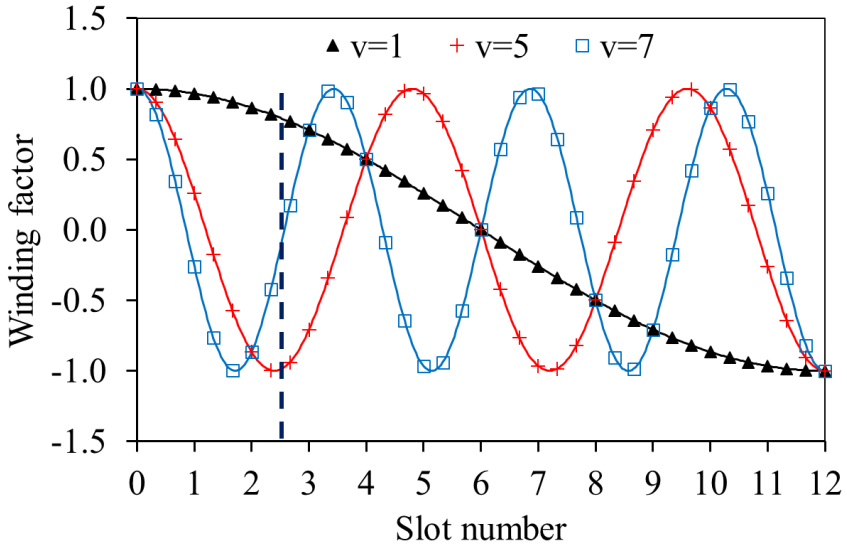

Fig. 1.13 Winding factor variation of the first 3 harmonics of the 24-slot 10 pole winding.

The associated MMF waveform and the harmonic spectrum of this combined winding layout is shown in Fig. 1.15. The 7th harmonics are significantly attenuated and the sub-harmonic is attenuated slightly. The method to reduce the sub-harmonic and further reduce the 7th harmonic amplitude is disclosed in [DAJ13a].

This is done in two steps:

1. The 7th harmonics can be reduced further by using teeth with uneven width to enable a phase shift slightly higher than 2.5 slot width so that the winding factor of the 7th harmonics is zero as seen from Fig. 1.13. This does not attenuate the sub-harmonics.
2. The sub-harmonic can be reduced by using a different number of turns per coil for the coils sharing the slots belonging to different phases. The ratio of the turns is between the phases is between 0.5 and 1 [DAJ13a].

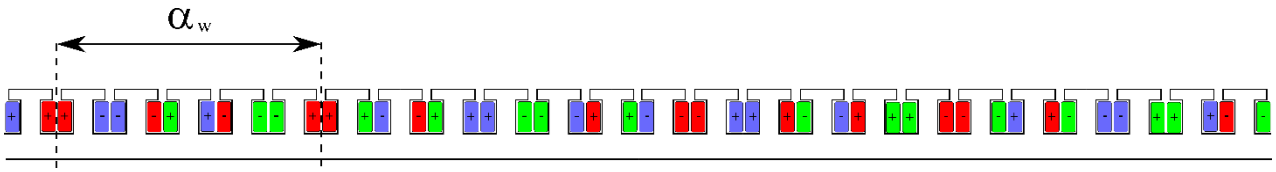

Fig. 1.14 Combination of both winding layouts.

This reduces the ability to automate the winding of the coils and also does not reduce the higher-order harmonics which still cause rotor losses. The windings proposed in [DAJ11] [DAJ13] [PAT14] that have the lowest harmonic content have stator windings which have a coil span of two slot pitches. This results in some degree of overlap of the windings. To overcome these limitations and reduce the overall axial length of the winding a dual stator winding where the multi-layer winding is arranged in two different radial locations is proposed in [SUN15]. The stator cross-section with the winding arrangement is shown in Fig. 1.16.

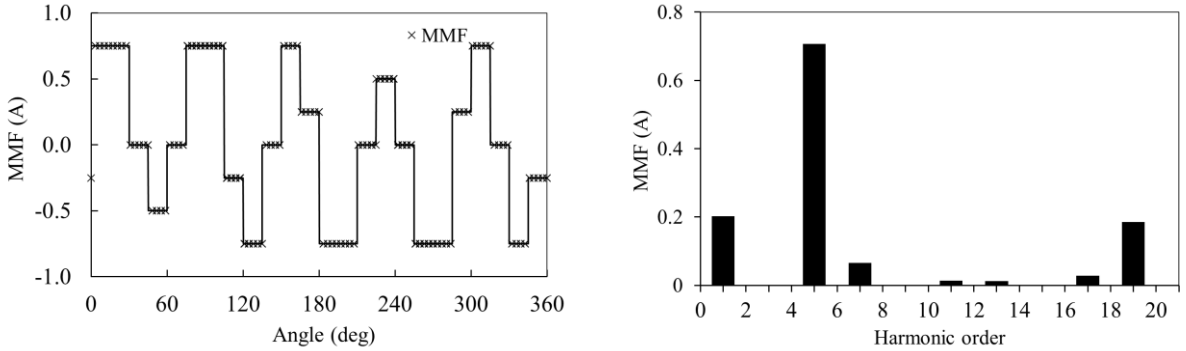

(a) MMF waveform (b) Harmonic spectrum

Fig. 1.15 MMF waveform and spectrum of the 24/10 winding layout.

Compared to the two-layer winding proposed in [DAJ13], the winding of [SUN15] eliminates the 17th harmonic. The arrangement of the winding in dual-slot layers as shown in Fig. 1.16 results in a shorter stack length. However, a dominant 19th harmonic remains and this result in rotor losses. Additionally, the fundamental winding factor of the 24-slot 10-pole winding is 10% lower than and equivalent distributed winding machine. This results in lower magnetising inductance and

subsequently lower overall efficiency. In [MOR15a], a dual stator winding in a wye-delta connection is proposed. The two sets of windings are housed in 12 slots are shifted to eliminate the 5^{th} and 7^{th} harmonics. The 2-pole fundamental harmonic is used for torque production. However, the winding factor of this winding is only 26% and this results in low magnetising inductance and poor efficiency.

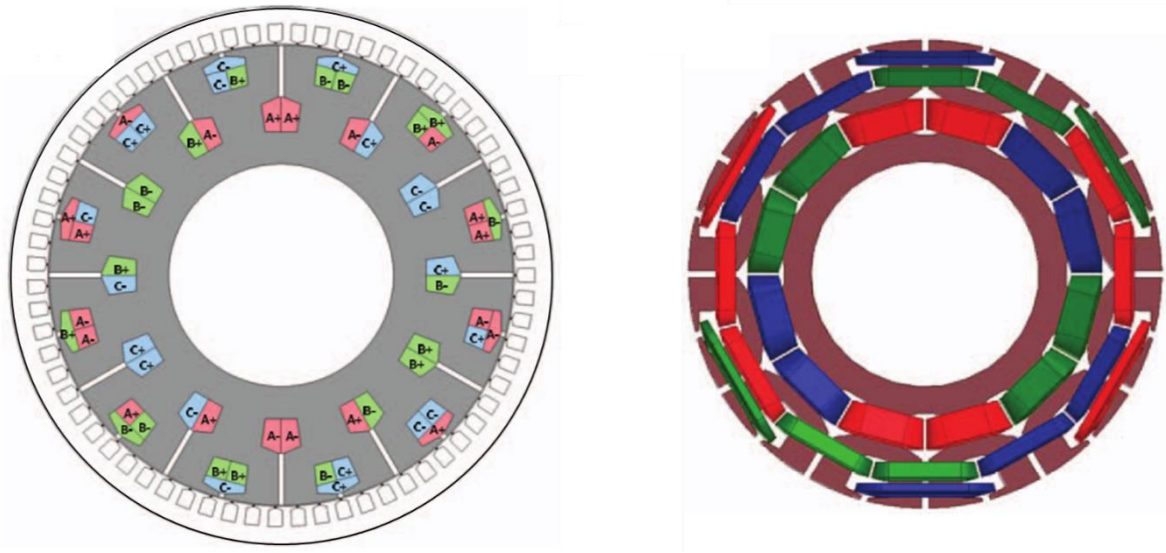

(a) Dual slot multi-layer stator winding (b) End winding connections

Fig. 1.16 Cross-section showing the winding layout of the dual-slot multi-layer stator [SUN15]

From the comparisons of the fractional slot windings possible for the induction machine summarised in TABLE 1-3, it is apparent that the presence of air gap harmonics of any magnitude comparable to the working harmonic results in a poor efficiency due to the rotor losses. Attempts to suppress these harmonics with multi-layer windings or phase-shifted windings results in the reduction of the fundamental winding factor reducing the magnetising inductance which reduces efficiency.

1.4.2 Bar windings

Due to the 48V, low DC bus voltage but high power required for SG applications, the phase current is usually quite high. As a result, the bar winding is used instead of stranded conductors for the stator winding. With bar conductors, hairpin windings can be used to reduce the end winding length, increase the slot fill factor and ensure a good thermal performance of the stator winding. Using bar winding required a parallel slot design, unlike a stranded winding where a parallel tooth design may be used. Bar windings also result in the lowest DC resistance due to the large conductor cross-section area. The AC resistance at high frequency is increased due to the eddy currents and

skin effect of the large area of conductors. Careful optimisation of the machine is necessary to minimise the impact of these losses on the overall performance of the machine. The efficiency map of the machine equipped with bar windings has a higher peak efficiency than the stranded winding machine. However, the efficiency is lower at high speeds due to the eddy current losses in the bar winding. While this is beneficial for the low-speed high current operating points, the efficiency of the machine is reduced in the high-speed region [JUR12] [JUR15] [BOJ16] [BOJ14] [CAV16] [CAV14] [BOJ16a]. Another advantage of the bar windings in a hairpin architecture is the inherent spacing that is achieved in the end windings of the machine. This improves the insulation life of the machine. A slot liner is needed to prevent the individual conductors from direct contact with each other within the slot. Three different kinds of slot insulation are shown in Fig. 1.17 to prevent the conductors from touching the stator walls. The B-type insulation is shown in Fig. 1.17(b) that can be used to eliminate the gaps in the corner of the conductors inherent in the S-type insulation of Fig. 1.17(a). Alternatively, a two-part insulation can be used to simplify the manufacturing process of hairpin windings using bar conductors as shown in Fig. 1.17(c). The inter conductor gap is lower as seen in Fig. 1.17(c) and this makes is more suitable for designs where the inter-turn voltages have been optimised to be as low as possible [RAH15] [RAH16].

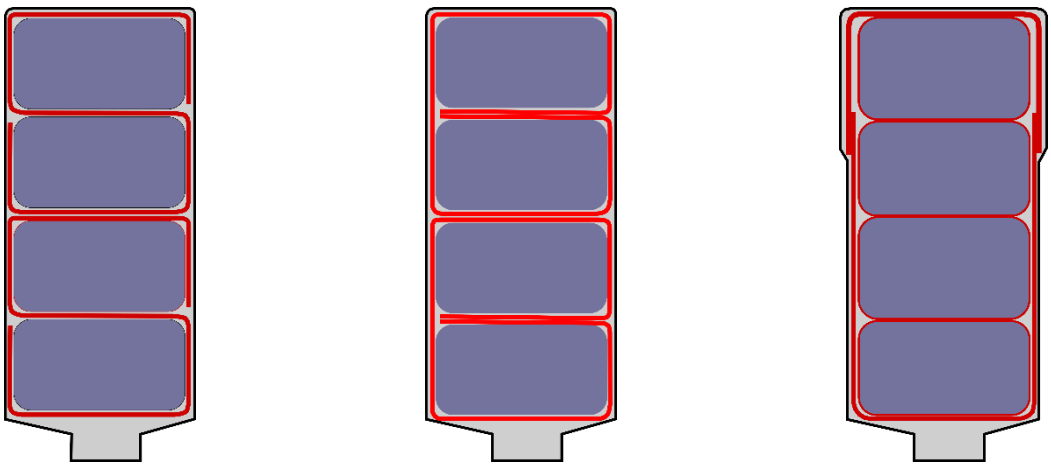

(a) S-type insulation (b) B-type insulation (c) Two part insulation

Fig. 1.17 Bar conductor insulation types.

The shape of the slot in the stator lamination needs to be slightly wider at the bottom of the slot to accommodate the second u-shaped piece of the insulation. This does not impact the saturation of the teeth because of the parallel slots necessary for accommodating bar windings. This wider slot bottom required for the two-part insulation extends into the portion of the tooth that is wider than the portion adjacent to the air gap and is unlikely to saturate. To overcome this limitation of high

eddy current losses, multiple layers of bar windings can be used to reduce the skin effect. In [BOJ16] [CAV16] [CAV16a] [CAV14] [BOJ14] [BOJ16a], a 4-layer bar winding is shown to be a good compromise between the electromagnetic performance deterioration due to the reduced slot-fill factor and the improved thermal performance due to the decreased eddy current losses. Another limitation of the bar windings is the limited number of slot pole combinations that can be used to accommodate the winding. The impact of this on the choice of the optimum number of slots is addressed in detail in Chapter 3.

1.4.3 Rotor Slot Optimisation

The operating speed range of inverter fed induction machines can be extended by operating the machine under flux weakening excitation conditions. This is achieved by the reduction of the magnetising current as the operating speed increases, to limit the terminal voltage to what is capable of being supplied by the DC bus. The family of curves which shows the operation of an inverter fed induction machine in the flux weakening region of operation is shown in Fig. 1.18. These curves assume that the inverter rated DC bus voltages reach the rated value at 1pu speed. The peak torque of the induction machine is inversely proportional to the square of the speed. This implies that to achieve a torque capability of 0.25pu at 4pu speed, the torque capability at rated speed needs to be 4 times the rated torque. Typical induction machines have 2-2.5pu breakdown torque capability resulting in a machine that needs to be significantly larger to achieve this kind of torque characteristics [ZHA00] [HAR95] [OSA96].

One method to increase the operating speed range of the induction machine requires an increase in the breakdown torque capability. The equation for the breakdown torque of the induction machine is given in (1.1) and (1.2) where X_m, p, L_l, R_s, X_s and T_{max} are the magnetising reactance, pole pairs, leakage inductance, stator resistance, stator leakage reactance and the breakdown torque respectively.

$$T_{max} \approx \frac{3}{2}\left(\frac{V_{eq}}{\omega}\right)^2 \frac{p}{2L_l} \tag{1.1}$$

$$V_{eq} = \frac{X_m}{\left[R_s^2 + (X_s + X_m)^2\right]^{\frac{1}{2}}} V_s \tag{1.2}$$

To increase the peak torque and to extend the speed range of the drive system, (1.1) points to the minimisation of leakage reactance as a key design strategy. Line fed induction machine designs have relied on the deep rotor bars to optimise the starting torque. With inverter fed induction

machines the rotor slot shape can be optimised to minimise the leakage reactance. Several papers have reached the same conclusion on the impact of the rotor slot shape and its effect on the leakage inductance and subsequently the flux weakening range of operation of the induction machine [MAG12] [ZHA00] [NEE95] [LIW05] [AKI94] [JUN15] [WAN05].

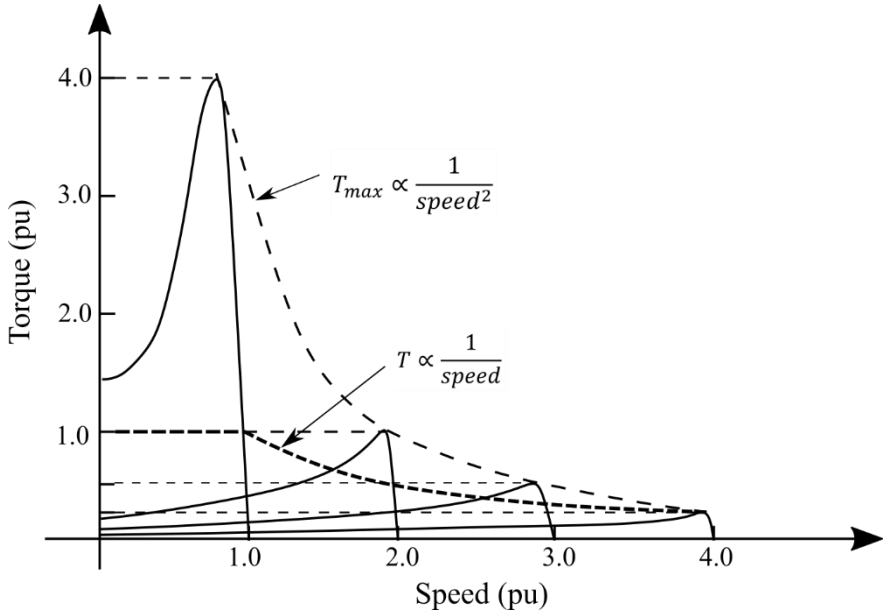

Fig. 1.18 Torque-speed curves of inverter fed induction machine showing the operation in the flux weakening region [BOL02].

For a trapezoidal-shaped rotor slot, the optimum shape of the slot is a shallow and wide slot as opposed to the narrow and deep slot commonly used in line fed induction machines. There is, however, no optimum slot shape that can maximise the breakdown torque, power factor and efficiency [JUN15]. A trade-off between these performance measures needs to be made to choose the best slot shape for the application [JUN15] [MAG12] [ZHA00]. Rotor slot shaping can improve the flux weakening range of the machine to a limited extent before other considerations of the inverter current limit become a constraint. Low leakage inductance results in an increase in the motor harmonic current components and a consequent increase in the torque ripple and copper losses [OSA96]. Another method to achieve the wide speed operating region is to reconfigure the number of poles and/or phases using mechanical or electronic means. Changing the number of poles or phases can be used to change the corner speed of the induction machine. The corner speed of an induction machine of a given stack length is inversely proportional to the number of series turns per phase. By changing the number of poles, the effective series turns per phase are changed and this results in a change in corner speed [OLD85].

1.4.4 Pole Changing Windings

Pole changing windings offer the most direct and impactful way of extending the operating speed range of induction machines in the flux weakening regions. Changing the number of poles changes the number of series turns per phase. With lower pole numbers, the corner speed and subsequently the flux weakening region of operation is increased. Different methods of changing the number of poles are compared and shown in TABLE 1.4.

TABLE 1.4 METHODS OF POLE CHANGING OF INDUCTION MACHINES.

Method	Pole Ratio	Advantages	Disadvantages	References
Separate windings	Arbitrary pole & phase number	Simple implementation, no inverter needed	Mechanical contactors result in low reliability. Poor slot utilisation	[BOL02]
Dahlander connection	1:2; same phase number	Simple implementation, no inverter needed	Mechanical contactors result in low reliability.	[BOL02] [DAH03]
Pole amplitude modulation	n:(n-1); same phase number	Six terminals, simple method to change poles	Only limited ratios of pole numbers close to each other possible	[RAW58]
Pole phase modulation	Arbitrary pole & phase number	Any pole number, phase number possible.	Higher copper losses with toroidal windings needed to realise potential. Poor winding factor at high torque with conventional winding	[BGE13] [BGE10] [SUN10].
Electronic pole changing	1:2; same phase number	Pole changing with inverter, online pole changing possible	Low winding factor with low pole number	[OSA96] [OSA97] [MOR97]

A. Dahlander connection

The Dahlander winding is a type of pole changing winding and achieves a 1:2 pole changing ratio by the reversal of current polarity in half of the higher pole number winding to achieve the lower number of poles. These two halves may be connected in star or delta connections or a combination of both. The Dahlander winding suffers from MMF cancellation when a 60^o phase belt full pitch winding is used for the higher pole number winding. When a 120^o phase belt is used, both winding configurations, have a fundamental winding factor lower than 0.85. In addition, the Dahlander winding requires mechanical contactors to change the number of poles resulting in the inability to change the number of poles during operation for continuous torque thus compromising the reliability and ruggedness that an induction machine is known to offer.

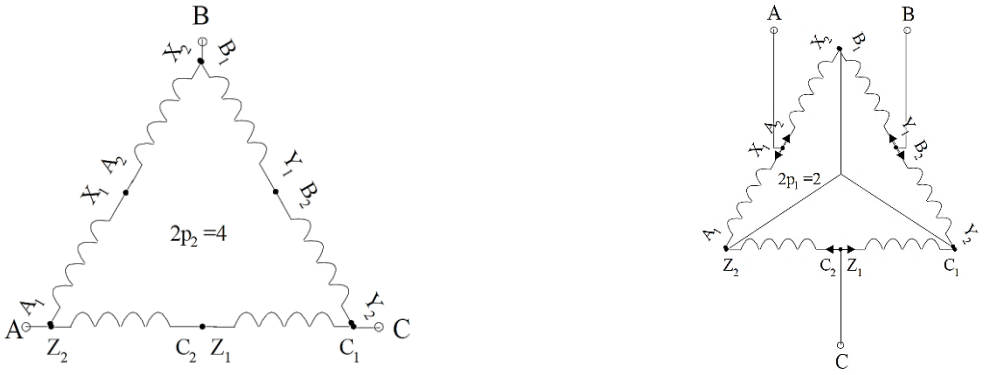

(a) 4-pole Delta connection (b) 2-pole 2Y connection

Fig. 1.19 A 4/2 pole Delta/2Y Dahlander connection pole changing winding [BOL02].

A Δ/2Y implementation of the Dahlander winding is shown in Fig. 1.19. Each of the three phases is split into two halves and for changing the number of poles the direction of currents is reversed in one half of the winding [BOL02] [DAH03].

B. Pole Amplitude Modulation

Pole amplitude modulation (PAM) is a method of changing the number of poles of the stator winding in the ratio of $p: p+1$ by reconfiguring the winding connections. Considering the single-phase MMF of a 3-phase winding shown in Fig. 1.20(a), the field strength is expressed as shown in (1.3) where *A* is the amplitude and *p* is the number of poles and the MMF is shown for 8-poles in Fig. 1.20(a). The amplitude of this field can be modulated in space by assuming the pole amplitude varies as shown in (1.5). The resultant field is shown in (1.6) and indicates that the field B_θ is composed of a double field of two-pole numbers $(p-2k)$ and $(p+2k)$ and in this particular case a 6-pole and 10-pole field as seen in Fig. 1.20(d) and Fig. 1.20(e). There are two methods to achieve this modulation in practice. The first is to reverse the current in the second half of the winding with respect to the first half. The second method is to omit a section from each half while the current in half the remaining portion can be reversed with respect to the first half. Consequently, in this case, the 4th and 8th groups of coils are omitted and the 5th, 6th and 7th are reversed with respect to the first three groups of coils. These methods can be achieved by the multiplication of the *p*-pole MMF waveform with the modulation waveforms of Fig. 1.20(b) and Fig. 1.20(c).

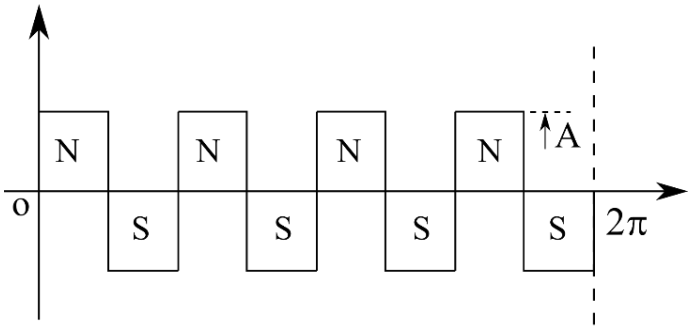

(a) Representation of a 3-phase 8-pole MMF

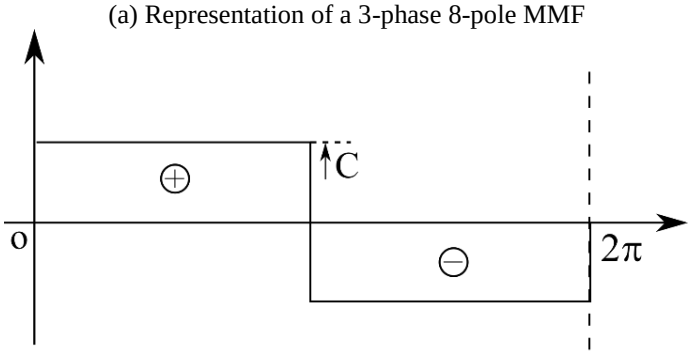

(b) Modulation waveform for 6-pole operation

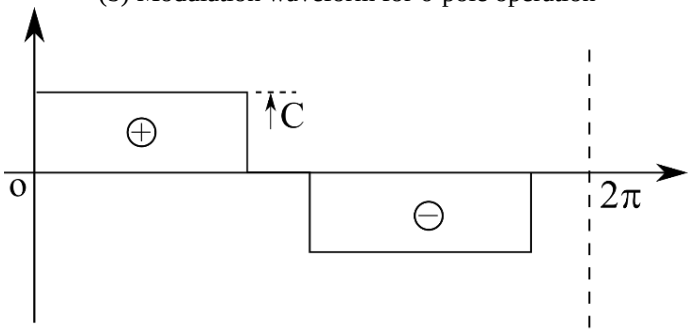

(c) Modulation waveform for 10-pole operation

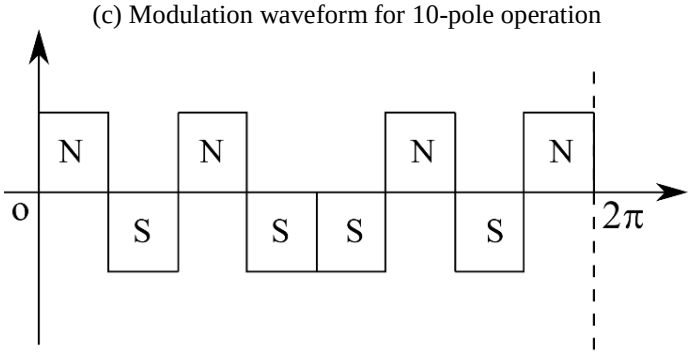

(d) 6-pole field

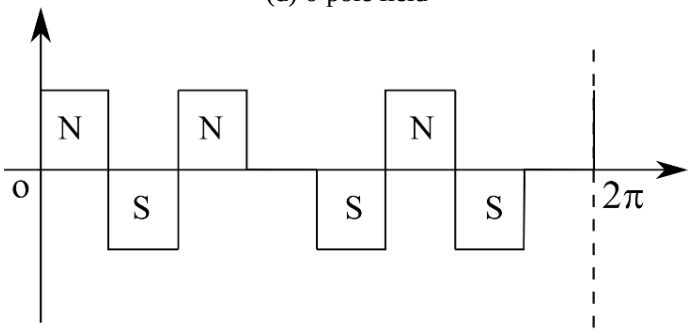

(e) 10-pole field

Fig. 1.20 Waveforms depicting the theory of pole amplitude modulation [RAW58].

The Dahlander winding is a specific case of PAM windings.

$$B_\theta = A \sin\left(\frac{p}{2}\theta\right) \tag{1.3}$$

$$A = C \sin k\theta \tag{1.4}$$

$$B_\theta = C \sin k\theta \sin\left(\frac{p}{2}\theta\right) \tag{1.5}$$

$$B_\theta = \frac{C}{2}\left[\cos\left(\left(\frac{p}{2} - k\right)\theta\right) - \cos\left(\left(\frac{p}{2} + k\right)\theta\right)\right] \tag{1.6}$$

To achieve PAM by simple current reversal, series-parallel connections can be used to modulate the number of poles. Therefore, for a 3-phase machine, for a 2:1 pole changing connection, 6-leads are required. Another method of achieving PAM is to omit certain coils that result in a different pole number. While the winding factor is improved when coils are omitted the torque density of the machine is poor since the windings are not optimally utilised [RAW58] [BOL02].

C. Pole Phase Modulation

Pole Phase Modulation (PPM) provides the most general way to achieve discrete speed control of the induction machine. For a given number of stator slots, the number of poles, phases and slots per pole per phase is variable with PPM windings. Integer q values have to be chosen to ensure a balanced magnetic circuit. The possible pole and phase combinations and integer SPP values with PPM windings are shown in TABLE 1-5 for 36 stator slots and 3 or more phases. Once a stator coil pitch is fixed however, the pole counts possible with a PPM winding are limited. The SPP of a fixed coil pitch winding is given by (1.7) where N_s is the number of stator slots and p_w is the number of poles for which the stator is wound. v is the ratio between the number of magnetic pole pairs p of the winding achievable through PPM. The phase belt length must be kept constant for all the number of poles, which implies that for a 4/12-pole winding selected from TABLE 1-4 only those combinations that have the same q values can be chosen resulting in 4-pole/9-phase and 12-pole/3-phase windings as an example.

$$q = \frac{N_s}{v p_w m} \tag{1.7}$$

The number of legs of the inverter required for a PPM winding is equal to the number of phases for the lower pole count winding. For a 2-pole/9-phase winding, the number of inverter legs

required would be 9 legs and the same winding can be reconfigured to behave as a 6-pole/3-phase winding.

TABLE 1-5 POLE/PHASE COMBINATIONS FOR A STATOR WITH 36 SLOTS AND PPM

Variable	$2p = 2$				$2p = 4$		$2p = 6$		$2p = 12$
m	3	6	9	18	3	9	3	6	3
q	6	3	2	1	3	1	2	1	1

PPM can be realised using conventional windings and toroidal windings. With conventional windings, the coil pitch is fixed by the physical construction of the coils and their placement in the slots. The full potential of the PPM winding, where the coil pitch can be effectively controlled by the inverter, is achieved with toroidal windings. A section of slots of a stator wound with toroidal windings is shown in Fig. 1.21(a).

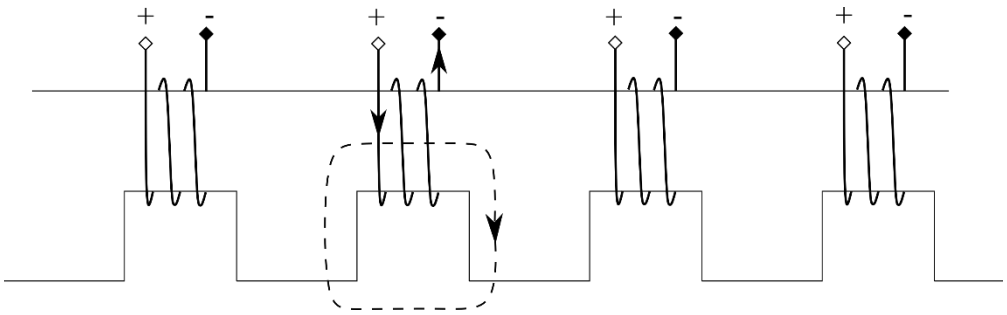

(a) Toroidal coil

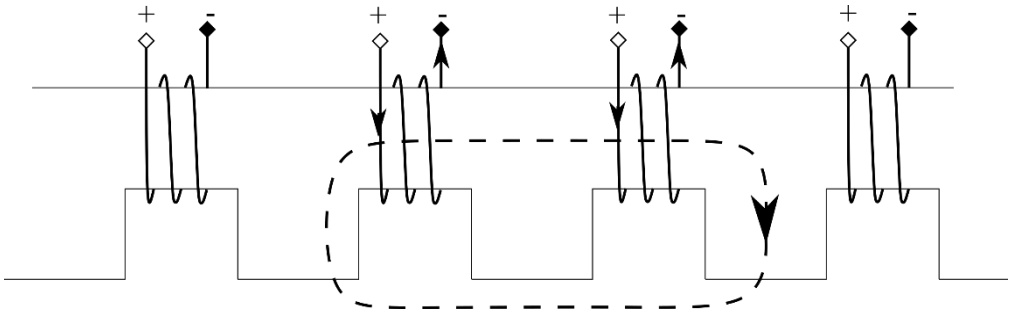

(b) Toroidal coil excitation showing variable pitch

Fig. 1.21 Toroidal stator windings of a PPM machine.

Current through one of the coils is insufficient in itself to produce a magnetic flux that links with the rotor to form a useful number of poles. When a pair of coils (not necessarily next to each other) are excited, the flux that they produce together can link the rotor to produce different pole numbers and the coil pitch can be controlled as shown in Fig. 1.21(b). While in theory any coil pitch

can be realised with toroidal winding, in practice, to keep the number of inverter legs to a minimum, interconnections between fixed sets of coils are required. This limits the number of pole-phase combinations for a given connection to two. Toroidal windings for PPM were firstly disclosed in [MIL99] where a 4-pole/9-phase and a 12-pole/3-phase toroidal wound induction machine with a 72 slot stator was discussed.

Advantages:

- Toroidal windings have the advantage of a short overhang length in the axial direction compared to conventional lap windings.
- Any coil pitch can be achieved by varying the phase of current flowing in the toroidal coils.

Disadvantages

- A water jacket that is placed in contact with the outer periphery of the stator lamination cannot be used to cool the machine effectively due to the presence of the overhang of the toroidal winding. Additionally, any gaps between the toroidal windings and the stator laminations will lead to hot spots on the windings.
- Due to the layered nature of the toroidal windings, a cooling system that cools the accessible overhang region of the windings will result in non-uniform heat dissipation reducing the life of the insulation and subsequently the winding.
- Machines with toroidal windings are not amenable to automated winding due to the difference in the inner and outer diameters of the coils requiring a manual placement of spacers to prevent coil movement [MIL99].
- Also, toroidal windings are by design single-layered windings and this result in higher harmonics in the MMF increasing rotor surface losses.

To effectively utilise the overhang region of the toroidal winding, a dual rotor machine is required. This type of machine has a dual air gap and has a complex bearing system, especially for high-speed operation [MIL99] [MIL01]. The performance of PPM induction machines with three types of windings are compared in [BGE13] [BGE10] and [SUN10]. A conventional distributed winding, a single-sided toroidal winding and a double-sided, dual rotor toroidal winding are compared with the same inner rotor diameter and pole, phase combinations. A PPM winding for a 36-slot stator that can switch between a 4-pole/9-phase and 12-pole/3-phase connection is discussed. The winding layout for a conventional winding is shown in Fig. 1.22(a) for the 4-pole/9-phase connection and Fig. 1.22(b) shows the 12-pole/3-phase connection.

Poles	N									S								N									S								
Slot N°	1	2	3	4	5	6	7	8	9	10	11	12	13	14	15	16	17	18	19	20	21	22	23	24	25	26	27	28	29	30	31	32	33	34	35	36
Layer 1	A	f	B	g	C	h	D	i	E	a	F	b	G	c	H	d	I	e	A	f	B	g	C	h	D	i	E	a	F	b	G	c	H	d	I	e
Layer 2	f	B	g	C	h	D	i	E	a	F	b	G	c	H	d	I	e	A	f	B	g	C	h	D	i	E	a	F	b	G	c	H	d	I	e	A

(a) 4-pole/9-phase winding mode.

Poles	N			S			N			S			N			S			N			S			N			S			N			S		
Slot N°	1	2	3	4	5	6	7	8	9	10	11	12	13	14	15	16	17	18	19	20	21	22	23	24	25	26	27	28	29	30	31	32	33	34	35	36
Layer 1	A	c	B	a	C	b	A	c	B	a	C	b	A	c	B	a	C	b	A	c	B	a	C	b	A	c	B	a	C	b	A	c	B	a	C	b
Layer 2	c	B	a	C	b	A	c	B	a	C	b	A	c	B	a	C	b	A	c	B	a	C	b	A	c	B	a	C	b	A	c	B	a	C	b	A

(b) 12-pole/3-phase winding mode.

Fig. 1.22 Winding layout of 4/12-pole PPM winding induction machine [BGE13].

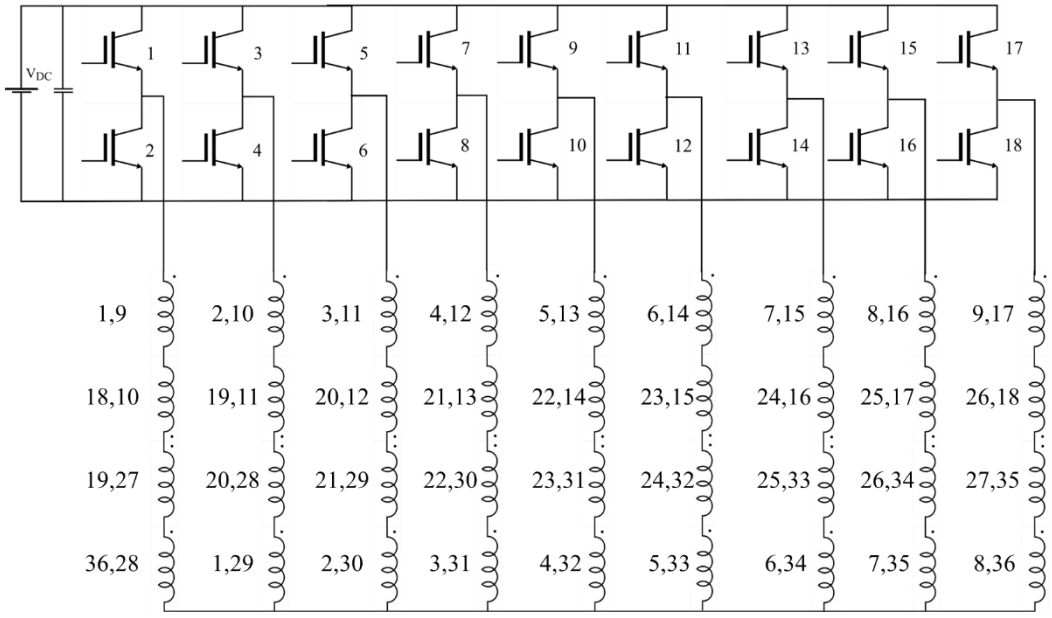

Fig. 1.23 Inverter connection for 36-slot PPM winding stator [BGE13].

For a conventional winding, the machine is wound with a one-slot short pitch winding for the 4-pole/9-phase mode. The inverter connection with 9 inverter legs corresponding to the winding layout of Fig. 1.22 is shown in Fig. 1.23. The coils corresponding to the 9 phases are connected in series. To change the number of poles, the phase of currents in the coils are appropriately adjusted corresponding to the 12-pole/3-phase connection shown in Fig. 1.22(b). Once the coil connections are made to correspond to the lower pole number the coil pitch is fixed and the fundamental winding factor for the 12-pole connection is reduced. The fundamental winding factor for the 4-pole/9-phase mode is quite high at 0.984. For PPM operation with conventional windings, the coil pitch is unchanged at 8-slot pitch when the machine is operated in the 12-pole/3-phase mode and the fundamental winding factor for this mode is reduced to 0.866. Additionally, with PPM windings, the coil pitch corresponds to the mode with the lower number of poles resulting in larger end winding length when low pole numbers are used. For starter-generator applications where the higher torque is required at low speeds when the low pole number winding mode is excited, the low fundamental

winding factor is a disadvantage. The performance of the toroidal winding with a single rotor is found to be inferior compared to the conventional winding as well as the dual rotor toroidal winding due to increased copper losses. The dual rotor toroidal winding machine has the highest torque/ampere value but has mechanical issues especially during high-speed operation [BGE13] [BGE10].

D. Stator Cage Induction Machine

Another recent innovation in the stator winding of induction machines was disclosed in [DAJ14a] and the associated inverter to run this type of machine was discussed in [DAJ17]. The machine has a cage winding both in the stator and the rotor laminations. Unlike the rotor where the cage is short-circuited at both ends of the cage, each bar one end of the stator cage winding is connected to the output of an H-bridge inverter that enables the control of magnitude and direction of current in the bar. The stator cage winding with one end short-circuited and the inverter at the other end is shown in Fig. 1.24. The number of half bridges required for controlling this machine is equal to the number of stator bars. An inverter connection for n-stator cage bars is shown in Fig. 1.25.

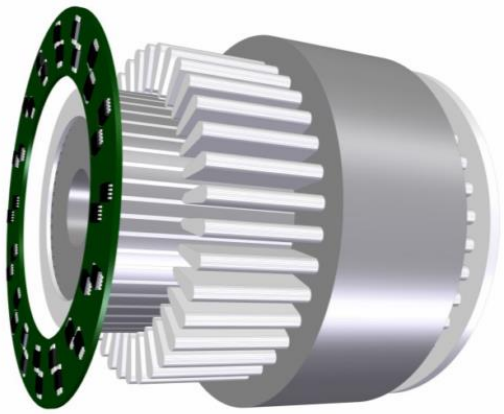

Fig. 1.24 Stator cage winding and associated inverter [PAT15].

Advantages:

1. The mechanical construction of the machine is advantageous since the stator can be die-cast or pre-fabricated bars can be inserted into stator slots, reducing the cost compared to the conventional winding.
2. The MMF of the stator can be controlled precisely since each slot current is independently controlled. This results in an MMF waveform with lower harmonics compared to the distributed winding and consequently lowest NVH.

3. High slot fill factor (almost 100%) is possible compared to the 60%-70% [ZHA19] achievable with bar windings and this improves the torque density of the stator cage winding machine.
4. The high slot fill factor combined with the shorted end ring on one end of the stator of improves the thermal performance and heat rejection capability of the slot. [DAJ14]

Disadvantages:

1. For 48V systems, like starter-generator systems, the high power requirement results in a high current per stator bar and the MOSFET/IGBT devices that drive these bars need to be rated for high current making the drive circuit expensive.
2. The number of current sensors required for a stator cage winding is equal to the number of stator bars and this results in a large number of current sensors for machines with a large number of slots.
3. The AC losses in the stator cage windings can be significantly high unless a large number of slots are used to produce a low pole number MMF with low harmonics. This, however, increases the cost of the power electronic converter and sensors.

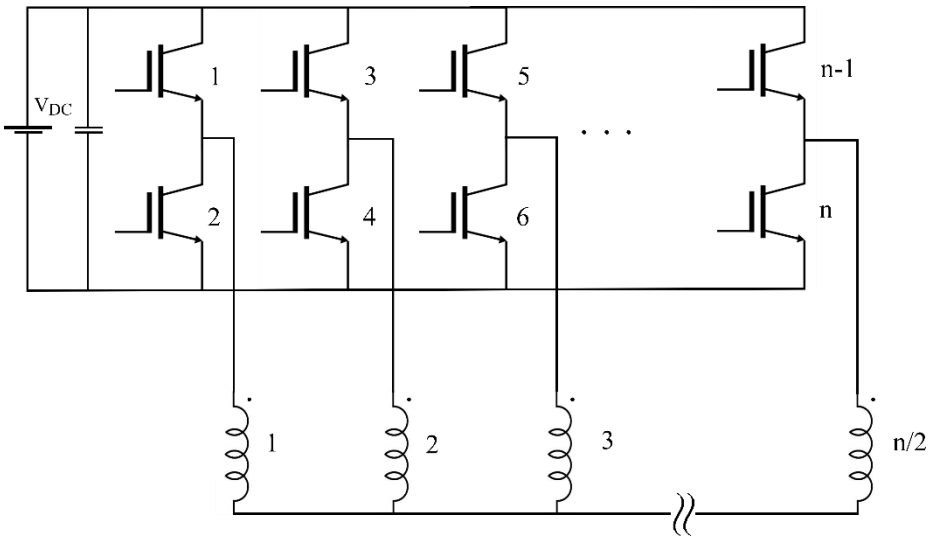

Fig. 1.25 Inverter for stator cage winding induction machine [PAT16].

E. Electronic Pole Changing

To extend the speed of the machine, the number of the poles could be changed during the normal operation of the machine. One way of doing this electronically, without resorting to slow mechanical contactors, is reported in [OSA96] [MOR97]. The principle of operation can be understood from the example of a 3-phase 24-slot, 4-pole machine and the winding pattern of phase A is shown in Fig. 1.26 for 4-pole operation.

Poles	N						S						N						S					
Slot N°	1	2	3	4	5	6	7	8	9	10	11	12	13	14	15	16	17	18	19	20	21	22	23	24
Layer 1	**A1**	**A1**	**A1**	**A1**									**A2**	**A2**	**A2**	**A2**								
Layer 2							**a1**	**a1**	**a1**	**a1**									**a2**	**a2**	**a2**	**a2**		

Fig. 1.26 Winding pattern of a 24-slot 4-pole machine.

The current in the phase A coil in slots 13-22 can be reversed and the resulting change in the number of poles can be seen from Fig. 1.27. The inverter connection and the MMF of the phase coils are shown in Fig. 1.28.

Poles	N						S						S						N					
Slot N°	1	2	3	4	5	6	7	8	9	10	11	12	13	14	15	16	17	18	19	20	21	22	23	24
Layer 1	**A1**	**A1**	**A1**	**A1**									**a2**	**a2**	**a2**	**a2**								
Layer 2							**a1**	**a1**	**a1**	**a1**									**A2**	**A2**	**A2**	**A2**		

Fig. 1.27 Winding pattern of a 24-slot 2-pole machine.

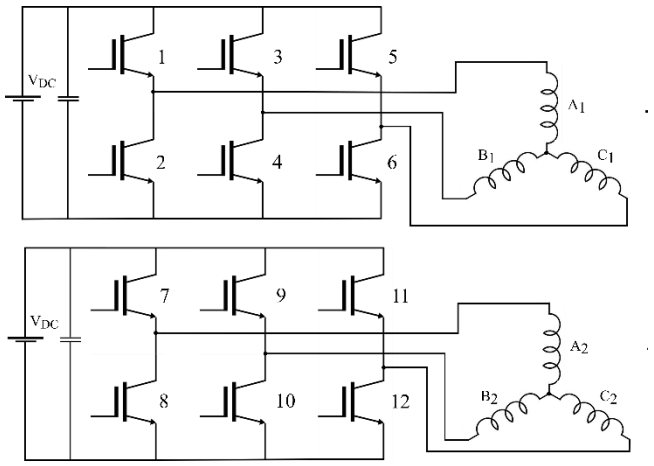

Fig. 1.28 Inverter for electronic pole changing.

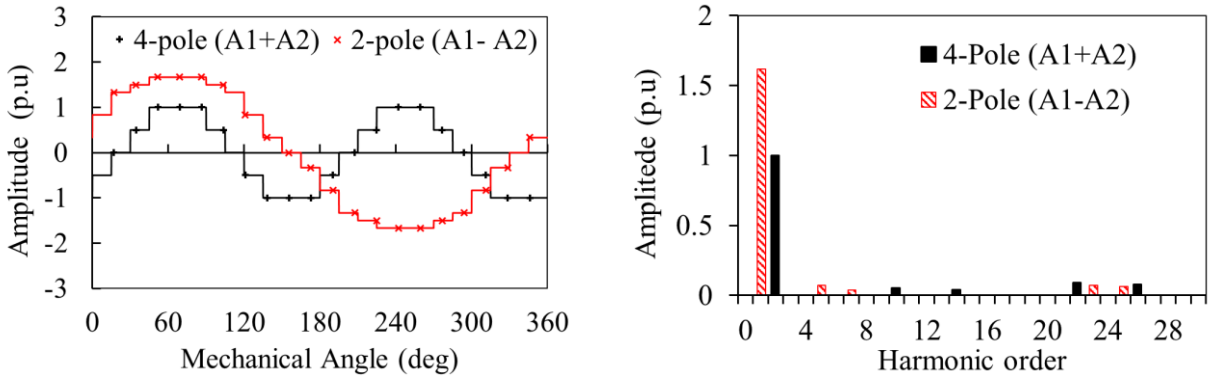

(a)MMF waveform for 4/2-pole operation.

(b)Harmonic spectrum of phase A MMF.

Fig. 1.29 MMF and harmonic spectrum of the electronic pole changing machine.

Since the current of only one of the two coils of the phase A needs to be reversed, the inverter required for such an operation is a 6-phase drive which allows the current to be reversed in one set of coils to facilitate the pole changing. The connection of the coils to the inverter is shown in Fig.

1.28. The MMFs of the coils ‘A1’ and ‘A2’ when added result in a 4-pole MMF, the difference of the MMFs in a 2-pole operation. The MMF waveforms and their corresponding harmonic spectrum are shown in Fig. 1.29.

$$K_{ds} = \frac{\sin\left(\frac{\sigma}{2}\right)}{q\sin(\frac{\sigma}{2q})} \tag{1.8}$$

The major limitation of the electronic pole changing winding is the poor winding factor in both modes of operation. The winding factor is calculated as shown in (1.8) where σ and q are the phase spread and slots per pole per phase respectively. For the machine under consideration, the phase A coil occupies 4 slots under one pole which equates to a phase spread of 120^o. This translates to a winding factor of 0.866. For a machine with a 60^o phase spread, the winding factor for the same machine would be 0.959 which is 10% higher. This implies that as compared to a full pitch winding, the torque is 10% lower due to the choice of the winding with 120^o phase belt. If a winding with a 60^o phase belt is chosen, pole changing operation will lead to MMF cancellation.

1.5 Scope and Contributions of the Thesis

This thesis investigates an improved electronic pole changing winding induction machine. The induction machine is identified as a suitable machine for starter-generator application amongst other machines as shown in Fig. 1.29. Within the possible methodologies for pole changing windings, the electronics pole changing windings is chosen for this application. Electronic pole changing windings as proposed in [OSA96] can extend the speed range in the flux weakening region of operation. The inverter and windings structure is simple and there is a possibility of applying this to low voltage 48V systems with the use of hairpin windings. However, 3-phase pole changing windings have a poor fundamental winding factor when used with a higher number of poles where the highest torque is needed for cranking. To overcome this issue, a 6-phase pole changing winding is proposed. In addition to having a higher fundamental winding factor, the torque during the lower pole number operation can be improved by the use of 3rd harmonic injection. The thesis is organised into 7 chapters to investigate the improved electronic pole changing winding induction machine.

In Chapter 1, a review of the literature discussing the relative merits and demerits of various machines used for starter-generator applications is presented. Specifically, the use of induction machines for starter-generator applications is investigated. Pole changing windings are identified as a means to improve the flux weakening region of operation of the induction machine. The different

methods of performing pole changing are described and their advantages and disadvantages are compared. The electronic pole changing windings is chosen as a suitable candidate for investigation.

In Chapter 2, the influence of different machine parameters on the performance of the induction machine is discussed. The influence of the number of slots, the number of poles and the number of rotor slots on the torque capability, torque ripple and flux weakening performance is investigated to determine an optimal machine configuration.

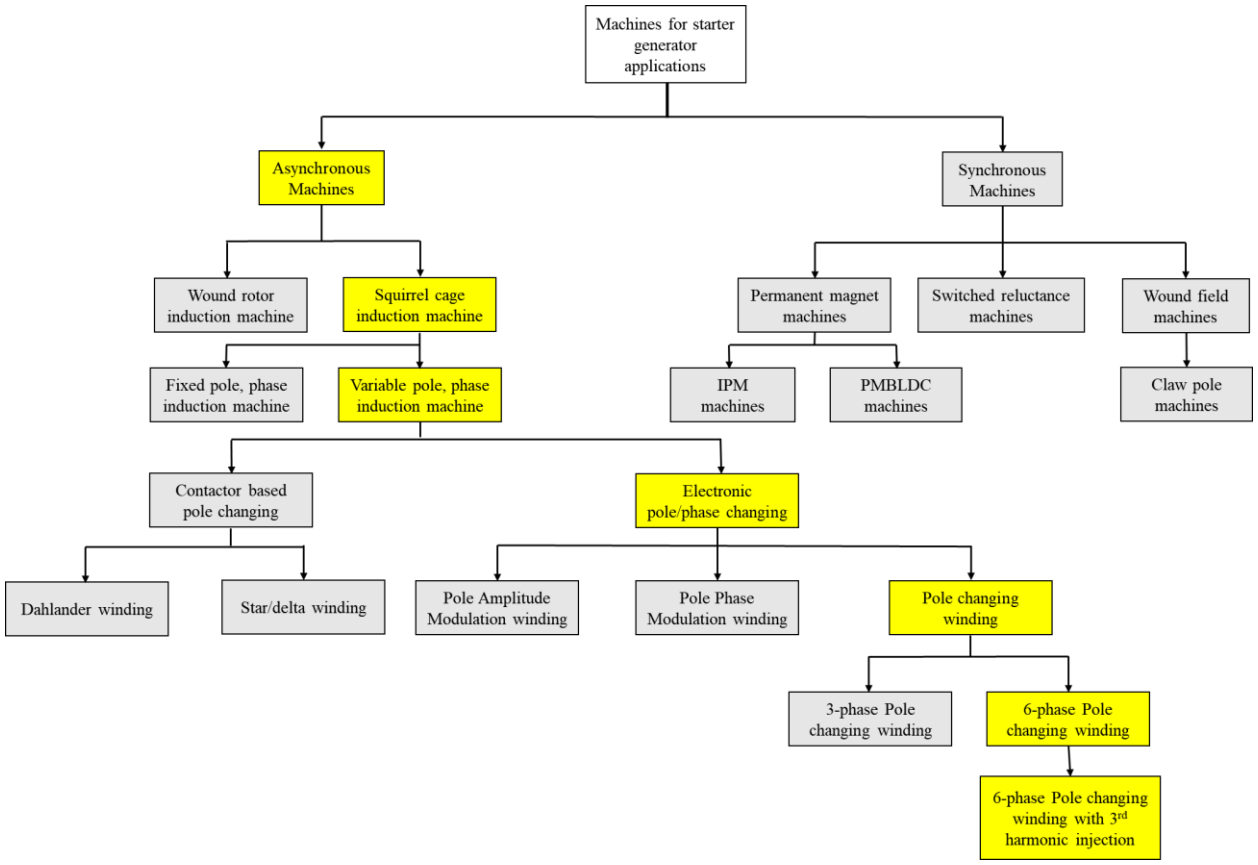

Fig. 1.29 Investigation of induction machines for starter-generator applications

In Chapter 3, a 3-phase, state of art electronic pole changing winding for a 48V starter-generator application is discussed. It is shown that the electronic pole changing winding induction results in an induction machine with shorter axial length but an inferior efficiency and thermal performance compared to the baseline induction machine with conventional windings. This is due to the poor fundamental winding factor of the electronic pole changing winding machine when used with a high number of poles.

In Chapter 4, the 6-phase pole changing winding is introduced as a way to improve the fundamental winding factor when operating with a higher number of poles. A comparison of the 6-

phase and 3-phase machines is performed using FEA and experimental results on a lower-rated prototype are presented to support the conclusions from the simulation.

In Chapter 5, the injection of 3rd harmonics to enhance the torque capability of the six-phase pole changing winding induction machine is discussed. The optimal ratio of the 3rd harmonic current to the fundamental current is determined. The influence of the 3rd harmonic injection on the torque capability curves and torque ripple are simulated. Experimental results with the 3rd harmonic injection are used to validate the simulations.

In Chapter 6, a dynamic model for the 3-phase winding is discussed and is extended to simulate the dynamic performance of the 6-phase pole changing winding induction machine. A dynamic model with non-linear inductances and rotor resistance to better match the test results are discussed. The transient behaviour of the pole changing winding machine under scalar control and field oriented control is simulated.

The appendices discuss the design equations and the 3-phase dynamic model of the induction machine. The geometrical and winding configuration of the prototyped induction machine is also shown.

1.5.1 Contributions

The major contributions of the thesis can be summarised as follows:

1. Improvement of the peak torque capability at low speed by 15% by the use of 6phase pole-changing winding compared to the state-of-art, 3-phase electronic pole changing windings.
2. Improvement of the peak torque capability at the corner speed by 21% using 3rd harmonic injection. The optimum ratio of the 3rd harmonic to the fundamental current that maximised the torque capability is determined.
3. A dynamic *d-q* model for the 6-phase pole changing winding is developed using the vector space decomposition method.

1.5.2 List of Publications from the Thesis

Patents:

[1]. J.C.Mipo, S.Personnaz, S.Mallampalli, Z.Q. Zhu, "Pole changing in order to increase the speed operation," Valeo, French patent application number: MFR1447, 26 July 2018.

[2]. Zi-Qiang Zhu, Srinivas Mallampalli Satsai, Jean Claude Mipo, Sophie Personnaz, "Rotating electrical machine with an optimized configuration," WO Patent Number: WO2020021087A1, Application Number: PCT/EP2019/070222, 30 Jan. 2020.

Journal and Conference Publications:

[1]. S. Mallampalli, Z. Q. Zhu, J. C. Mipo and S. Personnaz, "Six-phase pole-changing winding induction machines with 3rd harmonic injection," *IEEE Trans. on Energy Conversions*, (**in review**)

[2]. S. Mallampalli, Z. Q. Zhu, J. C. Mipo and S. Personnaz, " Six-phase pole-changing winding induction machines with improved performance," *IEEE Trans. on Energy Conversions*, 2020, *Early Access, doi: 10.1109/TEC.2020.3009190.*

[3] S. Mallampalli, Z. Q. Zhu, J. C. Mipo and S. Personnaz, "48V starter-generator induction machine with pole changing windings," *IEEE Trans. on Industrial Applications*, 2020, *Early Access, doi: 10.1109/TIA.2020.3012615.*

[4] S. Mallampalli, Z. Q. Zhu, J. C. Mipo and S. Personnaz, "48V starter-generator induction machine with pole changing windings," *Proc. IEEE Energy Conversion Congress and Exposition (ECCE)*, Baltimore, ML, USA, 2019.

[5]. S. Mallampalli, Z. Q. Zhu, J. C. Mipo and S. Personnaz, "Influence of rotor slot number on flux weakening characteristics of induction machines," *Proc. IEEE 21st International Conference on Electrical Machines and Systems (ICEMS)*, Jeju, pp. 549-554, Sep. 2018.

Chapter 2

Influence of Machine Parameters on Induction Machine Performance

The performance of induction machines is influenced by the choice of mechanical design parameters like the air gap, the overall and slot dimensions of the stator and the rotor dimensions as well as the electrical parameters like the number of turns per phase, current density and voltage rating of the windings. Despite the quantifiable nature of these parameters, the design of induction machines has been dominated by rules of thumb and empirical formulations that imbibe the experience of generations of designers and manufacturers [ALG51] [SAY70]. A lot of these techniques were aimed at line-start machines. With the widespread use of variable frequency drives, new design spaces have opened up for induction machine design. New materials as well as better manufacturing techniques (like FeCo laminations, hairpin windings) have resulted in hitherto unexplored designs and performance [BOL01]. For a starter generator application of the induction machine in hybrid vehicles, the requirements are for a higher starting torque as the primary requirement for cranking operations. This is followed by the requirement for a wide speed operation in the flux weakening region to enable the maximum extraction of power during highway cruising. In this chapter, the influence of the various parameters of the induction machine is studied in comparison to a baseline induction machine design. Beginning with a set of constraints, the influence of the stator dimensions and rotor dimensions are studied. From this design of experiments, optimisation is carried out under two scenarios of maintaining the same conductors per slot at 2 and varying the number of conductors per slot while maintaining the same series turns per phase. The influence of the rotor slot number on the average torque and torque ripple of the induction machine is studied particularly in relation to its influence in the flux weakening region. The method of analysis described in Chapter 2 is used to calculate the torque-speed characteristics of the machine and the optimum machine from this analysis is presented.

2.1 Influence of Machine Parameters

In designing an induction machine, the constraints are set by the application for which the machine is intended. In this instance, the baseline specifications of the induction machine are for the P0 location in a hybrid electric vehicle. The specifications determine the envelope available for the machine, the inverter specification determines the DC bus voltage and current available and the

cooling system specification constrains the coolant temperature and flow rate. Within these constraints, using the design methodology outlined in Appendix I, different slot/pole number combinations are investigated to determine the optimum induction machine design to meet the performance specifications. Due to the low voltage available at the DC bus, the current rating is high for the high power rating of the induction machine the phase resistance has a very strong influence on the performance of the induction machine and consequently the stator losses are high for a small increase in the number of turns. The lowest possible resistance is obtained by utilising hairpin conductors in the stator slots. The highest packing factor is possible for a two-layer winding (chosen to minimise the MMF harmonics) while accommodating two conductors per slot. The influence of the number of series turns per phase (W) on the corner speed and the limited DC bus voltage provides a narrow choice for W as discussed during the optimisation.

2.1.1 Baseline IM Parameters

The baseline induction machine specifications used in this thesis for analysis and optimisation studies are shown in TABLE 2.1. These specifications are overlaid onto a representative torque-speed characteristics shown in Fig. 2.1. The blue circled points represent the specifications. For an induction machine, the peak torque capability is inversely proportional to the square of the speed as indicated by the dashed red curve in Fig. 2.1. To meet the requirement of the cranking torque of 60Nm at 1200 rpm and 12Nm at 6000rpm (1:5 ratio), the peak torque capability of the machine will be 5 times the cranking torque at 300Nm. Induction machines usually have a peak torque to rated torque ratio of 2-2.5 p.u. A machine designed with such high peak torque capability will be large and underutilised. To overcome this issue the corner speed of the machine can be increased, which would require a higher voltage or lower number of turns per phase so that the DC bus voltage limit is reached at a higher speed, thus extending the flux-weakening region of operation. The peak torque reduces and can be brought down to within 2 p.u of the operating rated torque. A torque of 12Nm at 6000rpm with a corner speed of 2000rpm results in torque of 108Nm at the corner speed. It can also be observed in Fig. 2.1 that the machine that meets the specifications are 20000rpm is required to be even larger. As previously discussed, for 48V machine drives, the low DC bus voltage combined with the high current rating results in a limited choice of the number of conductors per slot. The need for a wide flux-weakening region narrows the choice of series turns per phase to ensure that the corner speed is high enough to extend the flux weakening region of operation. Therefore, a baseline machine is chosen to study the influence of W. For the same electric loading and air-gap flux density, the corner speed of the induction machine is inversely proportional to W. This occurs because for a higher number of series turns the speed at which the voltage limit of the

inverter is reached is lower. The torque at the corner speed, on the other hand, is proportional to both the number of series turns and the stack length. These relationships are shown in (2.1) and (2.2) [OLD85].

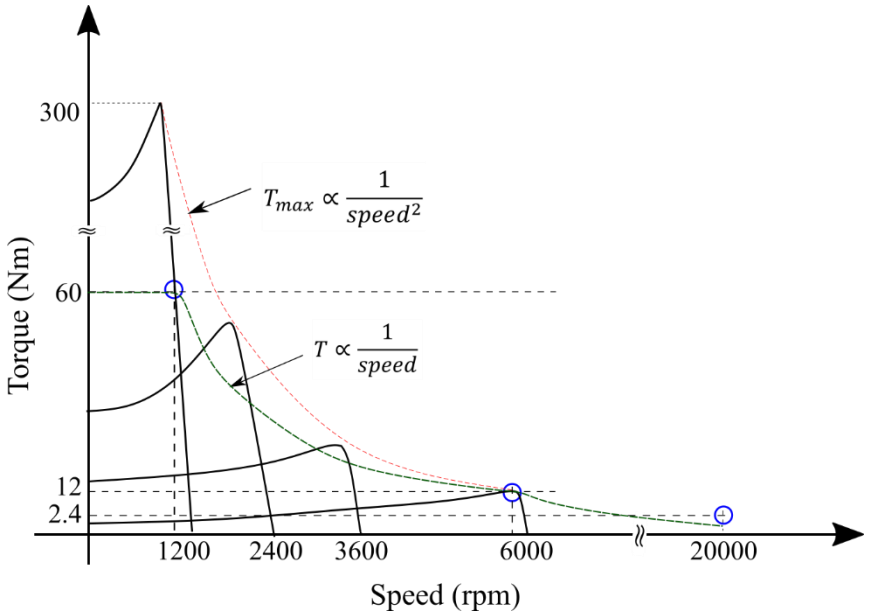

Fig. 2.1 Representative torque-speed characteristics of the induction machine

$$\frac{T_{new}}{T_{old}} = \frac{Stack\ Length_{new}}{Stack\ Length_{old}} \frac{W_{new}}{W_{old}} \tag{2.1}$$

$$\frac{Corner\ Speed_{old}}{Corner\ Speed_{new}} = \frac{Stack\ Length_{new}}{Stack\ Length_{old}} \frac{W_{new}}{W_{old}} \tag{2.2}$$

Consider a baseline 3-phase, 4 pole induction machine with three different values of *W*. The outer diameter and stack length of the machine are constrained to the specifications in TABLE 2.1. The current and average air-gap flux density are both kept constant. The influences of *W* on torque-speed and power-speed characteristics are shown in Fig. 2.2(a) and Fig. 2.2(b) respectively. The stator with *W*=12 (or other feasible integer values close to 12) has the optimum corner speed that can meet the torque specifications at both low speed and high speed. Subsequently, for optimisation studies, the number of series turns per phase is kept close to 12 which will result in a corner speed of 2000rpm as a reference value depending on the number of slots per pole per phase (SPP) and the pole number under investigation.

2.1.2 Assumptions

A. Cooling & Current Density

For the water-cooled induction machine with a stator cooling jacket, as per the specifications the cranking operations are intermittent and of short-term duty. The rest of the operation occurs within the torque-speed envelope where the operation is of continuous duty. Consequently, the stator copper loss is kept fixed at a value for peak torque operation resulting in a lower current density for other operating points within the operating envelope. The current density of the conductors is calculated at this loss value to ensure it is within the limits allowable by the cooling system [GAI19].

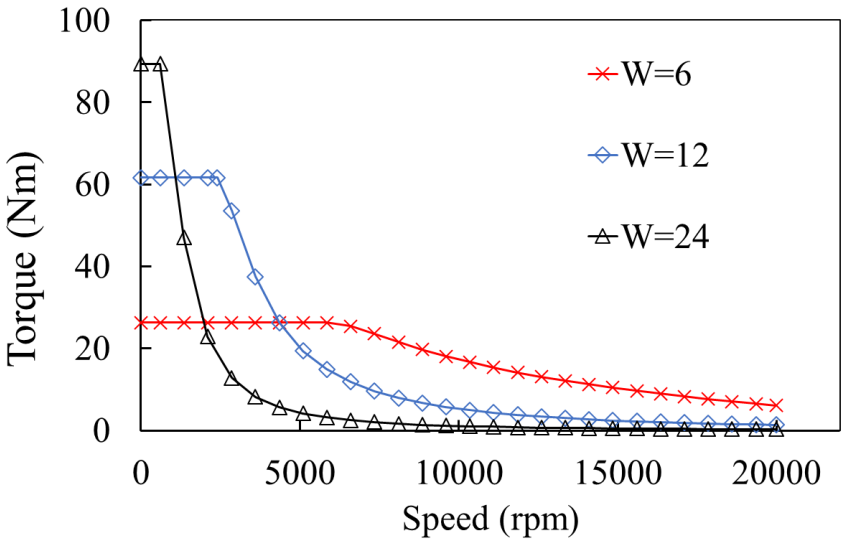

(a) Torque-speed characteristics.

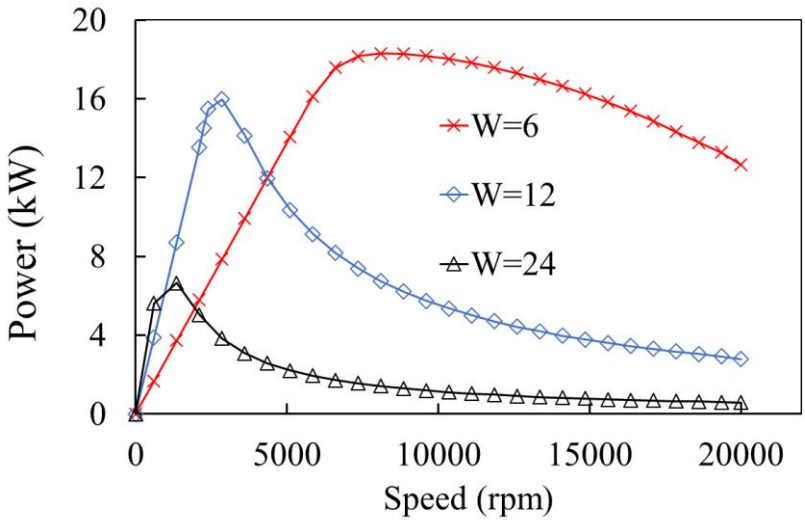

(b) Power-speed characteristics.

Fig. 2.2 Influence of the number of series turns per phase on the torque-speed and power-speed characteristics.

TABLE 2.1 P0 INDUCTION MACHINE SPECIFICATIONS

Peak Power Mode for 30s @85% Efficiency			
Power (kW)	Speed (rpm)	Environment	DC Bus Voltage (V)
10 (31Nm)	3000	80°C air and 105°C water	52
15 (23Nm)	6000	80°C air and 105°C water	52
Permanent Power Generation Mode (continuous)			
Power (kW)	Speed (rpm)	Environment	DC Bus Voltage (V)
3.2	2400	120°C air and 105°C water	36, 42, 52
5	6000	120°C air and 105°C water	36, 42, 52
5	20000	120°C air and 105°C water	36, 42, 52
Cranking Mode (Duration of 500ms)			
Torque (N)	Speed (rpm)	Environment	DC Bus Voltage (V)
60 (4kW)	0	120°C air and 105°C water	36
60 (10kW)	1200	120°C air and 105°C water	36
12 (7.5kW)	6000	120°C air and 105°C water	36
Drive Specifications			
V_{DC}=48V $I_{phase} = 230Arms$ (6 Phase Cranking) $I_{phase} = 160Arms$ (6 Phase Generating)			
Packaging			
Stack Length +End Winding=84mm Diameter External=144mm			

B. Material Properties

The material for the stator and the rotor laminations is chosen to be M-19 24Ga. The rotor bars are die-cast aluminium and the shaft is non-magnetic steel. The stator windings are copper. All material characteristics used in simulations are included in Appendix I.

Geometric Constraints: The stator outer diameter is fixed based on the specifications of TABLE 2.1. The stack length is fixed at 66mm and is chosen to ensure that the sum of the active stack length and overhang of the end-windings is within the specifications. The air-gap of all the designs is limited to 0.35mm based on manufacturability and tolerances for this size of the induction machine.

C. Current and Voltage Limits

The inverter rating determines the current limit per phase and the available phase voltage is limited by the DC bus voltage and the control method used. In all of the simulation methods, a space vector modulation method is used which limits the available rms line-to-line voltage to $V_{DC}/\sqrt{2}$ [KAR02].

2.1.3 Influence of Number of Slots per Pole per Phase (SPP)

To study the influence of different slot and pole numbers, different combinations of stator slots and poles are investigated for optimisation. The relationship between the number of series turns per phase (*W*), the number of parallel paths *(a*), the slots per pole per phase (*SPP*), the number of poles (*2p*) and the number of conductors per phase (n_s) is given by (2.3).

$$W = \frac{n_s pq}{a} \tag{2.3}$$

Due to the high differential leakage inductance of stator windings with SPP of 1, this combination is not investigated [BOL02]. Induction machines with 2 poles result in large overhang lengths and are also not considered. As the number of poles and *SPP* are changed, the number of parallel paths and the conductors per slot can be varied. The number of conductors per slot necessarily needs to be an even number for double layer windings and the number of poles needs to be an integer multiple of pole pairs. Due to the low number of series turns per phase (*W*=12), the number of conductors per slot is also quite low. Also, for some combinations of *SPP* and pole number, the number of conductors per slot cannot be kept constant for the same value of *W*. To account for this, two different scenarios are simulated where in the first scenario, the number of conductors per slot and parallel paths are varied for all combinations of *SPP* and *p* to keep the value of *W* fixed at 12. In the second scenario, the number of conductors per slot is kept fixed at 2 and the number of parallel paths is adjusted to keep the value of *W* as close to 12 as feasible. These combinations for both scenarios are shown in TABLE 2.2. For each combination in TABLE 2.2, using the procedure detailed in Chapter 2 and subject to constraints imposed by the specifications as described in Section 3.1.1, the induction machine is designed and optimised. The number of rotor

bars is kept constant at 56 for all the machines and the influence of the rotor bars is then studied separately in the next section where it is seen to not have a major influence on average torque, especially in the constant torque region, but a rather significant effect on the torque ripple.

TABLE 2.2 SCENARIOS OF INVESTIGATED SLOT/POLE COMBINATIONS

Parameters			**Scenario 1**			**Scenario 2**		
SPP	***2p***	***Ns***	n_s	***a***	***W***	n_s	***a***	***W***
2	4	24	6	2	12	2	1	8
2	6	36	6	3	12	2	1	12
2	8	48	6	4	12	2	1	16
2	10	60	6	5	12	2	2	10
2	12	72	6	6	12	2	2	12
3	4	36	4	2	12	2	1	12
3	6	54	4	3	12	2	1	18
3	8	72	4	4	12	2	2	12
3	10	90	4	5	12	2	2	15
3	12	108	4	6	12	2	3	12
4	4	48	6	4	12	2	1	16
4	6	72	6	6	12	2	2	12
4	8	96	6	8	12	2	2	16
4	10	120	6	10	12	2	5	8
4	12	144	6	12	12	2	4	12

A. Optimisation Procedure and Results

For every combination in TABLE 2.2, the optimum dimensions of the machine that maximises the torque at the corner speed achievable for W=12 are determined. For a fixed outer diameter, stack length, air-gap, rated inverter current and DC bus voltage, the geometric parameters that influence

the torque are the stator bore diameter and the stator and rotor slot dimensions. The influence of these parameters is determined by varying the split ratio (SpR) and stator tooth-width to slot pitch ratio (b_{ts}) and the rotor tooth-width to slot pitch ratio (b_{tr}), respectively. The stator copper loss is kept constant to ensure that the thermal performance of the machines is comparable. The genetic algorithm (GA) is used to determine the optimum values of the three input variables subject to constraints that maximise the torque capability at the reference corner speed of 2000rpm.

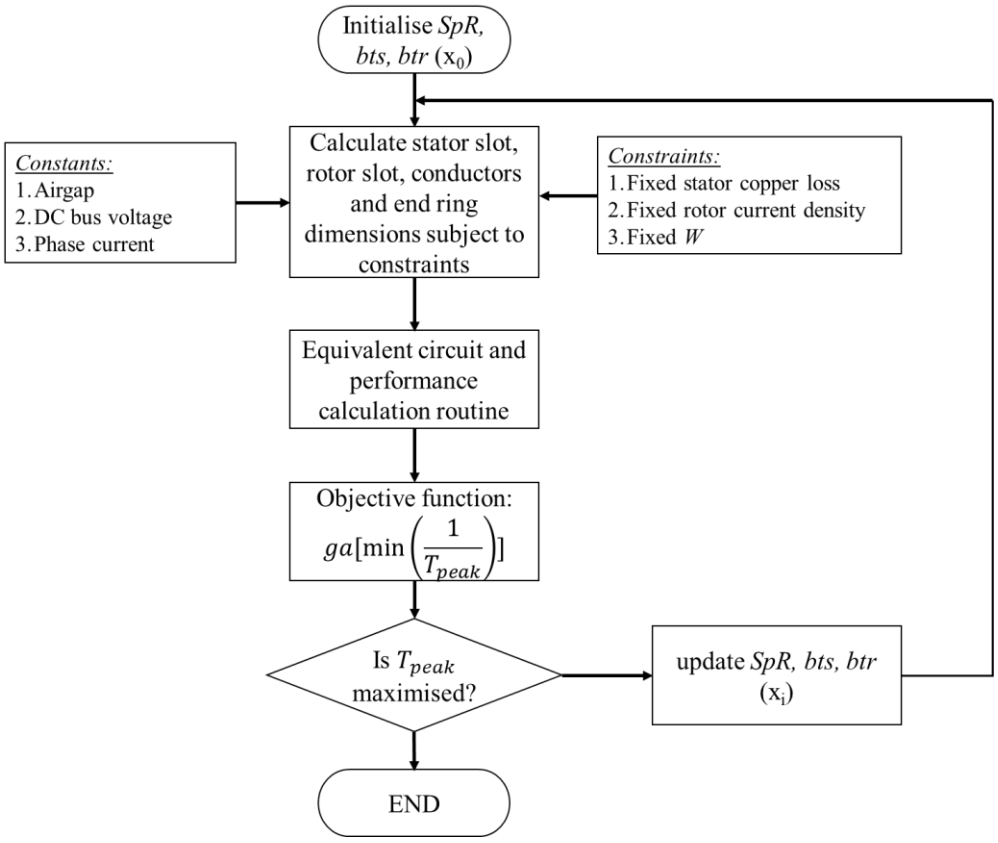

Fig. 2.3 Flowchart of the peak torque optimisation procedure.

The flow chart of the process is shown in Fig. 2.3. With a randomly chosen set of input variable values within the lower and upper bounds, the stator slot, rotor slot, the conductor cross-section area and the end ring dimensions are computed according to the procedure detailed in Appendix I while subject to the constraints shown in Fig. 2.3. Using these computed values, the equivalent circuit parameters and performance characteristics are determined. The objective function is the maximisation of the peak torque and the input parameters are varied by the GA algorithm to determine the optimum values that achieve this objective. Using the equivalent circuit shown in Appendix I, the torque of the induction machine is determined at every iteration of the genetic algorithm,

B. Slotfill Factor

For machines with rectangular conductors, the slot fill factor (defined here as the ratio of the copper area to the available slot area) is a strong function of the number of conductors per slot. This is due to the fixed conductor insulation layer thickness occupying increasing space in the slot as the number of conductors per slot increases. This implies that, for scenario 1, the slot fill factor for an SPP of 3 is expected to be higher than that for the machines with an SPP of 2 or 4, due to lower number of conductors per slot. Whereas, in scenario 2, the slot fill factor of all the compared machines will be similar since the number of conductors per slot is fixed at 2. Schematics of a single slot of fixed dimensions with 2, 4 and 6 conductors per slot of a double layer winding are shown in Fig. 2.4(a), Fig. 2.4(b) and Fig. 2.4(c), respectively. In a slot with several turns, the conductor insulation area occupies very little of the slot area available for the copper. This influence is seen in the slot fill factor calculation from (2.6). The reduction in slot fill factor is higher when the available slot area is lower as is the case in machines with higher SPP for the same pole number.

$$Copper\ area = Slot\ area - Liner\ area + ns \times (conductor\ insulation\ area) \tag{2.4}$$

$$slot\ fill\ factor = \frac{Copper\ area}{Slot\ Area} \tag{2.5}$$

$$slot\ fill\ factor = 1 - \frac{Liner\ area + ns \times (conductor\ insulation\ area)}{Slot\ area} \tag{2.6}$$

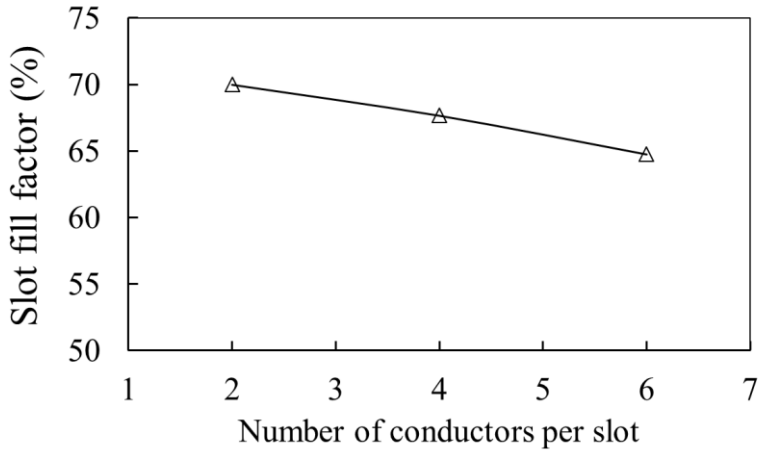

Fig. 2.5 Slot fill factor variation with the number of conductors per slot for two-layer winding.

The variation of slot fill factor with an increasing number of conductors is shown in Fig. 2.5. Using this constraint on the slot fill factor, the optimum values of the variables to maximise torque are determined and the results are shown as follows.

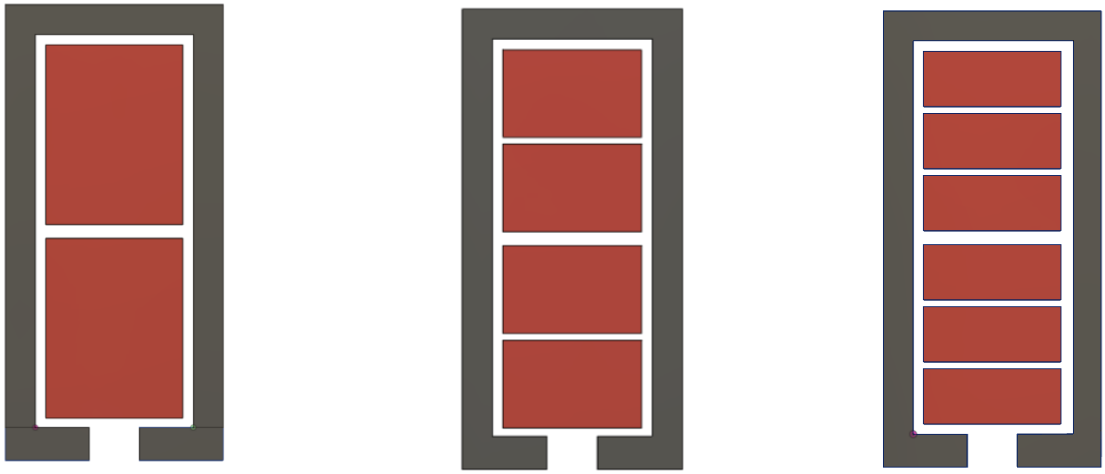

(a) Two conductors per slot (b) Four conductors per slot (c) Six conductors per slot

Fig. 2.4 Rectangular conductor slot layout with an increasing number of conductors per slot for (a) two, (b) four and (c) six conductors per slot.

C. Scenario 1

The variation of the split ratio at the maximum torque point, with increasing SPP and the number of poles, is shown in Fig. 2.6. As the pole number increases the split ratio increases since a smaller yoke section is required to carry the flux per pole. The stator and rotor tooth-width to slot pitch ratios are shown in Fig. 2.7 and Fig. 2.8, respectively. The stator and rotor slot pitch ratios represent the split of magnetic and electric loading where the current carried by the conductors in the slot represents the electric loading and the flux in the teeth is indicative of the magnetic loading. Since the main flux is common between the stator and the rotor, and the MMF balance between the stator and the rotor is maintained by transformer action, the stator and rotor tooth-width to slot pitch ratios are almost identical. The peak torque is maximised for the case for an SPP of 2 and 8 poles as seen in Fig. 2.9. The variation of the torque in the high-speed, flux-weakening region at 20000rpm, however, follows an inversed trend where the torque is higher for higher SPP as seen in Fig. 2.10. The power factor variation at the corner speed is shown in Fig. 2.12 and for the 8-pole machine the power factor is the lowest for SPP=2 and the power factor is similar for SPP=3 and SPP=4. The torque-speed and power-speed characteristics of the 8-pole machine for different SPP are shown in Fig. 2.13 and Fig. 2.14, respectively. For a starter generator application where cranking torque is a critical parameter, the 8-pole machine with SPP=3 is a reasonable compromise between the higher low-speed cranking torque and the flux weakening power, and, for scenario 1, represents the optimum machine topology.

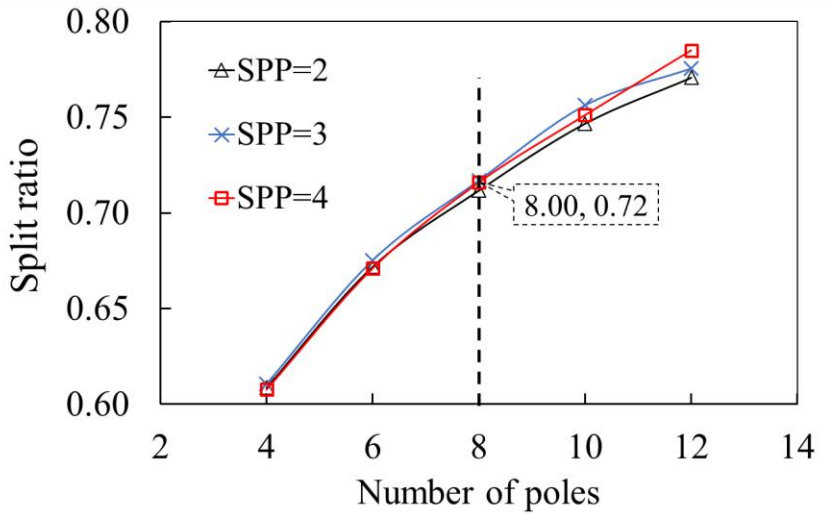

Fig. 2.6 Split ratio variation with pole number and SPP for scenario 1.

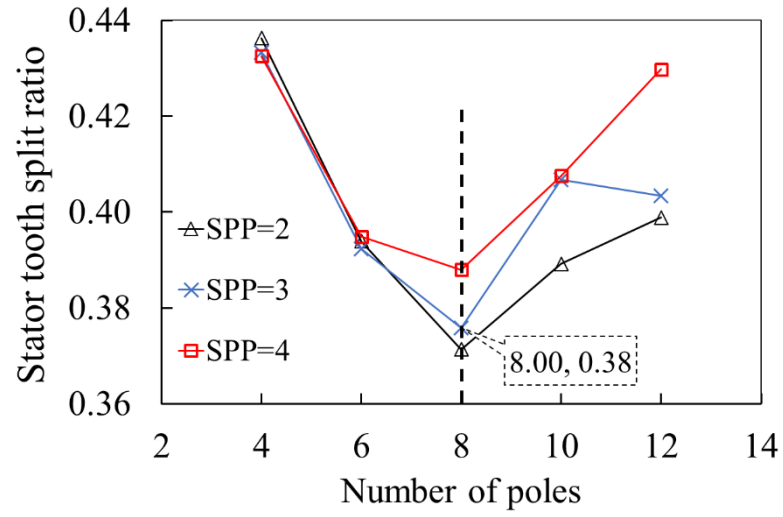

Fig. 2.7 Stator tooth split ratio variation with pole number and SPP for scenario 1.

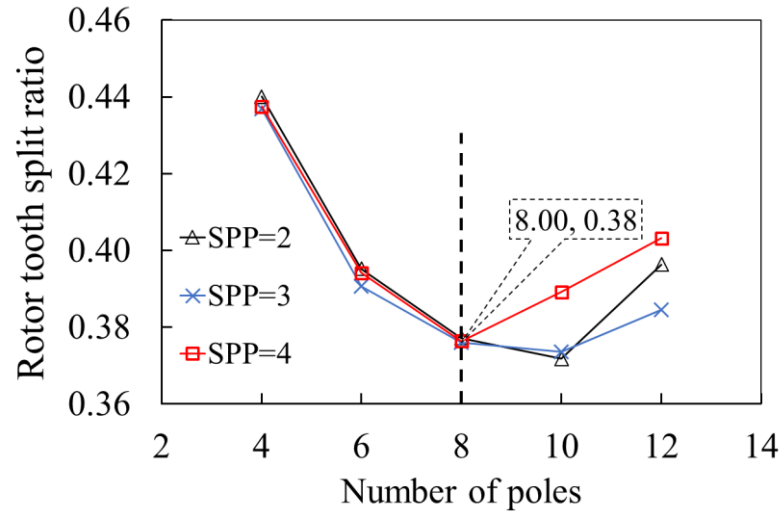

Fig. 2.8 Rotor tooth split ratio variation with pole number and SPP for scenario 1.

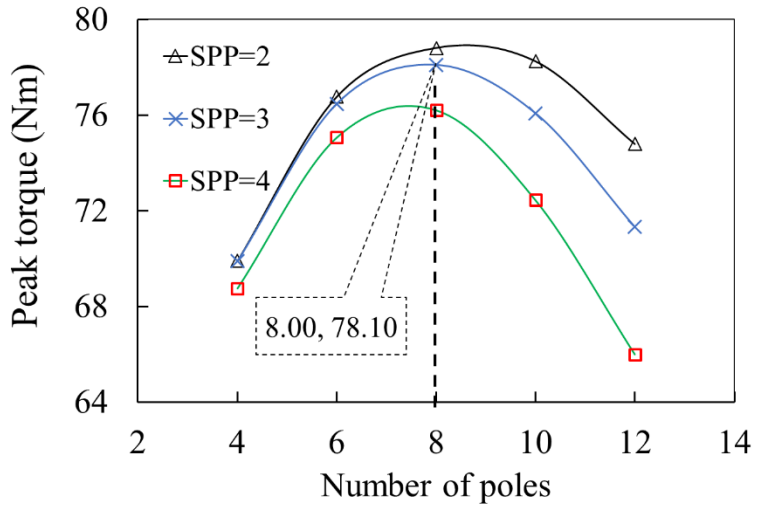

Fig. 2.9 Peak torque variation with pole number and SPP for scenario 1.

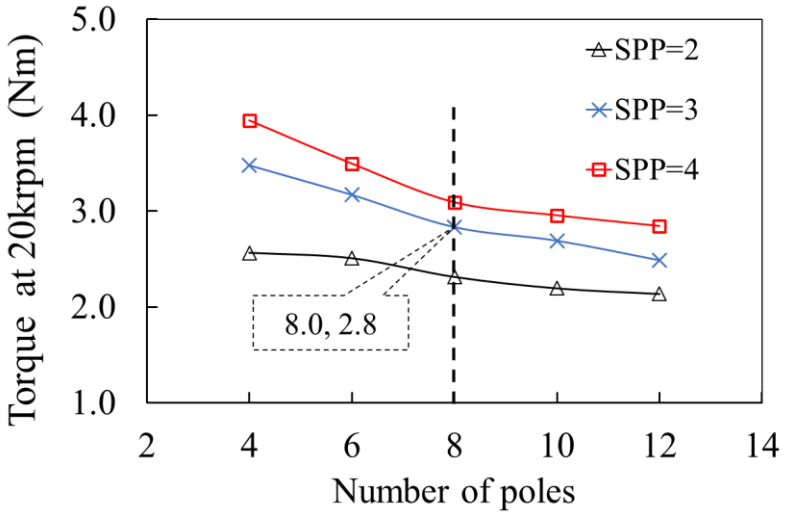

Fig. 2.10 Variation of torque at 20000rpm with pole number and SPP for scenario 1.

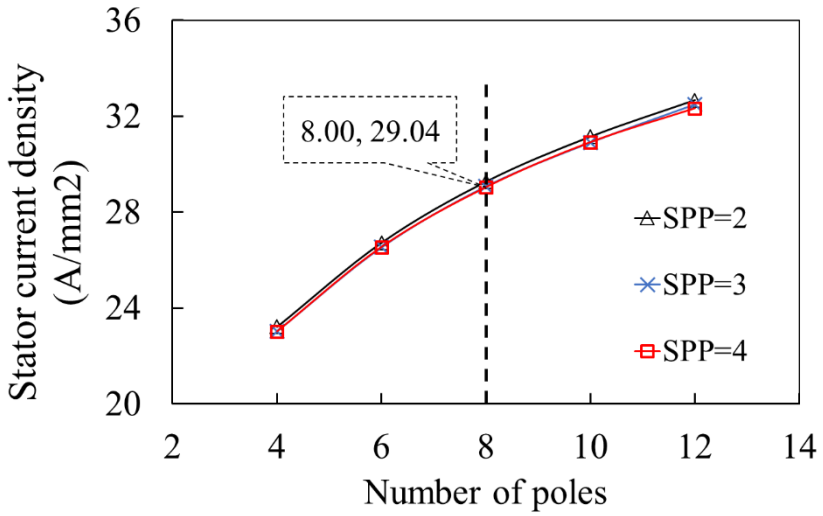

Fig. 2.11 Stator current density variation with pole number and SPP for scenario 1.

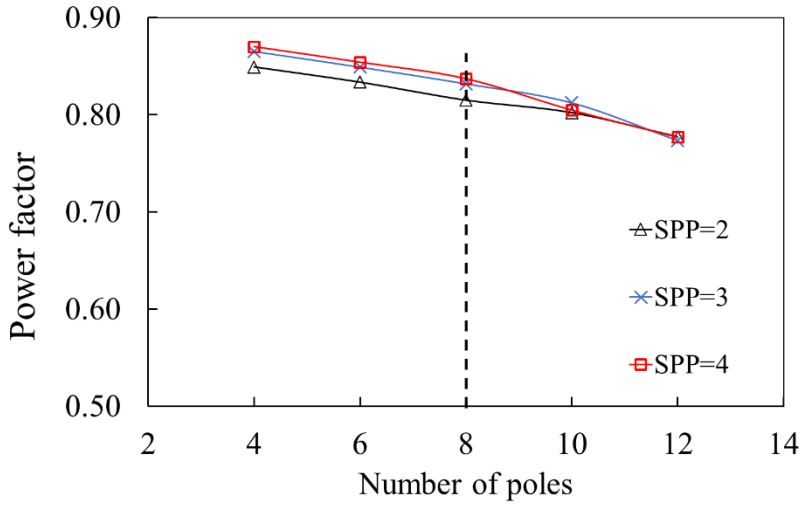

Fig. 2.12 Variation of power factor with pole number and SPP at a corner speed of 2000rpm for scenario 1.

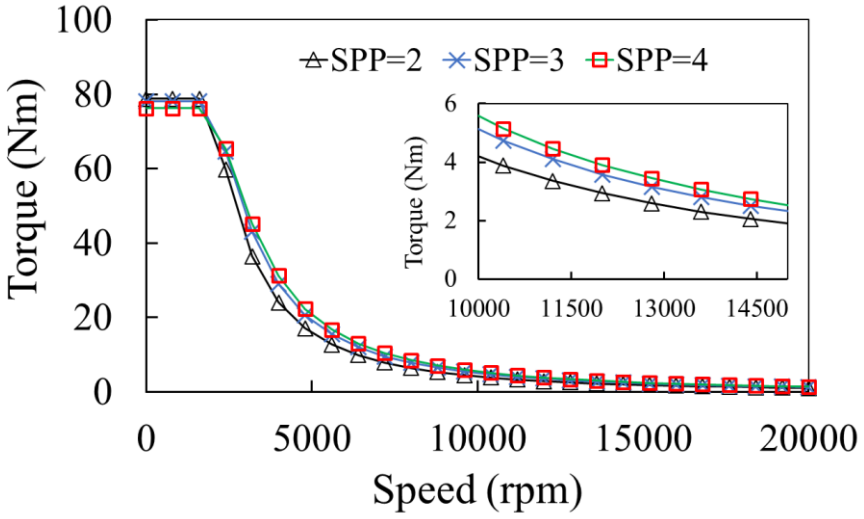

Fig. 2.13 Torque-speed characteristics of 8-pole machines for SPP=2, 3 and 4 for scenario 1.

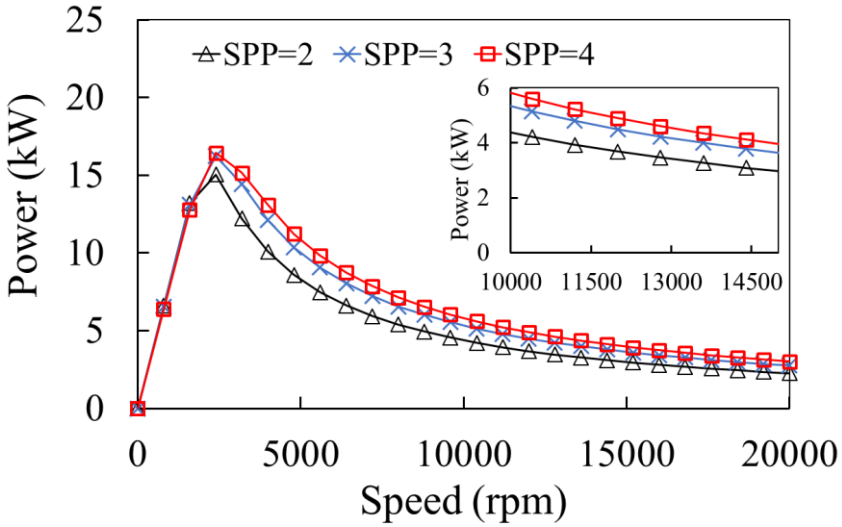

Fig. 2.14 Power-speed characteristics of 8-pole machines for SPP=2, SPP=3 and SPP=4 for scenario 1.

D. Scenario 2

For scenario 2, as seen from TABLE 2.2, the number of conductors per phase is kept fixed at 2 and the number of parallel paths is adjusted to result in the number of series turns per phase being as close as possible to 12. This is not always feasible under the constraints of the allowable number of parallel paths which must be a multiple of the number of poles. As a result, the corner speed varies considerably for each of the designs. The variation of the optimum split ratio that maximises the torque at the reference corner speed of 2000rpm, with different pole number for various SPP, is shown in Fig. 2.15. The split ratio variations with the number of poles for the machines with SPP of 2 and SPP of 4 are similar except for the case where the number of poles is 10. This is due to their difference in the number of series turns per phase for this case. The optimum split ratio for machines with SPP=3 is also different from the machines with SPP of 2 and 4 because the number of series turns per phase is different for this value of SPP compared to the others. The stator and rotor tooth width to slot pitch ratios are shown in Fig. 2.16 and Fig. 2.17, respectively. These values are expectedly different for SPP of 2 and 4 despite similarities in the number of series turns per phase since the tooth width is affected by the number of stator and rotor tooth numbers which are different for different SPP values. Unlike in scenario 1, due to the number of series turns per phase being different, the peak torque of the machines are different than the torque at the reference corner speed of 2000rpm. The variation of peak torque with various SPP and an increasing number of poles is shown in Fig. 2.18. The variation of torque at 2000rpm is shown in Fig. 2.19. Consider the peak torque value from Fig. 2.18 for an SPP of 3 for the case where the number of poles is 6, 8 and 10. The corresponding numbers of series turns per phase are 18, 12 and 15, respectively. The higher the number of series turns per phase, the higher the peak torque but correspondingly the lower the corner speed. As a result, while the peak torque is higher for the 6-pole and 10-pole machines, the torque at 2000rpm which is beyond their respective corner speeds, is lower than that of the 8-pole machine. Furthermore, the 8-pole machine with 12 series turns per phase has the highest torque at 2000rpm. It can also be observed that the 6-pole machine with SPP of 2 which also has 12 series turns per phase performs similarly. The stator conductor current density variation is shown in Fig. 2.21. The variation of the power factor at the corner speed is shown in Fig. 2.22 and for the 8-pole machines is seen to be substantially better for an SPP of 3. The power factor of the 8-pole SPP 3 machine is also higher than that of the 6-pole SPP 2 machine due to the lower end winding length and consequently lower leakage inductance. Finally, the torque-speed and power-speed characteristics of the 8-pole machines are compared in Fig. 2.23 and Fig. 2.24 respectively where the wide speed flux weakening region of the machine with SPP of 3 can be observed.

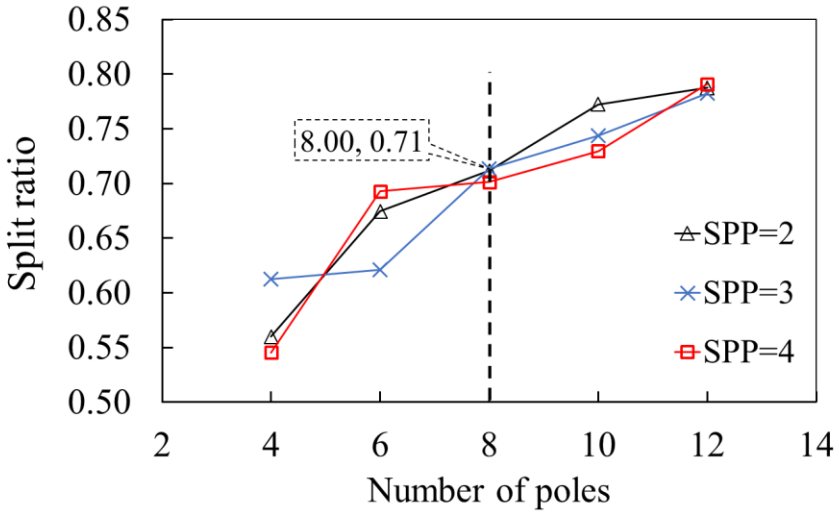

Fig. 2.15 Split ratio variation with pole number and SPP for scenario 2.

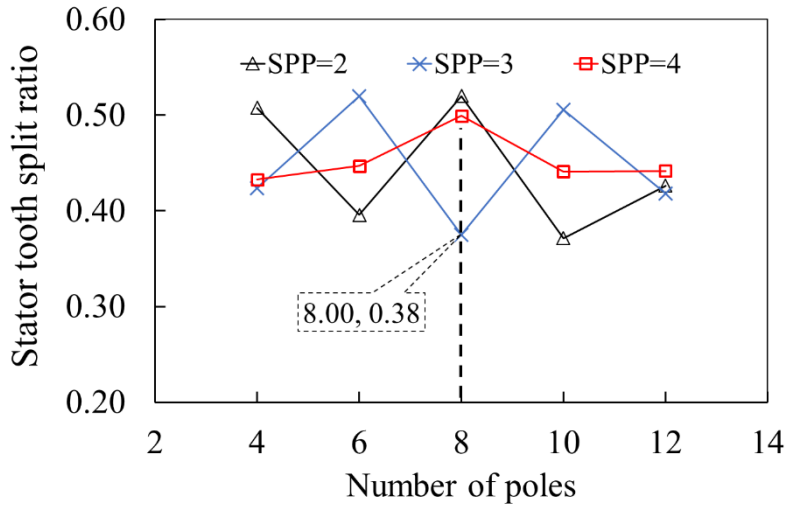

Fig. 2.16 Stator tooth split ratio variation with pole number and SPP for scenario 2.

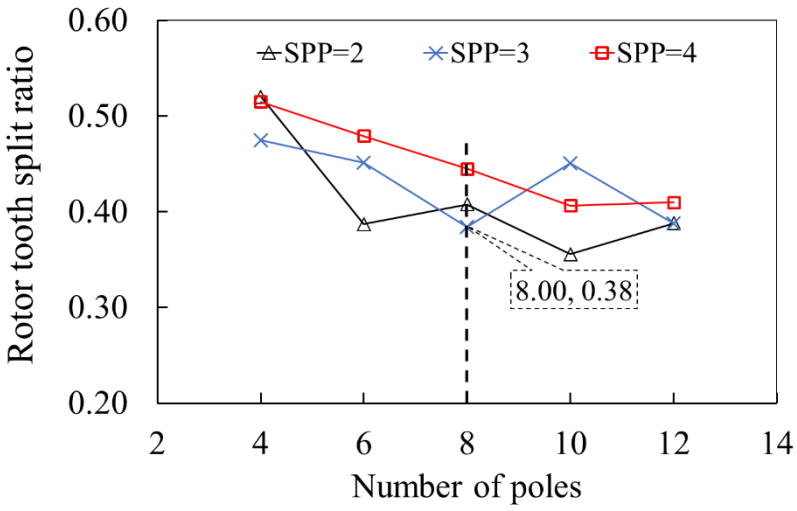

Fig. 2.17 Rotor tooth split ratio variation with pole number and SPP for scenario 2.

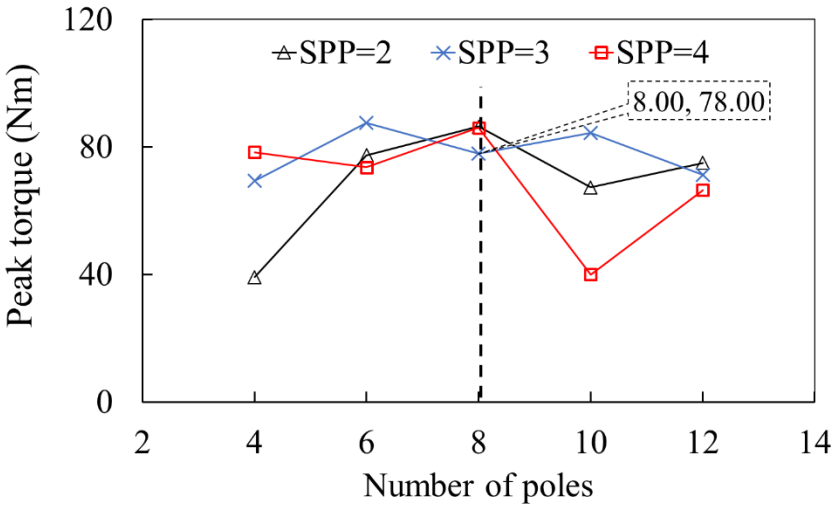

Fig. 2.18 Peak torque variation with pole number and SPP for scenario 2.

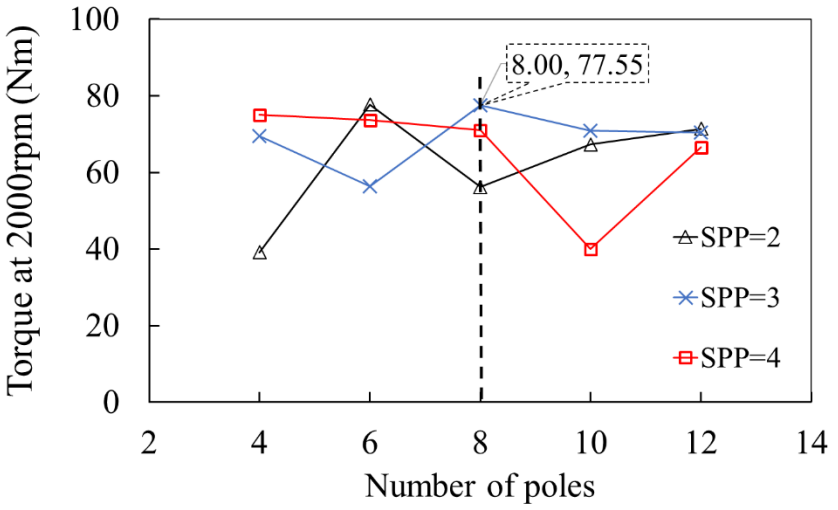

Fig. 2.19 Torque variation at 2000rpm with pole number and SPP for scenario 2.

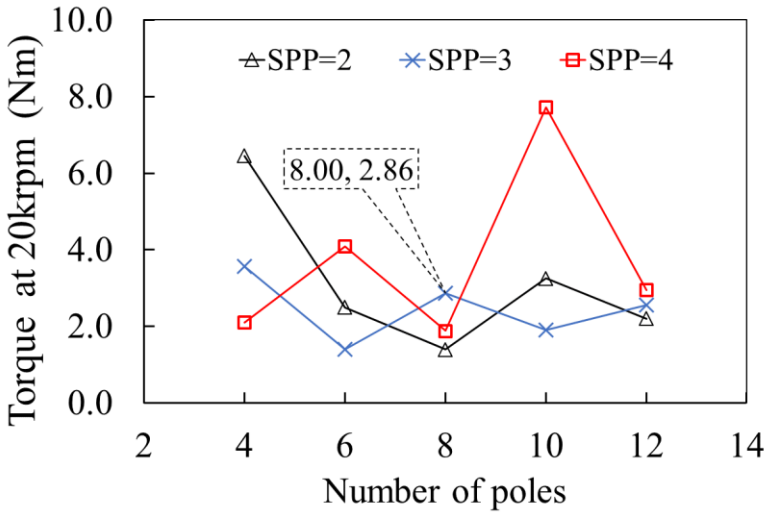

Fig. 2.20 Torque variation at 20000rpm with pole number and SPP for scenario 2.

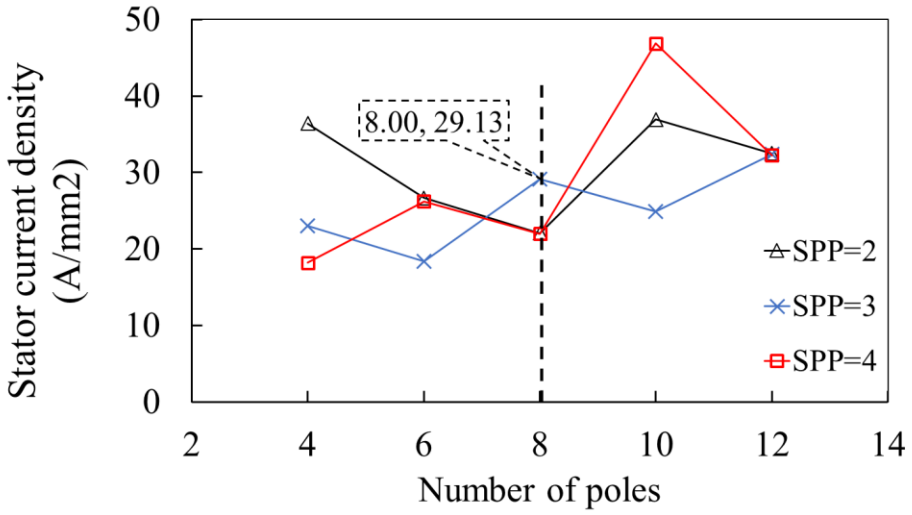

Fig. 2.21 Stator current density variation with pole number and SPP for scenario 2.

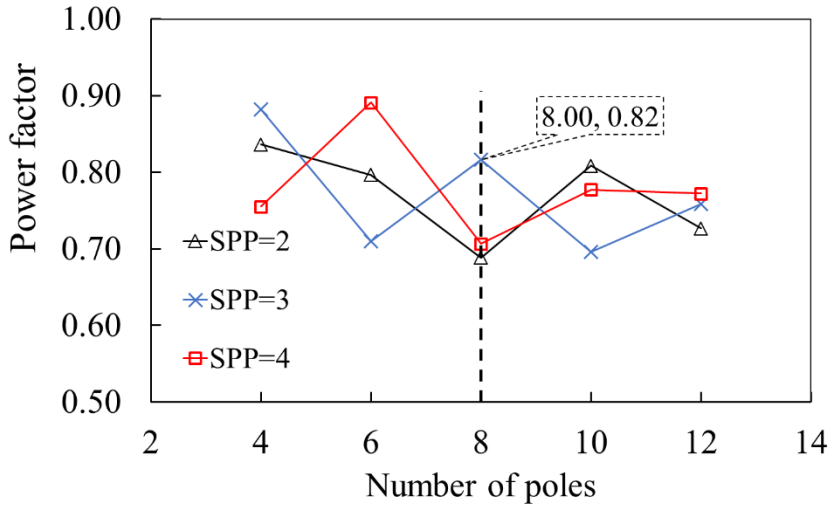

Fig. 2.22 Variation of power factor with pole number and SPP at a corner speed of 2000rpm for scenario 2.

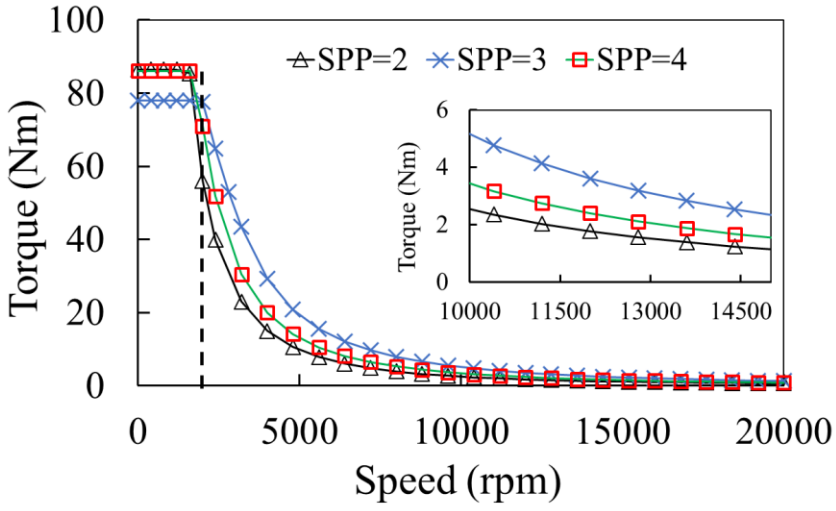

Fig. 2.23 Torque-speed characteristics of 8-pole machines for SPP=2, SPP=3 and SPP=4 for scenario 2.

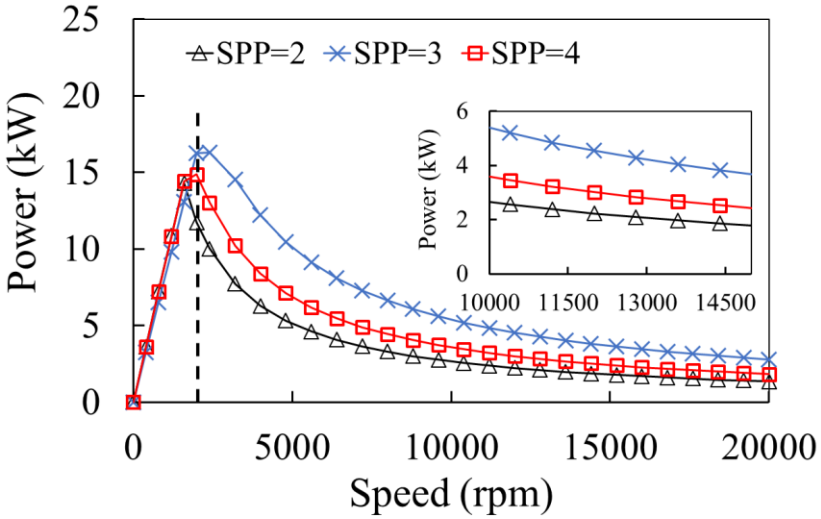

Fig. 2.24 Power-speed characteristics of 8-pole machines for SPP=2, SPP=3 and SPP=4 for scenario 2.

2.2 Influence of Rotor Slot Number on Flux Weakening Characteristics

The performance of an induction machine over the speed range depends on several parameters, such as rotor diameter, stack length, winding configuration, pole number, stator and rotor slot numbers [GUA15] [BIA97a] [GYF13] [FIR07] [LIA95]. The typical regions of the torque-speed curve of the induction machine are shown in Fig. 2.25. The corner speed at the end of the region I and the speed at the end of region II are inversely proportional to the number of turns and square of the number of turns, leakage inductance, respectively. The torque/power capability in all the three regions depends on the ratio of leakage inductance to magnetizing inductance. As the ratio of leakage inductance to magnetising inductance is decreased, the torque in the low speed as well as in the high-speed increases [OLD85] [KIM97]. While the leakage inductance affects the torque in all the regions, rotor resistance affects the torque only in the flux weakening region [GUA15]. Previously, the impact of rotor slot numbers has been discussed mainly concerning the noise vibration and unbalanced magnetic pull [BES09a] [HIR97]. Rotor slot shaping has been primarily discussed as a means to reduce leakage inductance to improve the torque capability of the induction machine [HLI17a] [HLI17b] [NEE95]. In this section, the influence of different slot/pole number combinations and rotor slot numbers on the torque ripple and the flux weakening performance of the induction machine is investigated. In the constant torque, low-speed region, the induction machine capability is usually limited by the inverter current rating while in the flux-weakening region it is limited by the breakdown torque achievable by the machine for a fixed, rated inverter voltage. The breakdown torque of the induction machine is inversely proportional to the leakage inductance of the machine. The choice of the stator and rotor slot numbers of line-fed induction machines is restricted to avoid standstill torque pulsations

and the phenomena of crawling and cogging during start-up. For variable-speed induction machines, the same constraints do not exist since the inverter can be used to control the slip from very low speeds. Rather, the choice of the stator/rotor slot number combinations is based on consideration of noise, torque ripple and machine performance [BES09]. The choice of rotor slot number influences the leakage inductance and the torque in the flux weakening region. To study the influence of the number of rotor slots on the performance of the induction machine, for the different slot/pole number combinations listed in TABLE 2.2 the scenario I, various rotor slot numbers listed in TABLE 3.3 are considered.

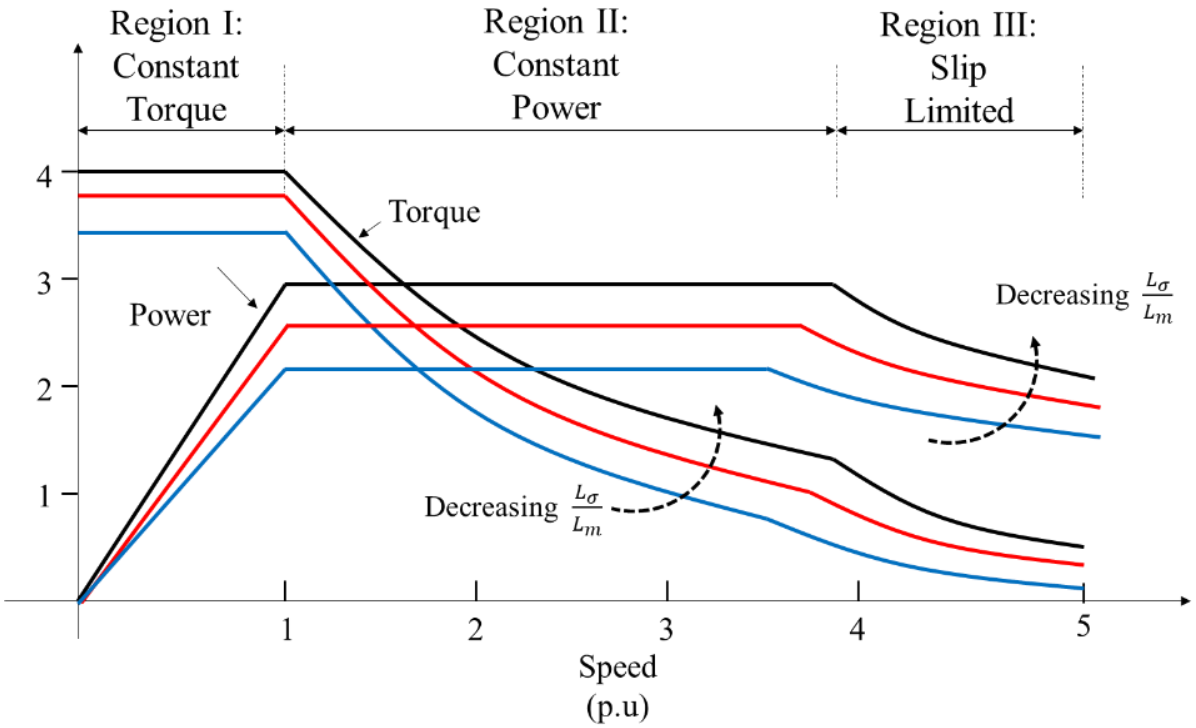

Fig. 2.25. Influence of ratio between leakage and mutual inductances on IM's flux-weakening performance.

The range of rotor slot numbers are chosen so that the number of rotor slots N_R is in the range of $0.75N_S \leq N_R \leq 1.25N_S$, where N_S and N_R are the number of stator and rotor slots respectively. A large difference in the numbers of stator and rotor slots leads to increased cogging torque. Additionally, the upper limit of the number of rotor slots is limited by manufacturing capability. Further results that justify this range of choice in the number of rotor slots is discussed following the presentation of the results.

TABLE 2.3 INVESTIGATED ROTOR SLOT NUMBERS FOR VARIOUS SLOT/POLE COMBINATIONS

q	*2p*	*Ns*	**Rotor Slot Number (N_R)**				
2	4	24	18	20	28	30	32
2	6	36	30	32	40	42	44
2	8	48	42	44	52	54	56
2	10	60	54	56	64	66	68
2	12	72	66	68	76	78	80
3	4	36	30	32	40	42	44
3	6	54	48	50	58	60	62
3	8	72	66	68	76	78	80
3	10	90	84	86	94	96	98
3	12	108	102	104	112	114	116
4	4	48	42	44	52	54	56
4	6	72	66	68	76	78	80
4	8	96	90	92	100	102	104
4	10	120	112	114	124	128	130
4	12	144	134	138	150	154	156

2.2.1 Variation of Inductances with Rotor Slot Number

Though different rotor slot shapes may be used for induction machines, the slot shape used to accommodate the rotor bars in all the machines of TABLE 2.3 is trapezoidal. For a fair comparison of the influence of the rotor slot numbers, the rotor is not skewed. Any skewing will only further reduce the torque ripple but also reduce the average torque. A typical cross-section of the stator and rotor slot shapes used for designing the different induction machines is shown in Fig. 2.26. Components of the rotor leakage inductance are shown in (2.7).

$$L_{lR} = L_{slR} + L_{dR} + L_{eR} = \frac{4m(WK_w)^2}{N_R}(\lambda_{slR} + \lambda_{dR} + \lambda_{eR}) \tag{2.7}$$

where L_{slR}, L_{dR}, L_{eR}, m, N_R, W, K_W, λ_{slR}, λ_{dR}, and λ_{eR} are the slot leakage inductance, the differential leakage inductance, the end leakage inductance, the number of phases, the number of rotor slots, the series turns per phase, the fundamental winding factor, the slot leakage coefficient, the differential leakage coefficient and the end leakage coefficient, respectively.

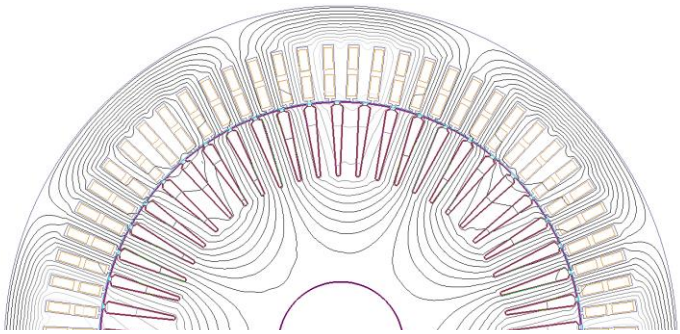

Fig. 2.26 Equipotential flux lines of an induction machine with SPP 3 and 8 poles.

Equations of approximate values of these inductances are reported in [BOL01] [LIP17] and are known to be dependent on the geometrical dimensions of the slot, pole number, air-gap length, stack lengths, number of rotor slots and end ring dimensions. For every combination of stator slot and pole numbers and a rated stator phase current, the rotor slot area A_{bar}, is calculated using (2.8).

$$A_{bar} = \frac{K_I \left(\frac{2mWK_w}{N_R}\right) I_{phase}}{J_R} \tag{2.8}$$

J_R and I_{phase} are the rotor bar current density and the stator RMS phase current, respectively. The effect of saturation on magnetising inductance is incorporated for the calculation of the torque-speed characteristics of the machine using the numerical method in [GUA14]. Torque ripple is calculated using FEM at full load and corner speed. Using the area of the rotor bar, the rotor slot dimensions and different components of leakage inductance are calculated. The variation of the rotor leakage inductance with the rotor slot number is shown in Fig. 2.27(a), Fig. 2.27 (b) and Fig. 2.27 (c) for SPP=2, SPP= 3 and SPP=4, respectively. As the rotor slot number increases, the leakage inductance reduces. The leakage inductance is also reduced for an increasing number of slots per pole per phase (SPP). In the scenario I, while the number of series turns per phase is the same, the leakage inductance is inversely proportional to the rotor slot number, and for higher SPP, the leakage inductance decreases. The stator leakage inductance is not affected by increasing the number of rotor slots while increasing the number of poles for a constant SPP decreases stator leakage.

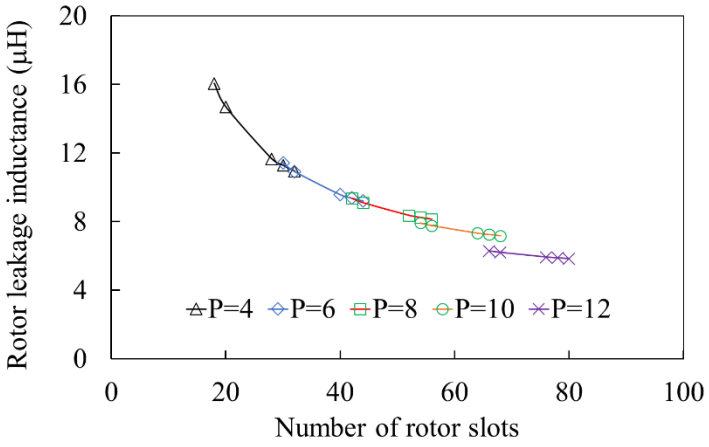

(a) SPP=2

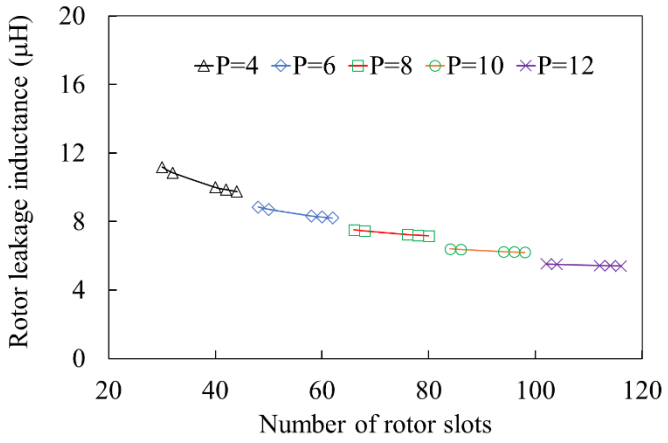

(b) SPP=3

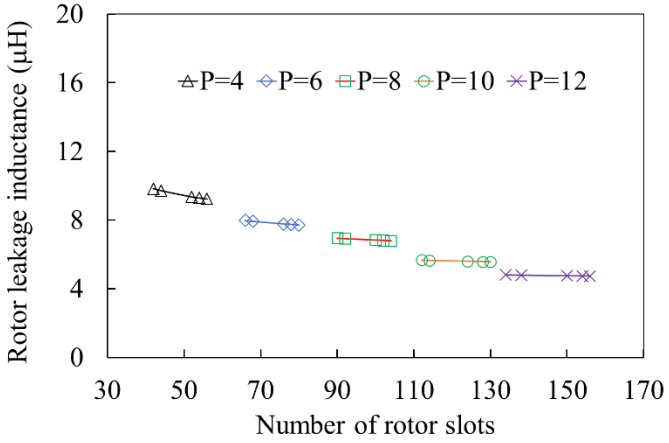

(c) SPP=4

Fig. 2.27 Rotor leakage inductance variation with increasing rotor slots.

The peak torque is inversely proportional to the total leakage inductance. The variation of total leakage inductance with increasing rotor slots is shown in Fig. 2.28 (a), Fig. 2.28 (b) and Fig. 2.28 (c) for SPP=2, SPP=3 and SPP=4, respectively.

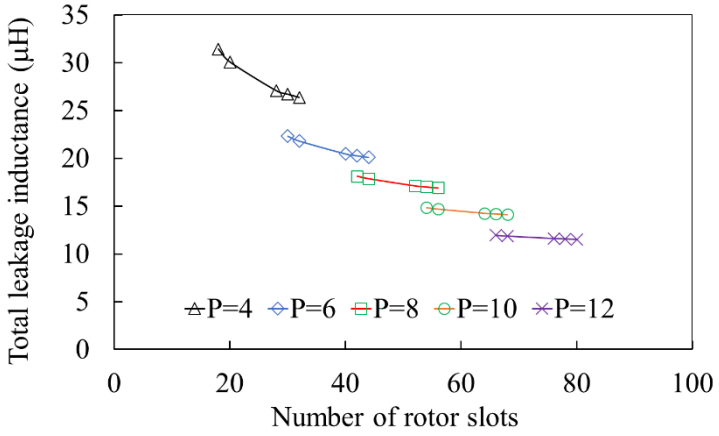

(a) SPP=2

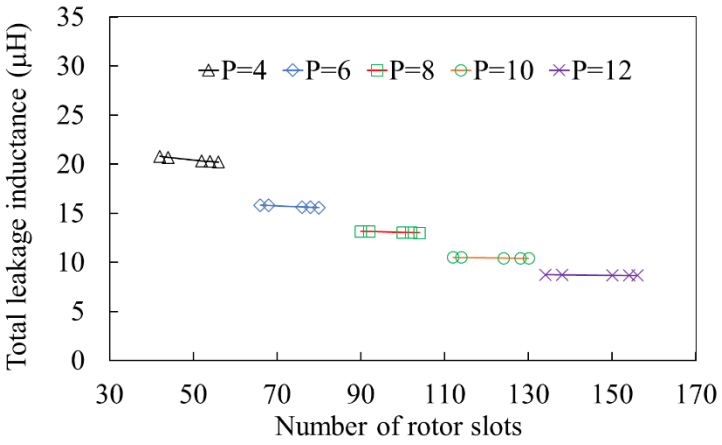

(b) SPP=3

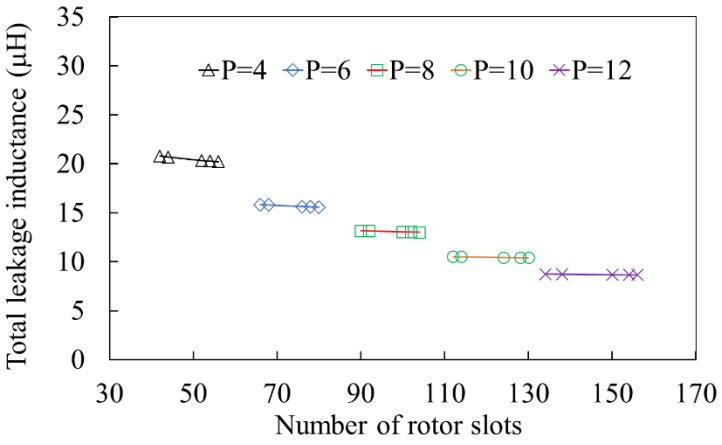

(c) SPP=4

Fig. 2.28 Total leakage inductance variation with increasing rotor slots.

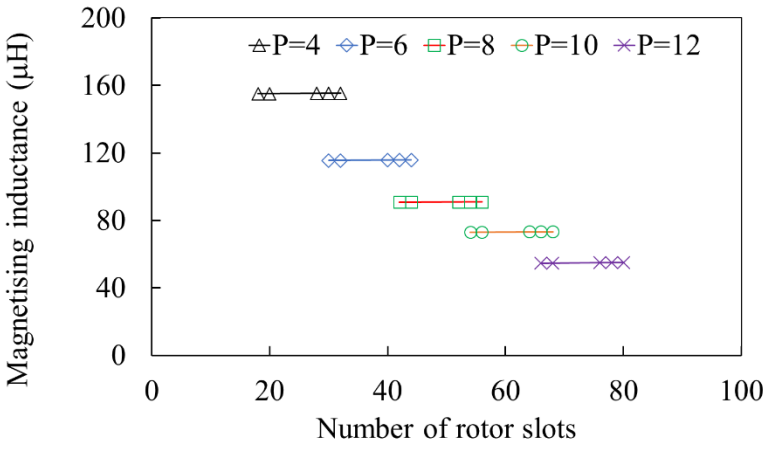

(a) SPP=2

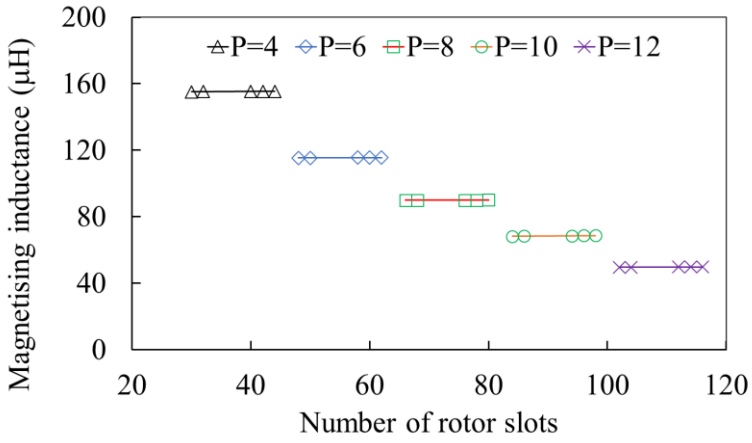

(b) SPP=3

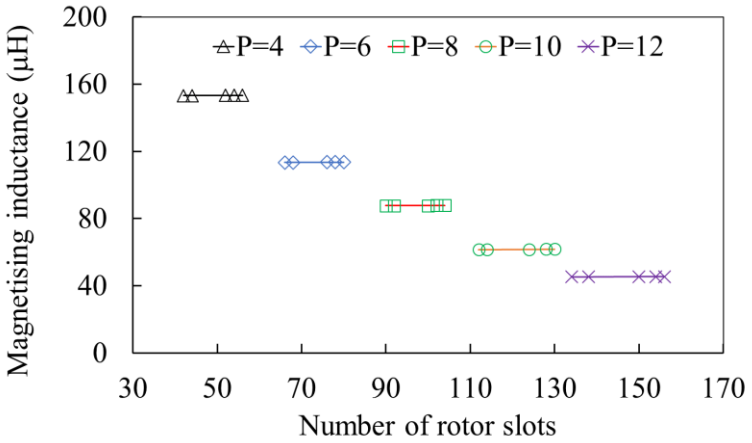

(c) SPP=4

Fig. 2.29 Magnetizing inductance variation with increasing rotor slots.

For a given SPP, as the pole number increases, the number of stator slots also increase. For higher stator and rotor slot numbers, the impact of the slotting is lower. This results in the change in the effective air gap due to slotting being higher for lower pole and rotor slot numbers. From the

total leakage inductance plots, it is seen that the number of rotor slots has a higher impact on the leakage inductance for lower pole numbers. The magnetizing inductance variation with SPP and pole number is shown in Fig. 2.29(a), Fig. 2.29(b) and Fig. 2.29 (c) for SPP=2, SPP=3 and SPP=3, respectively. The expression for unsaturated magnetizing inductance is shown in (2.9). As expected, magnetizing inductance is not influenced by the number of rotor slots.

2.2.2 Torque Capability Curves

As the number of pole increases for a given rotor slot number, the magnetizing and leakage inductances decrease. Increasing the number of poles increases the split ratio and hence the bore diameter. The magnetising inductance, however, is proportional to the stator bore diameter and inversely proportional to the square of the number of poles. The variations of peak torque and the torque at 20000rpm in the flux weakening region are shown in Fig. 2.30. Since the magnetizing inductance is almost constant and the leakage inductance decreases with an increasing number of rotor slots, the torques at the corner speed and the flux weakening region increase for a given pole number. As the number of poles increases for a given SPP, the decreasing magnetizing inductance results in the torque decreasing with pole number. The rate of decrease in leakage inductance is lower with an increasing number of rotor slots. As a result, the influence of the number of rotor slots on torque is higher for machines with a lower number of poles. The unsaturated magnetizing inductance is given in (2.9) where K_C, g, p and L_{stk} are Carter's coefficient, the air gap length, the number of pole pairs and the effective stack length of the machine, respectively.

$$L_m = \frac{3\mu_o}{\pi}\frac{D_{is}L_{stk}}{K_C g}\left(\frac{K_w W}{2p}\right)^2 \tag{2.9}$$

The peak torque capability and the torque in the flux weakening region follow the same trends as seen in Fig. 2.9 and Fig. 2.10 even with varying rotor slot number. The variation of the peak torque capability with increasing rotor slot numbers is shown in Fig. 2.30(a), Fig. 2.30(c) and Fig. 2.30(e), respectively. The variation of the torque at 20000rpm in the flux weakening region with increasing rotor slot numbers is shown in Fig. 2.30(b), Fig. 2.30(d) and Fig. 2.30(f), respectively.

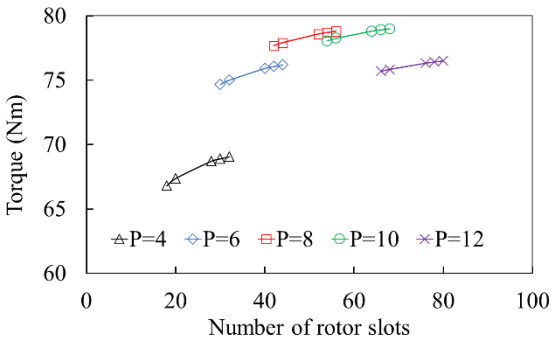

(a) Peak torque for SPP=2

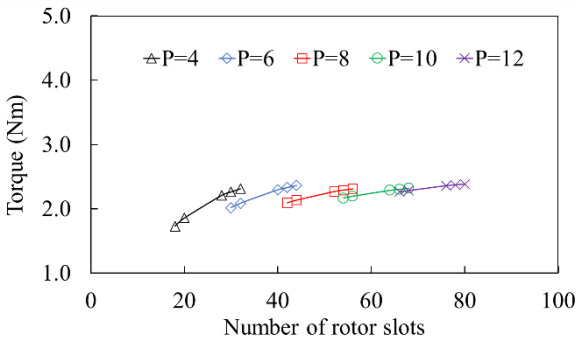

(b) Torque at 20000rpm for SPP=2

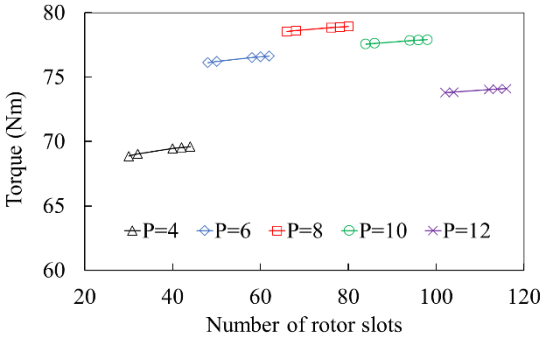

(c) Peak torque for SPP=3

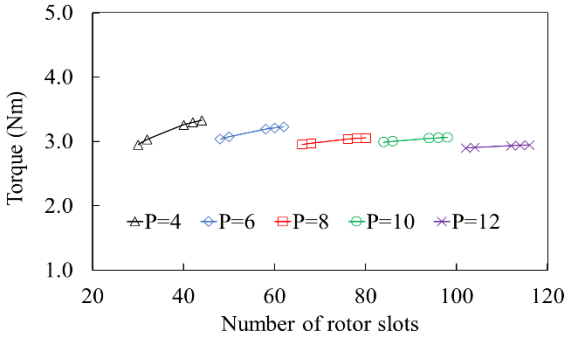

(d) Torque at 20000rpm for SPP=3

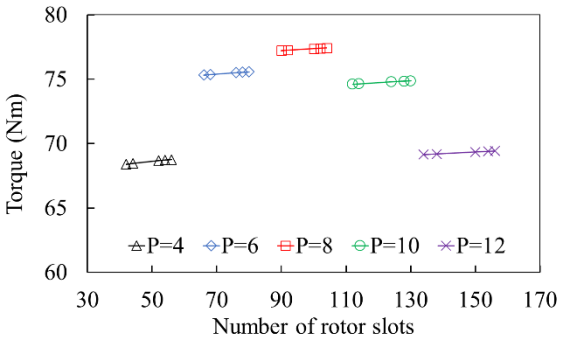

(e) Peak torque for SPP=4

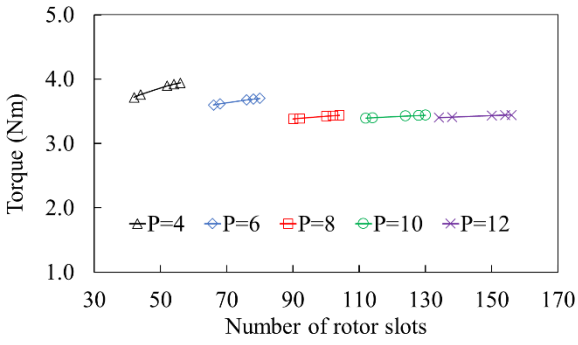

(f) Torque at 20000rpm for SPP=4

Fig. 2.30 Variation of peak torque and torque at 20000rpm with rotor slot numbers for varying SPP.

2.2.3 Influence of Rotor Slot Number on Torque Ripple

While torque ripple can be determined using analytical methods [JOK00], assumptions of infinitely permeable steel and neglecting the eddy currents in the rotor bar tips result in substantial approximations. Instead, to compare the torque ripple of the different slot pole combinations, a transient FEA model is created for each machine and the torque ripple (ratio of peak-to-peak amplitude and average torque at steady state) is computed. For each of the machines in TABLE 2.3,

the effect of increasing the number of rotor slots on the torque ripple and average torque at a corner speed of 2000 rpm for SPP=2, SPP=3 and SPP=4 are shown in Fig. 2.31, Fig. 2.32 and Fig. 2.33, respectively. While the number of rotor slots within a chosen range of $0.75N_S \leq N_R \leq 1.25N_S$ has minimum influence on the torque at the corner speed, the torque ripple is sensitive to the number of rotor slots and stator slots.

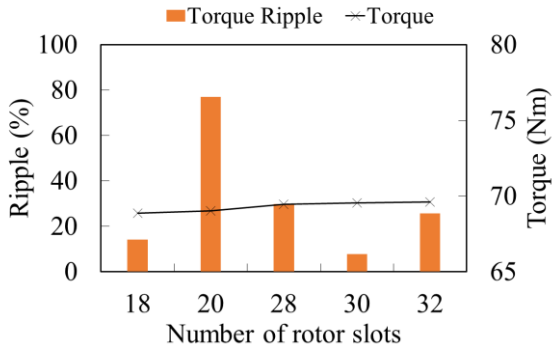

(a) 4-poles, 24 stator slots.

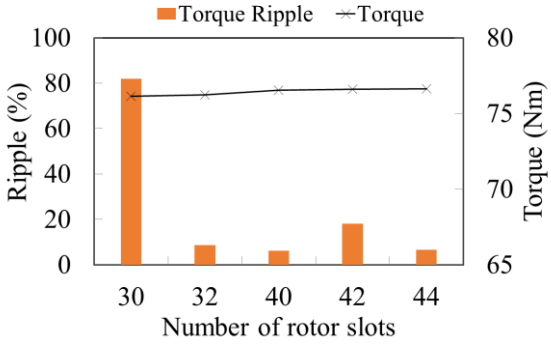

(b) 6-poles, 36 stator slots.

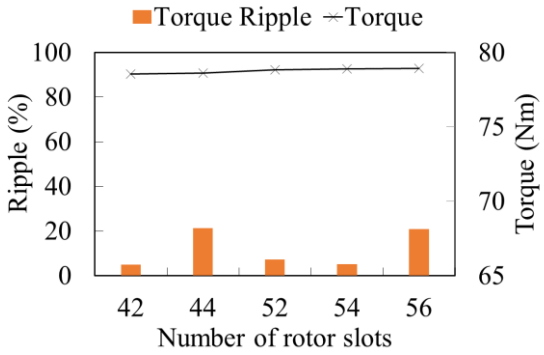

(c) 8-poles, 48 stator slots.

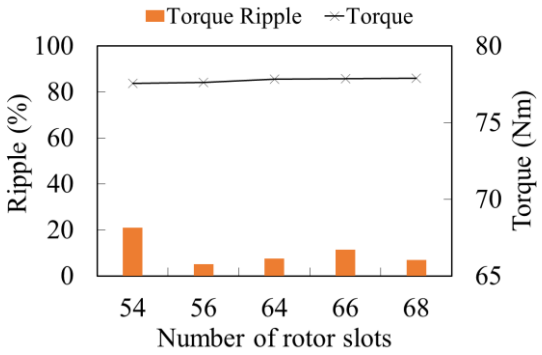

(d) 10-poles, 60 stator slots.

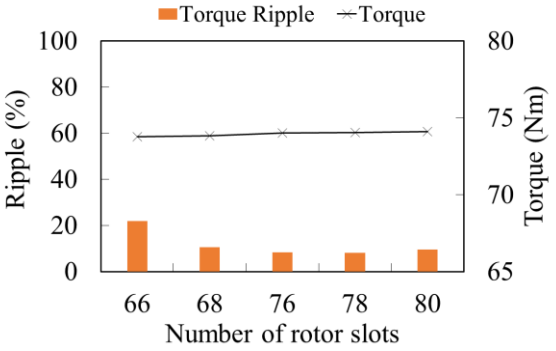

(e) 12-poles, 72 stator slots.

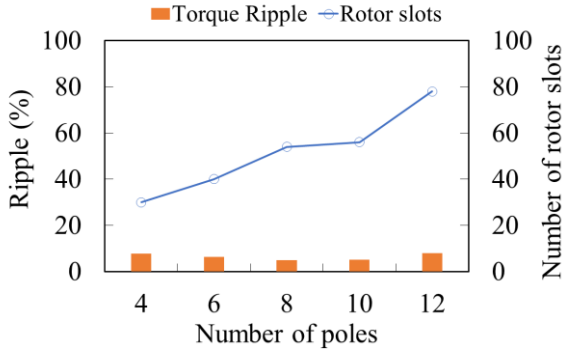

(f) Torque ripple for rotor slots with lowest torque ripple.

Fig. 2.31 Variation of torque at 2000 rpm and torque ripple with rotor slot number for SPP=2.

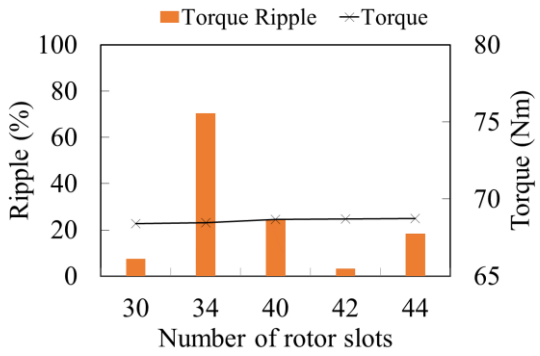

(a) 4-poles, 36 stator slots.

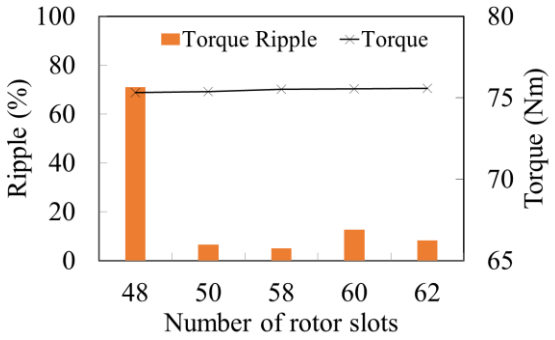

(b) 6-poles, 54 stator slots.

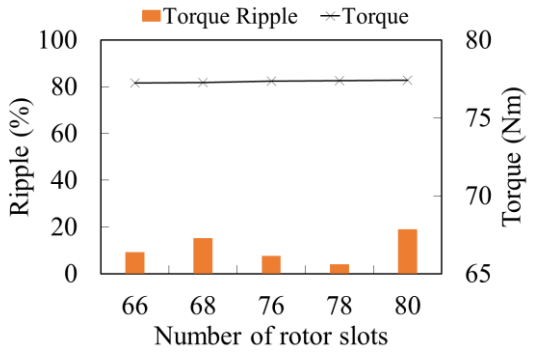

(c) 8-poles, 72 stator slots.

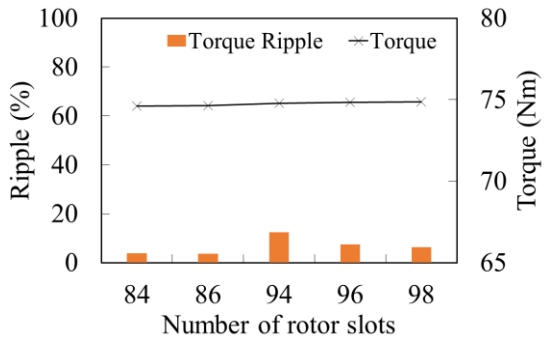

(d) 10-poles, 90 stator slots.

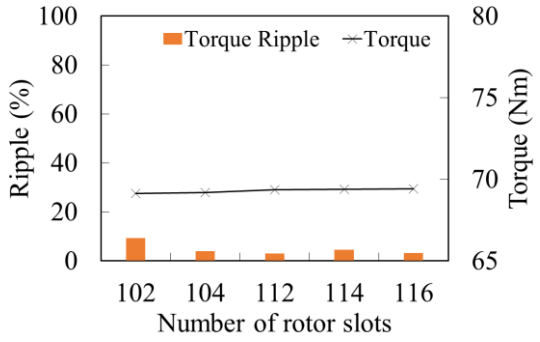

(e) 12-poles, 108 stator slots.

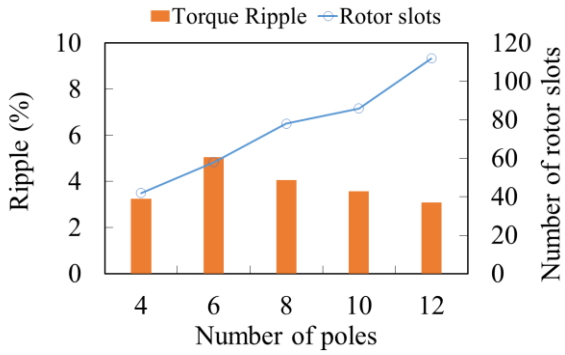

(f) Torque ripple for rotor slots with lowest torque ripple.

Fig. 2.32 Variation of torque at 2000 rpm and torque ripple with rotor slot number for SPP=3.

The optimum numbers of rotor slots that minimise the torque ripple for different pole numbers for SPP=2, SPP=3 and SPP=4 are shown in Fig. 2.31 (f), Fig. 2.32 (f), Fig. 2.33 (f), respectively.

It is observed that:

1 If the number of rotor slots is an odd multiple of poles, then the torque ripple is higher.

2 Torque ripple is low for the cases when the difference in the number of stator and rotor slots is not an integer multiple of the number of pole pairs.

3 From Fig. 2.31 (f), Fig. 2.32 (f), Fig. 2.33 (f), it is clear that the rotor slot number that minimises torque ripple and maximises torque increases with the number of poles.

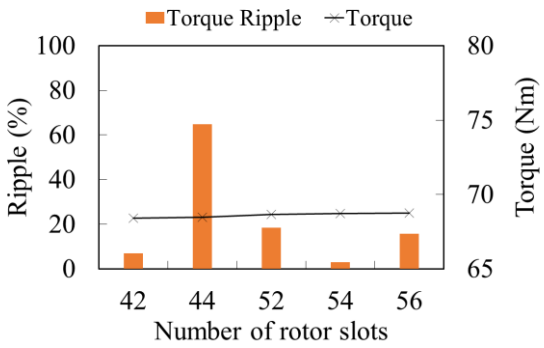

(a) 4-poles, 48 stator slots.

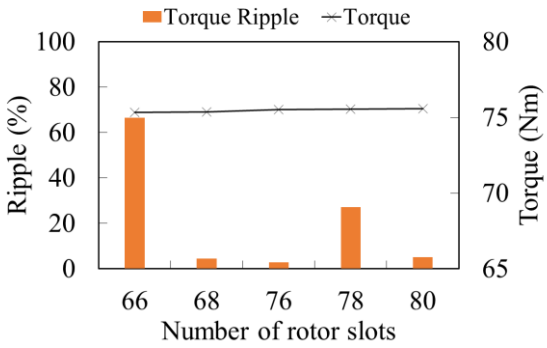

(b) 6-poles, 72 stator slots.

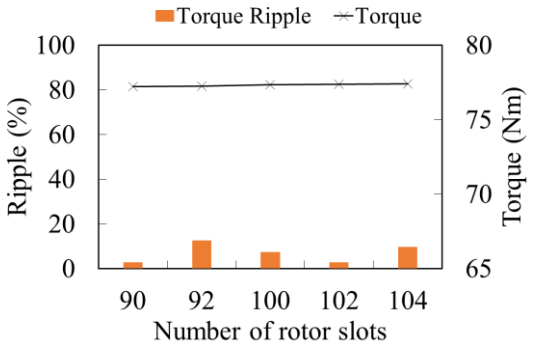

(c) 8-poles, 96 stator slots.

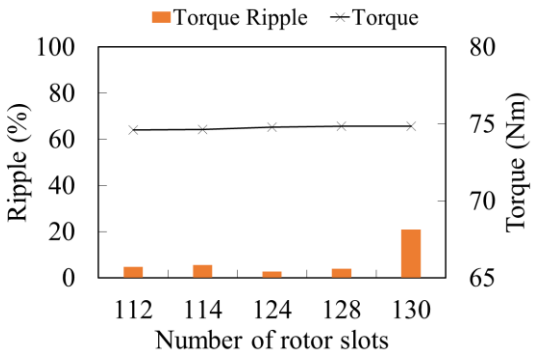

(d) 10-poles, 120 stator slots.

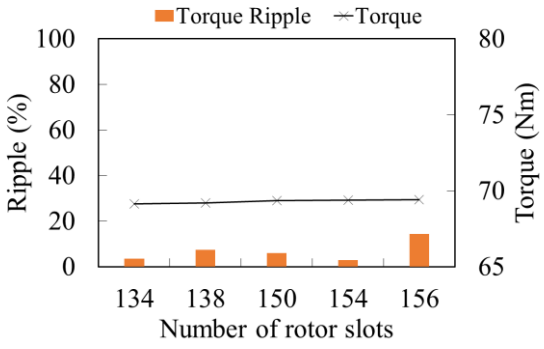

(e) 12-poles, 144 stator slots.

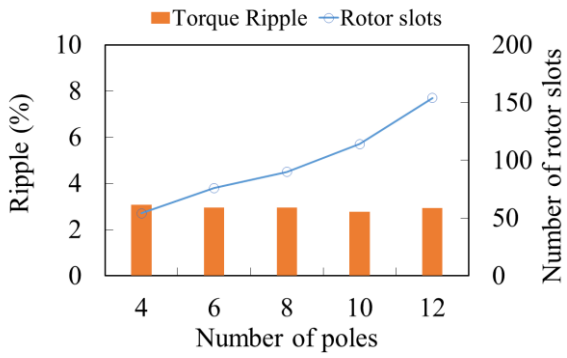

(f) Torque ripple for rotor slots with lowest torque ripple.

Fig. 2.33 Variation of torque at 2000 rpm and torque ripple with rotor slot number for SPP=4.

2.2.4 Optimal Range of Rotor Slot Number

From the discussion of leakage inductance variation with the number of rotor slots, it is clear that there is a specific range of the number of rotor slots that affects the torque of the induction machine. If the number of rotor slots is significantly lower than the number of stator slots, the torque capability is reduced, considering the case of the machine with SPP=2 and 8 poles which has 48 stator slots. For this type of machines, the range of rotor slots chosen is between 42 and 80. For 12 poles the number of stator slots is 72, the number of rotor slots is chosen to be between 44 and 80 and the leakage reactance variation is plotted for both machines in Fig. 2.34.

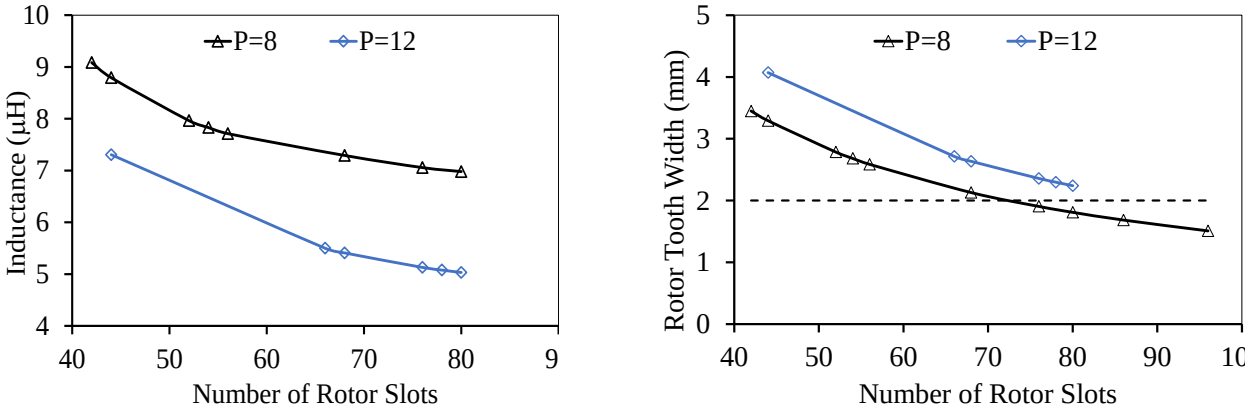

(a)Variation of total leakage inductance

(b) Rotor tooth width

Fig. 2.34 Variation of total leakage inductance and rotor tooth width with the number of rotor slots for 8 pole and 12 pole machines with SPP=2.

As the number of rotor slots is increased, the total leakage inductance reduces and the rotor tooth width also reduces for a fixed rotor current density. The rotor slot number cannot be increased beyond 80 for the 8-pole machine since the rotor tooth width becomes smaller than that is mechanically feasible as seen in Fig. 2.34(b). The rate of decrease of leakage inductance with an increasing number of rotor slots also reduces for the 8 pole machine and there is no benefit of increasing the number of rotor slots beyond 68 slots. When the number of rotor slots is 44 for a 12 pole machine (with 72 stator slots), it can be seen from Fig. 2.34 (a) that the leakage inductance is quite high compared to the case when the number of rotor slots is close to the number of stator slots. For this reason, the number of rotor slots is chosen close to the number of stator slots and within $0.75N_S \leq N_R \leq 1.25N_S$. The number of rotor slots that minimises the torque ripple in this range is then chosen as the optimum number of rotor slots.

2.2.5 Torque-speed and Power-Speed Characteristics

The torque and power versus speed characteristics over the entire speed range are plotted for the machines with SPP=3 and 8 poles for different rotor bar numbers to illustrate the influence of the number of rotor slots. The corner speed is unaffected by the change in the number of rotor slots. As the number of rotor slots is increased the peak power and torque at 20000rpm increase. The impact of the number of rotor slots on the power capability is seen to be an 11% increase in the flux weakening region compared to just a 2% increase in power in the low speed, constant torque regions for SPP of 2. From Fig. 2.35, Fig. 2.37 and Fig. 2.39, it can be seen that the influence of the rotor slot number diminishes as the SPP increases. This is because the peak torque is proportional to the ratio of the magnetizing inductance to leakage inductance and magnetizing inductance is lower in the low-speed region due to saturation [GUA15]. As a result, the influence of the reduction in leakage inductance due to the increase in the number of rotor slots is higher in the high-speed region compared to the low-speed region.

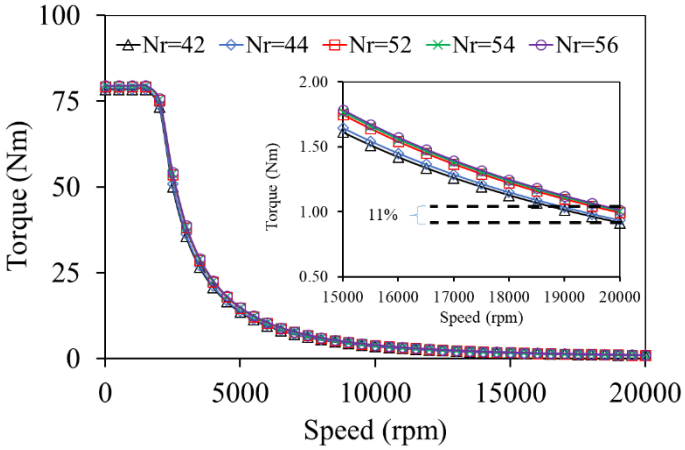

Fig. 2.35 Torque-speed characteristic for 8 pole machine with SPP=2 and a varying number of rotor slots.

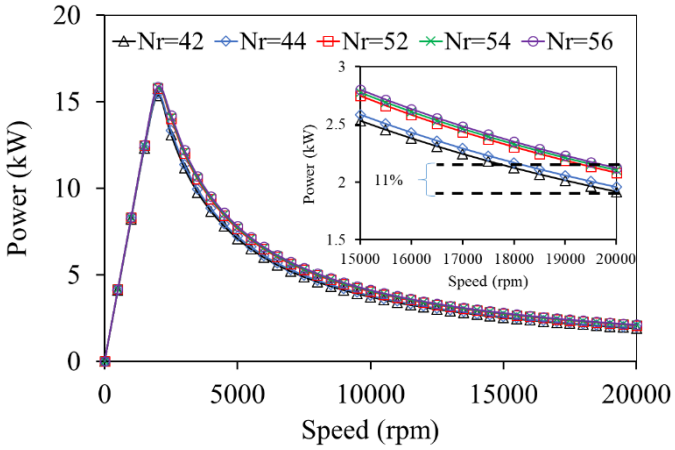

Fig. 2.36 Power-speed characteristic for 8 pole machine with SPP=2 and a varying number of rotor slots.

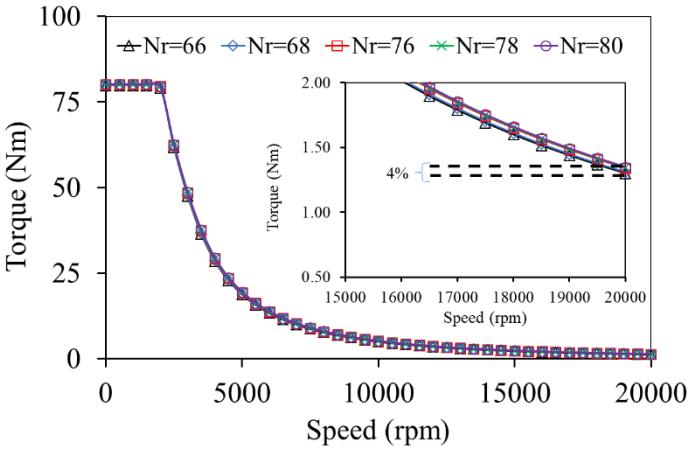

Fig. 2.37 Torque-speed characteristic for 8 pole machine with SPP=3 and a varying number of rotor slots.

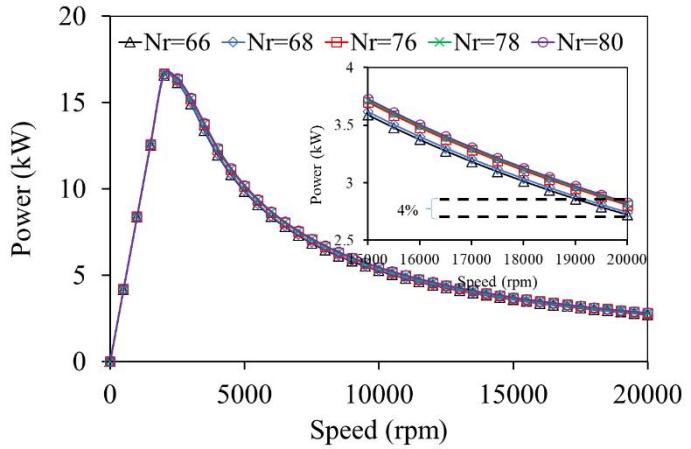

Fig. 2.38 Power-speed characteristic for 8 pole machine with SPP=3 and a varying number of rotor slots.

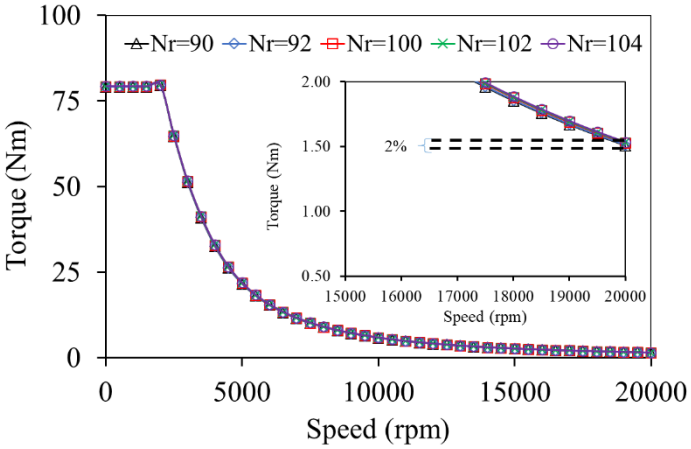

Fig. 2.39 Torque-speed characteristic for 8 pole machine with SPP=4 and a varying number of rotor slots.

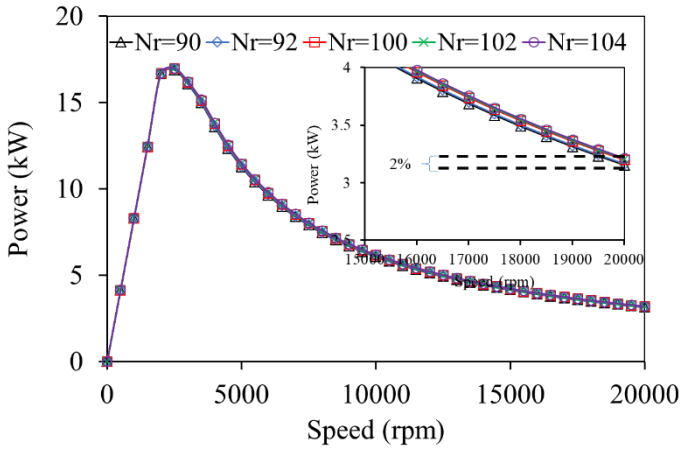

Fig. 2.40 Power-speed characteristic for 8 pole machine with SPP=4 and a varying number of rotor slots.

2.3 Optimal Machine

From the preceding analyses, the 8-pole machine with an SPP of 3 is the optimum stator slot/pole number combination. The optimum machine is determined based on the compromise between the cranking torque performance in the low speed region and the widest operating speed for the power in the flux weakening region. The machine with SPP=2 has a higher peak torque but lower power in the high speed region and this is reversed for SPP=4 machines. The SPP=3 machine has a compromise between these two extremes. The 8-pole SPP=3 optimal machine has 72 stator slots 78 rotor slots for minimising torque ripple. A FEA model is created for the optimal machine. To simulate the transient and steady state torque, the shaft speed is maintained constant and the voltage at a frequency corresponding to the shaft speed is applied to the stator terminals and the current and torque transients are allowed to evolve as shown in Fig. 2.43 and Fig. 2.44.

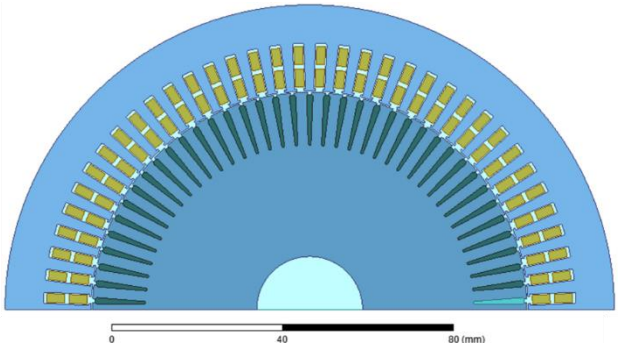

Fig. 2.41 Cross-section of the optimised 72 stator slot, 78 rotor slot 8-pole induction machine.

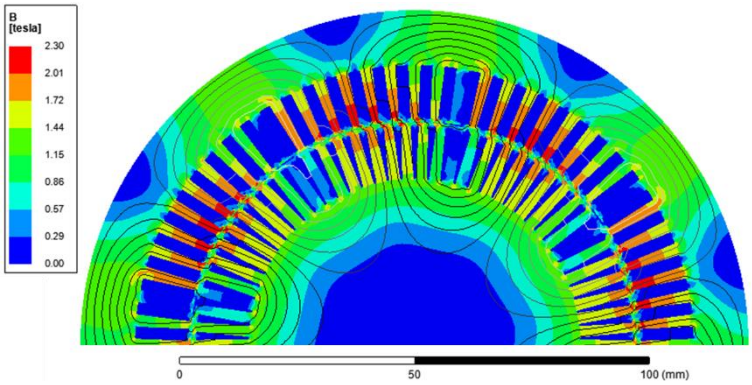

Fig. 2.42 Flux density plot of the optimised 72 stator slot, 78 rotor slot 8-pole induction machine at 2000rpm.

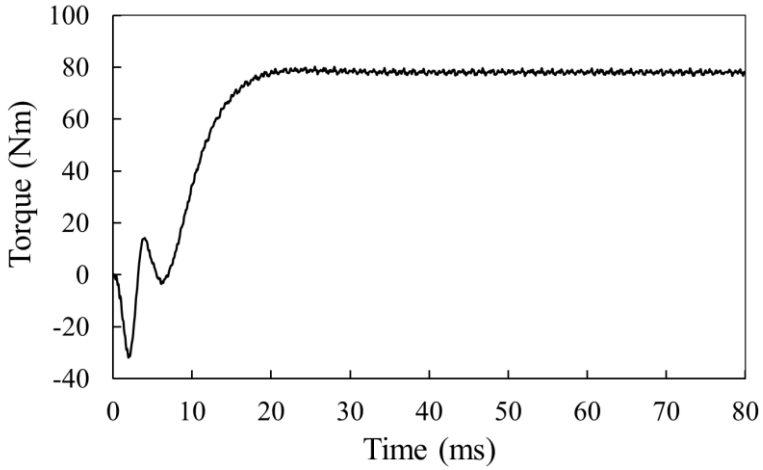

Fig. 2.43 Torque waveform of the optimised 72 stator slot, 78 rotor slot 8-pole induction machine at 2000rpm and 460Arms.

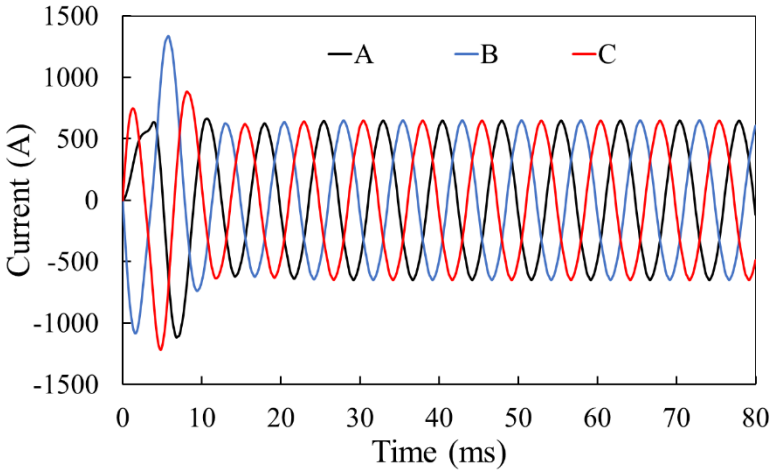

Fig. 2.44 Phase current waveforms of the optimised 72 stator slot, 78 rotor slot 8-pole induction machine at 2000rpm and 460Arms.

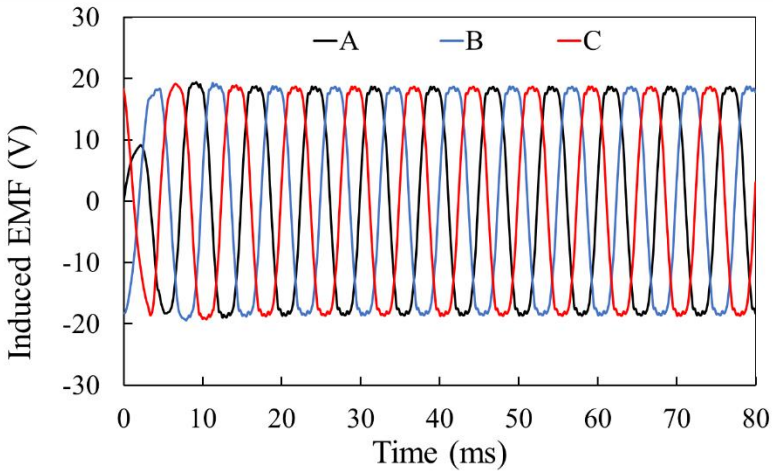

Fig. 2.45 Induced phase EMF of the optimised 72 stator slot, 78 rotor slot 8-pole induction machine at 2000rpm and 460Arms.

The number of rotor slots for this machine that results in the lowest torque ripple is 78. The cross-section of the machine used for FEA is shown in Fig. 2.41 and the corresponding flux density plot is shown in Fig. 2.42. The torque waveform at the corner speed and rated current of 460Arms is shown in Fig. 2.43 and the phase currents and induced phase EMF for this operating condition are shown in Fig. 2.44 and Fig. 2.45, respectively.

2.4 Conclusions

In this chapter, the influence of the number of poles, the number of stator slots and the number of rotor slots on the torque capability of the induction machine in the constant torque and flux-weakening region has been investigated. The following observations are noted:

1. Two scenarios have been investigated. In the first scenario, the number of series turns per phase is fixed at 12 to hold the corner speed fixed. In the second scenario, the number of conductors per slot is held fixed at 2 to maximise the slot-fill factor. In either scenario, the 8-pole induction machine with an SPP of 3 is determined to be optimum for peak torque and torque in the flux-weakening region.

2. The influence of the choice of the number of rotor slots has on the performance of the induction machine has been investigated. Specifically, increasing the number of rotor slots is shown to decrease the rotor leakage inductance for any value of SPP and number of poles. However, since the magnetizing inductance decreases with the increasing number of poles for a fixed stack length and outer diameter, the torque capability is reduced with the number of poles. The influence of a higher number of rotor slots on leakage inductance is significantly higher for lower pole numbers. Due to saturation and consequent reduction of magnetizing inductance, the number of rotor slots

has little influence in the low-speed high torque region compared to the high-speed region where the machine is unsaturated.

3. Finally, the variation of torque ripple, tooth width and leakage inductance with an increasing number of rotor slots are used to define an optimal range of the number of rotor slots with the number of stator slots for different SPP and number of poles.

Chapter 3

Three-phase Pole-changing Winding Induction Machines

Pure Electric Vehicles (EVs) offer the best solution to meeting future emission requirements of the automotive industry. However, the present energy density of the battery and lack of accessible charging infrastructure limit their operating range and widespread use. Hybrid electric vehicles (HEVs), on the other hand, permit the use of smaller internal combustion engines (ICE) and provide an interim method to reduce emissions. At the lowest end of hybridisation, 12V micro-hybrids incorporate a starter-generator with a start-stop functionality and limited regeneration and low fuel reduction potential. 48V architectures offer further hybridisation with a larger starter-generator that can provide start-stop functionality, regeneration over a wide engine speed range as well as a moderate torque boost capability thus offer significant fuel saving [SCH17]. This starter-generator can be either mounted on the flywheel in-line with the engine as an integrated starter-generator (ISG) or as a side-mounted machine coupled to the engine as a belt-driven starter-generator (BSG). While the former system allows a more compact packaging, the latter allows for a minimum change in existing engine layout [WAL04]. Different machine types, such as the claw pole, permanent magnet synchronous machines, switched reluctance and induction machines, have been compared for use in this application.

Induction machines offer a good alternative to other machine types for mild HEVs because of high overload capability, high efficiency at high speeds, relatively simple design, robustness, and lower cost due to the absence of rare-earth permanent magnets [ZHU07] [CAI04]. In BSG, the electrical machine is coupled to the engine via a belt and needs to operate intermittently at low speeds with high torque to crank the engine quickly and continuously at high speeds during the cruising period of the drive cycle requiring a machine with wide-speed operating characteristic. Induction machines that are designed for wide-speed operation need to be optimized for performance both in the low speed and high-speed regions. The corner speed and the torque at the corner speed of the induction machine determine the extent of the flux weakening region of the machine [DOR10]. One of the methods of extending the flux weakening region is by rotor slot shaping as a means to reduce leakage inductance to improve torque capability of the induction machine at the corner speed [HLI17] [NEE95]. Pole-phase modulation induction machines have also been investigated to extend the torque-speed capability. While this allows the induction

machine to work with different pole and phase combinations, the number of inverter legs needed for this machine is usually high [BGE13] [OSA96].

Electronic pole changing winding as a method to extend the flux weakening region of induction machines was first introduced in [OSA96] and [MIZ97] where an induction machine with a 4-pole to 2-pole, pole changing winding was investigated to demonstrate pole changing operation. The design and control of the pole changing induction machine by utilising the inverter to control the direction of the current in the individual coil of the phases were described in [OSA96] and the results were experimentally shown for a 1.2kW induction machine. In this chapter, the suitability of the electronic pole changing winding induction machine for BSG applications is investigated. It is shown that when the pole changing winding machine is used as a direct replacement for the baseline, a fixed pole number machine, the torque capability is degraded by 15% due to the reduced winding factor of pole changing winding machines. Utilising the intermittent loading duty cycle of the BSG application, this issue can be circumvented by appropriate choice of series turns per phase resulting in a pole changing winding induction machine of shorter stack length. For BSG applications where axial length is an important design parameter due to the limited space near the engine, this becomes an attractive option. With the increased series turns per phase and a reduced stack length, the thermal performance is slightly degraded and this trade-off is studied with a thermal resistive network model. The machine design process, performance maps and AC losses of the pole changing winding machine are compared with the fixed pole number baseline machine. Furthermore, the influence of winding phase belt on pole changing windings, the influence of pole changing windings on the torque capability and performance of the induction machine is also discussed with specific cases validated using experimental measurements. It is shown that while the reduction of active stack length of the pole changing winding machine is accompanied by a reduction in efficiency compared to the baseline machine in the high torque low-speed region, efficiency improvement can be achieved in the extended flux weakening region of operation due to the reduced AC losses. To demonstrate the efficacy of the finite element analysis models used in the analysis and experimentally verify the work in [MAL19], a 1kW, squirrel cage induction machine with pole changing windings is prototyped. Test data of torque capability curves and performance measurement maps as used to illustrate the pole changing behaviour and show the improved efficiency in the extended flux weakening region of the pole changing winding induction machine.

3.1 Pole-changing Windings for IMs

Induction machines with electronic pole changing windings were introduced and analysed in [OSA96] [MIZ97] and [OSA97b]. For a mild hybrid electric vehicle with a BSG, the electrical

machine is required to produce high torque at low speed for cranking of the engine. After the engine has been cranked and the vehicle is at cruising speeds, the electrical machine is required to provide a moderate amount of torque boost at medium speed and regenerate at high speeds to charge the battery [KRE00]. Induction machines have high torque overload capability for short durations that makes them a suitable choice for cranking operations. However, compared to permanent magnet (PM) machines, the speed range of the conventional induction machine is usually limited to 4 times the base speed [BUY15] as explained in detail in Chapter 3. Two approaches to increasing the speed range are to either increase the peak torque capability at the base speed or to increase the base speed of the induction machine. Increasing the peak torque increases the machine size while increasing the base speed of the machine for the same torque capability and DC bus voltage increases the current rating due to the reduced number of series turns per phase [GUA14a]. A three-phase induction machine with electronic pole changing windings is wound with independent stator coil groups such that their MMFs can be configured to produce either a high or a low pole number depending on the direction of the current that flows in the windings. Two three-phase inverters are required for electronic pole changing which allows for the directions of currents in the stator coils to be independently controlled. The basic structure of the connection of the windings to the inverter is shown in Fig 3.1.

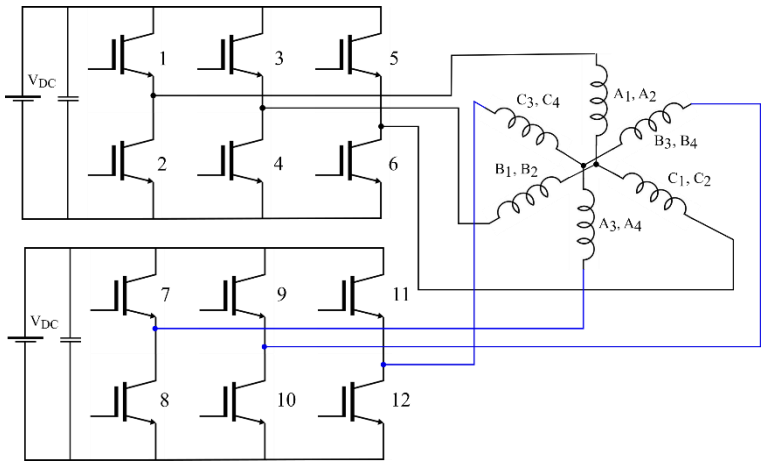

Fig 3.1 Dual inverter fed pole changing induction machine drive.

For the cranking operation where higher torque is required at low speed, the higher pole operation is used and for regeneration or torque boost the lower pole number is used to extend the operating speed range. The peak torque with the higher pole number is approximately double that with the lower pole number. A further advantage of using the pole changing winding in 48V mild hybrid systems is the reduction in AC losses at high speeds. Due to the low voltage, the number of conductors per slot is low resulting in conductors of large cross-section area. The high torque

requirement for cranking results in the large rated current. High speeds combined with high currents result in significant AC losses in the stator conductors. Since the number of poles at high speeds is halved with a pole changing winding machine, the frequency of operation is also halved which reduces the AC losses in the rectangular conductors typically used in 48V systems.

3.1.1 Working Principle

To explain the working principle of pole changing windings, consider a single coil winding fed with sinusoidal current *I* which produces a pulsating rectangular MMF [HEL77]. A symmetrical *m*-phase winding, distributed in Q_1 stator slots to create *P* poles, is composed of q coils where $q = 2\frac{Q_1}{Pm}$ for a 60° phase belt winding. For a 60° phase belt winding, the number of coils is *q/2*. Assuming a constant air-gap (g) permeance, a coil pitch of α_y and an infinitely permeable steel core in which the coils are distributed in the Q_1 slots, the equations of the MMF of the individual coils are shown in (3.1)-(3.4) where ζ is the coil axis expressed in a slot number.

$$F_1(\alpha) = \frac{2I}{\pi g}\sum_{\upsilon=1}^{\infty}\frac{1}{\upsilon}\sin\left(\frac{\upsilon\alpha_y}{2}\right)\cos(\upsilon\alpha - \zeta\alpha_1) \tag{3.1}$$

$$F_2(\alpha) = \frac{2I}{\pi g}\sum_{\upsilon=1}^{\infty}\frac{1}{\upsilon}\sin\left(\frac{\upsilon\alpha_y}{2}\right)\cos\left(\upsilon\left[\alpha - (\zeta+1)\alpha_1\right]\right) \tag{3.2}$$

$$F_3(\alpha) = \frac{2I}{\pi g}\sum_{\upsilon=1}^{\infty}\frac{1}{\upsilon}\sin\left(\frac{\upsilon\alpha_y}{2}\right)\cos\left(\upsilon\left[\alpha - (\zeta+2)\alpha_1\right]\right) \tag{3.3}$$

$$F_q(\alpha) = \frac{2I}{\pi g}\sum_{\upsilon=1}^{\infty}\frac{1}{\upsilon}\sin\left(\frac{\upsilon\alpha_y}{2}\right)\cos\left(\upsilon\left[\alpha - \left(\zeta+(q-1)\right)\alpha_1\right]\right) \tag{3.4}$$

The phase MMF is the summation of the MMF contributions due to the individual coils of (3.1)-(3.4) and is given by (3.5).

$$F_{coil}(\alpha) = \frac{2qI}{\pi g}\sum_{\upsilon=1}^{\infty}\left[\frac{1}{\upsilon}\sin\left(\frac{\upsilon\alpha_y}{2}\right)\frac{\sin\left(\frac{q\alpha_1}{2}\upsilon\right)}{q\sin\left(\frac{\alpha_1}{2}\upsilon\right)}\cos\left(\upsilon\left(\alpha - (q-1+2\zeta)\right)\frac{\alpha_1}{2}\right)\right] \tag{3.5}$$

The winding factor of the winding distribution can be discerned to be the first two sinusoidal terms from (3.5). In a pole changing winding machine, each phase is composed of two coil groups. A1, A2 form one group and A3, A4 form another. The MMFs of these coil groups are shown in (3.6)

and (3.7). To change the number of poles, the current direction in one of the coil groups is reversed. The two coil groups are separated by two pole pitches so the total MMF of one phase of a pole changing winding machine is given by the sum of the MMFs for the higher pole number and the difference for the lower pole number, as given by (3.8) and (3.9).

$$F_{A1,A2} = \frac{2I}{\pi g}\sum_{\upsilon=1}^{\infty}[\frac{1}{\upsilon}\sin\left(\frac{\upsilon\alpha_y}{2}\right)\frac{\sin\left(\frac{q\alpha_1}{2}\upsilon\right)}{qsin\left(\frac{\alpha_1}{2}\upsilon\right)}\cos\left(\upsilon\left(\alpha-(q-1+2\zeta)\frac{\alpha_1}{2}\right)\right)] \tag{3.6}$$

$$F_{A3,A4} = \frac{2I}{\pi g}\sum_{\upsilon=1}^{\infty}[\frac{1}{\upsilon}\sin\left(\frac{\upsilon\alpha_y}{2}\right)\frac{\sin\left(\frac{q\alpha_1}{2}\upsilon\right)}{qsin\left(\frac{\alpha_1}{2}\upsilon\right)}\cos\left(\mathrm{v}\left(\alpha-\left(\frac{Q_1P}{2}+q-1+2\zeta\right)\frac{\alpha_1}{2}\right)\right)] \tag{3.7}$$

$$F_{A(P-poles)} = F_{A1} + F_{A2} + F_{A3} + F_{A4} \tag{3.8}$$

$$F_{A\left(\frac{P}{2}-poles\right)} = F_{A1} + F_{A2} - (F_{A3} + F_{A4}) \tag{3.9}$$

As an example, consider a 72slot, 8/4-pole, pole-changing winding shown in Fig. 3.2 where the A-phase is wound with two coil groups, A1, A2 and A3, A4. The A-phase winding has a 120^o phase belt distribution, required for the pole-changing operation to be performed. The individual coil MMFs are shown in Fig 3.3(a). The higher pole number is obtained by maintaining the same sign and amplitude of currents in both coils. With the reversal of currents in the coils A3 and A4 occupying slots 37 to 72, the number of poles of the MMF is shown in Fig 3.3(b) where the currents in coils A3 and A4 are reversed. Other phase coil MMFs are also similarly calculated and the three-phase MMF can be determined. The air-gap MMF patterns and the harmonic spectra are shown in Fig. 3.4(a) and Fig. 3.4(b), respectively. Each of the two coil groups of every phase is connected to a 3-phase inverter set as shown in Fig. 3.1. This allows the direction of the current to be independently reversed in one coil set to enable online pole-changing. The pole changing behaviour obtained through the reversal of coil currents is illustrated in Fig 3.3 and Fig. 3.4**(a).** MMF waveforms of two of the four coils, A1 and A2, that make up the A phase of a 72-slot, 3-phase, 8-pole/4-pole stator winding are shown in Fig 3.3. An illustration of the pole changing behaviour obtained by reversing the current is illustrated in Fig. 3.4(a). When the currents in A1 and A2 (and the corresponding coils in phases B and C) are in the same direction, the stator MMF has an 8-pole fundamental MMF harmonic. When the current in the coil A2 is reversed, the fundamental MMF has 4 poles. The harmonic spectrum of the MMFs is shown in Fig. 3.4(b). During the transition of the poles, the 8-pole rotor flux must be decayed while the 4-pole field is established. There will be

a finite time delay involved in this transition that will result in a torque transient. This transient cannot be eliminated due to the finite time constant of the rotor circuit even with current control. In a BSG application where the period requiring minimum vibration is during cranking, this portion of the duty cycle is entirely driven with the 8-pole winding configuration. Transition to 4-pole is done when reaching cruising speeds and can be achieved with a slow ramp-down of the 8-pole field while building up the 4-pole field to minimise torque transients instead of a step-change in pole number. While there is a momentary reduction in the torque capability of the machine during the transition, this does not affect the ability of the machine to crank the engine which is the most critical function of the BSG [WAL04] [KRE00].

Poles	N									S								
Slot N°	1	2	3	4	5	6	7	8	9	10	11	12	13	14	15	16	17	18
Layer 1	A1	A1	A1	A1	A1	A1												
Layer 2										a1	a1	a1	a1	a1	a1			

Poles	N									S								
Slot N°	19	20	21	22	23	24	25	26	27	28	29	30	31	32	33	34	35	36
Layer 1	A2	A2	A2	A2	A2	A2												
Layer 2										a2	a2	a2	a2	a2	a2			

Poles	N									S								
Slot N°	37	38	39	40	41	42	43	44	45	46	47	48	49	50	51	52	53	54
Layer 1	A3	A3	A3	A3	A3	A3												
Layer 2										a3	a3	a3	a3	a3	a3			

Poles	N									S								
Slot N°	55	56	57	58	59	60	61	62	63	64	65	66	67	68	69	70	71	72
Layer 1	A4	A4	A4	A4	A4	A4												
Layer 2										a4	a4	a4	a4	a4	a4			

(a) 8-pole, 120-degree phase belt.

Poles	N									S								
Slot N°	1	2	3	4	5	6	7	8	9	10	11	12	13	14	15	16	17	18
Layer 1	A1	A1	A1	A1	A1	A1												
Layer 2										a1	a1	a1	a1	a1	a1			

Poles	S									N								
Slot N°	19	20	21	22	23	24	25	26	27	28	29	30	31	32	33	34	35	36
Layer 1	a2	a2	a2	a2	a2	a2												
Layer 2										A2	A2	A2	A2	A2	A2			

Poles	N									S								
Slot N°	37	38	39	40	41	42	43	44	45	46	47	48	49	50	51	52	53	54
Layer 1	A3	A3	A3	A3	A3	A3												
Layer 2										a3	a3	a3	a3	a3	a3			

Poles	S									N								
Slot N°	55	56	57	58	59	60	61	62	63	64	65	66	67	68	69	70	71	72
Layer 1	a4	a4	a4	a4	a4	a4												
Layer 2										A4	A4	A4	A4	A4	A4			

(b) 4-pole, and 120-degree phase belt.

Fig. 3.2 Phase A winding layout of a 72-slot 3-phase stator with a 120° phase belt.

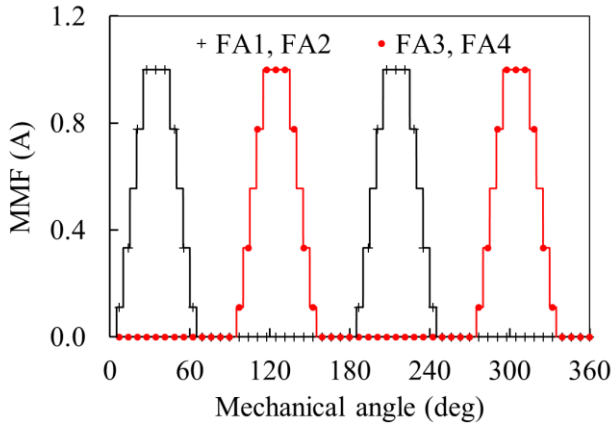

(a) Individual coil MMFs

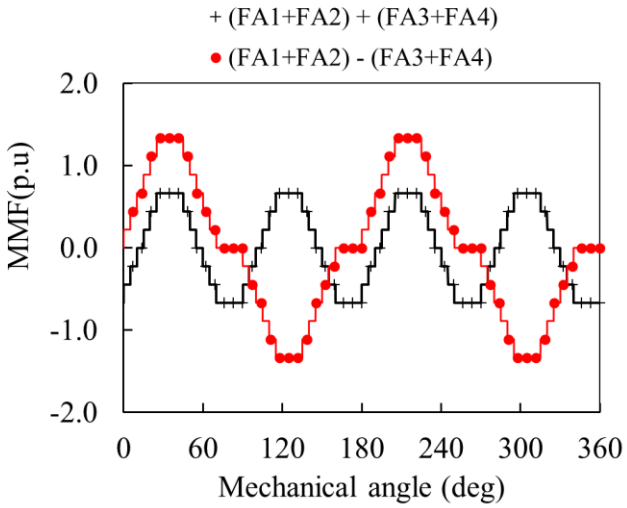

(b) Sum and difference of coil MMFs.

Fig 3.3 MMFs of phase A coils of an 8-pole and 4-pole changing winding machine from analytical equations.

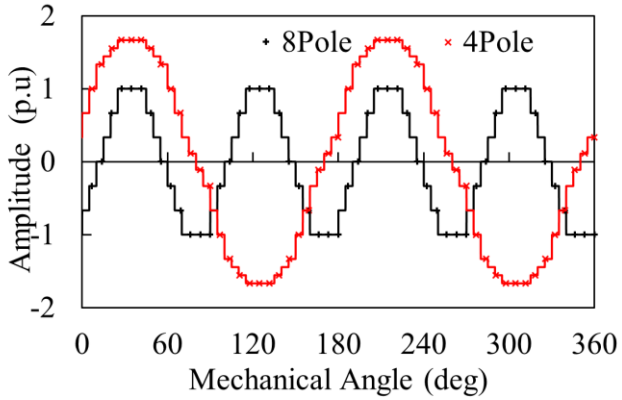

(a)MMF waveforms

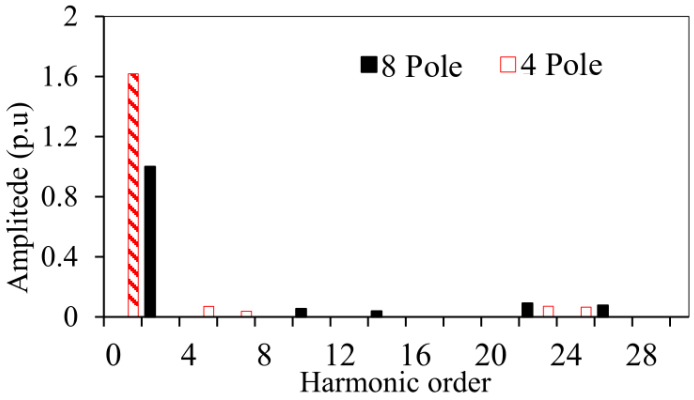

(b)Spectra of MMFs

Fig. 3.4 MMFs of pole changing winding machine for 8-pole and 4-pole configuration.

3.1.2 Impact of Phase Belt on Pole-changing Windings

Pole changing is achieved by the reversal of the current in alternating sets of coils in the induction machine. While a 60-degree phase belt is most widely used for 3 phase distributed windings, the choice of phase belt has a significant influence on the performance of the pole changing winding machine. This is shown using a 3-phase, 72 slot and 8-pole winding that can be reduced to 4 poles (corresponding to the 48V baseline machine discussed in the next section). To understand the impact of the phase belt on the pole changing windings, winding distributions with 60-degree and 120-degree phase belts are shown in Fig 3.5(a) and Fig 3.5(b) for phase A respectively. From the 8-pole connection of Fig 3.5(a), it can be seen that of the available 8 coils per phase, the current in 4 alternate coils, A2, A4, A6 and A8 need to be reversed to change the MMF distribution to 4 poles. This results in the cancellation of the MMF of 4 coils as seen from the shaded phase A coil sides in Fig 3.5(b). In contrast, for a phase belt of 120-degree in Fig 3.5(c) and Fig 3.5(d) the current reversal in coils A2 and A4, necessary for changing the number of poles, does not result in MMF cancellation. The coils in which current reversal is necessary are connected to the same inverter. MMF cancellation for pole changing is inefficient due to poor utilisation of the windings and the losses incurred in the coils that carry the currents but do not contribute to torque production. The effect of using the 120-degree phase belt, however, is the reduced fundamental winding factor of the winding. The winding factor of the 120-degree phase belt winding is approximately 15% lower than the 60-degree phase belt winding. This results in a 15% reduction in torque. To maintain the same air-gap flux density, a corresponding 15% increase in the magnetising current component is also required. The ratio of the power capability of the pole changing winding machine to a conventional machine approaches the ratio of winding factors as the machine rating increases and is lower for smaller machines due to the higher proportion of the rated current being

the magnetising current [WAL04]. The fundamental winding factor of the 120-degree phase belt 8-pole winding is 25% higher than that of the 2 pole winding.

Poles	N									S								
Slot N°	1	2	3	4	5	6	7	8	9	10	11	12	13	14	15	16	17	18
Layer 1	A1	A1	A1							a6	a6	a6						
Layer 2	A5	A5	A5							a1	a1	a1						

Poles	N									S								
Slot N°	19	20	21	22	23	24	25	26	27	28	29	30	31	32	33	34	35	36
Layer 1	A2	A2	A2							a7	a7	a7						
Layer 2	A6	A6	A6							a2	a2	a2						

Poles	N									S								
Slot N°	37	38	39	40	41	42	43	44	45	46	47	48	49	50	51	52	53	54
Layer 1	A3	A3	A3							a8	a8	a8						
Layer 2	A7	A7	A7							a3	a3	a3						

Poles	N									S								
Slot N°	55	56	57	58	59	60	61	62	63	64	65	66	67	68	69	70	71	72
Layer 1	A4	A4	A4							a5	a5	a5						
Layer 2	A8	A8	A8							a4	a4	a4						

(a) 8-pole, 60-degree phase belt.

Poles	N																	
Slot N°	1	2	3	4	5	6	7	8	9	10	11	12	13	14	15	16	17	18
Layer 1	A1	A1	A1							A6	A6	A6						
Layer 2	A5	A5	A5							a1	a1	a1						

Poles	S																	
Slot N°	19	20	21	22	23	24	25	26	27	28	29	30	31	32	33	34	35	36
Layer 1	a2	a2	a2							a7	a7	a7						
Layer 2	a6	a6	a6							A2	A2	A2						

Poles	N																	
Slot N°	37	38	39	40	41	42	43	44	45	46	47	48	49	50	51	52	53	54
Layer 1	A3	A3	A3							A8	A8	A8						
Layer 2	A7	A7	A7							a3	a3	a3						

Poles	S																	
Slot N°	55	56	57	58	59	60	61	62	63	64	65	66	67	68	69	70	71	72
Layer 1	a4	a4	a4							a5	a5	a5						
Layer 2	a8	a8	a8							A4	A4	A4						

(b) 4-pole, 60-degree phase belt.

Poles	N									S								
Slot N°	1	2	3	4	5	6	7	8	9	10	11	12	13	14	15	16	17	18
Layer 1	A1	A1	A1	A1	A1	A1												
Layer 2										a1	a1	a1	a1	a1	a1			

Poles	N									S								
Slot N°	19	20	21	22	23	24	25	26	27	28	29	30	31	32	33	34	35	36
Layer 1	A2	A2	A2	A2	A2	A2												
Layer 2										a2	a2	a2	a2	a2	a2			

Poles	N									S								
Slot N°	37	38	39	40	41	42	43	44	45	46	47	48	49	50	51	52	53	54
Layer 1	A3	A3	A3	A3	A3	A3												
Layer 2										a3	a3	a3	a3	a3	a3			

Poles	N									S								
Slot N°	55	56	57	58	59	60	61	62	63	64	65	66	67	68	69	70	71	72
Layer 1	A4	A4	A4	A4	A4	A4												
Layer 2										a4	a4	a4	a4	a4	a4			

(c) 8-pole, 120-degree phase belt.

Poles	N									S								
Slot N°	1	2	3	4	5	6	7	8	9	10	11	12	13	14	15	16	17	18
Layer 1	A1	A1	A1	A1	A1	A1												
Layer 2										a1	a1	a1	a1	a1	a1			

Poles	S									N								
Slot N°	19	20	21	22	23	24	25	26	27	28	29	30	31	32	33	34	35	36
Layer 1	a2	a2	a2	a2	a2	a2												
Layer 2										A2	A2	A2	A2	A2	A2			

Poles	N									S								
Slot N°	37	38	39	40	41	42	43	44	45	46	47	48	49	50	51	52	53	54
Layer 1	A3	A3	A3	A3	A3	A3												
Layer 2										a3	a3	a3	a3	a3	a3			

Poles	S									N								
Slot N°	55	56	57	58	59	60	61	62	63	64	65	66	67	68	69	70	71	72
Layer 1	a4	a4	a4	a4	a4	a4												
Layer 2										A4	A4	A4	A4	A4	A4			

(d) 4-pole, and 120-degree phase belt.

Fig 3.5 72-slot, 3-phase 8-/4-pole machine winding pattern for phase A with different phase belts.

3.1.3 Baseline IM Design

An 8-pole 3-phase induction machine is designed to meet the specification of cranking and continuous torque listed in TABLE 3-1. The following assumptions were used for designing the machine:

a)The outer diameter is kept constant.

b)The split ratio is optimized for maximum torque at the corner speed.

c)The rotor and stator current densities are fixed at 20A/mm^2 and 15A/mm^2 respectively.

d)The air gap is 0.35mm.

The numbers of stator slots and rotor slots that maximise the torque at corner speed are found to be an 8-pole machine with SPP=3, which corresponds to the optimal slot and pole number combination determined by using the optimisation process in Chapter 2. The winding used is a double layer full pitched winding with the number of series turns per phase of W=12, 2 parallel paths and 2 conductors per slot with a winding factor of 0.954. The machine performance is analysed using FEA and the torque-speed characteristics are computed by determining the optimum slip ratio at the peak current at every speed that maximises the torque. The process for design and optimisation of the induction machine is discussed in [GUA14b]. The torque at the corner speed and the value of the corner speed of the induction machine torque-speed curve determine the torque that is achievable in the flux weakening operation. The torque-speed and power-speed envelopes and the torque/power specifications requirements are shown in Fig 3.6(a) and Fig 3.6(b) respectively. A corner speed of

2400 rpm is required to provide the required cranking torque at 6000rpm. The induction machine that can provide this torque has an active stack length of 66mm. With 20mm long end windings, the overall axial length of the machine inclusive of end windings is 106mm.

TABLE 3-1STARTER GENERATOR MACHINE SPECIFICATIONS

Parameter	Value	Parameter	Value
Outer diameter (mm)	148	Maximum speed (rpm)	10000
Stack length (mm)	66	Cage bar/ end ring	Aluminium
DC bus voltage (V)	48	Cranking speed (rpm)	1300 & 6200
Lamination	M-19 24 Ga	Cranking torque (Nm)	60 & 11.5
Slot fill factor	0.6	Continuous speed (rpm)	2800 & 5500
RMS phase current (A)	440	Continuous torque (Nm)	12 & 7
Coolant	EWG	Coolant flow rate (l/min)	6

3.1.4 Pole Changing Winding Machine Design

Using the pole changing the winding scheme with a 120-degree phase belt as described in section 3.1.1 with an 8-pole and 4- pole winding, the induction machine is designed to meet the same specifications as the baseline machine. Replacing the winding of the stator of the baseline induction machine with a pole changing winding results in a reduced winding factor. For a 120-degree phase belt windings with W=12, 72 stator slots and 8-poles, the fundamental winding factor is 0.827. The 15% reduction in fundamental winding factor results in a proportional reduction in torque. Equation (3.10) shows the unsaturated magnetising inductance of the induction machine as a function of the physical machine parameters:

$$L_m = \frac{3\mu_o}{\pi} . \frac{D_{is} L_{stk}}{g_{effective}} . \left(\frac{k_w W}{2p}\right)^2 \tag{3.10}$$

where μ_o, D_{is}, L_{stk}, $g_{effective}$, k_w, W and p are the permeability of free space, bore diameter, stack length, effective air-gap, winding factor, number of series turns per phase and number of pole pairs respectively.

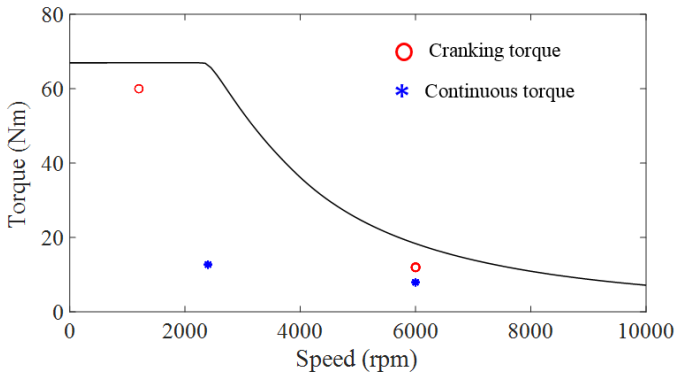

(a) Torque-speed curve.

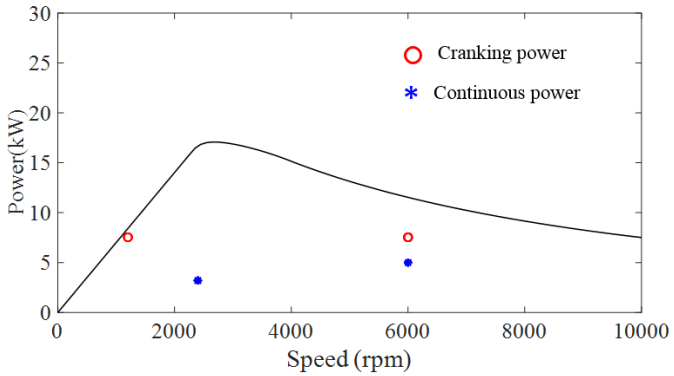

(b)Power-speed curve.

Fig 3.6 Characteristics of the baseline induction machine.

If the stack length and number of series turns per phase W are maintained the same for the pole changing machine, the magnetising inductance will be lower by 27% compared to the baseline machine. The reduction of the magnetising inductance due to the reduced stack length can be seen from (3.10) where the magnetising inductance is directly proportional to stack length. This will reduce the maximum torque achievable at rated current. The torque-speed and power-speed characteristics of such a machine are shown in Fig 3.7(a) and Fig 3.7(b) respectively. The resulting machine cannot meet the peak torque requirements at low speed but has a wider flux weakening range when the number of poles is changed from 8-pole to 4-poles using the inverter by reversing the currents. The number of series turns per phase, W and the stack length are inversely proportional to the corner speed. While the number of poles does not, in general, affect the torque capability, in this case of pole changing machine, the design of the 8-pole machine is for high peak torque and low corner speed. When the current in the windings are reversed to change the number of poles, the number of series turns per phase is reduced due to the number of poles being reduced by half for the same conductors per slot and parallel paths.

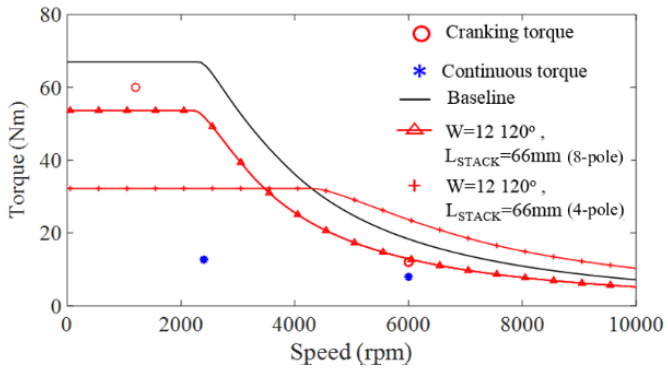

(a) Torque-speed curve.

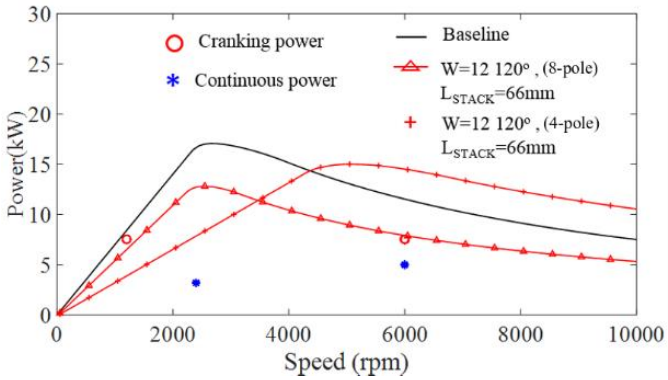

(b) Power-speed curve.

Fig 3.7 Characteristics of the baseline machine with pole changing windings and W=12.

Since the torque is proportional to the number of series turns per phase for the same stack length, the torque of the 4-pole machine is reduced by half [ION98] [OLD85]. The corner speed of the pole changing winding induction machine can be reduced to take advantage of the wider torque-speed region of the 4-pole operation to meet the peak torque requirement at low speed. The number of series turns per phase is given by $W = \frac{n_s pq}{a}$ where, n_s, p, q and a are the number of conductors per slot, pole pairs, slots per pole per phase (SPP) and the number of parallel paths. For SPP=3 and 8-poles for 4 parallel paths, the next feasible number of series turns per phase are W=18 which increases the peak torque at low speed and reduce the corner speed. This increases the number of conductors per slot from 2 to 6. The slot current density is maintained the same as the baseline machine for the same number of series turns per phase. However, when the number of series turns per phase is increased to 18, the number of conductors per slot increases from 4 to 6 and the number of parallel paths from 2 to 4, the conductor current density increases. For the same peak current, the conductor current density increases by 3/2 times that of the baseline. The impact of this on the thermal performance is detailed in Section 3.3.

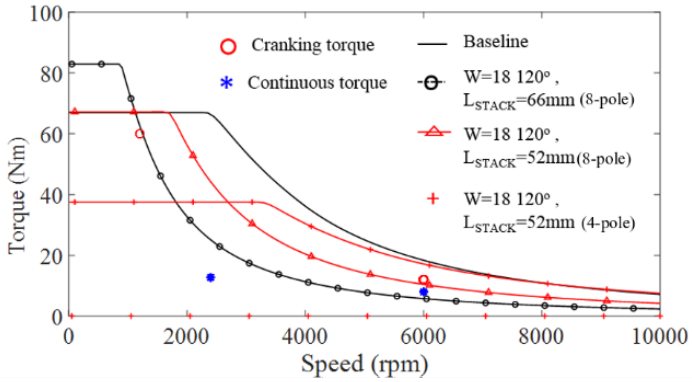

(a) Torque–speed curve.

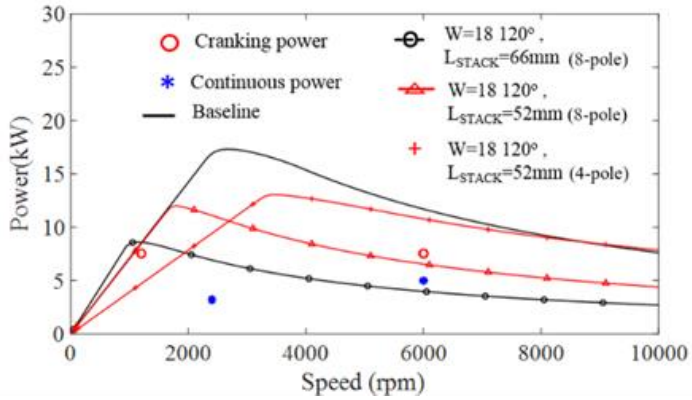

(b) Power–speed curve.

Fig 3.8 Characteristics of the pole changing winding induction machine with reduced stack length and W=18.

It is shown that due to the intermittent nature of the starter generator load, by suitably choosing the number of poles based on the region of operation the baseline machine and the winding hotspot of the pole changing winding machine is within 12ºC of each other and well within the maximum allowable temperature of the insulation. When the stack length is maintained the same as the baseline machine, with the increased number of series turns per phase, the peak torque increases compared to the specifications but the corner speed reduces. The stack length can now be reduced to 52mm to meet the requirements at the low speed and the flux weakening. The resulting torque-speed and power-speed characteristics with the increased number of series turns per phase are shown in Fig 3.8(a) and Fig 3.8(b) respectively. It is observed that the torque and power specifications are still met with a reduced length machine. The overall stack length with the pole changing winding is 92 mm with 40mm of total end-winding length which is a 15% reduction in overall length and a 20% reduction in active length compared to the baseline induction machine.

3.2 Performance Comparison of Baseline and Pole-changing Winding IM's

3.2.1 Comparison of Magnetic Loading

The rotor diameter and dimensions of the design are optimized for the 8-pole operation. However, a 4-pole machine has higher flux linkage and requires thicker yoke sections compared to an 8-pole machine for the same air-gap flux density. This will result in the 4-pole operation having higher saturation in the core. The flux density maps of the baseline machine and the pole changing machine in 8-pole and 4-pole operation for the peak current are shown in Fig 3.9(a) and Fig 3.9(b) respectively. The yoke section of the machine has higher flux density in the 4-pole operation compared to the 8-pole operation for the same air-gap flux density and magnetic circuit. The flux density over one pole in the middle of the yoke section is shown in Fig 3.10. This is due to a higher magnetizing current with the 4-pole winding. The magnetising current is reduced due to higher magnetising inductance. Magnetising inductance reduces due to the reduced number of pole pairs (which has a higher impact on winding factor due to its value reducing from 8-pole to 4-pole) despite the reduced winding factor during 4-pole operation. This relationship is seen from (3.1) where the magnetising inductance is proportional to the ratio of the winding factor and number of poles.

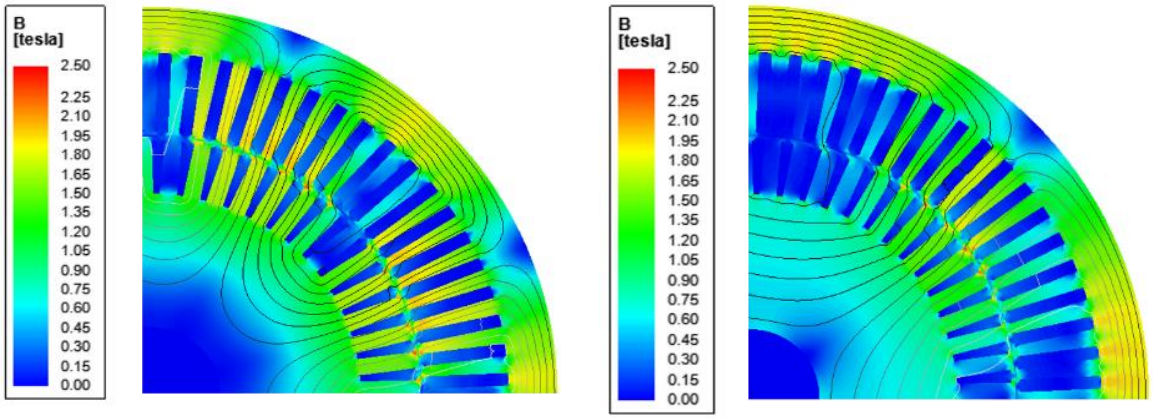

(a) 8-pole operation (b) 4-pole operation.

Fig 3.9 Flux density maps of the pole changing machine with maximum current and 1200rpm.

3.2.2 Comparison of DC and AC Copper Losses

The number of series turns per phase of the pole changing machine is higher than the baseline machine as described in Section II. This increase of the number of series turns from 12 to 18 results in 6 conductors per slot for the two-layer winding. Since the outer diameter is constant between the designs, the increased number of conductors per phase in the same slot area results in a higher conductor current density for the pole changing machine. The increased number of conductors also

results in a slightly reduced slot fill factor due to a larger area of the slot being occupied by more insulation needed for the 6 conductors. The increased series turns per phase and the reduced cross-section area of the conductors also results in a higher phase resistance compared to the baseline machine, which results in higher stator losses. The advantage of using the higher number of conductors per slot is a significant reduction in the AC losses. Apart from the increased number of conductors per slot, the reduction of the frequency of operation at higher speeds results in the reduction of AC losses. The effect of the increased number of conductors per slot results in the decrease in AC losses in the 8-pole machine. The 4-pole machine has further reduced losses due to the decrease in frequency [LWU14]. To determine the AC losses in the baseline and the pole changing winding machine, time-harmonic FEA at various frequencies and peak current values are performed to determine a transfer function of the ratio of AC to DC resistance. The variation of this ratio with speed and currents is shown in Fig 3.11 for the baseline machine. The ratio decreases with current due to increased saturation [JUR15] [ZHA14]. The variation of the ratio of AC to DC resistance of the pole changing induction machine with 8-pole and 4-pole operation is shown in Fig 3.12. The ratio is seen to be significantly less for the pole changing windings machine due to the increased number of strands per slot. This coupled with the ability to change to a lower number of poles at higher speeds provides the possibility to reduce the stator copper losses significantly.

The variation of the phase resistance is shown in Fig 3.13(a) and the corresponding losses are shown in Fig 3.13(b). The effect of increased phase resistance at speeds beyond 4000rpm of the baseline machine compared to the pole changing winding machine results in higher peak efficiency at higher speeds. At the low speed during cranking operation, the losses of the pole changing winding machine will be expected to be higher than the baseline.

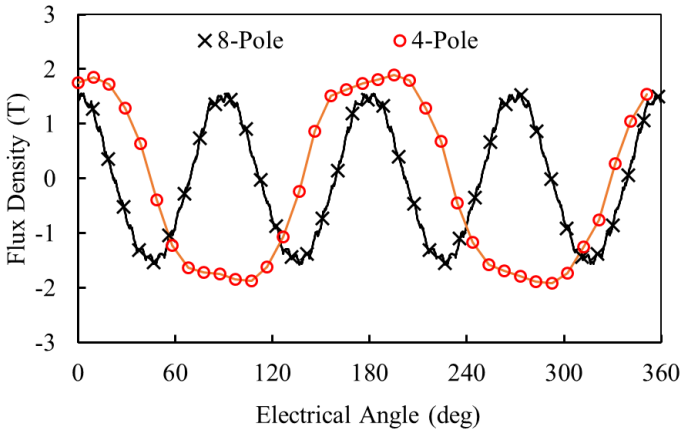

Fig 3.10 Yoke flux density waveforms for 8-pole and 4-pole operation.

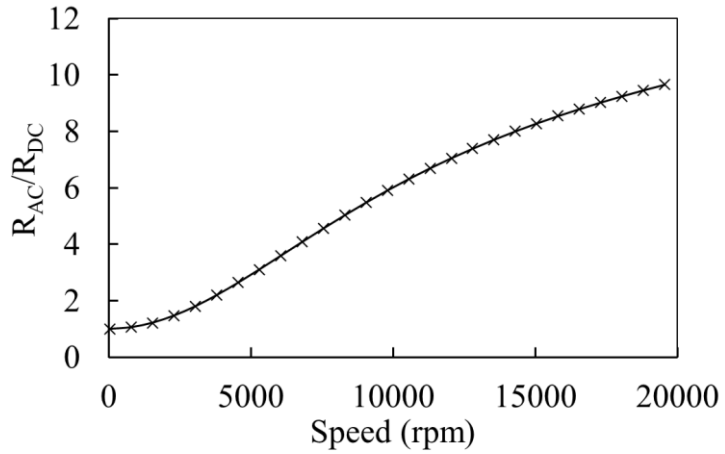

Fig 3.11 Variation of AC to DC resistance ratio of the baseline machine.

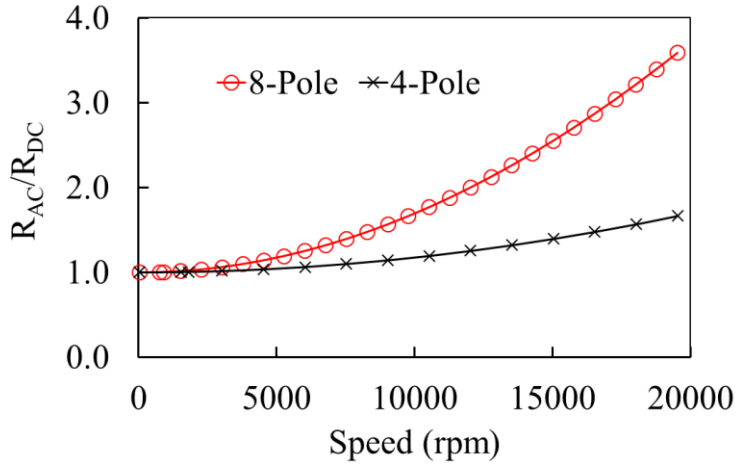

Fig 3.12 Variation of AC to DC resistance ratio of the pole changing machine for different pole numbers.

3.2.3 Influence of Pole-changing Windings on Torque Ripple

The torque ripple of the baseline machine and the pole changing machine in 8-pole and 4-pole operation are shown in Fig 3.14(a) and Fig 3.14(b) respectively. The torque ripple is calculated with a 6.5 degrees rotor skew which is a 1 rotor slot skew to minimize torque ripple. The torque ripple of the baseline machine is 7.8%. The torque ripple for the pole changing winding machine with 8 and 4-poles is 6.5% and 5.6% respectively. The torque ripple during operation at 8000rpm and rated current in the flux weakening region is shown in Fig 3.14(c). After the pole changing operation has completed and pole-transition to 4-poles is complete, there is no detrimental effect on the torque ripple of the motor since no additional harmonics are introduced as a result of using the pole changing windings in the 4-pole connection.

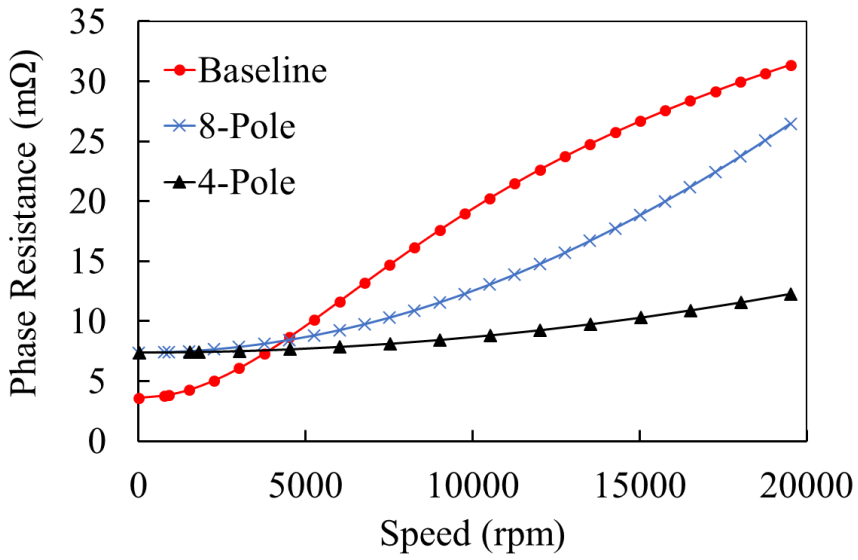

(a) Phase resistance.

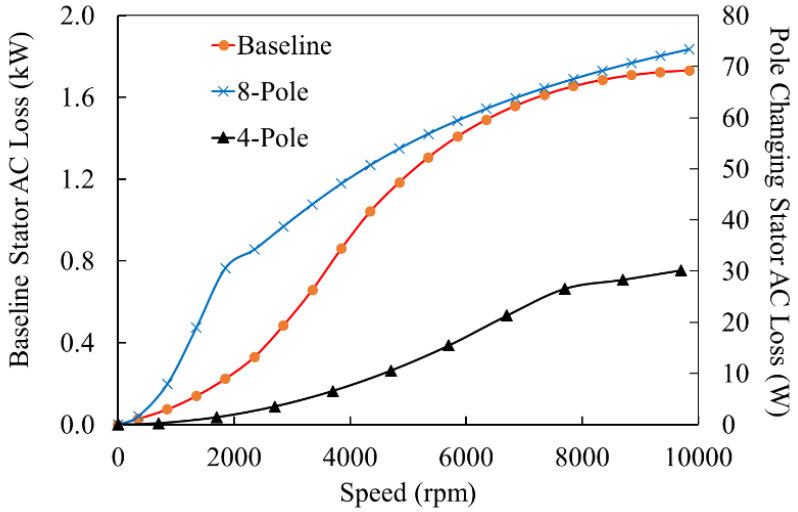

(b) Stator copper loss for a peak current of 650A.

Fig 3.13 Stator phase resistance and AC loss comparison of baseline machine with pole changing winding machine.

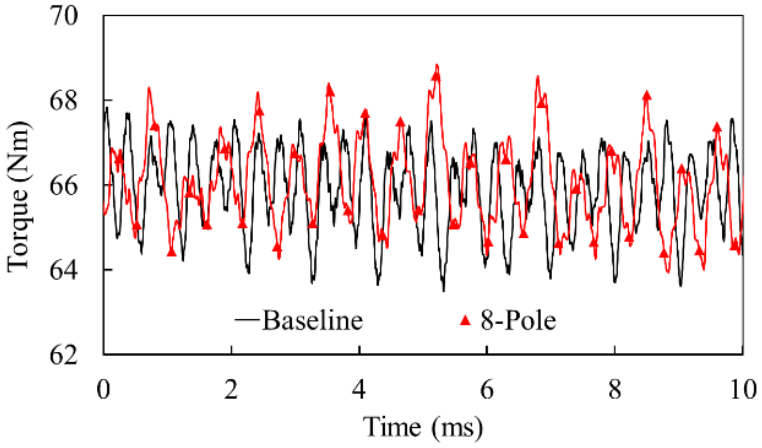

(a) Baseline and 8-pole machine at 1500rpm and rated current

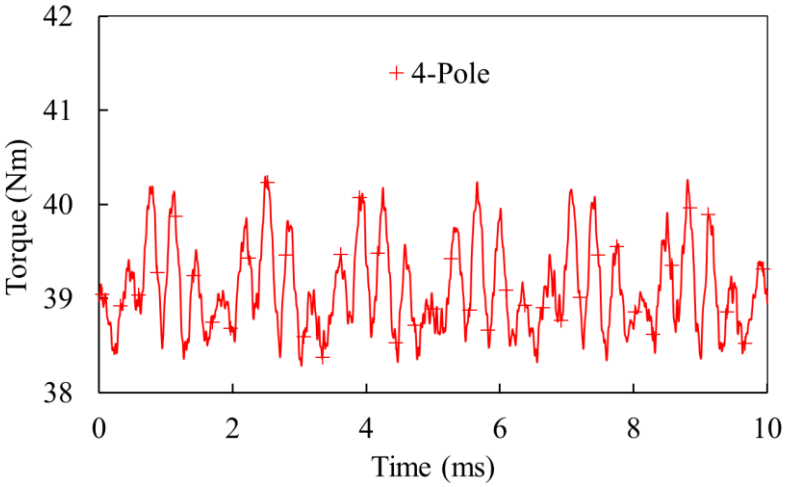

(b) 4-pole at 1500rpm and rated current

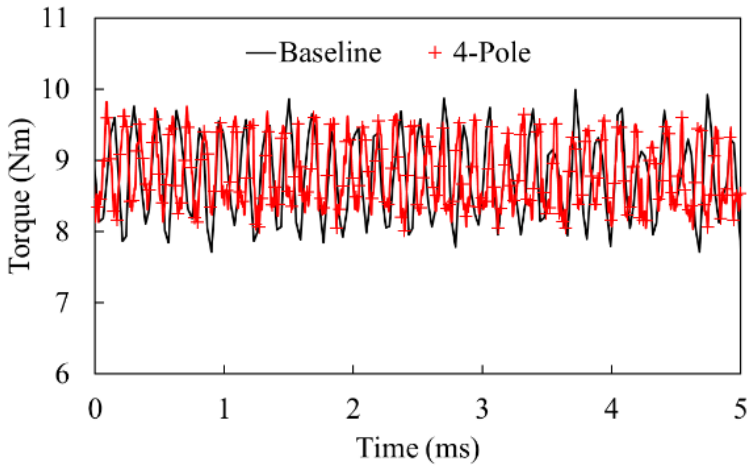

(c) Baseline and 4-pole machine at 8000rpm at rated current.

Fig 3.14 Torque ripple at rated current in constant torque and flux-weakening region.

3.3 Thermal Performance of pole Changing Winding Induction Machine

For a starter-generator application, as previously described, the duty of operation is varied at different points on the torque-speed curve. The cranking operation includes a series of operations. During the initial spin-up phase, the motor spins up the engine against the static friction of the drive train. After the cranking operation, the machine assists in an acceleration phase that allows the engine to crank quickly and smoothly with limited vibrations. Finally until the engine fires and reaches idle speed, there is a combustion ramping phase where combustion is initiated and the engine torque is ramped up while the motor torque is gradually reduced. This acceleration profile is pre-determined based on the engine and other operating conditions. The initial spin-up phase operation where peak torque is demanded is intermittent and this usually lasts for 0.45s. The total cranking operation lasts less than 1s [WAL04] [CAI04]. A thermal model of the baseline machine

and the pole changing winding induction machine in 8-pole and 4-pole operation is built using MotorCAD to study the behaviour of the baseline machine and the pole changing winding machine under these operating conditions. The stator of the machine is cooled with a water jacket. The ambient temperature of the machine due to the location of the machine in the engine compartment can range from -40^{o}C to 125^{o}C and the coolant temperature can reach a maximum of 105^{o}C. The same coolant is used to cool the inverter before being circulated in the water jacket around the stator of the machine. While the peak slot current density is maintained the same between the baseline machine and the pole changing machine, the number of conductors per slot is higher for the pole changing machine resulting in a higher conductor current density. To compare the thermal performance of the machines, a transient thermal simulation for a 3s operation under nominal ambient conditions is performed. A 1s peak torque demand, a 5s continuous operation followed by a 30s shutdown is used to study the hotspot temperature of the machine instead of a complete hybrid vehicle model which is beyond the scope of this study [LEE15] [BOG16]. Steady-state thermal simulation at the continuous operating regions is used to determine the hot spot of the windings at the two continuous operating points. The baseline machine and the pole changing winding machine with 8-pole and 4-pole operation are modelled in MotorCAD. The axial schematic of the machine and the water cooling jacket is shown in Fig. 3.15(a).

3.3.1 Thermal Model

A detailed thermal resistance network is generated by MotorCAD and the schematic is shown in Fig. 3.15 (b). The thermal resistances are calculated based on the lamination, copper insulation material properties and geometric details of the machines. The heat transfer coefficients of the water jacket are based on the cooling duct dimensions, coolant thermal properties and flowrate [STA06] [BOG08]. The thermal resistance and heat transfer coefficient calculation methodology are kept constant between the baseline and pole-changing winding induction machine for a direct comparison of thermal performance. The slot cross-sections of the baseline and the pole changing machine with 2 conductors per slot (W=12) and 6 conductors per slot (W=18) are shown in Fig. 3.15 (c). The losses from the electromagnetic simulation are input to the thermal resistance network model. Other inputs include the material properties, coolant and ambient temperatures. For comparison of the different machines, the thermal model assumes battery performance remains unchanged with temperature. The MotorCAD model also does not model the velocity of air in the housing due to temperature variation.

3.3.2 Transient Thermal Performance

To study the effect of the high torque demand during the engine cranking operation, the temperature rise of the stator winding (hotspot) is determined under the highest ambient and coolant temperature. The simulation is performed at the boundary conditions of 125^{o}C ambient and inlet temperature of the coolant is 105^{o}C. The temperature rises of the winding hotspot of the baseline and the pole changing winding induction machine for a transient duration of 3s is shown in Fig. 3.16(a). The higher resistance per phase of the pole changing winding results in a higher stator copper loss. The pole changing winding is also of a shorter stack length leaving a lower contact area for the water jacket to extract the heat, the pole changing winding hotspot temperature is predictably higher. At the end of 1s and 3s, the temperature rises of the pole changing winding machine are 2^{o}C and 8^{o}C higher than those of the baseline machine respectively. In actual operation, the cranking operation is a short duty operation and to determine the thermal behaviour of the machines, a transient cycle of 1s peak torque at 1300rpm followed by 5s of continuous operation at 5800rpm and a 30s off period is simulated [BOG16]. The thermal steady-state is shown in Fig. 3.17(b). Both machines are simulated at the boundary conditions of 125^{o}C ambient and inlet temperature of the coolant is 105^{o}C as before. At steady-state, the pole changing winding machine has a winding hotspot temperature 12^{o}C (170^{o}C as compared to 148^{o}C) higher than the baseline machine.

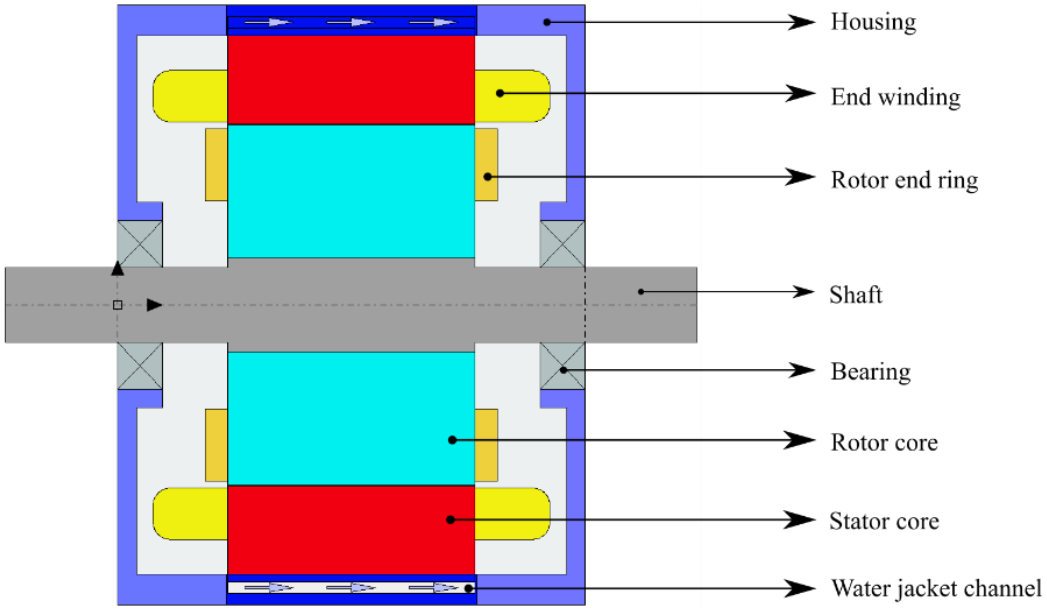

(a) Axial section

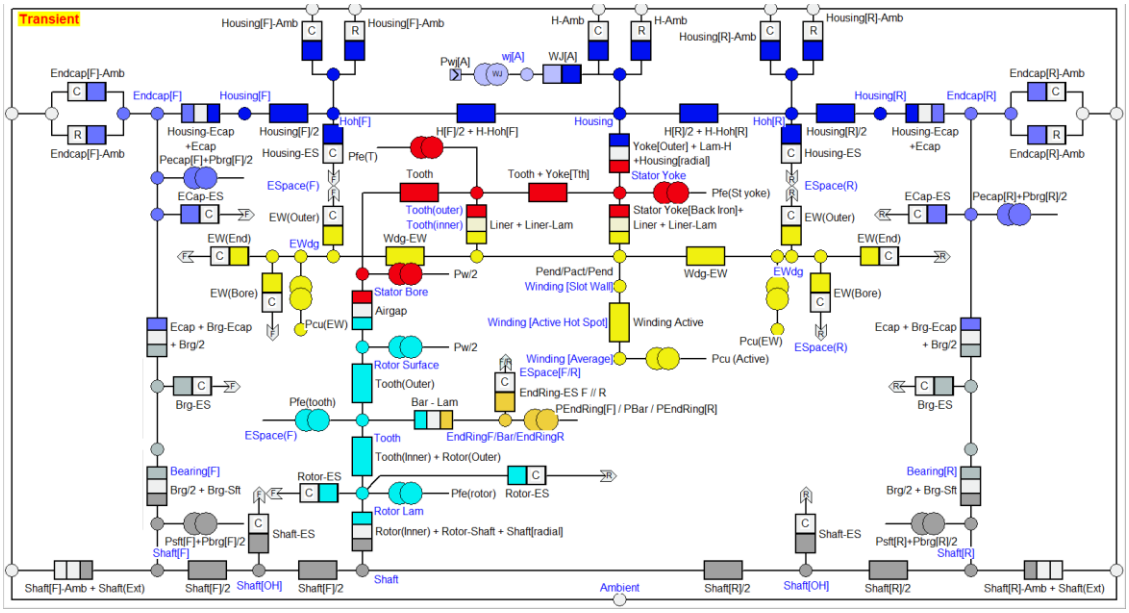

(b) Thermal resistance network

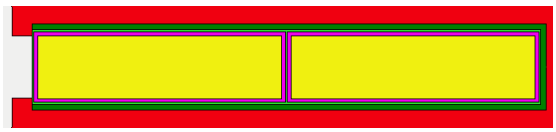

(c) Slot cross-section of baseline machine.

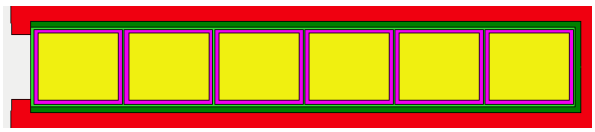

(d) Slot cross-section of pole changing winding machine.

Fig. 3.15 MotorCAD model for thermal analysis.

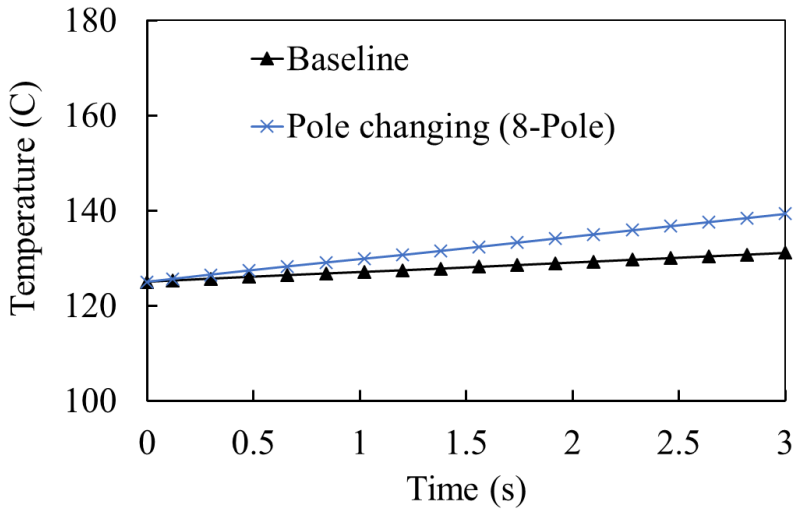

(a) Full load cranking operation for 3s.

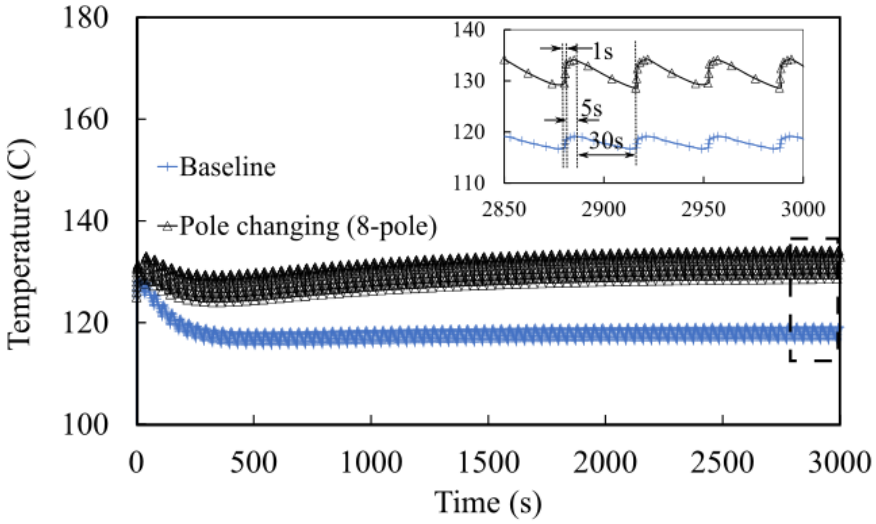

(b) A transient cycle of 1s peak torque at 1300rpm followed by 5s of continuous operation at 5800rpm and a 30s off period.

Fig. 3.16 Winding hotspot for baseline and pole-changing winding machines from the transient thermal analysis.

3.3.3 Steady-State Thermal Performance

The thermal model is simulated to study the steady-state temperature performance under continuous operating conditions to determine the winding hotspot of the two machines. The hotspot temperatures when running at 2800 rpm at 12Nm torque for the baseline and the pole changing winding machine with 8-pole and 4-pole excitation are shown in Fig. 3.17(a). At the lower speeds, the machine configured for 4-poles is inefficient and the hotspot temperature is higher whereas the machine configured for 8-poles has a hot spot temperature of 13.14^{o}C higher than the baseline machine but still within the temperature limit of the insulation which is 180^{o}C for continuous duty. This scenario is reversed when the operation is at the second continuous point of operation at 5800rpm as shown in Fig. 3.18(b). The winding hotspot of the machine configured for 4-poles is 12.27^{o}C hotter than that of the baseline machine. This inversion of thermal behaviour is consistent with the AC resistance of the stator winding as shown in Fig 3.13(a) where the resistance of the baseline machine is sufficiently higher than that of the 4-pole winding configuration to offset the copper loss. The thermal FEA temperature maps of the baseline induction machine and the pole changing winding machine stator slot section are shown in Fig. 3.19(a) and Fig. 3.20(b) respectively. It can be seen that the conductor section closest to the air-gap has the highest temperature in slot sections of both machines.

3.4 Simulated Performance Maps: Baseline vs Pole Changing Machine

The efficiency map of the baseline induction machine is shown in Fig. 3.19. The efficiency map is computed as follows. For every stator frequency corresponding to the speed range, transient FEA is carried out to find the corresponding maximum output torque. In constant torque region, the maximum allowable stator current with the specific frequency and slip ratio is applied to determine the operating envelope. The output torque can be obtained after the rotor current reaches the steady state. Many different torque values can be obtained for different slip ratios and different current levels, among which the maximum output torque is searched with the condition that the stator terminal voltage does not exceed the allowable value. In flux-weakening region, the maximum allowable voltage with the specific frequency and slip ratio applied. The output torque can be obtained after the stator and rotor currents reach the steady state. Again, many torque values can be obtained for different slip ratios, among which the maximum output torque for the specific frequency is searched with the condition that the stator current does not exceed the allowable value [GUA14a]. The efficiency at the cranking points and the continuous mode of operation shown marked to indicate the operating points of interest for the BSG application.

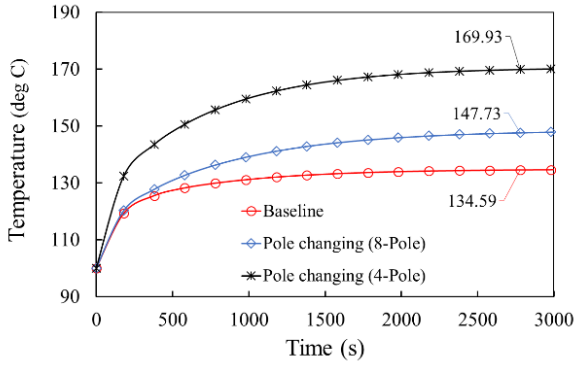

(a) Operation at 2800 rpm at 12Nm

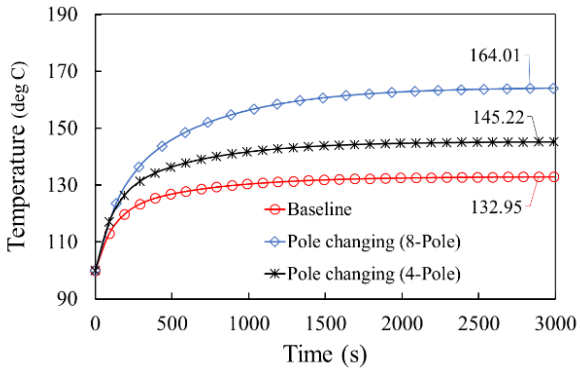

(b) Operation at 2800rpm and 7Nm.

Fig. 3.17 Winding hotspot from the steady-state thermal analysis.

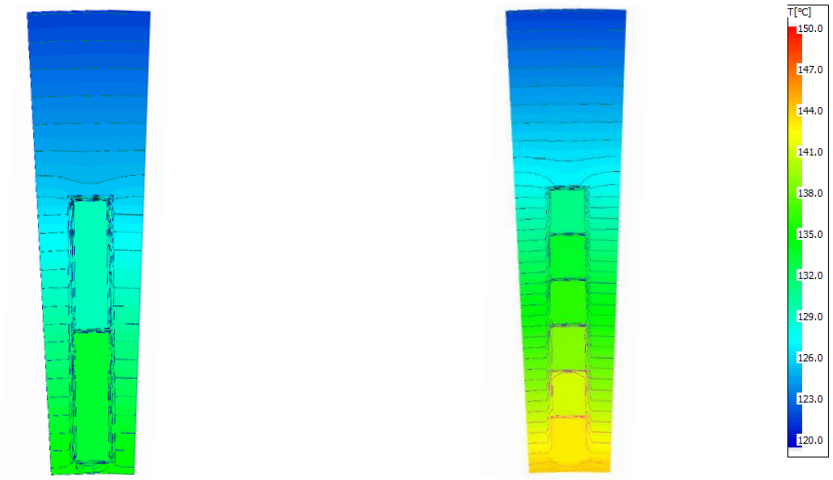

(a) Baseline

(b) Pole changing winding machine

Fig. 3.18 Thermal FEA temperature map at 2800rpm and 12Nm at steady-state.

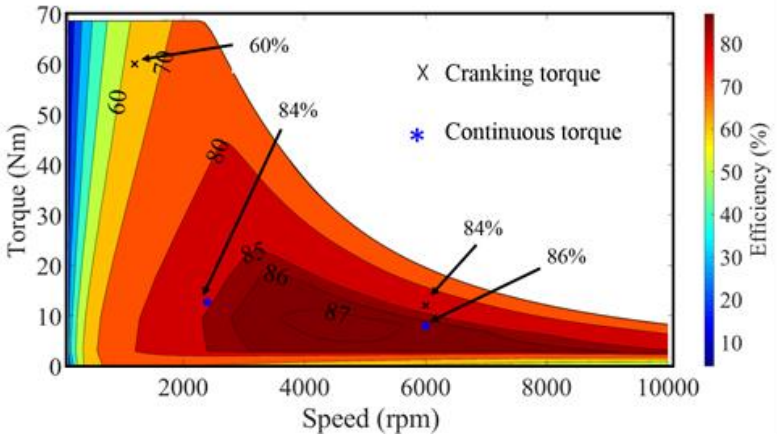

Fig. 3.19 Efficiency map of the baseline induction machine.

All the performance maps are generated for the same DC bus voltage and rated inverter current. For comparison, the performance at the same operating points for the 8-pole and 4-pole operation are shown in Fig. 3.20 and Fig. 3.21 respectively. The efficiency at the high torque region is lower for the pole changing winding machine due to the increased stator copper loss as a result of higher phase resistance as discussed from Fig 3.13(a). This is because of the higher series turns per phase in the pole changing winding. However, the efficiency at the high speed and continuous operating region is higher for the pole changing winding machine when the 4-pole operation is chosen at high speeds beyond 4000rpm. At speeds greater than 6000rpm efficiency improvements of 3% or more can be obtained when the 4-pole winding is used.

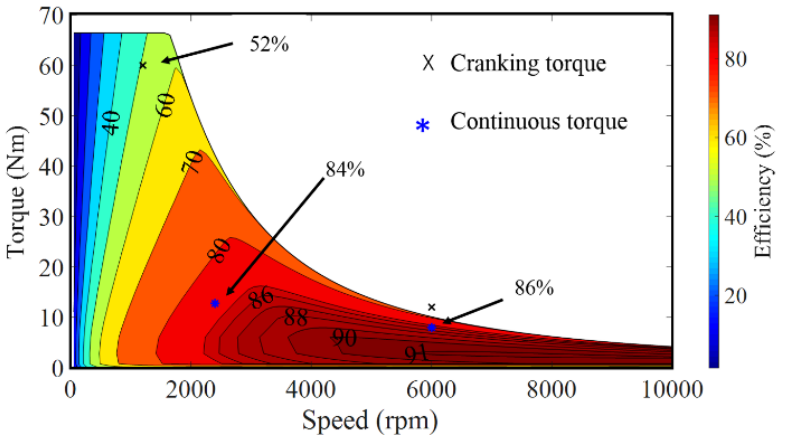

(a) 8-pole operation.

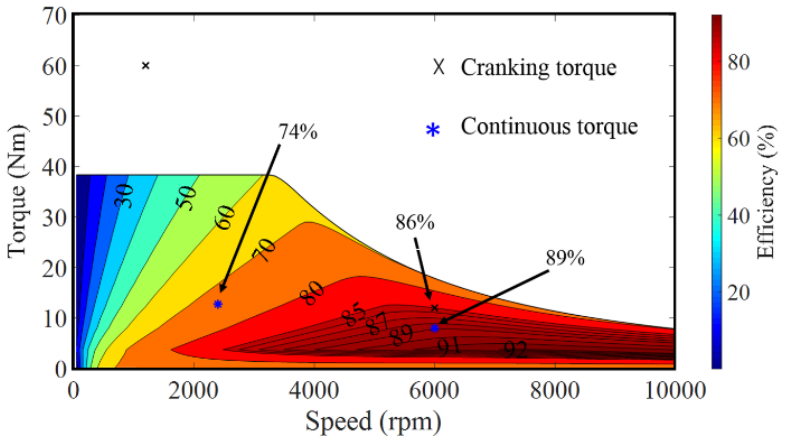

(b) 4-pole operation.

Fig. 3.20 Efficiency maps of pole changing induction machine.

The shift of the speed at which peak efficiency occurs can be explained by the distribution of the losses. The distribution of the stator and rotor losses (both AC and DC losses) of the baseline and the pole changing winding machine are shown in Fig. 3.21(a) to Fig. 3.21(d). The higher stator losses at low speed and high current are due to the phase resistance being higher at low speeds for the pole changing winding machine. The rotor losses are slightly higher for the pole changing winding machine in the same region. This can be explained from the expression of the bar current:

$$I_{bar} \propto \frac{2mWk_wI_{phase}}{N_R} \tag{3.11}$$

where m, W, k_w, I_{phase} and N_R are the number of phases, the number of series turns per phase, winding factor, phase current and number of rotor bars. From (3.11), the bar current for a given phase current is proportional to the number of series turns per phase and winding factor. The number of series turns per phase is 33% higher and the winding factor 15% lower for the pole changing

winding machine resulting in the higher rotor loss. The power factor maps for the baseline machine, the pole changing winding induction machine for 8-pole operation and 4-pole operation are shown in Fig. 3.22(a), Fig. 3.22(b) and Fig. 3.22(c) respectively. The envelope of power factor curves for these machines when operating at the rated current is shown in Fig. 3.22(d). The power factor of the baseline machine and the pole changing winding induction machine for 8-pole operation are similar due to the similar magnetising inductances. The magnetising inductance of the pole changing winding in 4-pole operation is higher as previously discussed. This results in a higher power factor as seen from Fig. 3.22(c) and Fig. 3.22(d).

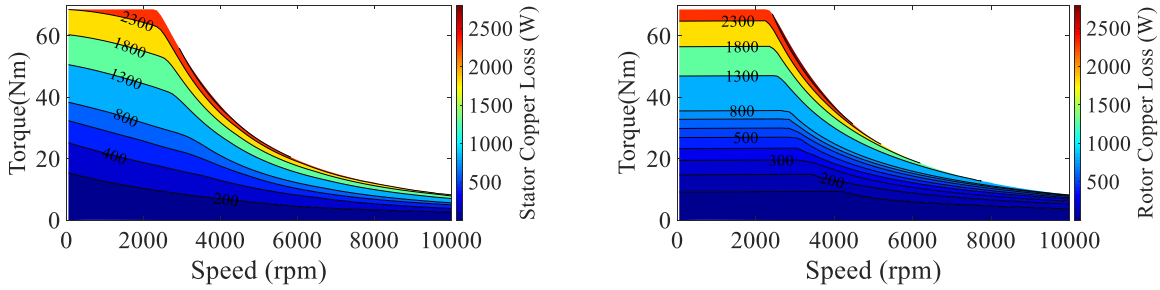

(a) Baseline machine, 8-pole operation

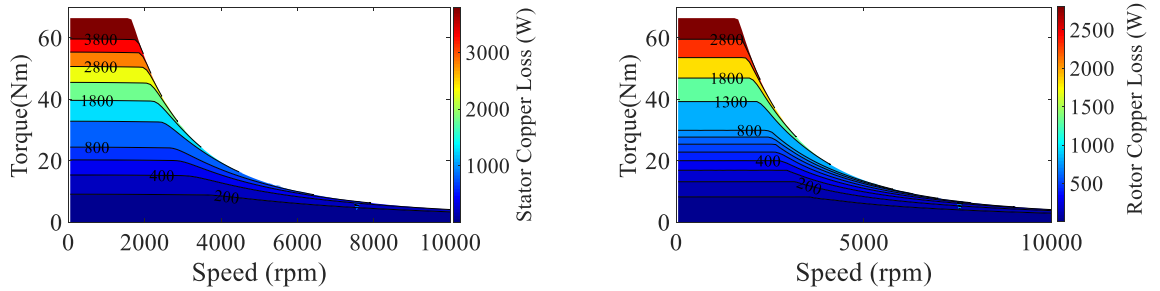

(b) Pole changing machine, 8-pole operation

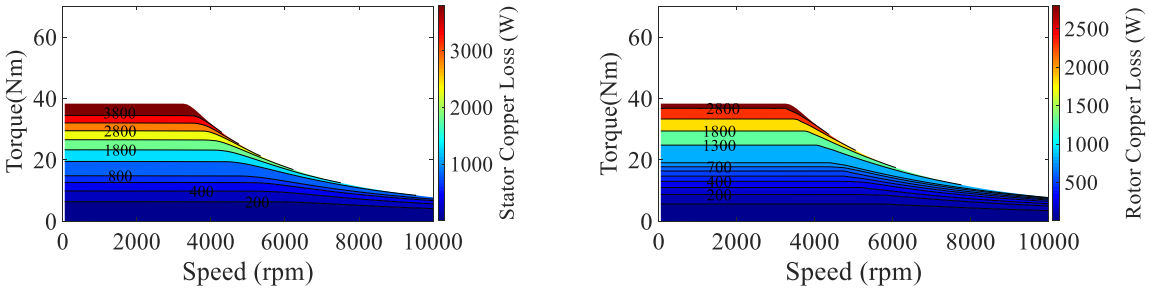

(c) Pole changing machine, 4-pole operation.

(I). Stator loss (II). Rotor loss

Fig. 3.21 Loss distribution maps of baseline and pole changing machine.

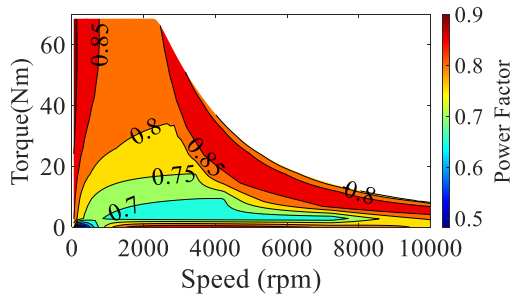

(a) Baseline machine, 8-pole operation

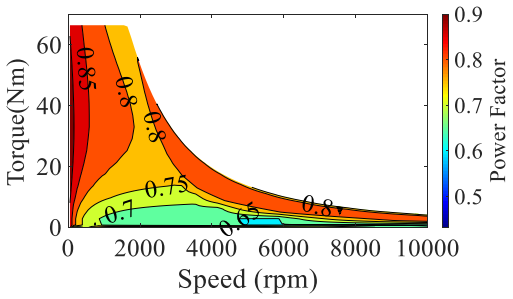

(b) Pole changing machine, 8-pole operation

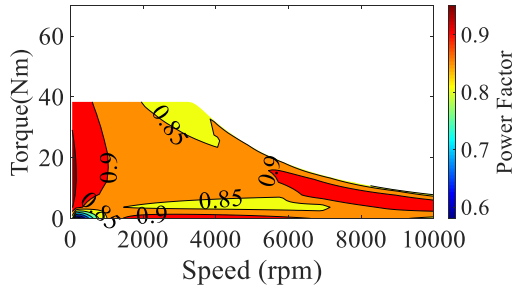

(c) Pole changing machine

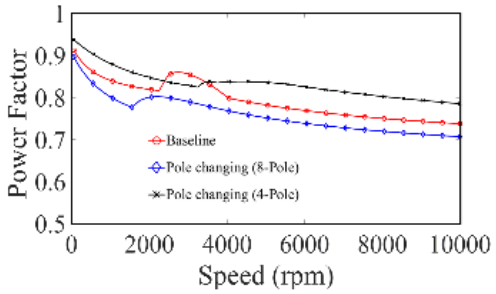

(d) Power factor curves for operation on torque speed envelope.

Fig. 3.22 Power factor plots.

3.5 Experimental Results and Comparison with Predicted Results

To determine the relative performance of a pole changing winding machine, a prototype induction machine was fabricated. Due to the time and budget constraints involved in fabricating a one-off aluminium die-cast squirrel cage rotor, an off the shelf induction machine rotor of known dimensions was chosen for the prototype machine. The prototyped induction machine is of lower power and is intended to demonstrate the feasibility and accuracy of the FEA models and their applicability in predicting the behaviour and performance of pole changing winding induction machines. The stator of the induction machine was optimized and fabricated for this rotor, with a pole changing winding. All the coils terminals of the stator winding are brought out to a terminal box to allow for the connection of the windings in different pole number configurations. The machine is coupled to a dynamometer which is used as a brake, to measure the torque capability and steady-state performance over the operating speed range. The experimental setup is shown in Fig. 3.23. The specifications of the prototype are listed in TABLE 3-2. The 48 slots of the stator are wound with 12 coils each coil occupying 8 slots and all the 24 terminals of the coils are brought out to the terminal box where external connections can be made to configure the machine either as a 3-phase

4-pole, 60-degree phase belt machine or as a 3-phase 4-pole, 120-degree phase belt machine and as a 3-phase 2-pole, 120-degree phase belt machine.

TABLE 3-2 PROTOTYPE INDUCTION MACHINE SPECIFICATIONS

Parameter	Value	Parameter	Value
Outer diameter (mm)	136	Phase current (A)	2.8 Arms
Stack length (mm)	130	Maximum speed (rpm)	3000
Number of poles	4	Cage bar/ end ring	Aluminium
DC bus voltage (V)	400	Number of stator and rotor slots	48/26
Lamination	M-19 24 Ga	Number of series turns/phase	272
Slot fill factor	0.38		

3.5.1 Experimental Setup and Test Methodology

The induction machine parameters required for field orientation are determined under each of the connection types. As shown in Fig. 3.23, the prototype induction machine is coupled to the dynamometer load machine through a torque sensor. A three-phase inverter is used to control the machine with dSPACE on which indirect field-oriented control is implemented to control the induction machine in the constant torque and flux weakening region. The dynamometer is run at a certain fixed speed and each speed, the peak current supplied by the inverter is held fixed and the q-axis and d-axis current components are varied to determine the maximum torque per ampere point at each corresponding speed [WAL92]. This process is repeated for different values of peak current to determine the torque-speed curve and efficiency map. Results from one such test for the induction machine with 3-phase 4-pole 120-degree phase belt connection is shown in Fig. 3.24. For an increasing stator line current of 2A to 4A, the q-axis current is swept to determine the q-axis current that maximizes the torque.

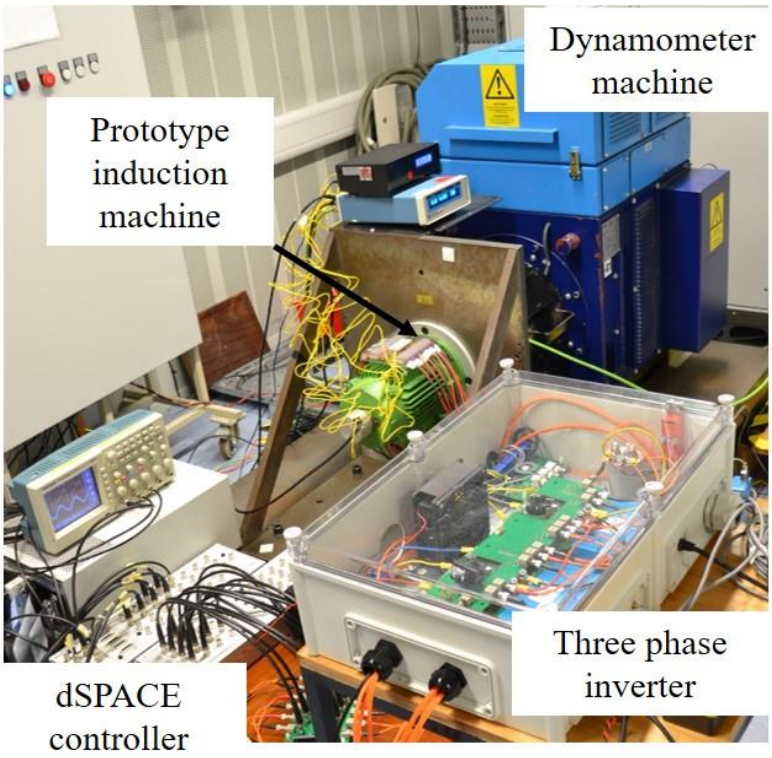

Fig. 3.23 Experimental setup showing prototype induction machine coupled to a dynamometer for performance measurement.

3.5.2 Measured and Predicted Torque and Power Capability Curves

Using the test methodology discussed previously, the torque capability of the machine with different current levels from zero speed to 3000rpm for the three different configurations of induction machines is measured.

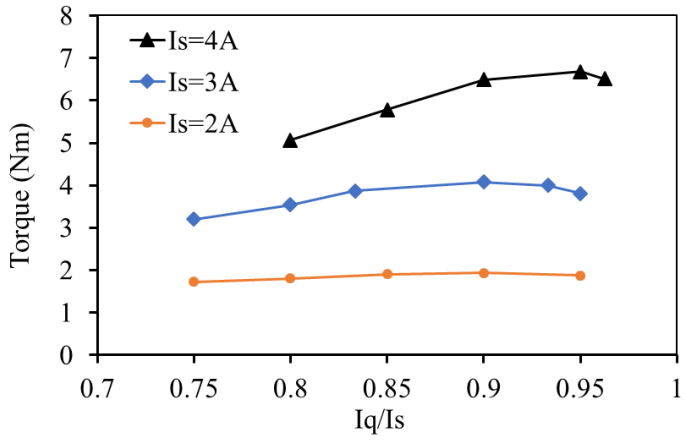

Fig. 3.24 Test results showing the variation of torque with increasing q-axis-current to stator current ratio of a 3-phase 4-pole 120-degree phase belt connection induction machine.

The comparison of the torque and power from the experiment and finite element analysis for the 3-phase, 4-pole, 60-degree phase belt, 3-phase, 4-pole, 120-degree phase belt and 3-phase, 2-

pole, 120-degree phase belt is shown in Fig. 3.25, Fig. 3.26 and Fig. 3.27 respectively. A good agreement with an average error of less than 8% is observed between measured and calculated values over the range of speeds and machine configurations.

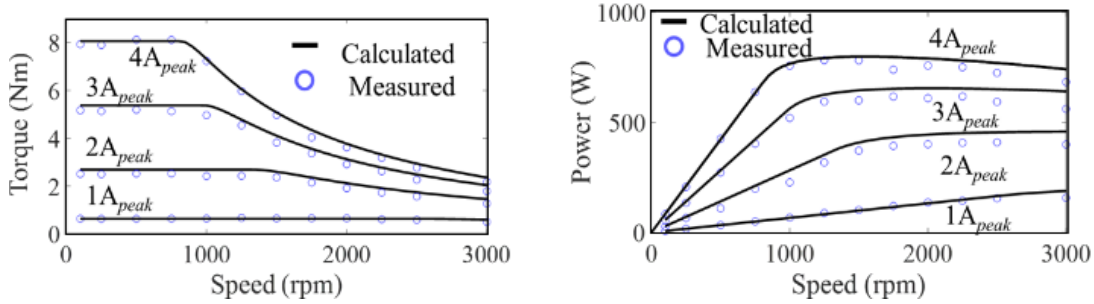

(a)Torque-speed curve. (b) Power speed curve.

Fig. 3.25 Measured and FE predicted performance curves of the 3-phase 4-pole 60-degree phase belt connection induction machine.

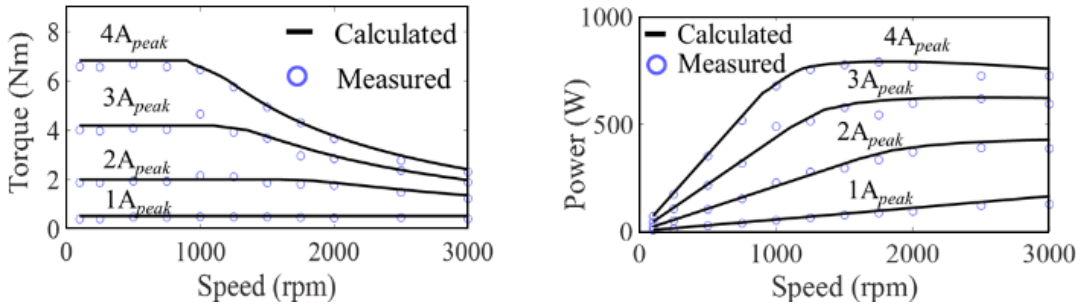

(a)Torque-speed curve. (b) Power speed curve.

Fig. 3.26 Measured and FE predicted performance curves of the 3-phase 4-pole 120-degree phase belt connection induction machine.

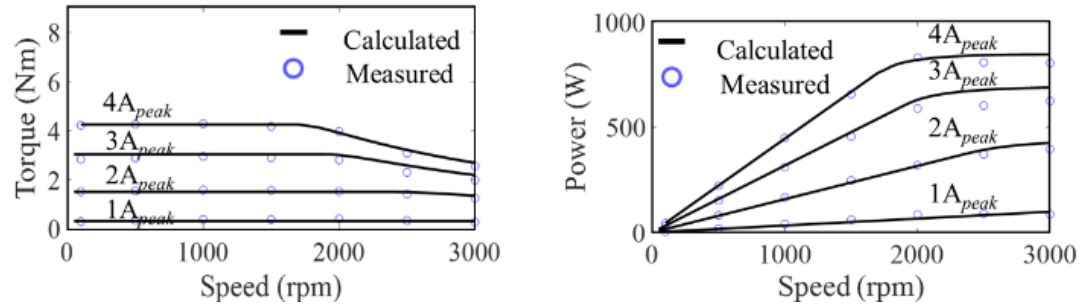

(a)Torque-speed curve. (b) Power speed curve.

Fig. 3.27 Measured and FE predicted performance curves of the 3-phase 2-pole 120-degree phase belt connection induction machine.

The torque at rated current of the 3-phase, 4-pole, 60-degree phase belt and 3-phase 4-pole 120-degree phase belt machines are 8.1Nm and 6.7Nm respectively which are in proportion to the

respective winding factors of 0.957 and 0.83. The torque capability while lower for the 3-phase, 2-pole, 120-degree phase belt configuration, this machine configuration has a corner speed is double that of the 4-pole operation resulting in an extended range of flux weakening speed operation. A comparison of the torque and power speed envelopes of the three machines with the rated current is shown in Fig. 3.28. The extended field weakening region as a result of changing the number of poles from 4 to 2 can be seen in the power capability from Fig. 3.28(b).

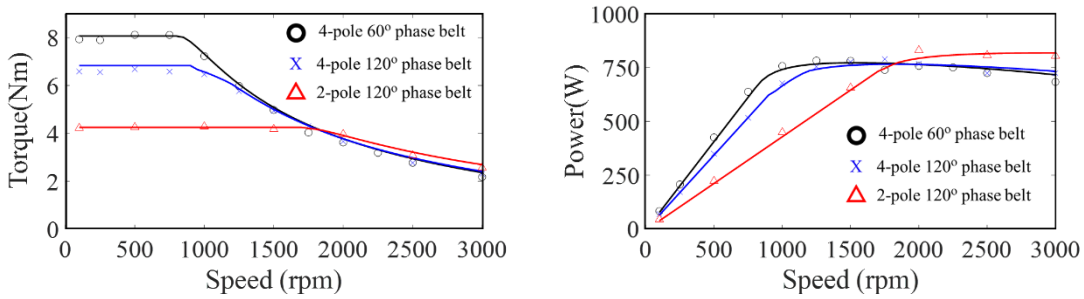

(a)Torque-speed curve.

(b) Power speed curve.

Fig. 3.28 Comparison of measured performance curves of the 3-phase 60-degree and 120-degree phase belt connection induction machines.

3.5.3 Measured and Predicted Efficiency Maps

The efficiencies of the three configurations of the machine are measured and calculated over the entire speed range. The measured and calculated efficiency maps are shown in Fig. 3.29, Fig. 3.30 and Fig. 3.31. In contrast to the efficiency map of the machine of shorter stack length discussed in Fig. 3.20(a), the 3-phase 120-degree phase belt 4-pole machine has similar efficiency as the 3-phase 60-degree phase belt 4-pole machine due to the machine in Fig. 3.20(a) having lower stack length and a higher number of conductors per phase resulting in reduced AC losses at higher speeds. The prototype machine, however, has the same number of stranded turns on both the 60-degree phase belt and 120-degree phase belt machine and this results in little difference in efficiency between the two configurations of machines as seen from Fig. 3.24(b) and Fig. 3.25(b). The efficiency of the 120-degree phase belt 4-pole machine, at low loads, across the speed range, is higher when compared to its 2-pole counterpart. This is in contrast to the simulated, 48V starter-generator pole changing winding induction machine efficiency maps in Fig. 3.20(a) and Fig. 3.20(b). For the prototype induction machine, at high speeds, the iron losses have a significant contribution and the AC losses in the windings have no contribution due to the use of stranded windings. Whereas, the losses at high speed in the simulated 48V machine are dominated by the AC losses in the solid conductors.

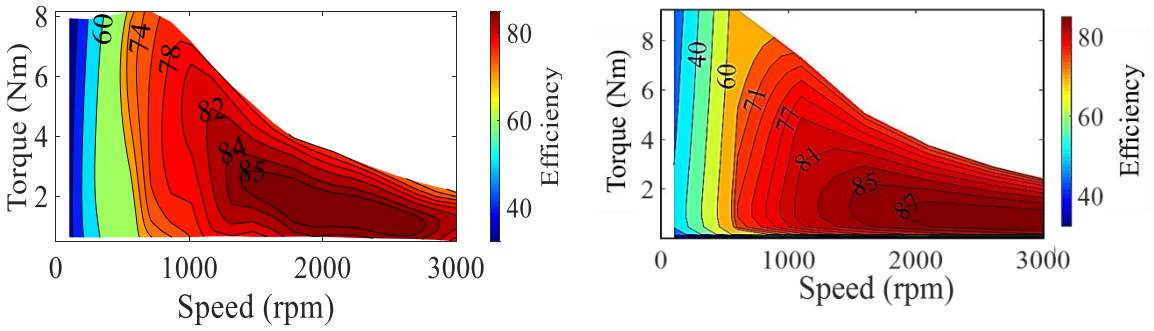

(a) Measured (b) Calculated

Fig. 3.29 Efficiency map of 3-phase 4-pole 60-degree phase belt connection induction machines.

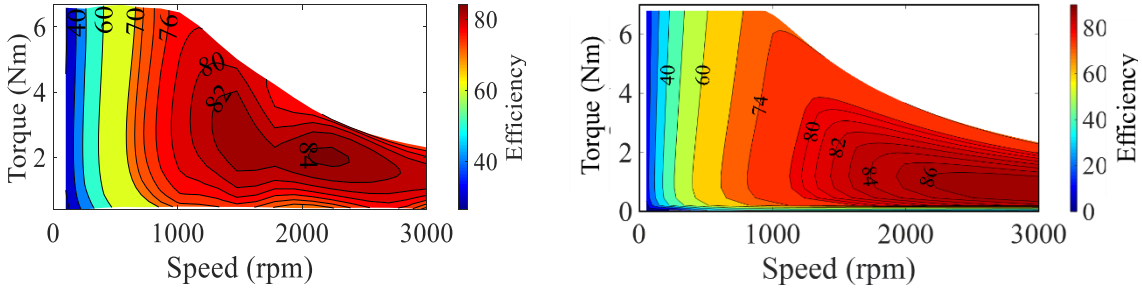

(a) Measured (b) Calculated

Fig. 3.30 Efficiency map of 3-phase 4-pole 120-degree phase belt connection induction machines.

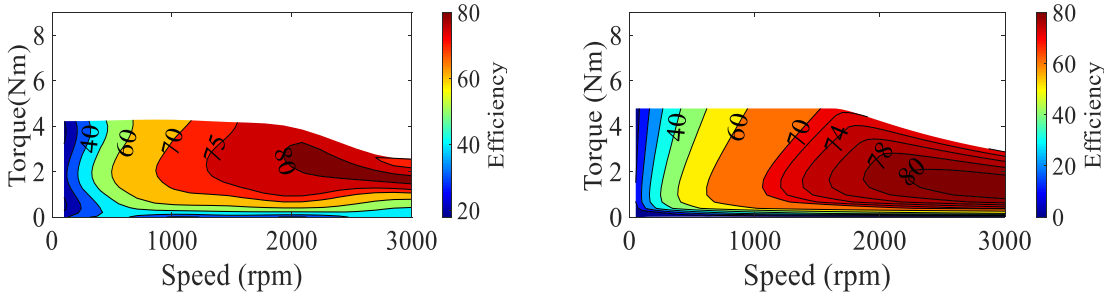

(a) Measured (b) Calculated

Fig. 3.31 Efficiency map of 3-phase 2-pole 120-degree phase belt connection induction machines.

The benefits of improved power capability and efficiency with the pole changing machine can be seen from Fig. 3.32 where the experimentally measured power-speed characteristics with constant efficiency contours are plotted for the 3-phase 120-degree phase belt 4-pole and 2-pole operation. It can be observed that the region in which the flux weakening region of operation is extended by using the 2-pole configuration of operation, the achievable efficiency is higher than the efficiency achievable by the 4-pole configuration of operation.

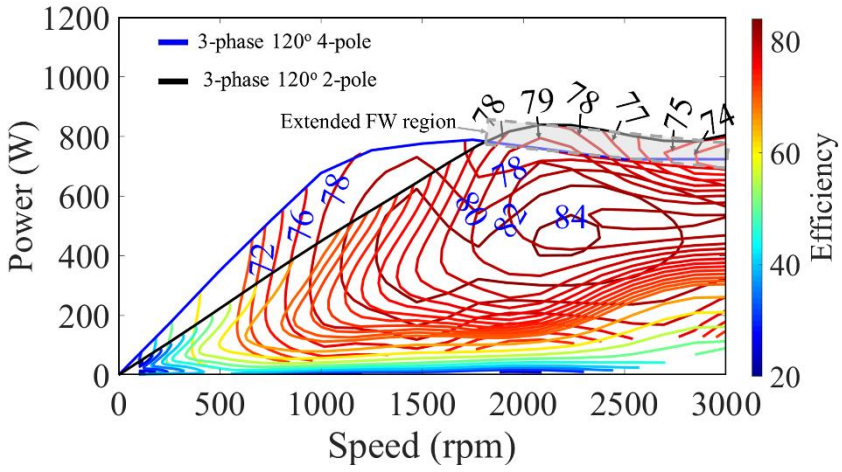

Fig. 3.32 Measured power vs speed curve with constant efficiency contours showing extended flux weakening region of operation for 3-phase 120-degree phase belt 4-pole and 2-pole operation.

3.6 Conclusions

A pole changing winding induction machine with 8-pole and 4-pole operation has been designed and compared with a standard three-phase 8-pole induction machine for a starter-generator application. A prototype induction machine of lower power rating has been tested to demonstrate pole changing capability and validate the finite element models used for analysis. The salient points are summarized below:

- For machines with the same outer diameter stack length and number of series turns per phase, the pole changing winding machine despite a wider operating speed range has a lower torque capability in the low-speed region due to poor winding factor.
- The induction machine with pole changing windings requires a higher number of series turns per phase and a shorter stack length. The resulting machine is 20% reduced in the overall length while capable of meeting the specifications at cranking and continuous operation.
- While the stack length is reduced, during low-speed operation the efficiency is reduced due to the increased phase resistance. However, at higher speed and continuous operating regions, the peak efficiency of the pole changing winding machine is higher by 3% compared to the baseline across continuous torque operating points.
- This happens at speeds higher than 6000rpm when the phase resistance of the baseline machine increases due to the dominating AC resistance. While in theory, the pole changing winding induction machine offers a solution to increase the flux weakening range of an induction machine, a compromise needs to be made between the stack length and the efficiency in the constant torque region.

- The efficiency of the induction machine in the achievable extended flux weakening region of operation is higher than the achievable efficacy of the higher pole number machine configuration for comparable speeds.

In conclusion, for a starter-generator application where space is axially limited and the majority of continuous operation occurs at higher speeds and only intermittent cranking operations are required, the lower efficiency during cranking operation can be accepted for a reduced stack length.

Chapter 4

Six-Phase Pole-Changing Winding Induction Machines with Improved Performance

Induction machines with three phases are preferred over machines with one or two phases due to their well-known ability to produce higher torque without producing a pulsating torque at twice the rated frequency. However, with an increasingly higher proportion of induction machines being supplied with inverters, the use of multiphase induction machines with the number of phases greater than three has become more widespread. Multiphase machines offer the benefit of lower space harmonic content for a given stator excitation. Multiphase machines also offer fault tolerance and are less susceptible to time harmonics producing torque ripples. Another significant property of multiphase machines is that provided a concentrated winding is used, torque production can be enhanced by the injection of higher stator current harmonics [LEV07]. While this is possible for all multiphase induction machines with an odd number of phases, enhancing torque production for even number of phases is only possible for a 6-phase machine with an asymmetric distribution between the phases [LYR02]. In this chapter, a method to overcome the inherently low winding factor of the 3-phase pole changing winding machines is discussed. The poor winding factor results from the need to use a 120^o phase belt winding for facilitating the pole changing operation. As opposed to the more widely used 60^o phase belt which has the highest possible winding factor, the 120^o phase belt winding has a 15% lower winding factor resulting in a proportionally reduced torque. In this chapter, the influence of the choice of phase belt on the winding factor for a six-phase machine is discussed to demonstrate the improvement in fundamental winding factor while preserving the ability to perform pole changing operation. The design of the six-phase pole changing winding prototype machine is discussed and the results from FEA are presented and compared with experimental results.

4.1 Six-Phase Pole-Changing Windings

Induction machines with electronic pole changing windings were introduced and analysed in [OSA96] [MIZ97] and [OSA97b]. Adopting the more widely used 60^o phase belt winding results in the highest fundamental winding factor but cannot be used for pole changing winding operation due to the MMF cancellation that occurs as was discussed in detail in Chapter 4. To avoid this in [OSA96]

a 120^o phase belt winding was used. However, the poor winding factor of this winding arrangement results in a 15% torque reduction. Six-phase pole changing windings can overcome this limitation.

4.1.1 Influence of Phase Belt on Winding Factor and MMF Harmonics

3-phase distributed windings are usually wound with a 60^o phase belt distribution for the highest fundamental winding factor. However, in a double layer pole-changing winding, when a 60^o phase belt is used, the reversal of current in one of the coils will result in cancellation of the MMF produced by the coils as explained in [MAL19]. MMF cancellation is inefficient due to the losses from the current flowing in the coils but not contributing to torque production. This cancellation of MMF can be prevented while retaining the pole-changing behaviour via current reversal, by using windings that have a 120^o phase belt distribution. This, however, reduces the winding factor by 15% compared to the 60^o phase belt which results in a proportionate decrease in the torque capability of the machine. The expression for unsaturated magnetizing inductance is shown in (4.1) where $m, k_w, W, p, D_{is}$and L_{stk} are the number of phases, the fundamental winding factor, the number of series turns per phase, the number of pole pairs, the stator bore diameter and the stack length. Using the machine data provided in Appendix I, the unsaturated magnetizing inductance of the windings with different phase belts is shown in TABLE 4.1.

$$L_m = \frac{m\mu_o}{\pi g_{effective}}\left(\frac{k_w W}{p}\right)^2 D_{is} L_{stk} \tag{4.1}$$

TABLE 4.1 MAGNETIZING INDUCTANCE FOR DIFFERENT PHASE BELTS

Q_s	p_1	m	L_m (H) (60^o phase belt)	L_m (H) (120^o phase belt)
48	4	3	0.651	0.488
48	2	3	-	1.295
48	4	6	1.396	1.302
48	2	6	-	2.778

The magnetizing inductance which is proportional to the winding factor decreases with a 120^o phase belt winding resulting in a higher magnetizing current for given frame size. To maintain the same air-gap flux density as that of the 60^o phase belt windings, a 120^o phase belt winding machine will require a corresponding increase in the magnetizing current by 15%. The ratio of power

capability of a pole-changing winding induction machine to a conventional winding induction machine approaches the ratio of the corresponding fundamental winding factors as the rating of the machines increases. Lower rated machines have a lower power capability ratio due to a larger proportion of the rated current being the magnetizing current. The torque of an induction machine can be expressed as a function of air-gap flux density (B_g) and electric loading (A_T) as shown in (4.2), where D_{is}, L_{stk}, n and k_w are the stator bore diameter, the stack length, the speed in revolutions per second and the fundamental winding factor[OSA96].

$$T = \frac{1.11 k_w \pi^2 D_{is}^2 L_{stk} n A_T B_g}{60} \tag{4.2}$$

It can be seen that for a given frame size, magnetic and electric loadings, the torque capability is proportional to the winding factor which results in the 120° phase belt winding having poorer torque capability compared to the 60° phase belt winding which has a higher fundamental winding factor, every other parameter in (4.2) being the same.

4.1.2 Winding Factor Improvement with Six-Phase Windings

The winding factor reduction due to the 120° phase belt winding 3-phase winding can be determined for a given winding distribution from the summation of the EMF phasors as shown in the equations (4.3) and (4.4) [LIB04]. k_w, Q_s, m, n_l, v, p are the winding factor, the number of stator slots, and the number of phases, the number of winding layers, the harmonic number and the number of pole pairs, respectively. $\vec{E}$ is the EMF phasor of each of the coil of one phase in the slot of the machine that is defined by the connection matrix $C_{conx}(i)$.

$$k_w = \frac{\left| \sum_{i=1}^{\frac{2Q_s}{m}} \vec{E} \right|}{n_l Q_s / m} \tag{4.3}$$

$$\vec{E} = e^{\frac{j2\pi v p}{Q_s} C_{conx}(i)} \tag{4.4}$$

The rows of the connection matrix consist of the stator slot numbers that accommodate the phase coil sides. The return sides of the coils are represented as negative numbers. Using this equation the winding factor for a 48 slot machine is determined for both 60° and 120° phase belt phase belts with 4 poles and 2 poles when pole-changing is feasible. The values of winding factor for the fundamental, 5th and 7th harmonic orders are listed in TABLE 4.2, TABLE 4.3 and TABLE 4.4, respectively. The slot/pole number combination chosen here for illustrating the improvement of the

winding factor is the same slot/pole number combination of the prototype induction machine fabricated for experimental verification. From these tables, it can be seen that the winding factor of the 60^o phase belt phase winding is higher than that of the 120^o phase belt phase winding for 4 poles. Pole-changing is not feasible with a 60^o phase belt phase and the winding factor for the 2-pole case for this winding are left blank. For the 120^o phase belt winding, it can be seen that for a 6-phase winding distribution has a higher fundamental winding factor than the 3-phase counterpart winding by 15.5% for the higher pole operation and by 3.5% for the lower pole operation resulting in a machine winding configuration with higher peak torque capability when operated with the higher pole number.

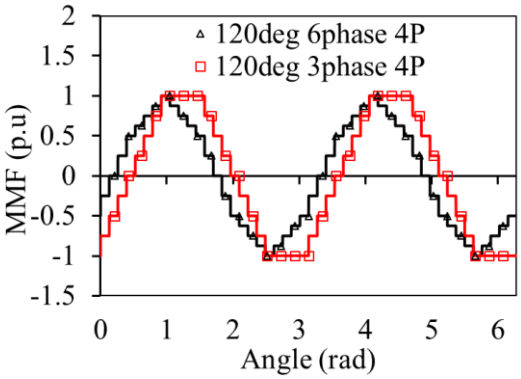

(a) 4-pole winding MMFs

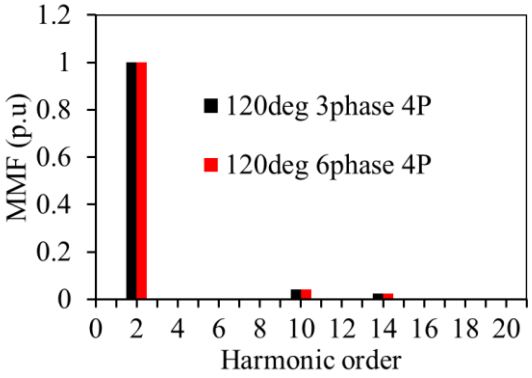

(b) 2-pole winding MMFs

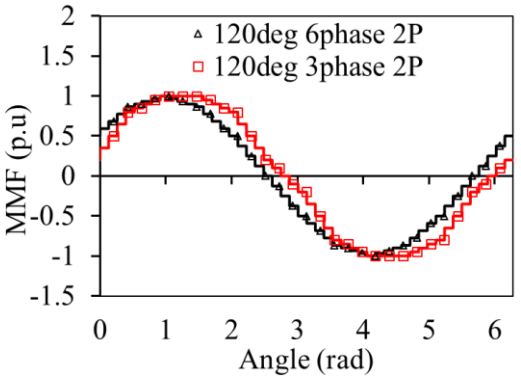

(c) 4-pole winding MMF harmonic spectra

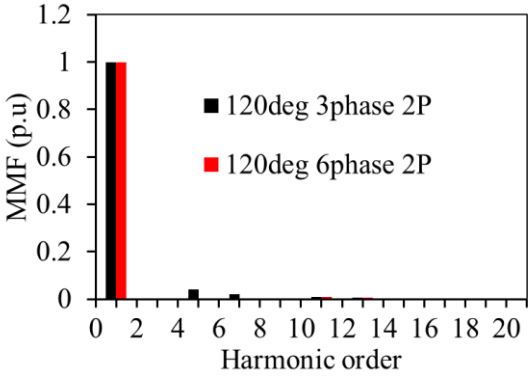

(d) 2-pole winding MMF harmonic spectra.

Fig. 4.1 Normalized 120^o phase belt 6-phase and 3-phase winding.

With a higher fundamental winding factor of the 6-phase pole-changing winding, the issue of the increase in the current due to the lower magnetizing inductance and the reduced power capability as a result when compared to the 3-phase 120^o phase belt is resolved. The 5th and 7th harmonic winding factors for the 6-phase 120^o phase belt are higher compared to the corresponding harmonics of the 3-phase 120^o phase belt winding. While the winding factors are not zero for the 5th and 7th

harmonic components, the 5th and 7th harmonics do not exist in the MMF harmonics for the 6-phase winding configurations.

TABLE 4.2 FUNDAMENTAL WINDING FACTORS FOR DIFFERENT PHASE BELTS

Q_s	p_1	m	k_w (60° phase belt)	k_w (120° phase belt)
48	4	3	0.957	0.829
48	2	3	-	0.675
48	4	6	0.991	**0.957**
48	2	6	-	**0.699**

TABLE 4.3 5TH HARMONIC WINDING FACTORS FOR DIFFERENT PHASE BELTS

Q_s	p_1	m	k_w (60° phase belt)	k_w (120° phase belt)
48	4	3	0.205	0.177
48	2	3	-	0.137
48	4	6	0.793	**0.205**
48	2	6	-	**0.531**

TABLE 4.4 7TH HARMONIC WINDING FACTORS FOR DIFFERENT PHASE BELTS

Q_s	p_1	m	k_w (60° phase belt)	k_w (120° phase belt)
48	4	3	0.157	0.136
48	2	3	-	0.099
48	4	6	0.608	**0.157**
48	2	6	-	**0.386**

However, the impact of these harmonics on the losses is better represented by the harmonic content of the MMF of these winding configurations. The MMF of the 4 different winding configurations and their harmonic spectra are shown in Fig. 4.1. The 3-phase and 6-phase 120°, 4-pole phase belt windings MMF waveforms are compared in Fig. 4.1 (a) and the corresponding 2-

pole MMF waveforms are shown in Fig. 4.1 (c). While the winding factors of the 6-phase windings are seen to be higher when a 120^o phase belt winding is used, the MMF harmonics are not significantly higher. In fact, with a 6-phase 120^o phase belt winding operating in 2-pole mode, the 5th and 7th order harmonics are lower than the corresponding 3-phase 120^o phase belt winding harmonics as seen from Fig. 4.1 (b). As such, the rotor losses due to the MMF harmonics are not expected to be higher in the 6-phase 120^o phase belt windings.

4.1.3 Inverter for Six-Phase Pole-changing Winding IM

To realize the improvement in the fundamental winding factor when a 6-phase, 120^o phase belt winding is utilized while performing electronic pole-changing, the inverter required for this needs to be modified. Electronic pole-changing requires that the current in half of the coils of each phase of the induction machine to be reversed. Six inverter legs were required for a 3-phase pole-changing machine. Similarly, for a 6-phase pole-changing winding machine, 12 inverter legs will be required as shown in Fig. 4.2. It is important to note that these are four standard 3-phase inverters. The machine has 6-phases, each of which is split into two coil sets A1, A2, B1, B2, C1, C2, X1, X2, Y1, Y2, Z1 and Z2, and each 3-phase set is connected to the 3 legs of the inverter. Using this arrangement, the current in the coils of the phases can be reversed independently for electronic pole-changing. The number of switches required for the 6-phase pole-changing winding machine is doubled compared with the number of switches required for a 3-phase pole-changing winding machine.

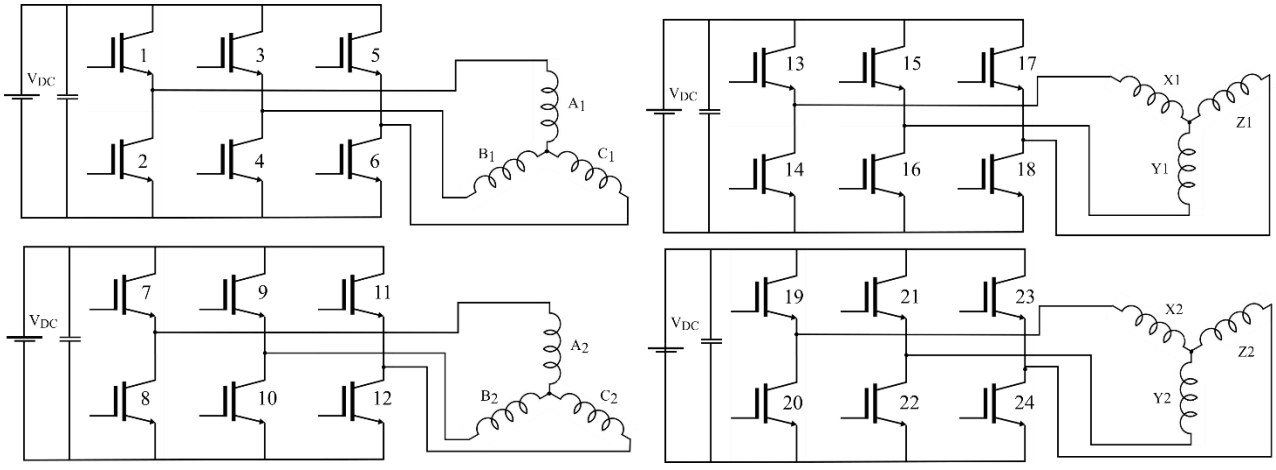

Fig. 4.2 Twelve inverter legs for a 6-phase machine to facilitate pole-changing operation.

However, for a given power rating and voltage rating of the induction machine, the required current per phase is reduced resulting in the overall volt-ampere rating of the inverter remaining constant. This results in the inverter required for driving a 6-phase pole-changing winding induction machine having a lower current rating per switch. In higher volumes where the inverter is

constructed with discrete devices, this results in a lower overall cost of the inverter for a given volt-ampere rating [SOZ16]. When the number of phases increases for the same current rating per phase, the efficiency degrades due to increased conduction losses. However, when compared for the same power rating (especially for a power rating greater than 100kW), the multi-phase inverters have higher efficiency than their 3-phase counterparts and this improvement gets better as the power rating increases further. This is due to the reduction of the conduction losses as the same current is spread over a larger number of devices resulting in lower current per device both reducing cost as well as conduction losses [ZAR10]. The number of turns and parallel paths of the 6-phase windings have to be appropriately adjusted to result in similar electric loading to the 3-phase winding and this will be explained using the prototype machine as an example in the next section.

4.2 Design of Pole-changing Winding Induction Machine

A prototype induction machine with a stator winding that can be configured as a three-phase as well as a six-phase winding is fabricated to demonstrate the performance improvement of a six-phase pole changing winding over the conventional three-phase pole changing winding induction machine.

4.2.1 Stator Winding

To demonstrate the improvement of the performance of the 6-phase pole-changing winding induction machine, a 1kW prototype machine with 48 stator slots and a squirrel cage rotor with 26 slots is analysed and prototyped. The parameters of the machine are provided in Appendix I. To demonstrate the pole-changing behaviour of the existing topology of pole-changing windings and the proposed 6-phase pole-changing winding, a 4/2-pole-changing combination was chosen. To prevent the slots per pole per phase (SPP) from being fractional and/or equal to 1 (due to the high leakage inductance with SPP=1 [BOL02]) for any pole and phase combination, the number of stator slots was chosen as 48. Since a commercially available induction machine rotor was used for the prototype, the number of rotor bars was fixed at 26. For a 1kW air-cooled induction motor, a 90 frame size is appropriate and the outer dimensions of the lamination are selected to be accommodated in a 90 frame casing. The stator slot dimensions are calculated (using the measured rotor slot dimensions) using the method outlined in [GUA14]. FE analysis is used to determine the parameters and performance of the machine. The number of conductors per slot is chosen to achieve a copper slot fill factor of 38% which results in 34 turns per coil. The prototype machine is wound with individual coils brought out to a terminal box to allow for different winding configurations to

be connected within the same machine. The winding layout of the individual coils for the 6-phases is shown in Fig. 4.3.

Poles	N												S											
Slot N°	1	2	3	4	5	6	7	8	9	10	11	12	13	14	15	16	17	18	19	20	21	22	23	24
Layer 1	A1	A1	A1	A1	B1	B1	B1	B1	C1	C1	C1	C1	Z1	Z1	Z1	Z1	X1	X1	X1	X1	Y1	Y1	Y1	Y1
Layer 2	z2	z2	z2	z2	x2	x2	x2	x2	y2	y2	y2	y2	a1	a1	a1	a1	b1	b1	b1	b1	c1	c1	c1	c1

Poles	N												S											
Slot N°	25	26	27	28	29	30	31	32	33	34	35	36	37	38	39	40	41	42	43	44	45	46	47	48
Layer 1	A2	A2	A2	A2	B2	B2	B2	B2	C2	C2	C2	C2	Z2	Z2	Z2	Z2	X2	X2	X2	X2	Y2	Y2	Y2	Y2
Layer 2	z1	z1	z1	z1	x1	x1	x1	x1	y1	y1	y1	y1	a2	a2	a2	a2	b2	b2	b2	b2	c2	c2	c2	c2

Fig. 4.3 Winding layout of 6-phases of the prototype machine.

With the terminals of the individual coils available, the induction machine prototype can be configured as any one of the machines listed in TABLE 4.5 with the connections for one phase being indicated in the table and the other phases being similarly connected. The base speed of the machine is 1000rpm and this is based on the DC bus voltage in the experimental setup. For a maximum available voltage of 400V at the DC bus, the number of turns of the double layer winding was chosen for a corner speed of 1000rpm for the baseline M3, 4P machine. This results in 34 turns per coil with 2 parallel paths for the M3, 4P machine and 1 parallel path for the M6, 4P machines. The stack length of the machine is comparable to the diameter of the machine with the ratio of the stator bore to active stack length being 0.66. For this aspect ratio, the effects of 3D fringing of fields are not dominant. While 2D FEA simulations are used to compute the performance of the induction machine, to improve the accuracy of the simulations, 3-D effects that have been considered include the end winding inductance, overhang resistance and rotor end-plate inductance and resistance that have been computed analytically and included in the external circuit of the 2D FEA [BOL02].

TABLE 4.5 WINDING CONNECTION CONFIGURATION OF PROTOTYPE MACHINE

Phase-A Connection Diagram	Machine Configuration	Machine ID
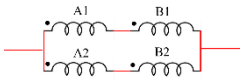	3 Phase 120° phase belt 4-poles (A-B, X-Y, C-Z)	M3,4P (baseline)
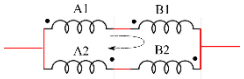	3 Phase 120° phase belt 2-poles (A-B, X-Y, C-Z)	M3,2P (baseline)
	6 Phase 120° phase belt 4-poles (A,Z, X,B,Y,C)	M6,4P
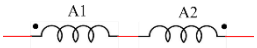	6 Phase 120° phase belt 2-poles (A,Z, X,B,Y,C)	M6,2P

4.2.2 Baseline Induction Machine

The winding factor of the state-of-art 3-phase pole changing windings, which necessarily require 120^o phase belt windings is poor. Pole changing operation is not possible with a 60^o phase belt winding due to the fundamental MMF cancellation. This is an inherent limitation of all 3-phase pole changing winding (including the Dahlander winding). A pole changing machine equipped with two separate windings for different pole numbers has poor torque density due to half the windings being idle with low slot utilisation coupled with high leakage inductance of the winding at the slot bottom [OSA96] [BOL02]. Due to this, the baseline machine chosen is the 3-phase 120^o phase belt machine that allows for pole changing operation. The proposed 6-phase machine has a 120^o phase belt but superior fundamental winding factor both in the high pole number and low pole number operation. The peak torque of the 6-phase 120^o phase belt machine in the low-speed region is identical to the 3-phase 60^o phase belt machine. However, the latter has inferior flux weakening performance compared to the 3-phase 120^o phase belt machine. The connections of the baseline 3-phase 120^o phase belt winding machine configuration (M3, 4P and M3, 2P) and the proposed 6-phase configuration of the machine (M6, 4P and M6, 2P) can be obtained by considering the individual coils of the machine. From Fig. 4.3, it is seen that the coils A and B span a 120^o phase belt for a 3-phase 4-pole configuration and similarly X and Y and C and Z for the other 3 phases span a 120^o phase belt. The spatial separation between the three phases remains at 120^o for both 4-pole and 2-pole operations as shown in Fig. 4.4(a) and Fig. 4.4(b) respectively. To change the number of poles from 4 to 2, the direction of current in coils A2, B2, X2, Y2, C2 and Z2 are reversed, as shown by the dot convention in TABLE 4.4. As observed in Fig. 4.4(b), the phase sequence of the M3, 2P machine has to be reversed in addition to the current reversal for maintaining the same direction of rotation after pole changing. The number of series turns per phase can be calculated as shown in (4.5).

$$W = \frac{n_s p q}{a} \tag{4.5}$$

where W, n_s, p, q and a are the number of series turns per phase, the number of conductors per slot, SPP and the number of parallel paths. To ensure that, for a given DC bus voltage, the rated current is constant across all the machines, 2 parallel paths are chosen for the M34P and M32P machines. For a double layer winding with 34 turns per coil, the number of series turns per phase is W=272. The vector potential and flux densities plots for the M3, 4P and M3, 2P machines at rated current and 800 rpm are shown in Fig. 4.5(a) and Fig. 4.5(b), respectively. A lower pole number

machine requires a larger yoke section for a given air-gap flux density and as a result, as seen in Fig. 4.5(a) and Fig. 4.5(b), the yoke section of the 2-pole excited machine has a higher flux density while the teeth of the 4-pole excited machine see higher flux density.

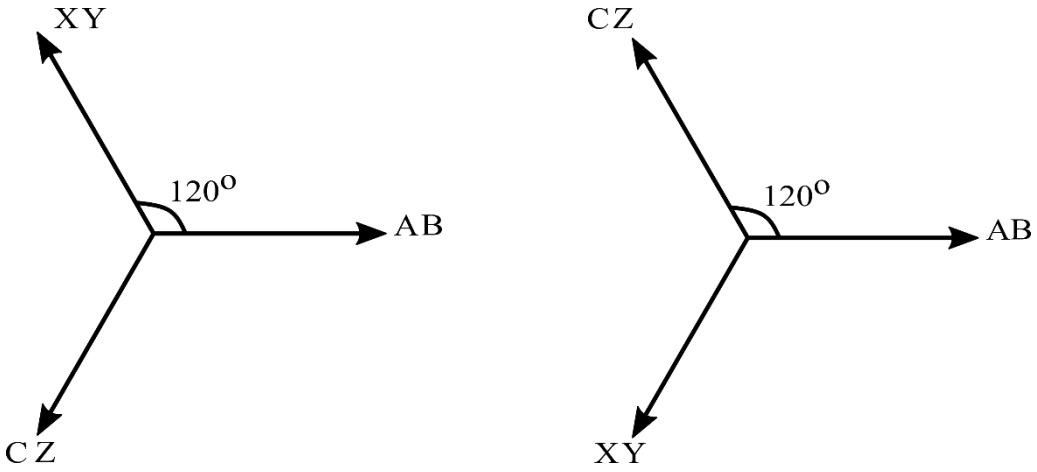

(a) M3, 4P (b) M3, 2P

Fig. 4.4 Phasor diagram of winding configurations.

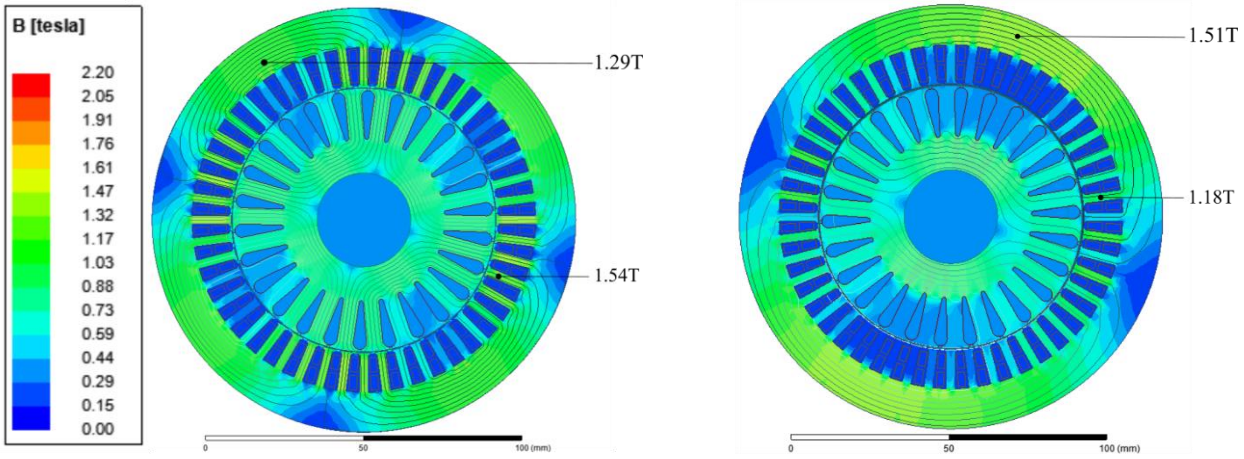

(a) 4-pole operation (b) 2-pole operation

Fig. 4.5 Flux plot of 3-phase 120° pole-changing winding configuration.

4.2.3 Six-Phase Induction Machine

The winding configurations of phase A of the proposed 6-phase120° phase belt pole-changing winding machine are shown as M64P and M62P in TABLE 4.5. For the 4-pole operation, the winding sets A, B, C and X, Y, Z are connected as two 3-phase machines shifted by 60° as seen from the phasor diagram of Fig. 4.6(a). The current in the coils A1 and A2 are in the same direction for the

4-pole operation and the direction of the current is reversed in coil A2, B2, C2, X2, Y2 and Z2. From the coil connections it can be seen there is only 1 parallel path for the 6-phase operation. This ensures that per phase impedance is increased relative to the 3-phase configuration ensuring that the total DC bus current at the rated DC bus voltage remains constant across the machine configurations. The vector potential and flux density plots for the 6-phase 4-pole and 2-pole, 120^o phase belt winding machine configurations at rated current and 800rpm are shown in Fig. 4.7. The flux-density maps are shown at 800rpm where all the four machine configurations are at peak torque capability with rated current and excited with constant flux.

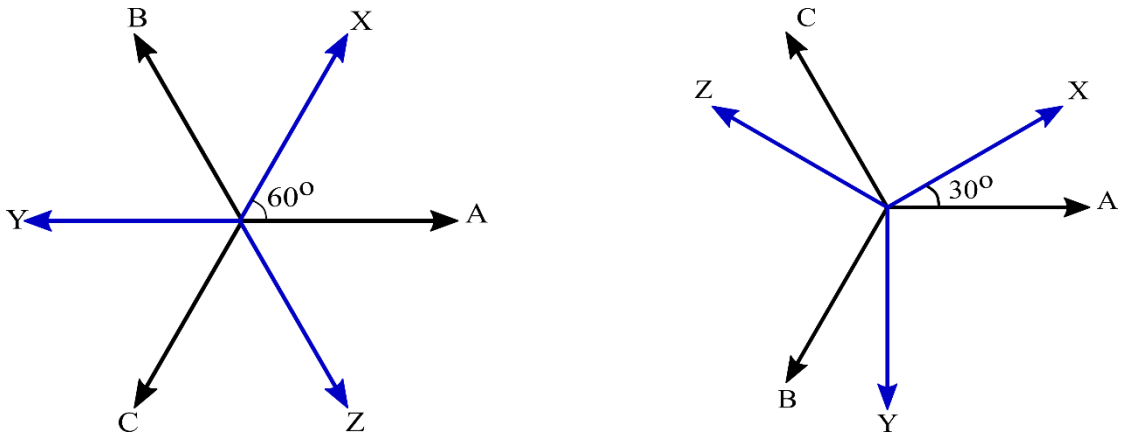

(a) M6, 4P (b) M6, 2P.

Fig. 4.6 Phasor diagram of winding configurations.

When the direction of current is reversed to change the winding to 2-pole operation, the spatial separation between the two 3-phase sets reduces to 30^o as seen in Fig. 4.6(b).

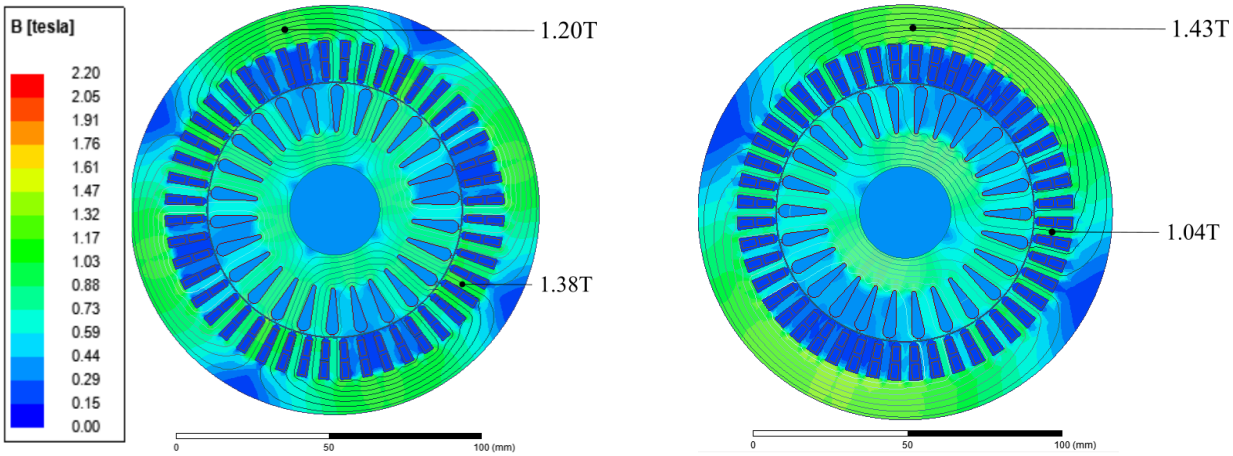

(a) 4-pole (b) 2-pole

Fig. 4.7 Flux plot of 6-phase 120° pole-changing winding configurations with 4-pole and 2-pole operation.

However, the relative flux density relationships remain the same across speeds. Similar levels of saturation differences from the 4-pole to the 2-pole operation are seen in the flux density maps of the 6-phase machine as seen previously in the flux maps of the 3-phase machine. The air-gap flux density and the associated harmonic spectra for the four different machine configurations are shown in Fig. 4.8, obtained from FEA.

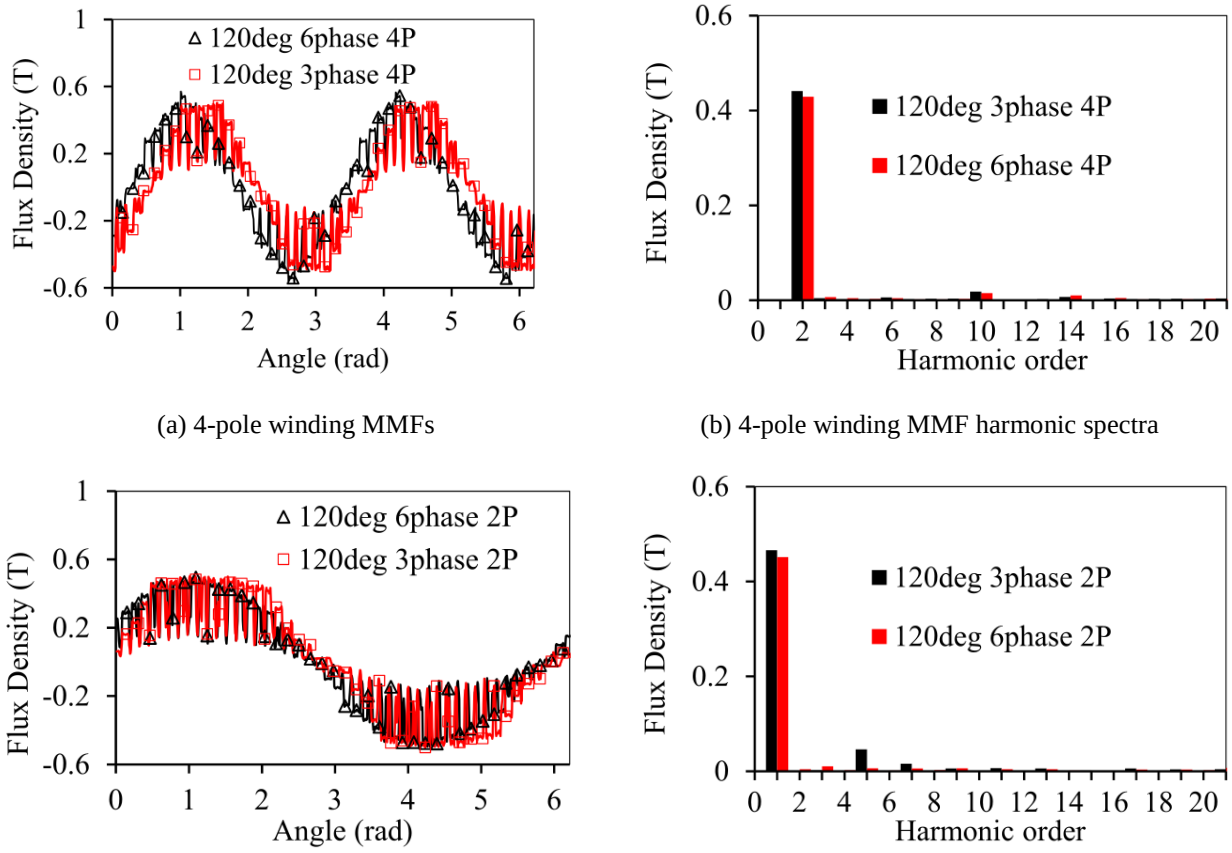

(a) 4-pole winding MMFs

(b) 4-pole winding MMF harmonic spectra

(c) 2-pole winding MMFs

(d) 2-pole winding MMF harmonic spectra

Fig. 4.8 Air-gap flux density plot of 120° phase belt 6-phase and 3-phase windings.

4.3 Simulated Performance Comparison of Pole-changing Winding Configurations

The performance capability envelope curves are determined for the three-phase and six-phase induction machine pole configurations by supplying the machine with peak rated current at different speeds.

4.3.1 Performance Capability Curves

Four different induction machine configurations are simulated and the torque-speed characteristics and performance maps are determined using a combination of analytical and FEA methods [GUA14]. The simulation results that compare the torque-speed envelope of the machines when supplied by the same rated line current of 4Arms are shown in Fig. 4.9. It can be seen from Fig. 4.9(a) that the peak torque achievable for the M6, 4P machine is 15% higher than the peak torque due to the higher winding factor for this winding configuration. In the flux weakening region, the 2-pole configurations have a wider speed operation as seen from Fig. 4.9(b). The M6, 2P has a slightly higher power capability in the flux weakening region due to the winding factor being higher than the M3, 2P machine.

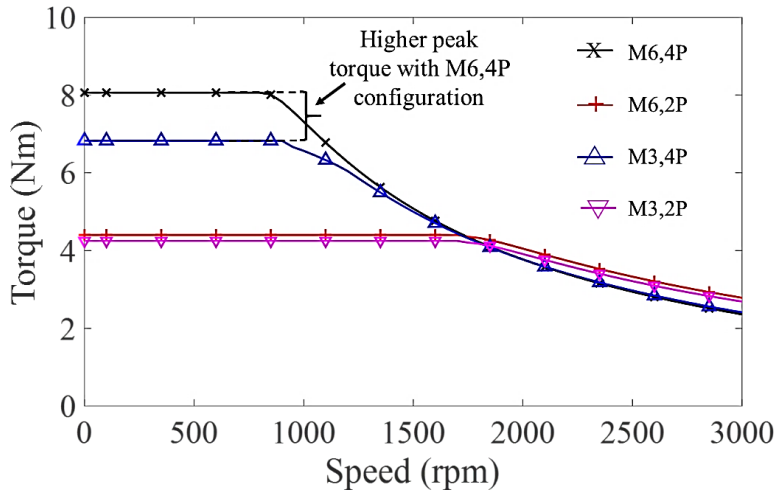

(a) Torque-speed

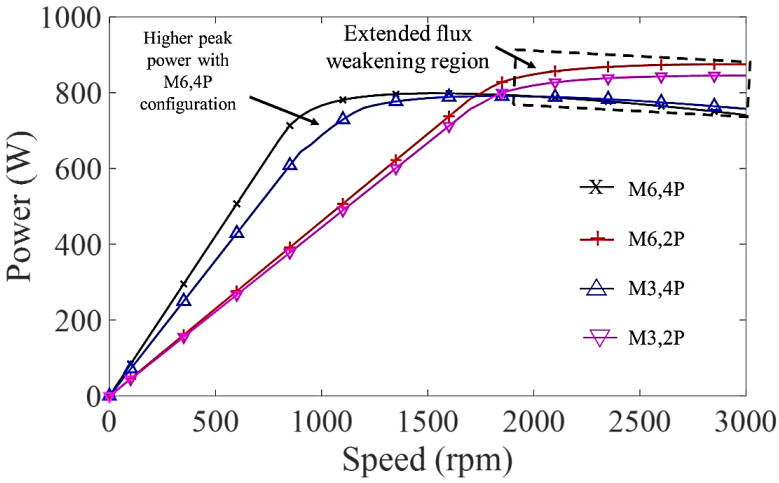

(b) power-speed curves

Fig. 4.9 Torque/power capability curves of induction machine configurations

The power factor curves of the induction machine configurations are shown in Fig. 4.10. The 4-pole induction machine power factor is higher than the two-pole configurations at low speed due

to the higher magnetising current of the 2 pole machines. As the speed increases into the flux weakening regions, the power factor of the 2-pole architecture increases over the 4-pole machines due to the lower drop in the leakage path since the frequency of operation of the 2-pole winding for a given speed is half of that of the 4-pole operation.

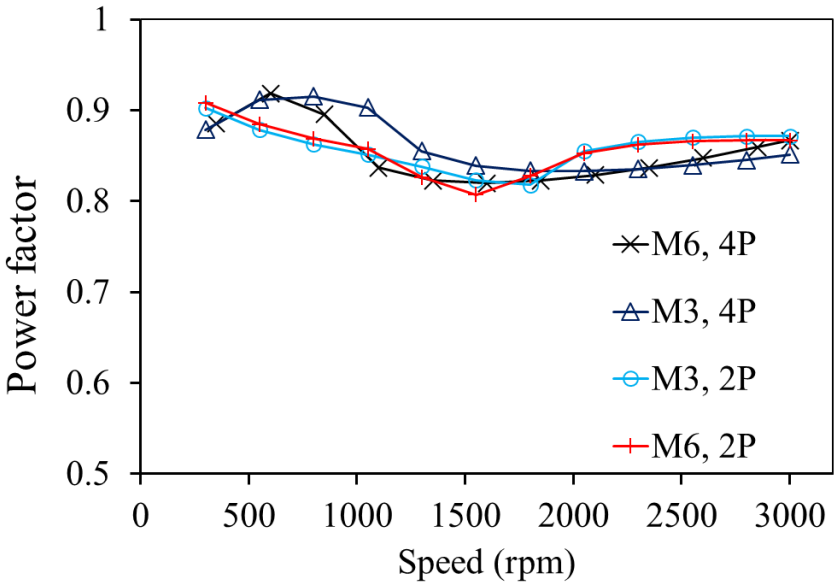

Fig. 4.10 Power factor curves of induction machine configurations.

4.3.2 Torque Ripple

The steady-state torques of the four machine configurations are shown in Fig. 4.11. It can be seen that the torque ripple of the 2-pole operation is significantly lower than that of the 4-pole operation.

The torque ripple of the M3, 4P, M6, 4P and the M3, 4P, M6, 4P machines are comparable as expected from the results of the space harmonic index factor in TABLE 4.4. The torque ripple of the baseline M3, 4P machine and the proposed 6-phase M6, 4P machine are similar since space harmonic index factors are almost equal. The average torque of the M6, 2P machine is slightly higher than the average torque of the M3, 2P machine due to the higher winding factor of the six-phase machine as seen from TABLE 4.2. The lower torque ripple of the 2-pole winding machines compared to the 4-pole winding machines can be explained using an analytical expression for torque ripple assuming infinitely permeable steel and the electrical loading due to the windings at the slot openings. The electromagnetic torque is represented as the integral of the Lorentz's force density over the air-gap surface multiplied by the radius of the rotor as shown in (4.6). D, L_{stk}, B_g and K are the rotor diameter, the air-gap flux density and the electric loading due to the stator winding.

$$\tau = -\frac{D^2 L_{stk}}{4} \sum_{v} \sum_{\xi} \int_0^{2\pi} B_{gv}(v) K_{\xi}(v) dv \tag{4.6}$$

The air-gap flux density is a result of the stator and rotor excitation and can be represented as an integral of the product of the total air-gap MMF and permeability. With the stator and rotor slot dimensions remaining the same for all the four machine configurations, the air-gap permeance for the torque ripple analysis is assumed constant. The MMF due to the stator or the rotor is a function of the winding factor, the current carried by the conductors and number of turns as shown in (4.7)

$$F_{s,r}\,(v) = \sum_{v=1}^{\infty} -\frac{mK_{wv}NI}{2\pi} \cos(v\theta - \omega t) \tag{4.7}$$

where v, K_w, θ, and ω are the harmonic order, the winding factor, the spatial angle over the air-gap, the excitation frequency, respectively, of a winding with N turns and carrying current I.

From (4.7) the air-gap flux density for an air-gap of g can be defined as shown in (4.8) and the stator electric loading is defined in (4.9).

$$B_g(v) = \frac{\mu_o}{g} \sum_{v=1}^{\infty} F_s(v) + F_r(v) \tag{4.8}$$

$$K(v) = \frac{mK_{wv}NI}{\pi D} \sin(v\theta - \omega t) \tag{4.9}$$

From (4.6)-(4.9), the space-harmonics interaction index is defined in (4.10) as:

$$I_{shi} = \frac{\sum_{v=1}^{\infty} \frac{K_{wsv} K_{wrv}}{v}}{\frac{K_{wsp} K_{wrp}}{p}} \tag{4.10}$$

This index is calculated for the four different configurations of the machines. Since the rotor is a squirrel cage in all the machine configurations, the winding factor for the rotor is assumed to be unity for all harmonics in the absence of skew [BOL02]. From the results shown in TABLE 4.6, the space harmonics index factors for the 2-pole configurations are almost half that of the 4-pole configurations and the torque ripple values and waveforms reflect this behaviour as shown in Fig. 4.11. Space harmonic index factors are a function of the winding factor of the harmonics. The M3, 2P baseline machine has lower harmonics winding factors as seen from TABLE 4.2, TABLE 4.3 and

TABLE 4.4 compared to the M6, 2P machine. This is reflected in the space harmonic index factor as well as the torque ripple waveform in Fig. 4.11. However, due to the higher fundamental winding factor of the M6, 4P machine, the average torque is higher than the M3, 4P machine. The rotor of the prototype machine used for experimental validation is from an off the shelf induction machine whose characteristics and dimensions were available. The off-the-shelf rotor has no skew resulting in significant torque ripple as seen from Fig. 4.11. The relative decrease of torque ripple between the 4-pole and 2-pole operation would remain the same even with optimal skew. The loss maps of the four machine configurations are shown in Fig. 4.12(a), Fig. 4.12(b), Fig. 4.12(c) and Fig. 4.12(d). It can be seen that the stator losses of the M3, 4P machine are similar to the losses of the M6, 4P machine for the same peak current but the peak torque is higher for the latter. The iron loss distributions of the machine topologies are shown in Fig. 4.13. The 3-phase 120^o phase belt windings are seen to have slightly higher iron losses both in the 4-pole and 2-pole modes of operation. This is accounted for by the higher magnetising inductances in the 6-phase machine topologies due to higher winding factor resulting in the lower magnetising current and hence lower iron losses.

TABLE 4.6 SPACE HARMONIC INDEX FACTOR FOR DIFFERENT MACHINE CONFIGURATIONS

Machine Configuration	I_{sih}	Torque Ripple (%)
M3,4P	3.26	27.2
M3,2P	2.53	9.60
M6,4P	3.62	28.3
M6,2P	2.90	17.1

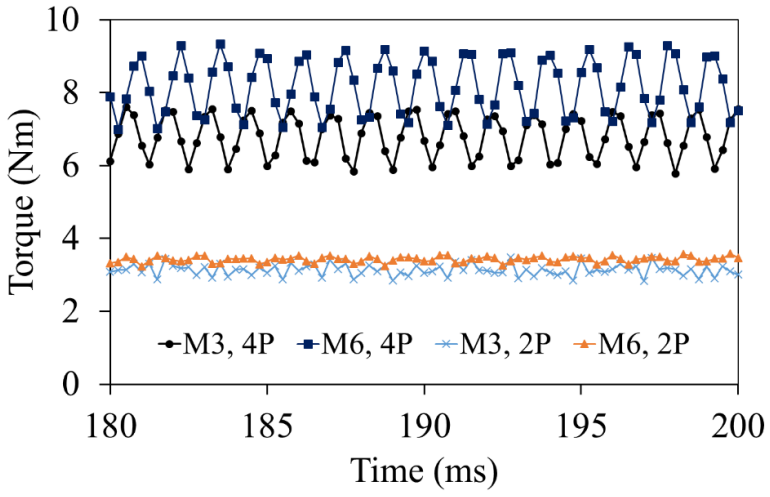

Fig. 4.11 FEA results of steady-state torque of M3, 4P, M3, 2P, M6, 4P, and M6, 2P machines at rated voltage and line current at 800rpm.

4.3.3 Losses and Efficiency Maps

The efficiency map is determined for different machine configurations using a series of transient FEA simulations as explained in 3.4. For every stator frequency in the constant torque region, the peak torque and losses at different currents are determined. The slip that maximises the torque at each speed and current combination is determined. This is repeated in the flux weakening region with the limit of the DC bus voltage used to determine the operating envelope. The simulated efficiency maps of the four machine configurations are shown in Fig. 4.14(a), Fig. 4.14(b), Fig. 4.14 (c) and Fig. 4.14(d). While the efficiency of the M3, 2P and the M6, 2P machines are similar, due to the increased fundamental winding factor, the efficiency of the M3, 4P is higher than the M6, 4P, as seen in Fig. 4.14(a) and Fig. 4.14 (c) respectively. The poorer efficiency of the 2-pole excited machines compared to the 4-pole counterparts can be explained by referring to the relative stator and rotor copper losses between the 4-pole and 2-pole excitations of Fig. 4.12 which show higher copper losses in the stator and rotor windings at similar speeds of operation. The corner speed is higher for the 2-pole operation resulting in higher current being drawn for the same power level causing higher losses in the stator and rotor conductors.

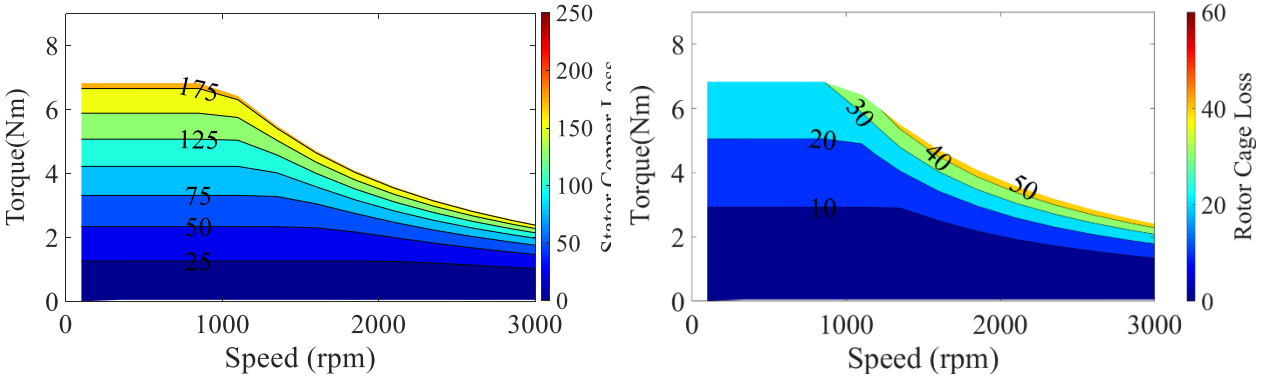

(a) M3, 4P

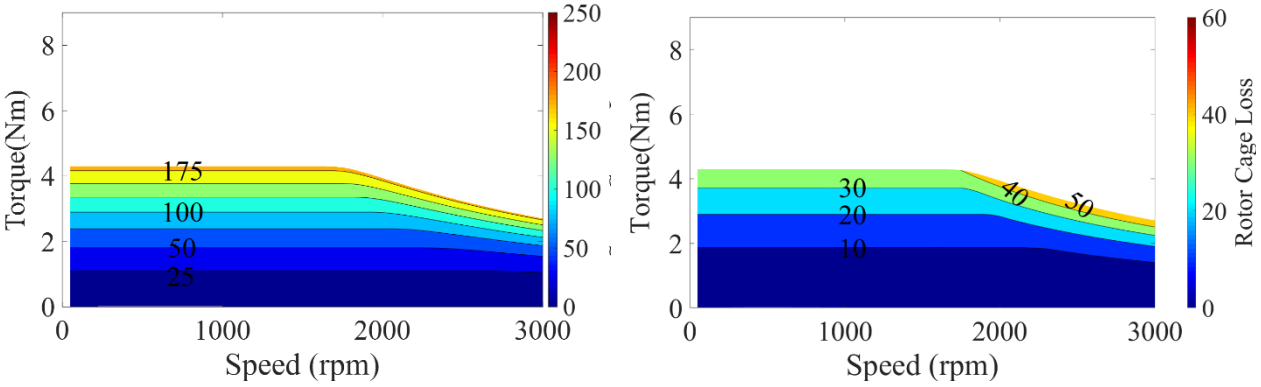

(b) M3, 2P

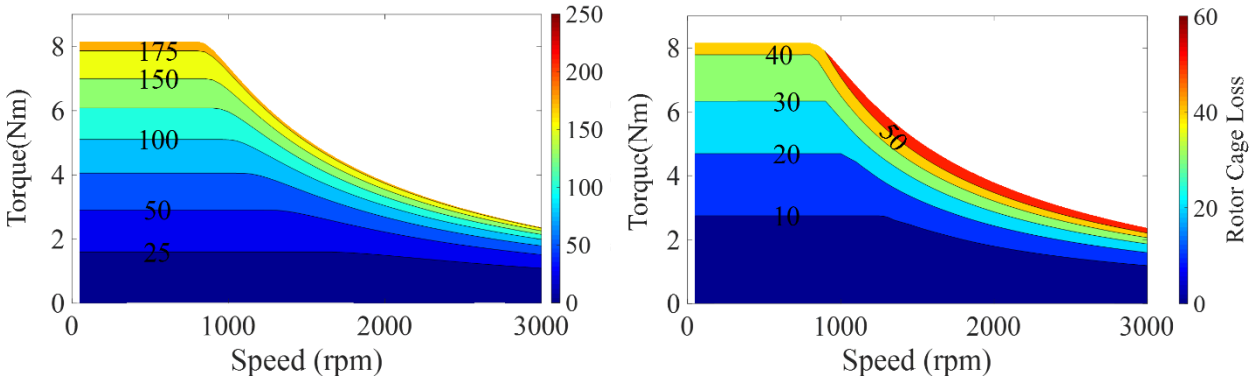

(c) M6, 4P

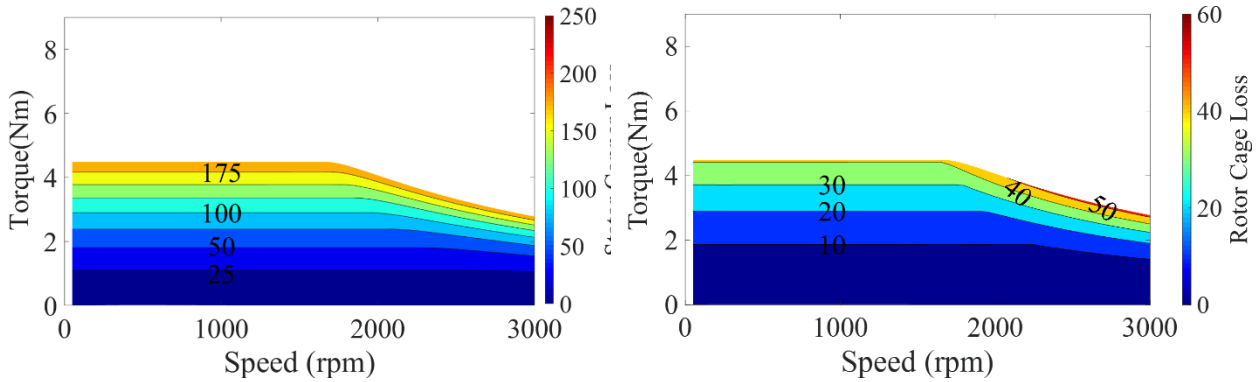

(d) M6, 2P

(I) Stator loss (II) Rotor cage loss

Fig. 4.12 Stator and rotor loss distribution maps of the pole-changing winding induction machine. (a) M3, 4P, (b) M3, 2P, (c) M6, 4P,(d) M6, 2P.

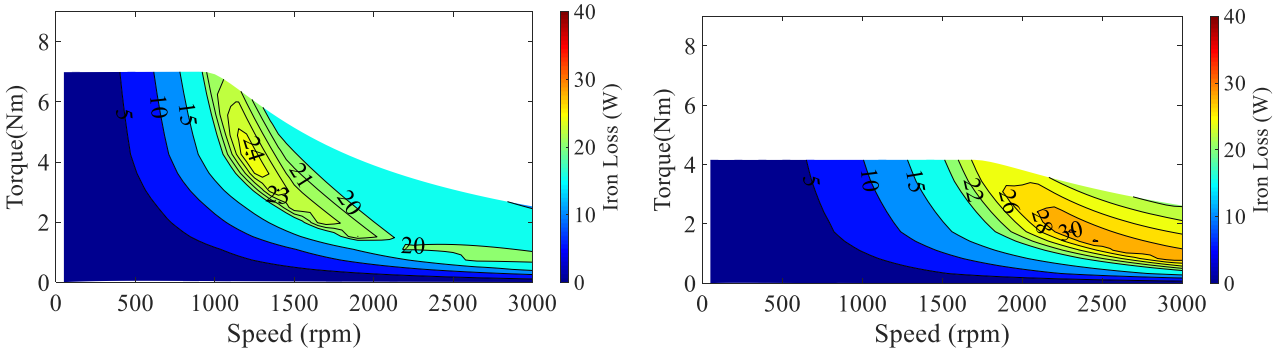

(a) M3, 4P (b) M3, 2P

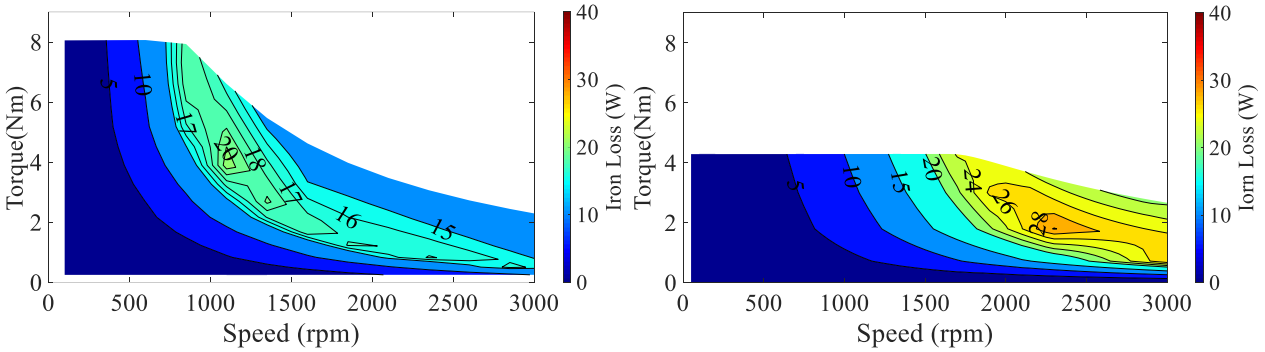

(c) M6, 4P (d) M6, 2P

Fig. 4.13 Iron loss distribution maps of the pole-changing winding induction machine.

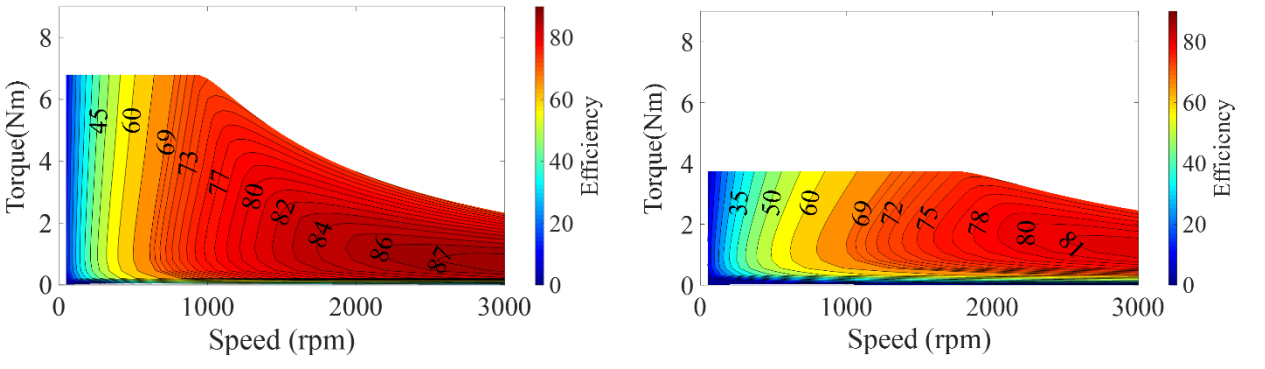

(a) M3, 4P (b) M3, 2P

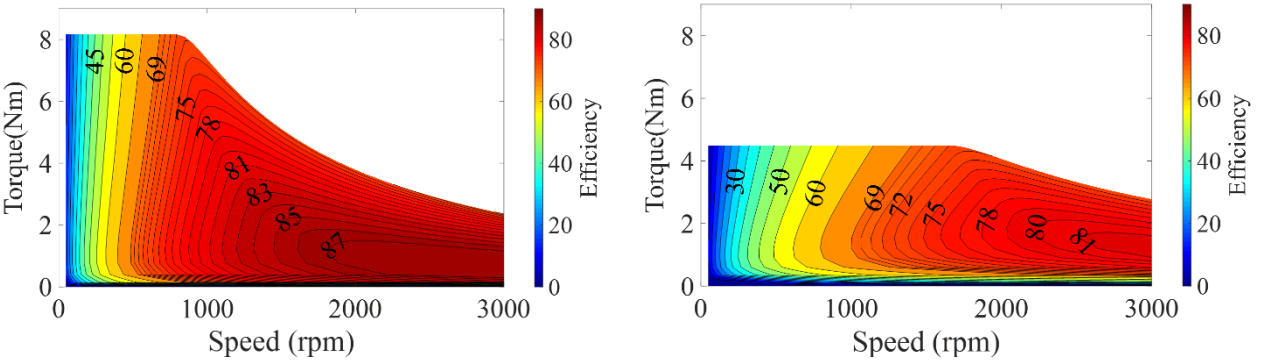

(c) M6, 4P (d) M6, 2P

Fig. 4.14 Efficiency maps of the pole-changing winding induction machine.

4.4 Experimental Results and Comparison with Predicted Results

A dynamometer is used to test the prototype machine and measure torque capability and performance maps. The stator windings are arranged in the four different configurations shown in TABLE 4.5 and supplied with appropriate excitation from a voltage source inverter. The inverter is controlled using an indirect rotor field-oriented control with the rotor position measured using an

encoder mounted at the non-load end of the prototype machine shaft. The field-oriented control algorithm and data acquisition are performed on a dSPACE 1006 controller. The experimental layout is shown in Fig. 4.15. The torque capability at each speed is determined using the Maximum torque per ampere (MTPA) control. The model of an induction machine under rotor field orientation is obtained by aligning the rotor flux along the d-axis resulting in the zero q-axis rotor flux. The equations for rotor flux, torque and slip as functions of machine parameters and –axis and q-axis currents are shown in (4.11)-(4.15).

$$p\psi_{dr}^{e} + r_r i_{dr}^{e} = 0 \tag{4.11}$$

$$L_m i_{ds}^{e} + L_r i_{dr}^{e} = \psi_{dr}^{e} \tag{4.12}$$

$$L_m i_{qs}^{e} + L_r i_{qr}^{e} = \psi_{qr}^{e} = 0 \tag{4.13}$$

$$\omega_s = \frac{\frac{L_m}{\tau_r} i_{qs}^{e}}{\psi_{dr}^{e}} \tag{4.14}$$

$$T_e = \frac{3}{2}\frac{P}{2}\frac{L_m^2}{L_r}\, i_{ds}^{e} i_{qs}^{e} \tag{4.15}$$

where $\psi_{dr}^{e}, \psi_{qr}^{e}, i_{dr}^{e}, i_{qr}^{e}, i_{ds}^{e}, i_{qs}^{e}, L_m, L_r, r_r, \tau_r$ and P are the rotor d-axis, q-axis flux, rotor d-axis, q-axis currents, stator d-axis, q-axis currents in the rotating reference frame, magnetizing inductance, referred rotor self-inductance, referred rotor resistance, rotor time constant and the number of poles respectively. The inverter DC bus and the current limit (I_s) of the drive and motor set limits on the torque production in steady-state at different speeds. The maximum torque per ampere with a limit on the stator current is found by the optimal split of the d and q-axis currents at a particular speed subject to the constraints in (4.16) and (4.17)

$$i_{ds}^{e\ 2} + i_{qs}^{e\ 2} = I_{smax}^2 \tag{4.16}$$

$$(\omega_e L_s i_{ds}^{e})^2 + \left(\omega_e L_s^t i_{qs}^{e}\right)^2 \leq V_{smax}^2 \tag{4.17}$$

where $I_{smax}, \omega_e, L_s, L_s^t$ and V_{smax} are the stator current limit, synchronous frequency, stator self-inductance, stator transient inductance and maximum allowable voltage limit, respectively. For the unsaturated case where the magnetizing inductance is constant, the optimal split of q-axis and d-axis currents is $0.707 I_{smax.}$ However, due to the non-linear relationship between the magnetizing inductance and current, as the machine is increasingly saturated the ratio of q-axis to d-axis current

increases. The current and voltage limits in (4.16) and (4.17) describe a circle and ellipses of frequency-dependent radii as shown in Fig. 4.16. As the speed increases the region of operation narrows as shown in the shaded regions of Fig. 4.16 due to the limit imposed by the DC bus [KIM93][WAL94].

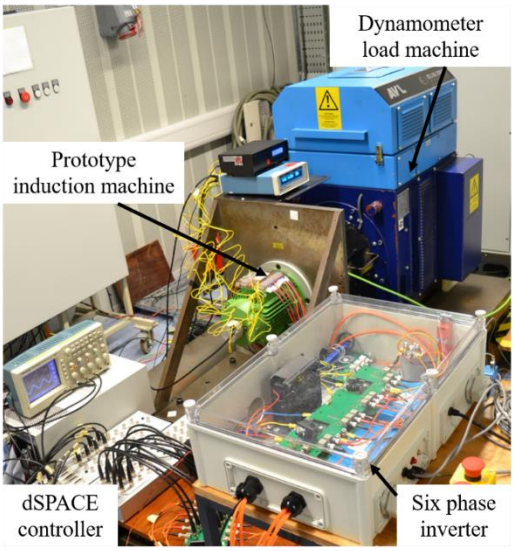

Fig. 4.15 Experimental setup showing prototype induction machine coupled to a dynamometer for performance measurement.

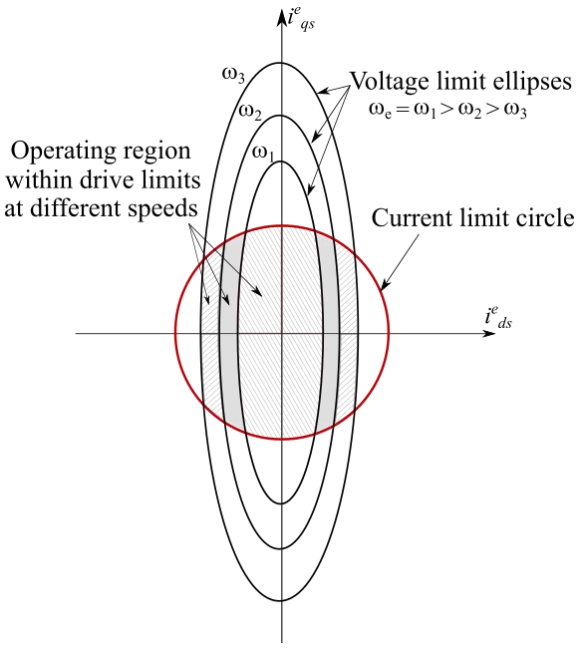

Fig. 4.16 Voltage and current-limit envelopes for inverter fed induction motor control.

To determine the MTPA point within these limits in the test, the dynamometer speed is fixed and rotor field orientation is achieved by using the rotor position from the encoder and calculated using the parameters of the machine. At the fixed speed, the peak line current per phase is fixed and the q-axis current is varied to determine the value at which the torque is maximized. This is the

MTPA point corresponding to that speed. This process is repeated across a range of speeds and currents to form a map of torque capability. For each of these points, the input power, shaft power and efficiency are measured using a Yokogawa WT3200 power analyser. An illustration of the MTPA curves at a single speed is shown in Fig. 4.17 for the M3, 4P machine for current varying from 2A to 4A. With I_s=4A the influence of saturation is much more pronounced due to which the maximum torque point is more apparent than with the case of I_s=2A.

4.4.1 Torque Capability

The comparison of the experimental results and the finite element analysis is shown in Fig. 4.18, Fig. 4.19, Fig. 4.20 and Fig. 4.21for the M3, 4P, M3, 2P, M6, 4P and M6. 2P machines, respectively.

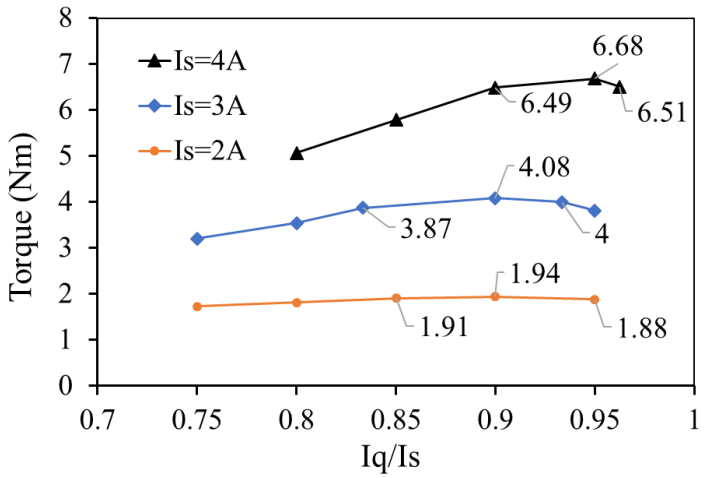

Fig. 4.17 Test results showing the variation of torque with increasing q-axis-current to stator current ratio of a 3-phase 4-pole 120o phase belt connection induction machine.

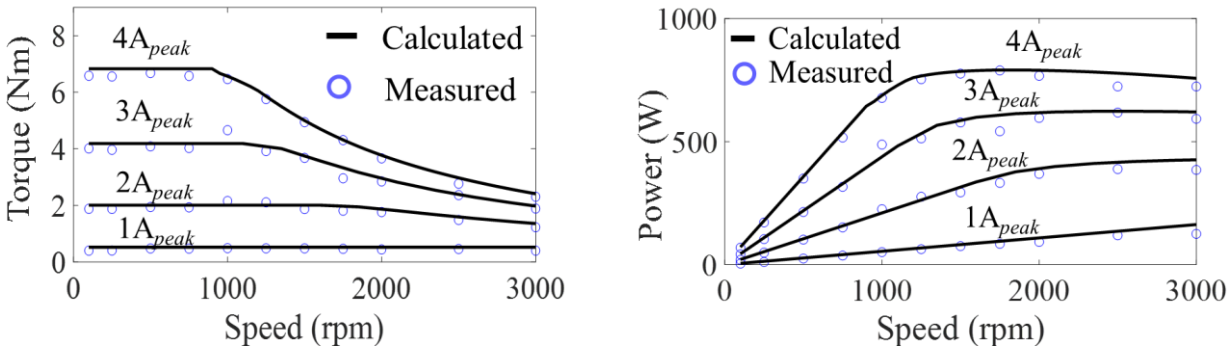

(a) Torque

(b) Power

Fig. 4.18 Measured and FE predicted torque/power-speed curves of a 3-phase 4-pole 120^o phase belt connection induction machine.

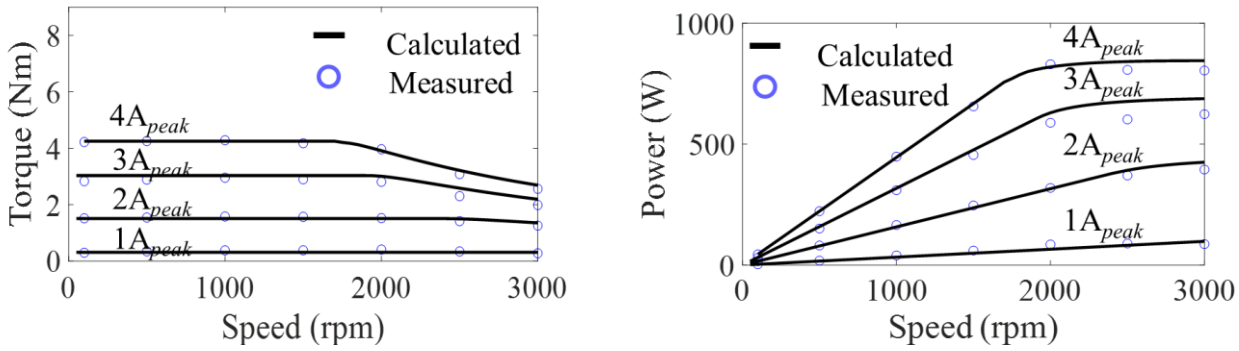

(a) Torque (b) Power

Fig. 4.19 Measured and FE predicted torque/power curves of a 3-phase 2-pole 120º phase belt connection induction machine.

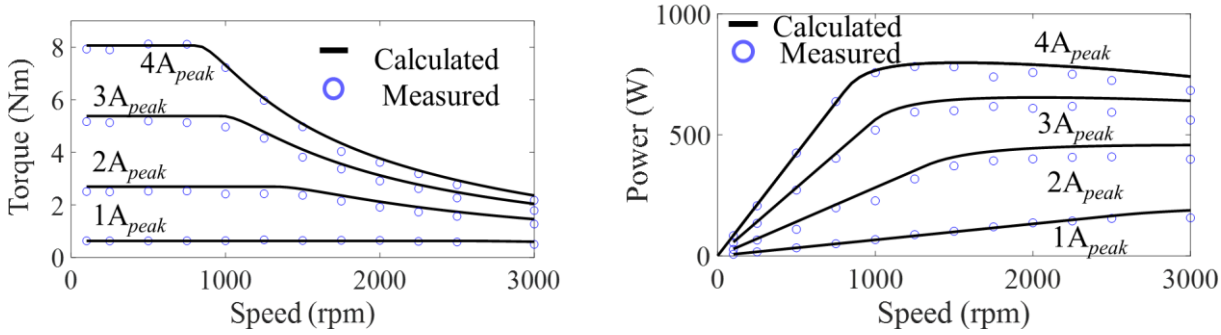

(a) Torque (b) Power

Fig. 4.20 Measured and FE predicted torque/power curves of a 6-phase 4-pole 120º phase belt connection induction machine.

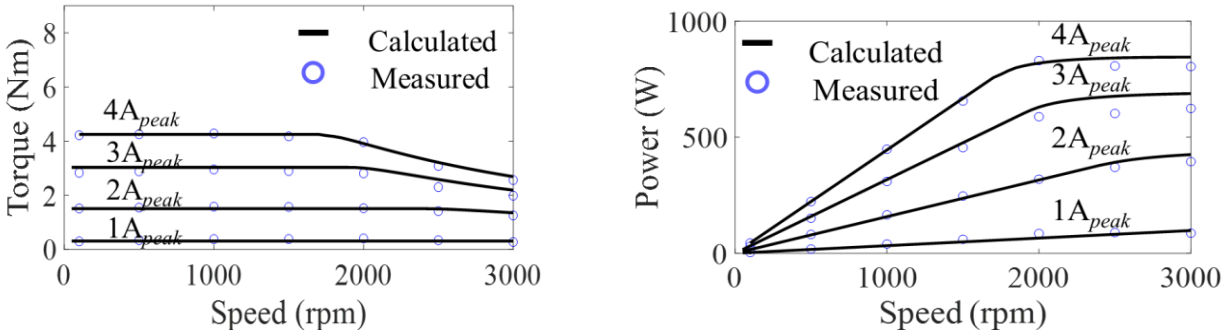

(a) Torque (b) Power

Fig. 4.21 Measured and FE predicted torque/power curves of a 6-phase 2-pole 120º phase belt connection induction machine.

The experimental and simulation results are in good agreement with an average error of less than 8% over the measured speed range. The torque at rated current of the M6, 4P and M3, 4P are

8.1Nm and 6.7Nm, respectively, which are in proportion to the respective winding factors of 0.957 and 0.83.

4.4.2 Efficiency Maps

The efficiency maps of the four different configurations are measured and calculated over the entire speed range. The results are shown for the M3, 4P, M3, 2P, M6, 4P and M6. 2P machines in Fig. 4.22, Fig. 4.23, Fig. 4.24 and Fig. 4.25, respectively.

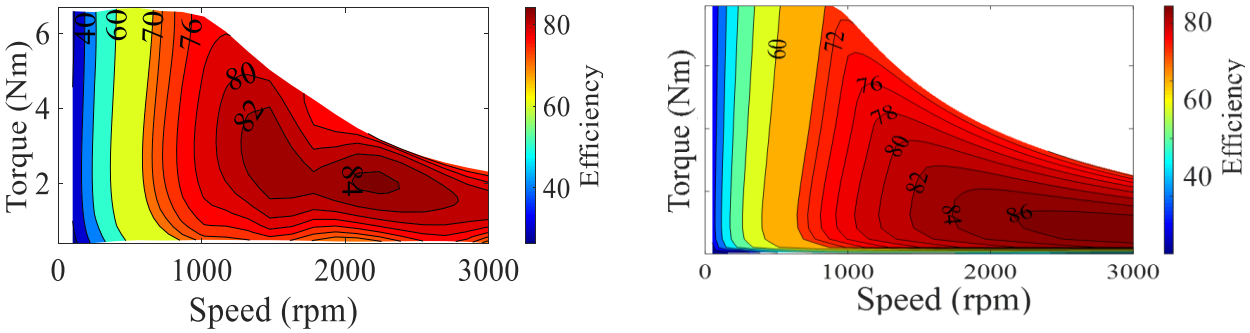

(a) Measured (b) Calculated

Fig. 4.22 Efficiency map of 3-phase 4-pole 120º phase belt connection induction machines.

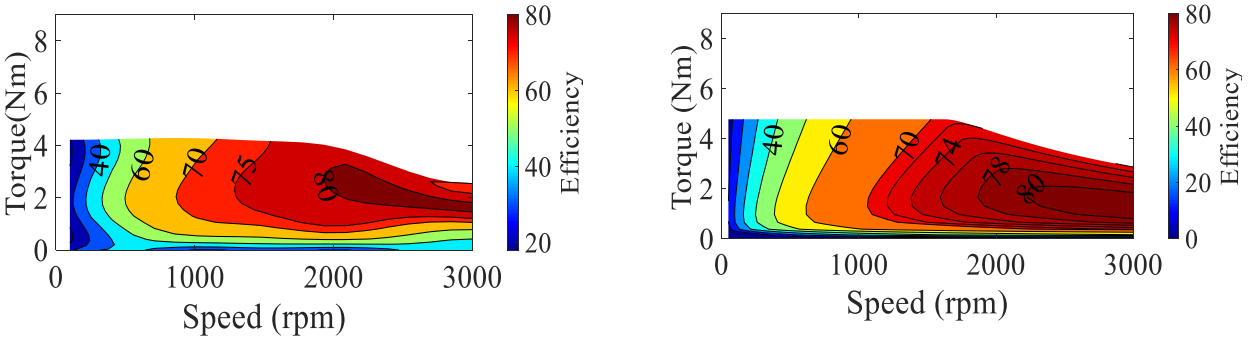

(a) Measured (b) Calculated

Fig. 4.23 Efficiency map of 3-phase 2-pole 120º phase belt connection induction machines.

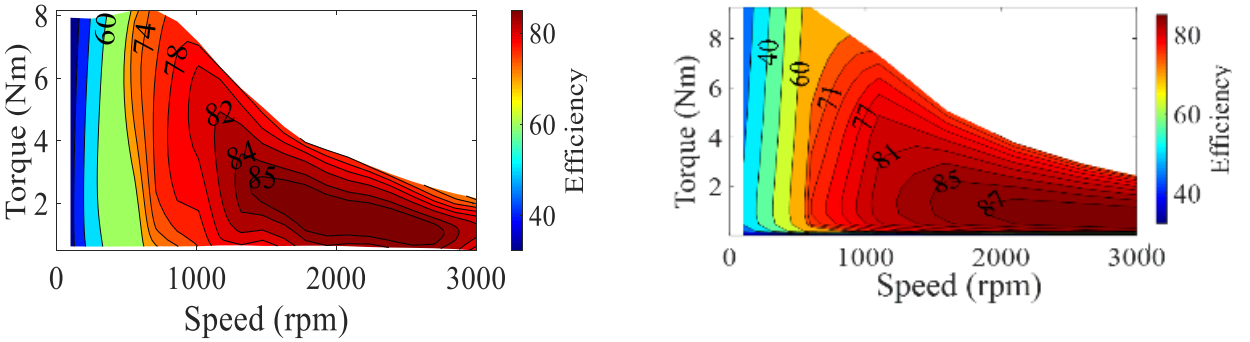

(a) Measured (b) Calculated

Fig. 4.24 Efficiency map of 6-phase 4-pole 120º phase belt connection induction machines.

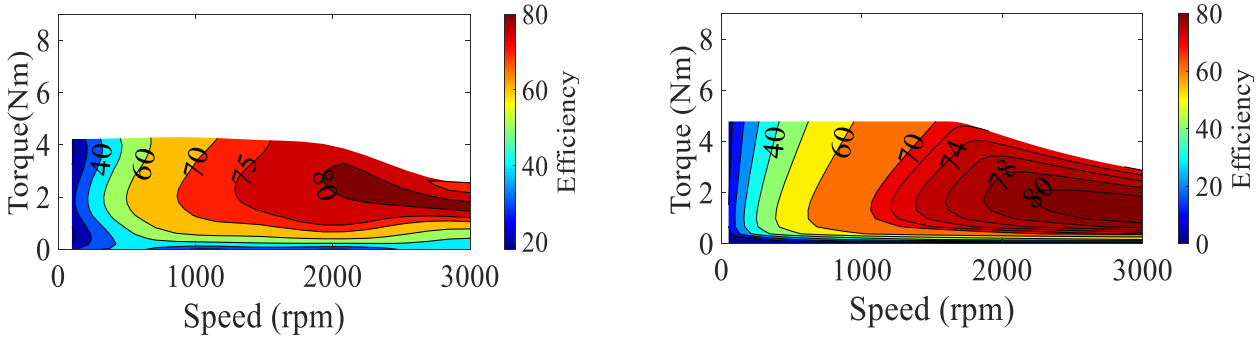

(a) Measured (b) Calculated

Fig. 4.25 Efficiency map of 6-phase 2-pole 120º phase belt connection induction machines.

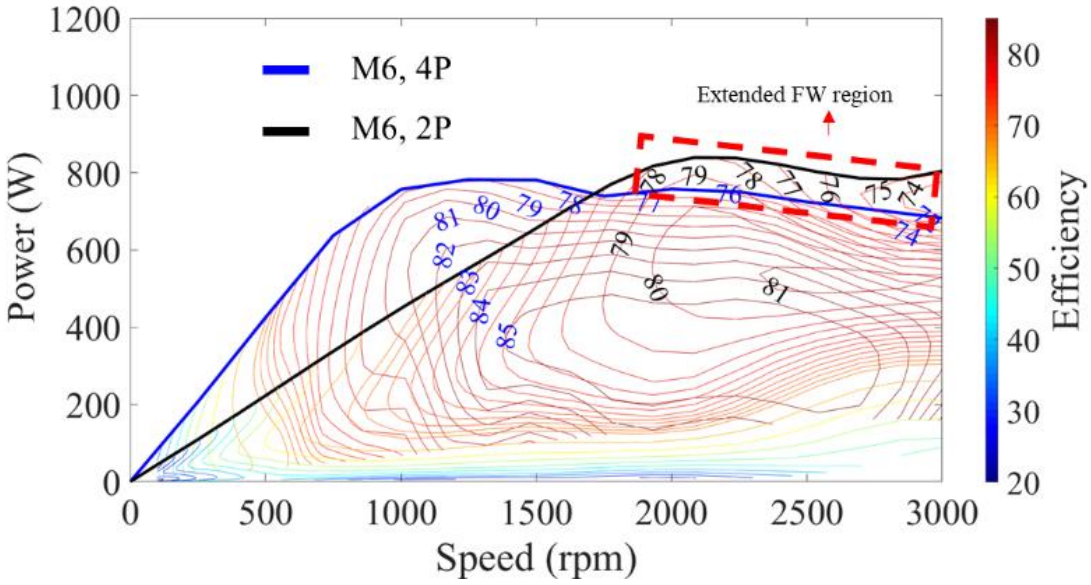

Fig. 4.26 Measured power vs speed curve with constant efficiency contours showing extended flux weakening region of operation for 3-phase 120o phase belt 4-pole and 2-pole operation.

The efficiency of the M3, 4P machine is lower than the efficiency of the M6, 4P due to the higher winding factor of the latter as seen from Fig. 4.22(a) and Fig. 4.23(a). The efficiency of the M3, 4P machine across the speed and at low torque is seen to be lower than that of the M3, 2P machine. This is due to the higher corner speed of the machine resulting in higher iron losses over a larger speed range thus reducing the efficiency for similar speed operations. The benefits of improved power capability and efficiency with the pole-changing machine can be seen from Fig. 4.26 where the experimentally measured power-speed characteristics with constant efficiency contours are plotted for the M6, 4P and M6, 2P machines. It can be observed that the region in which the flux weakening region of operation is extended by using the 2-pole configuration of operation, the achievable efficiency is higher than the efficiency achievable by the 4-pole configuration of operation.

4.5 Conclusions

The limitation of poor torque density of conventional two-speed induction machines and the poor winding factor, mechanical contactors of a Dahlander winding and the reduced winding factor of the 3-phase 120^o phase belt winding can be overcome by utilising the proposed 6-phase 120^o phase belt winding. The performance of the proposed 6-phase pole-changing winding induction machine with high fundamental winding factor is discussed which results in a 15% improvement in peak torque while retaining the ability to extend the flux-weakening region by electronically changing the number of poles resulting in a 23% increase in power generation capability at higher speeds. While a larger number of inverter legs and sensors are required for performing the pole-changing operation of the 6-phase machine, with the VA rating of the inverter remaining the same and for a given DC bus voltage, the current rating of the inverter being reduced, the trade-off of increased flux weakening region, higher power generation and efficiency are satisfactory especially for higher power ratings. The 6-phase pole-changing induction machine has almost identical performance with the lower number of poles when compared to the 3-phase pole-changing induction machine. The efficiency of the 6-phase induction machine has a higher efficiency region compared to the 3-phase 4-pole operation due to the higher fundamental winding factor. The efficiency of the 6-phase induction machine in the achievable extended flux weakening region of operation with the lower pole number is similar to the efficiency of the 3-phase induction machine.

Chapter 5

Six-Phase Pole-changing Winding Induction Machine with Third Harmonic Injection

A well-established phenomenon of multiphase machines is the ability to inject higher-order harmonics for enhanced torque production [LEV07]. For an odd phase number *k*, all the odd harmonics between 1 and *k* can be utilised to couple with the MMF harmonics to produce useful average torque. While this is possible for all odd number of phases, the only possible way to leverage this phenomenon for enhanced torque production with an even number of phases is with a six-phase winding as shown in [LYR02]. Asymmetric six-phase machines are the most commonly analysed multiphase induction machines for high power applications. In the early days of the multiphase induction motor drives (when six-step VSIs were more common than PWM inverters) the choice of the asymmetric six-phase machine was driven by the need to eliminate the sixth harmonic of the torque ripple, caused by the fifth and seventh harmonics of the stator current [NEL74]. However, utilisation of PWM switching control for a six-phase VSI results in an asymmetric and symmetrical six-phase machine having identical performance [LEV07]. In this chapter, with a theoretical analysis of the three-phase winding, it is demonstrated that the 3rd harmonic currents only produce pulsating fields. This is extended to the symmetrical and asymmetric six-phase winding showing that while in the former winding, the 3rd harmonic currents cannot yield useful torque, in the latter case the 3rd harmonic currents can result in producing synchronously rotating magnetic field that can be employed to produce useful torque. Subsequently, continuing from Chapter 4, it is shown that in a six-phase pole changing winding, the higher pole number winding (in this case 4-pole) is a symmetrical six-phase winding whereas the lower pole number (2-pole) connection results in an asymmetric winding. Due to this, in the 2-pole operation, with the neutral points of the two three-phase sets that comprise the six-phase winding connected, the 3rd harmonic currents can be injected to improve torque capability within the voltage limit of the machine. An optimal 3rd harmonic current is determined and the machine torque and power capability curves are shown with such an operation. The simulation results are then experimentally validated in the final section of the chapter.

5.1 Enhanced Torque Capability of Six-Phase IM with 3rd Harmonic Injection

The phases of a symmetrical *m*-phase induction machine winding are displaced by $2\pi/m$ and the coils comprising these phases are uniformly distributed in slots in a manner that results in a

winding as sinusoidal as possible. The resulting MMF is a stepped waveform and can be represented as a Fourier series, components of which are called space harmonics [HEL77] [NET99]. The MMF of a single coil with a pitch of α_y is given by (5.1). Factor $0 < \beta \leq 1$ represents the extent of short pitching of the coil. I_a is the current carried by the coil and ζ, α and α_1 represent the coil group axis, the mechanical angle around the periphery and the slot pitch in electrical degrees. $\alpha_1 = 2\pi p/Q_1$ where p and N_s represent the number of pole pairs and the number of stator slots, respectively.

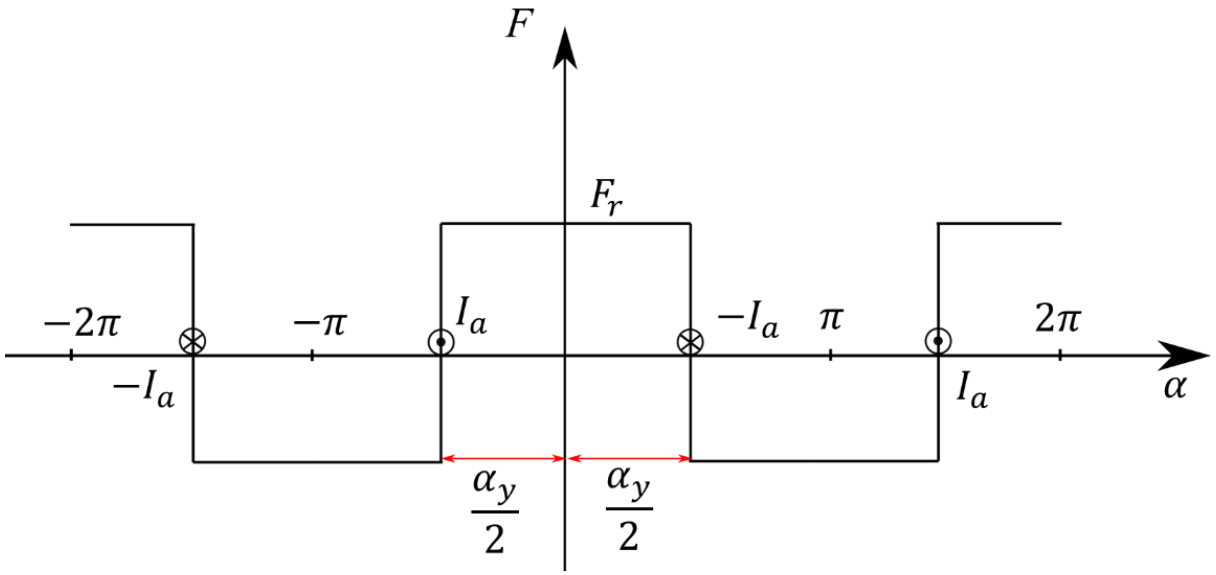

Fig. 5.1 Distribution of magnetic field intensity of a single turn.

$$F_x(\alpha) = \frac{2I}{\pi g} \sum_{\upsilon=1}^{\infty} \left[\frac{1}{\upsilon} \sin\left(\upsilon \frac{\alpha_y}{2}\right) \cos\left(\upsilon\left[\alpha - \left(\zeta + (x-1)\right)\alpha_1\right]\right) \right]; \alpha_y = \beta\pi \tag{5.1}$$

When $q = N_s/2pm$ of these coils comprising an m-phase winding are distributed in N_s slots, the field produced by these coils has been derived in (4.5) of Chapter 4 and is reproduced in (5.2).

$$F_{coil}(\alpha) = \frac{2qI}{\pi g} \sum_{\upsilon=1}^{\infty} \left[\frac{1}{\upsilon} \sin\left(\frac{\upsilon\alpha_y}{2}\right) \frac{\sin\left(\frac{q\alpha_1}{2}\upsilon\right)}{qsin\left(\frac{\alpha_1}{2}\upsilon\right)} \cos\left(\upsilon\left(\alpha - (q-1+2\zeta)\right)\frac{\alpha_1}{2}\right) \right] \tag{5.2}$$

The MMF for a symmetrical m-phase winding with integer q and N coil turns per slot, fed with a sinusoidal current of (5.3), is given in (5.4).

$$i_k = I_{km} \sin\left(\omega_1 t - \frac{k-1}{m} 2\pi\right) \tag{5.3}$$

$$F_{m-phase}(\alpha) = 4\sqrt{2}\frac{qNI}{\pi g}\sum_{v=1}^{\infty}\left[\begin{array}{c}\frac{1}{v}\sin\left(\frac{v\alpha_y}{2}\right)\sin\left(v\frac{mq\alpha_1}{2}\right)\frac{\sin\left(\frac{q\alpha_1}{2}v\right)}{qsin\left(\frac{\alpha_1}{2}v\right)} \\ \sum_{k=1}^{\infty}\left[\sin\left(v\frac{2\alpha+(1-k\,4q)\alpha_1}{2}\right)\sin\left(\omega_1 t-\frac{k-1}{m}2\pi\right)\right]\end{array}\right] \tag{5.4}$$

The equation for the *m*-phase MMF can be applied to the 3-phase case resulting in the MMF of (5.5) for the fundamental current being supplied to the winding.

$$F_{3-phase}(\alpha) = 4\sqrt{2}\frac{qNI}{\pi g}\sum_{v=1}^{\infty}\left[\begin{array}{l}\frac{1}{v}\sin\left(\frac{v\alpha_y}{2}\right)\sin\left(v\frac{3q\alpha_1}{2}\right)\frac{\sin\left(\frac{q\alpha_1}{2}v\right)}{qsin\left(\frac{\alpha_1}{2}v\right)}\times \\ \left[\begin{array}{c}\sin\left(v\frac{2\alpha+(1-4q)\alpha_1}{2}\right)\sin(\omega_1 t) \\ +\sin\left(v\frac{2\alpha+(1-8q)\alpha_1}{2}\right)\sin\left(\omega_1 t-\frac{2}{3}\pi\right) \\ +\sin\left(v\frac{2\alpha+(1-12q)\alpha_1}{2}\right)\sin\left(\omega_1 t-\frac{4}{3}\pi\right)\end{array}\right]\end{array}\right] \tag{5.5}$$

The fundamental component, the 3rd, 5th and 7th harmonic components of the three-phase MMF are given by (5.6), (5.7), (5.8) and (5.9), respectively.

$$F^1_{3-phase_1}(\alpha) = 4\sqrt{2}\frac{qNI}{\pi g}\sin\left(\frac{\alpha_y}{2}\right)\sin\left(\frac{3q\alpha_1}{2}\right)\frac{\sin\left(\frac{q\alpha_1}{2}\right)}{qsin\left(\frac{\alpha_1}{2}\right)}\left[\frac{3}{2}\cos\left(\alpha+\frac{(1-4q)}{2}\alpha_1-\omega_1 t\right)\right] \tag{5.6}$$

$$F^1_{3-phase_3}(\alpha) = 0 \tag{5.7}$$

$$F^1_{3-phase_5}(\alpha) = \frac{4}{5}\sqrt{2}\frac{qNI}{\pi g}\sin\left(\frac{5\alpha_y}{2}\right)\sin\left(\frac{15q\alpha_1}{2}\right)\frac{\sin\left(\frac{5q\alpha_1}{2}\right)}{qsin\left(\frac{5\alpha_1}{2}\right)}\left[\frac{3}{2}\cos\left(5\alpha+\frac{5(1-4q)}{2}\alpha_1+\omega_1 t\right)\right] \tag{5.8}$$

$$F^1_{3-phase_7}(\alpha) = \frac{4}{7}\sqrt{2}\frac{qNI}{\pi g}\sin\left(\frac{7\alpha_y}{2}\right)\sin\left(\frac{21q\alpha_1}{2}\right)\frac{\sin\left(\frac{7q\alpha_1}{2}\right)}{qsin\left(\frac{7\alpha_1}{2}\right)}\left[\frac{3}{2}\cos\left(7\alpha+\frac{7(1-4q)}{2}\alpha_1-\omega_1 t\right)\right] \tag{5.9}$$

While the fundamental and the 7th harmonic can generate rotating magnetic fields in the forward direction, the 5th harmonic results in a backwards rotating magnetic field. The forward rotating field of the 7th harmonic, however, can only produce useful torque from zero speed to 1/7th of the synchronous speed. The 5th harmonic field only produces braking torque. In a star connected

winding, if a neutral is provided for a 3rd harmonic current to flow, the MMF due to such a current being fed into the machine is given by (5.10).

$$F^{3}_{3-phase_3}(\alpha) = \frac{4}{3}\sqrt{2}\frac{qNI}{\pi g}\sin\left(\frac{3\alpha_y}{2}\right)\sin\left(\frac{9q\alpha_1}{2}\right)\frac{\sin\left(\frac{3q\alpha_1}{2}\right)}{qsin\left(\frac{3\alpha_1}{2}\right)}\left[3\sin\left(3\alpha+\frac{3(1-4q)}{2}\alpha_1\right)\sin(\omega_1 t)\right] \quad (5.10)$$

This MMF is not rotating but rather a pulsating MMF and produces pulsating torque which does not contribute to useful work. With a six-phase winding, two three-phase winding sets can be either arranged to have a 60° phase displacement between the winding sets making a symmetrical six-phase winding or an asymmetric six-phase winding with a 30° separation between the phase sets as shown in Fig. 5.2.

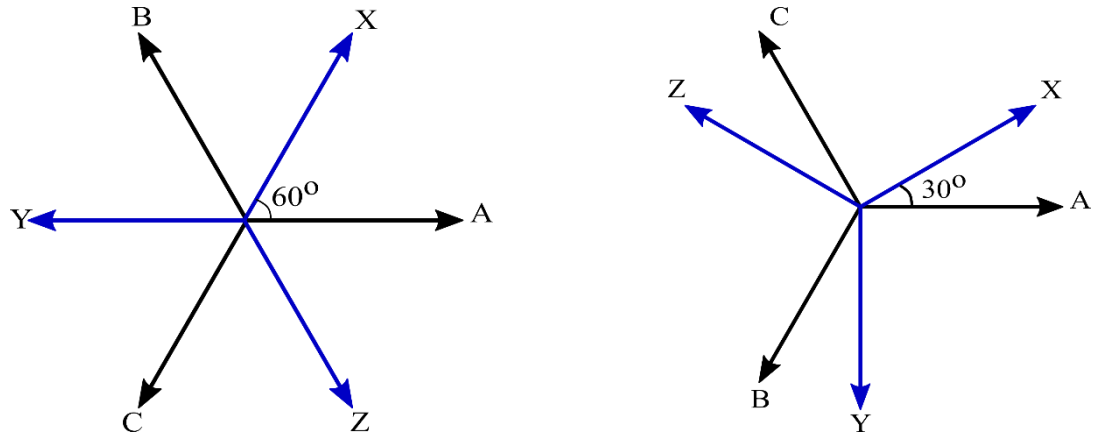

(a) Symmetrical winding (b) Asymmetric winding

Fig. 5.2 Phasor diagram of six-phase winding configurations.

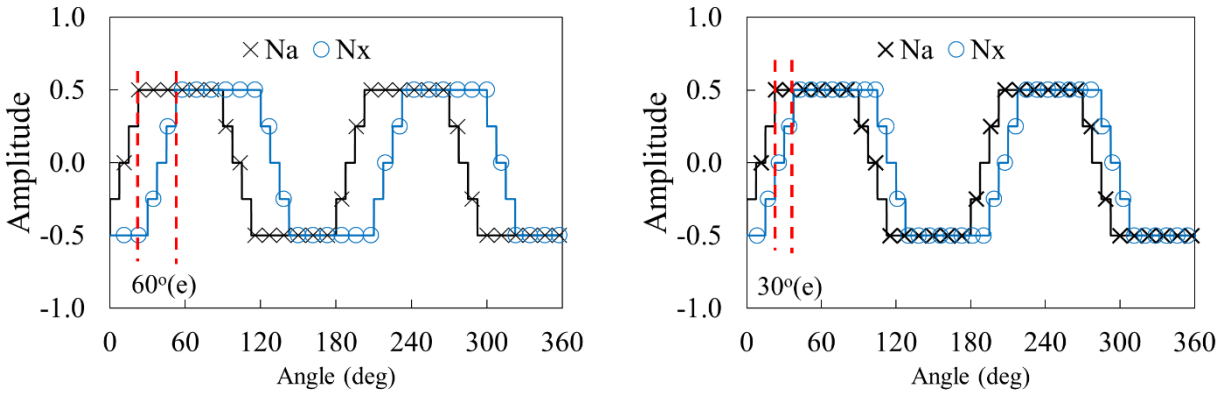

(a) Symmetrical winding (b) Asymmetric winding

Fig. 5.3 MMF waveforms of A and X-phases of 4-pole 6-phase windings.

$$F_{6-phase}(\alpha)$$

$$= 4\sqrt{2}\frac{qNI}{\pi g}\sum_{v=1}^{v=\infty}\left[\begin{array}{c}\frac{1}{v}\sin\left(\frac{v\alpha_y}{2}\right)\sin\left(v\frac{3q\alpha_1}{2}\right)\frac{\sin\left(\frac{q\alpha_1}{2}v\right)}{qsin\left(\frac{\alpha_1}{2}v\right)} \\ \left\{\begin{array}{c}\left[\begin{array}{c}\sin\left(v\frac{2\alpha+(1-4q)\alpha_1}{2}\right)\sin(\omega_1 t) \\ +\sin\left(v\frac{2\alpha+(1-8q)\alpha_1}{2}\right)\sin\left(\omega_1 t-\frac{2}{3}\pi\right) \\ +\sin\left(v\frac{2\alpha+(1-12q)\alpha_1}{2}\right)\sin\left(\omega_1 t-\frac{4}{3}\pi\right)\end{array}\right] \\ +\left[\begin{array}{c}\sin\left(v\frac{2\alpha+(1-4q)\alpha_1}{2}-v\frac{\pi}{3}\right)\sin\left(\omega_1 t-\frac{\pi}{3}\right) \\ +\sin\left(v\frac{2\alpha+(1-8q)\alpha_1}{2}-v\frac{\pi}{3}\right)\sin(\omega_1 t-\pi) \\ +\sin\left(v\frac{2\alpha+(1-12q)\alpha_1}{2}-v\frac{\pi}{3}\right)\sin\left(\omega_1 t-\frac{5}{3}\pi\right)\end{array}\right]\end{array}\right\}\end{array}\right] \tag{5.11}$$

$$F_{6-phase}(\alpha)$$

$$= 4\sqrt{2}\frac{qNI}{\pi g}\sum_{v=1}^{v=\infty}\left[\begin{array}{c}\frac{1}{v}\sin\left(\frac{v\alpha_y}{2}\right)\sin\left(v\frac{3q\alpha_1}{2}\right)\frac{\sin\left(\frac{q\alpha_1}{2}v\right)}{qsin\left(\frac{\alpha_1}{2}v\right)} \\ \left\{\begin{array}{c}\left[\begin{array}{c}\sin\left(v\frac{2\alpha+(1-4q)\alpha_1}{2}\right)\sin(\omega_1 t) \\ +\sin\left(v\frac{2\alpha+(1-8q)\alpha_1}{2}\right)\sin\left(\omega_1 t-\frac{2}{3}\pi\right) \\ +\sin\left(v\frac{2\alpha+(1-12q)\alpha_1}{2}\right)\sin\left(\omega_1 t-\frac{4}{3}\pi\right)\end{array}\right] \\ +\left[\begin{array}{c}\sin\left(v\frac{2\alpha+(1-4q)\alpha_1}{2}-v\frac{\pi}{6}\right)\sin\left(\omega_1 t-\frac{\pi}{6}\right) \\ +\sin\left(v\frac{2\alpha+(1-8q)\alpha_1}{2}-v\frac{\pi}{6}\right)\sin\left(\omega_1 t-\frac{5\pi}{6}\right) \\ +\sin\left(v\frac{2\alpha+(1-12q)\alpha_1}{2}-v\frac{\pi}{6}\right)\sin\left(\omega_1 t-\frac{9}{6}\pi\right)\end{array}\right]\end{array}\right\}\end{array}\right] \tag{5.12}$$

$$F^3_{6-phase_3}(\alpha) = 4\sqrt{2}\frac{qNI}{\pi g}\sin\left(\frac{3\alpha_y}{2}\right)\sin\left(\frac{9q\alpha_1}{2}\right)\frac{\sin\left(\frac{3q\alpha_1}{2}\right)}{qsin\left(\frac{3\alpha_1}{2}\right)}\left[\sin\left(3\left(\alpha+\frac{(1-4q)}{2}\alpha_1\right)\right)\sin(\omega_1 t)\right] \tag{5.13}$$

$$F^3_{6-phase_3}(\alpha) = 4\sqrt{2}\frac{qNI}{\pi g}\sin\left(\frac{3\alpha_y}{2}\right)\sin\left(\frac{9q\alpha_1}{2}\right)\frac{\sin\left(\frac{3q\alpha_1}{2}\right)}{qsin\left(\frac{3\alpha_1}{2}\right)}\left[\cos\left(3\left(\alpha+\frac{(1-4q)}{2}\alpha_1-\omega_1 t\right)\right)\right] \tag{5.14}$$

The MMF for the symmetrical connection is given in (5.11) and the corresponding connection for the asymmetric winding connection is shown in (5.12). The fundamental, 5th and 7th harmonics of the six-phase winding MMF create the same magnetic fields as is the case for the three-phase winding. The difference is observed when the six-phase windings have a single neutral point and a zero-sequence current has a path to flow. The MMFs due to this current for the symmetrical and asymmetric windings are shown in (5.13) and (5.14). From these equations, it can be inferred that while a 3rd harmonic injection into the symmetrical six-phase winding results in a pulsating magnetic field, the same current when injected into the asymmetric winding results in a rotating magnetic field that is synchronous with the magnetic field created by the fundamental and can be used to produce an additional, fundamental synchronised torque. The MMF equations of (5.11) and (5.12) are applied to the design of a 48-slot, 4-pole, six-phase stator winding with a 60^{o}(electrical) separation and 30^{o}(electrical) separation between the three-phase sets as shown in Fig. 5.3(a) and Fig. 5.3(b) respectively for A-phase and X-phase. The MMFs due to a fundamental stator current flowing in the symmetrical and the asymmetric windings having the same time-phase displacement as the corresponding windings are shown in Fig. 5.4(a) and Fig. 5.5(a), respectively. The corresponding harmonic spectra are shown in Fig. 5.4(b) and Fig. 5.5(b), respectively.

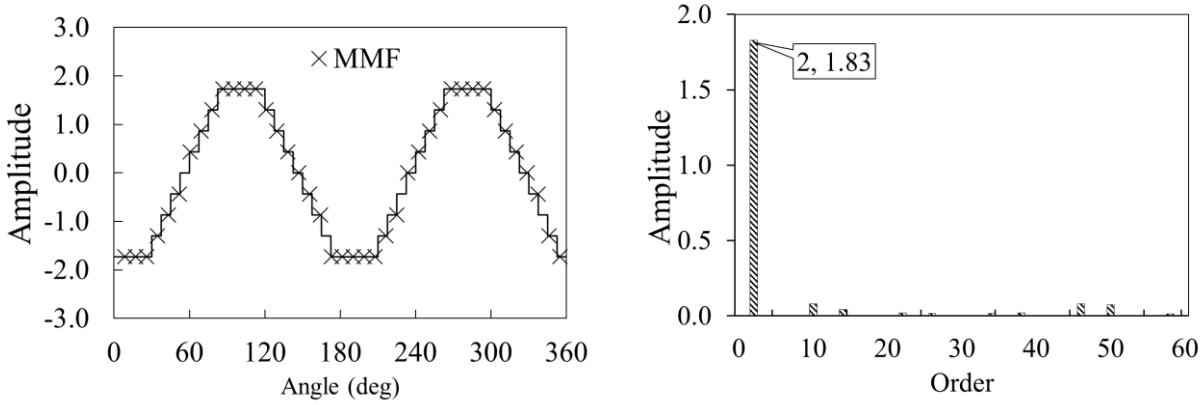

(a) MMF waveform (b) Harmonic spectrum

Fig. 5.4 MMF due to fundamental stator current in the symmetrical six-phase winding.

It can be observed that the 5th and 7th harmonics in the MMF when a fundamental current is injected in the asymmetric winding are reduced to zero resulting in better torque ripple performance. This is numerically shown in Section 5.3.1 for the prototype machine. When a 3rd harmonic current is injected into the symmetrical six-phase winding, the resulting MMF is pulsating and cannot be therefore used to do any useful work as previously described. When the 3rd harmonic current is injected into the asymmetric winding, the 3rd harmonic MMF developed and the corresponding harmonic spectrum are shown in Fig. 5.6(a) and Fig. 5.6(b). Due to this 3rd harmonic having the

same speed as the fundamental, it subtracts from the fundamental and makes it increasingly flat-topped.

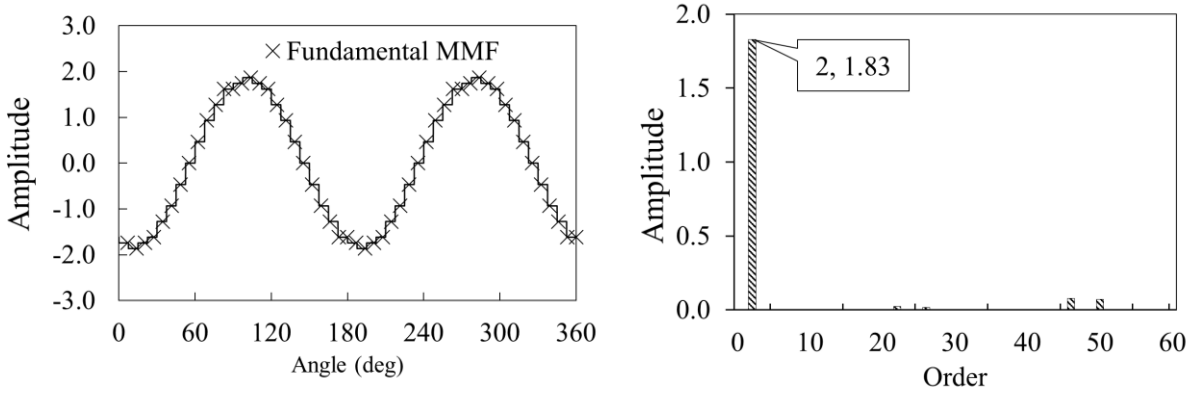

(a) MMF waveform (b) Harmonic spectrum

Fig. 5.5 MMF due to fundamental stator current in the asymmetric six-phase winding.

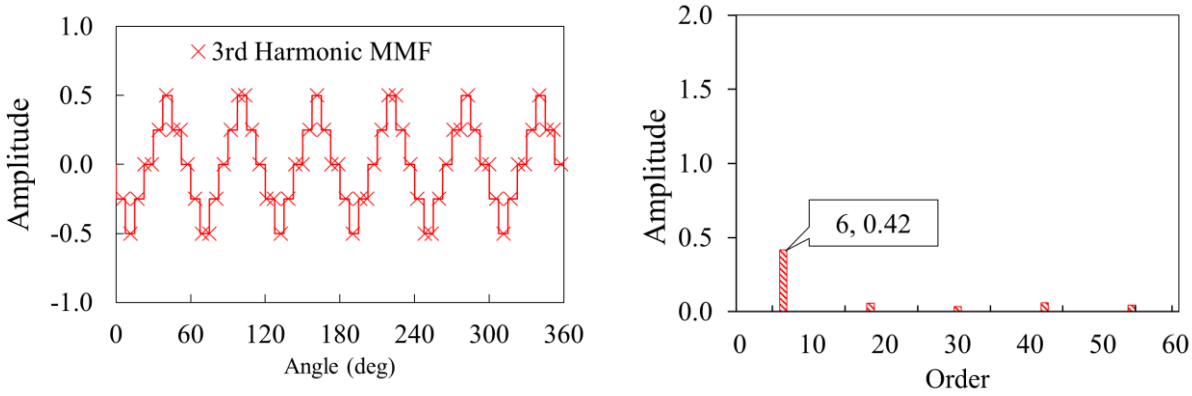

(a) MMF waveform (b) Harmonic spectrum

Fig. 5.6 MMF due to third harmonic stator current in the asymmetric six-phase winding.

This can be used to increase the fundamental current and thus increase the torque capability of the overall machine. This is exploited in a pole changing winding machine as discussed in Section 5.2.3.

5.2 Six-Phase Pole-changing Windings

5.2.1 Three Phase and Six-Phase Pole Changing Windings

Electronic pole changing winding induction machines introduced in [OSA96] [SUZ97] employ the inverter to reverse the direction of current in a portion of the phase windings to change the pole number. In [OSA96], a six-phase inverter was used to change the number of poles of the induction machine from 4 to 2 by utilizing a 3-phase stator winding with a 120^{o} phase belt distribution. In [MAL19] it was shown that the use of 120 ^{o} phase belt winding distribution was

necessary to prevent the MMF cancellation that would occur if the more common 60° phase belt winding with higher winding factor was used. The 120° phase belt winding has a fundamental winding factor that is 15% lower than the 60° phase belt winding which results in a proportionate reduction in torque when pole changing windings are used.

Poles	N												S											
Slot N°	1	2	3	4	5	6	7	8	9	10	11	12	13	14	15	16	17	18	19	20	21	22	23	24
Layer 1	A1	A1	A1	A1	A1	A1	A1	A1	c1	c1	c1	c1	c1	c1	c1	c1	B1	B1	B1	B1	B1	B1	B1	B1
Layer 2	C2	C2	C2	C2	b2	b2	b2	b2	b2	b2	b2	b2	a1	a1	a1	a1	a1	a1	a1	a1	C1	C1	C1	C1

Poles	N												S											
Slot N°	25	26	27	28	29	30	31	32	33	34	35	36	37	38	39	40	41	42	43	44	45	46	47	48
Layer 1	A2	A2	A2	A2	A2	A2	A2	A2	c2	c2	c2	c2	c2	c2	c2	c2	B2	B2	B2	B2	B2	B2	B2	B2
Layer 2	C1	C1	C1	C1	b1	b1	b1	b1	b1	b1	b1	b1	a2	a2	a2	a2	a2	a2	a2	a2	C2	C2	C2	C2

(a) 3-phase 4-pole

Poles	N												S											
Slot N°	1	2	3	4	5	6	7	8	9	10	11	12	13	14	15	16	17	18	19	20	21	22	23	24
Layer 1	A1	A1	A1	A1	A1	A1	A1	A1	c1	c1	c1	c1	c1	c1	c1	c1	B1	B1	B1	B1	B1	B1	B1	B1
Layer 2	c2	c2	c2	c2	B2	B2	B2	B2	B2	B2	B2	B2	a1	a1	a1	a1	a1	a1	a1	a1	C1	C1	C1	C1

Poles	S												N											
Slot N°	25	26	27	28	29	30	31	32	33	34	35	36	37	38	39	40	41	42	43	44	45	46	47	48
Layer 1	a2	a2	a2	a2	a2	a2	a2	a2	C2	C2	C2	C2	C2	C2	C2	C2	b2	b2	b2	b2	b2	b2	b2	b2
Layer 2	C1	C1	C1	C1	b1	b1	b1	b1	b1	b1	b1	b1	A2	A2	A2	A2	A2	A2	A2	A2	c2	c2	c2	c2

(b) 3-phase 2-pole

Poles	N												S											
Slot N°	1	2	3	4	5	6	7	8	9	10	11	12	13	14	15	16	17	18	19	20	21	22	23	24
Layer 1	A1	A1	A1	A1	X1	X1	X1	X1	c1	c1	c1	c1	y1	y1	y1	y1	B1	B1	B1	B1	Z1	Z1	Z1	Z1
Layer 2	Y2	Y2	Y2	Y2	b2	b2	b2	b2	z2	z2	z2	z2	a1	a1	a1	a1	x1	x1	x1	x1	C1	C1	C1	C1

Poles	N												S											
Slot N°	25	26	27	28	29	30	31	32	33	34	35	36	37	38	39	40	41	42	43	44	45	46	47	48
Layer 1	A2	A2	A2	A2	X2	X2	X2	X2	c2	c2	c2	c2	y2	y2	y2	y2	B2	B2	B2	B2	Z2	Z2	Z2	Z2
Layer 2	Y1	Y1	Y1	Y1	b1	b1	b1	b1	z1	z1	z1	z1	a2	a2	a2	a2	x2	x2	x2	x2	C2	C2	C2	C2

(c) 6-phase 4-pole

Poles	N												S											
Slot N°	1	2	3	4	5	6	7	8	9	10	11	12	13	14	15	16	17	18	19	20	21	22	23	24
Layer 1	A1	A1	A1	A1	X1	X1	X1	X1	c1	c1	c1	c1	y1	y1	y1	y1	B1	B1	B1	B1	Z1	Z1	Z1	Z1
Layer 2	y2	y2	y2	y2	y2	B2	B2	B2	Z2	Z2	Z2	Z2	a1	a1	a1	a1	x1	x1	x1	x1	C1	C1	C1	C1

Poles	S												N											
Slot N°	25	26	27	28	29	30	31	32	33	34	35	36	37	38	39	40	41	42	43	44	45	46	47	48
Layer 1	a2	a2	a2	a2	x2	x2	x2	x2	C2	C2	C2	C2	Y2	Y2	Y2	Y2	b2	b2	b2	b2	z2	z2	z2	z2
Layer 2	Y1	Y1	Y1	Y1	b1	b1	b1	b1	z1	z1	z1	z1	A2	A2	A2	A2	X2	X2	X2	X2	c2	c2	c2	c2

(d) 6-phase 2-pole

Fig 5.7 Phase A winding layouts in slots of a 48-slot 120° phase belt stator winding.

Additionally, to maintain the same air-gap flux density as the 60° phase belt winding, the magnetizing current of the 120° phase belt winding will be 15% higher. The ratio of power capability of a 120° phase belt winding induction machine to a conventional 60° phase belt winding induction machine approaches the ratio of the corresponding fundamental winding factors as the rating of the machines increases. Due to a larger portion of the rated current being the magnetizing current, lower-rated machines have a lower power capability ratio [OSA96]. The improved fundamental winding factor, avoiding MMF cancellation and pole changing operation can be achieved by utilizing a six-phase winding. The A-phase winding layout of a 3-phase and 6-phase winding of a 48 slot stator is shown in Fig 5.7. The 3-phase 4-pole and 2-pole operations are shown in Fig 5.7(a) and Fig 5.7(b) while the 6-phase 4-pole and 2-pole operations are shown in Fig 5.7(c) and Fig 5.7(d) respectively. The winding factors of these four cases of winding distribution are shown in Fig 5.8 (a) for the 4-pole configuration and in Fig 5.8(b) for the 2-pole configuration. The fundamental winding factor of the 6-phase machine with the 4-pole operation is higher than that of the 3-phase machine by 15%. The fundamental winding factor of the 2-pole operation is comparable for 6-phase and 3-phase windings. Using the 6-phase winding enables electronic pole changing while resulting in higher fundamental winding factor and hence higher torque for the same input current compared to the 3-phase pole changing winding described in [LYR02]. The inverter required to achieve electronic pole changing with the 6-phase windings will be discussed in the next section.

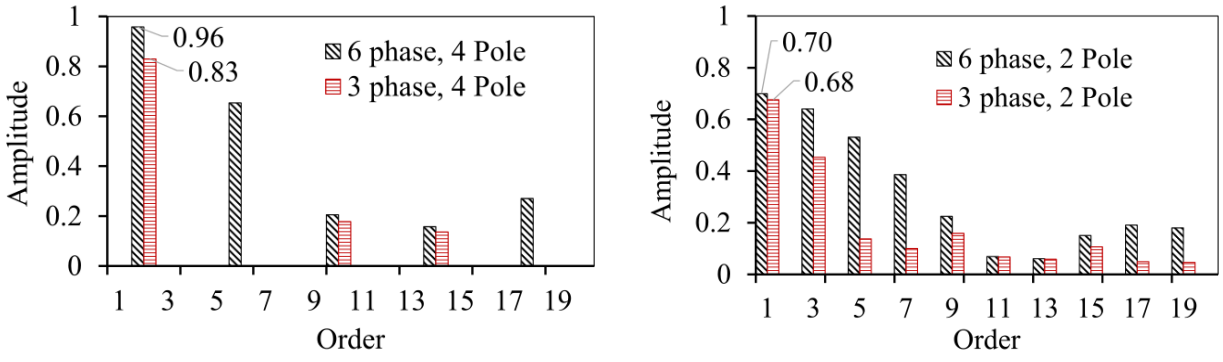

(a) 4-pole operation (b) 2-pole operation

Fig 5.8 Comparison of winding factors of 6-phase and 3-phase windings.

5.2.2 MMF of 6-phase Pole Changing Windings

The MMF patterns of phase A (comprised of two coils, A1 and A2) of the machine in 4-pole and 2-pole operation are shown in Fig. 5.9(a) and Fig. 5.9(c). The corresponding MMF spectra are shown in Fig. 5.3(b) and Fig. 5.3(d). Both the modes of operations exhibit phase winding MMFs with substantial 3rd harmonic components that are necessary for using this harmonic for torque production. For the 4-pole operation, the spatial separation between the phase axes is 60°. When

electronic pole changing is used to reduce the number of poles to 2, the spatial separation between the phases reduces to 30°. The fundamental MMF is reduced and as seen from the MMF spectra of Fig. 5.9(b). The spatial separation of 30° allows for the injection of the 3rd harmonic currents for average torque production.

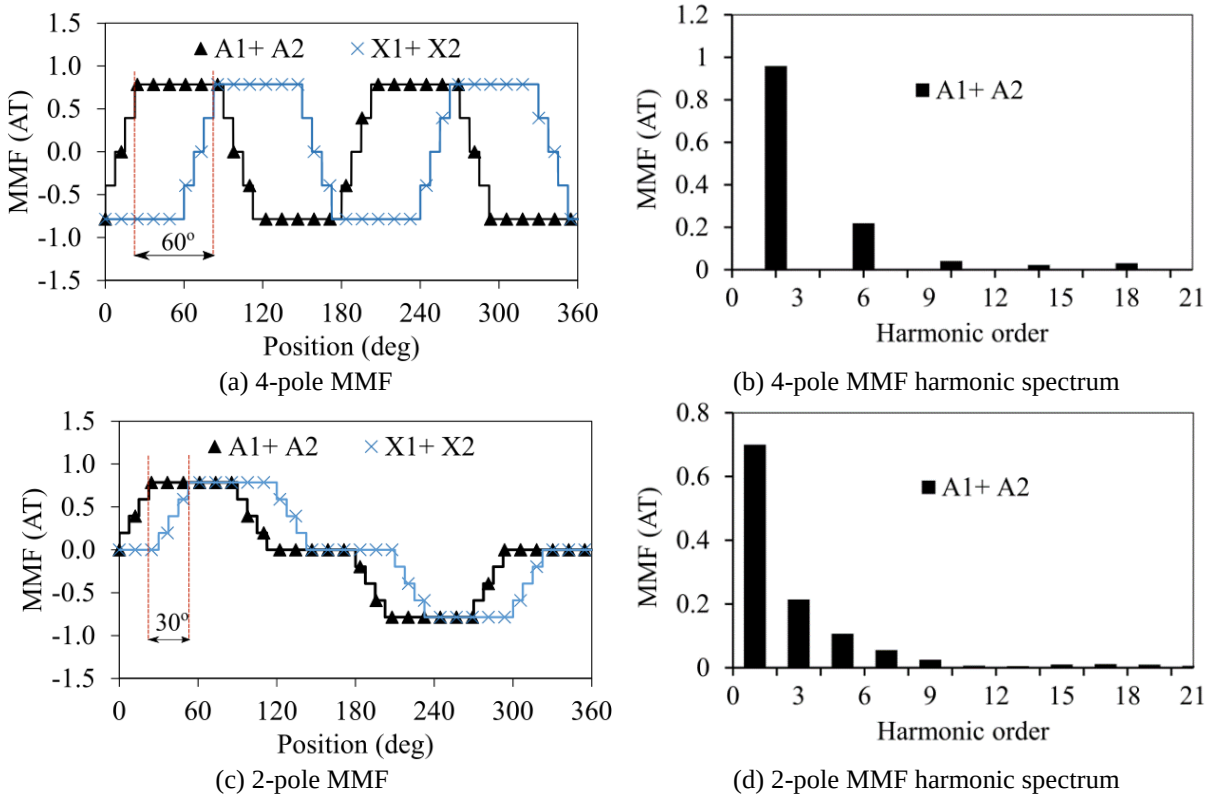

(a) 4-pole MMF

(b) 4-pole MMF harmonic spectrum

(c) 2-pole MMF

(d) 2-pole MMF harmonic spectrum

Fig. 5.9 Phase winding MMF and harmonic spectrum of 6-phase pole changing winding machine.

5.2.3 Influence of 3rd Harmonic Injection

In the 4-pole configuration when the spatial separation between the phase axes is 60°, the 3rd harmonic currents cannot flow even when a path is provided due to the vector sum of the 3rd harmonic currents in the phases being zero. When the direction of current in the second half of the windings is reversed to reduce the number of poles to 2, the spatial separation between the phase axes reduces to 30° and the 3rd harmonic current can flow when a path is provided. The MMF set up by the third harmonic component creates a rotating magnetic field with a synchronous speed being the same as the MMF setup due to fundamental current injection. The air gap flux density with 3rd harmonic injection is defined as shown in (5.15)

$$B_g(\theta) = B1\sin(\theta) + B_3\sin(3\theta) \tag{5.15}$$

To ensure that iron utilization is maximized and flux density is maintained at the permissible peak value for the steel, the optimum value of the 3rd harmonic and fundamental components are given by (5.16) [SOZ16] [WAN15]:

$$B_g(\theta) = \frac{2}{\sqrt{3}} B_{max} \left[\sin(\theta) + \frac{1}{6}\sin(3\theta)\right] \tag{5.16}$$

The MMF with fundamental current excitation, the 3rd harmonic current and the resultant MMF due to both currents are shown in Fig. 5.10(a). The airgap MMF with the 3rd harmonic current injection results in a reduction of the peak value of the MMF. To keep the airgap flux with the 3rd harmonic current injection the same as with fundamental current, the fundamental current can be increased as shown in Fig. 5.10(a). From the harmonic spectrum of Fig. 5.10(b) it can be seen that the additional torque that is produced by the 3rd harmonic injection is achieved by the increase in torque due to an increase in the fundamental current as well as the smaller torque increase due to the synchronously rotating 3rd harmonic MMF. The fundamental current can be increased when the peak current is maintained constant. The RMS phase current with the 3rd harmonic injection is higher when the peak current is maintained the same resulting in higher stator and rotor copper losses.

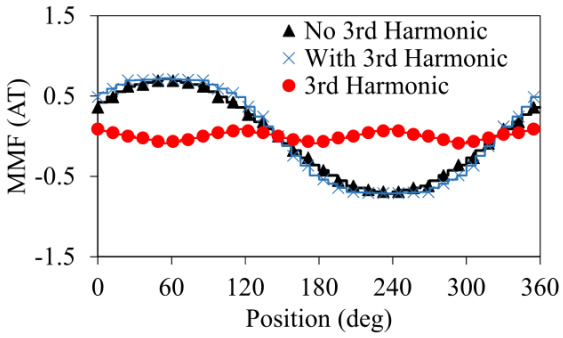

(a) MMF waveforms

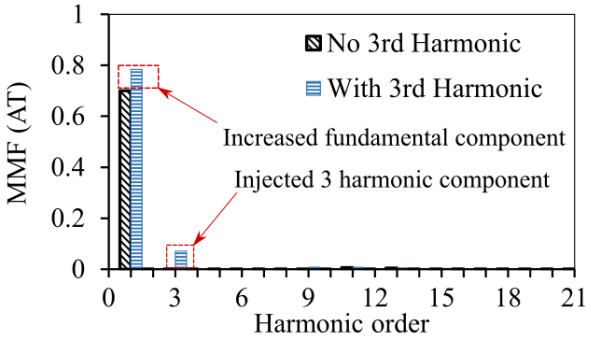

(b) MMF spectra with and without 3rd harmonic injection.

Fig. 5.10 6-phase pole changing winding MMF with 2-pole excitation and 3rd harmonic injection.

5.2.4 Inverter for 6-phase Pole Changing Windings

The inverter required to drive a six-phase winding with electronic pole changing is shown in Fig. 5.11. Since each of the phases has to be split into two coil groups for enabling electronic pole changing, the number of switches required for a six-phase winding are doubled to 24. However, for a given power rating and voltage rating of the induction machine, the required current per phase is reduced resulting in the overall volt-ampere rating of the inverter remaining the same as a standard 12 switch inverter driving a 6-phase machine.

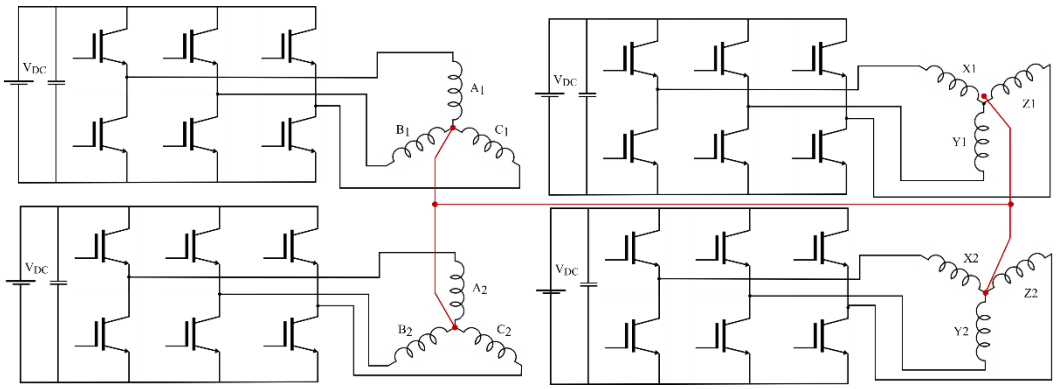

Fig. 5.11 Inverter for driving six-phase machine for electronic pole changing.

This results in the inverter required for driving a 6-phase pole-changing winding induction machine having a lower current rating per switch. In higher volumes where the inverter is constructed with discrete devices, this results in a lower overall cost of the inverter for a given volt-ampere rating [SOZ16]. In the 4-pole operation, the third harmonic currents cannot flow since the total of the third harmonic components is zero for a 60^o spatial separation between the phases. However, with the 2-pole operation, with 30^o spatial separation between the phases, the 3rd harmonic currents can flow between the phases. To allow the 3rd harmonic currents to flow, the neutrals of the phases are connected as shown in Fig. 5.11.

5.3 Simulation Model

To determine the performance of the six-phase pole changing winding induction machine with the 3rd harmonic injection in the 2 pole operation, a 1kW, 48 stator slot induction machine with a squirrel cage rotor having 26 slots is designed. The 4-pole and 2-pole winding connection of the phases is shown in TABLE 5-1. The details of the simulated model and the subsequently fabricated prototype machine are provided in Appendix II. An FEA model is used to predict the performance of the machine with 4-pole and 2-pole excitations. The speed of the rotor component is held fixed in the FEA model and the stator winding is supplied with phase currents at a frequency corresponding to the slip that maximises the torque for the applied current. The 2-D cross-sections of the modelled induction machine with 4-pole and 2-pole excitation are shown in Fig. 5.12(a) and Fig. 5.12(b), respectively

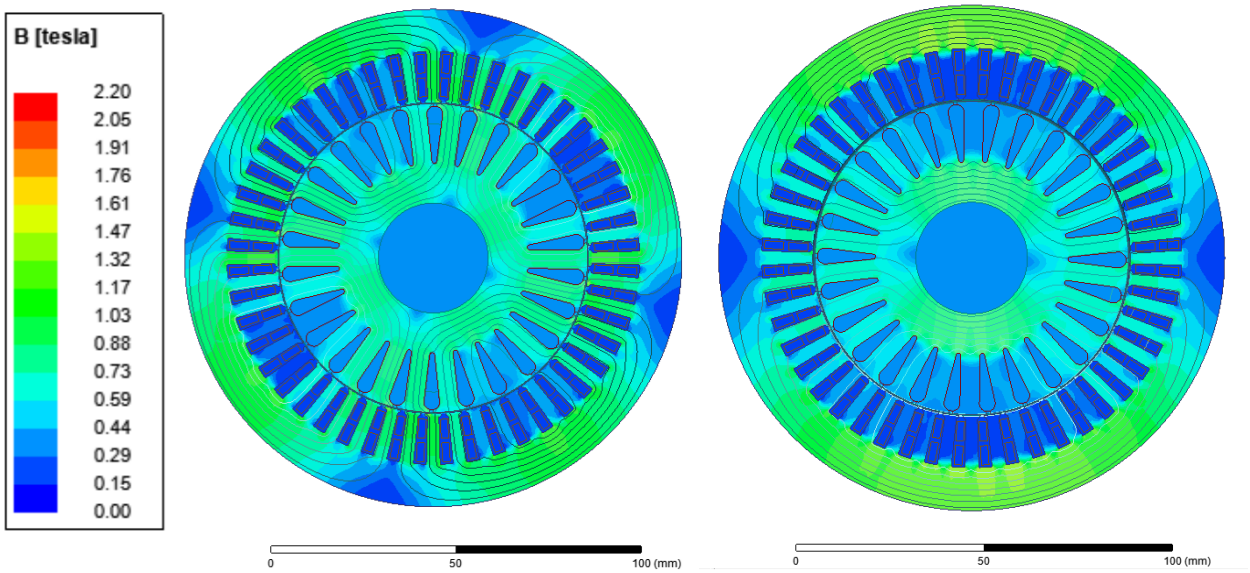

(a) 4-pole operation (b) 2-pole operation

Fig. 5.12 Flux plots of 6-phase 120-degree pole-changing winding configurations at 600rpm and rated current of 1.9A.

TABLE 5-1 WINDING CONNECTION CONFIGURATION OF PROTOTYPE MACHINE

Phase Connection Diagram	Machine Configuration
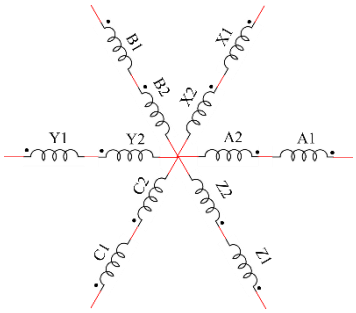	6 Phase 120° phase belt 4-poles (A,Z, X,B,Y,C)
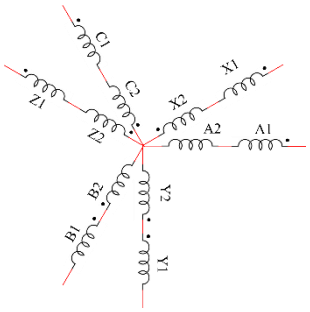	6 Phase 120° phase belt 2-poles (A,Z, X,B,Y,C)

5.3.1 Torque Ripple

The FEA model is excited with the rated phase current of 1.9Arms at a slip value that maximises the torque which is 7.23% for 4-pole operational and 13.44% for the 2-pole operation. The steady-state torque at this operating condition is shown in Fig. 5.13(a) and the harmonic

spectrum of the AC components is shown in Fig. 5.13(b). The average torque of the 4-pole operation is higher than that of the 2-pole operation. The fundamental frequency of the current for a synchronous speed corresponding to 600rpm is 21.56Hz and the frequency for the 2-pole operation is 11.55Hz.

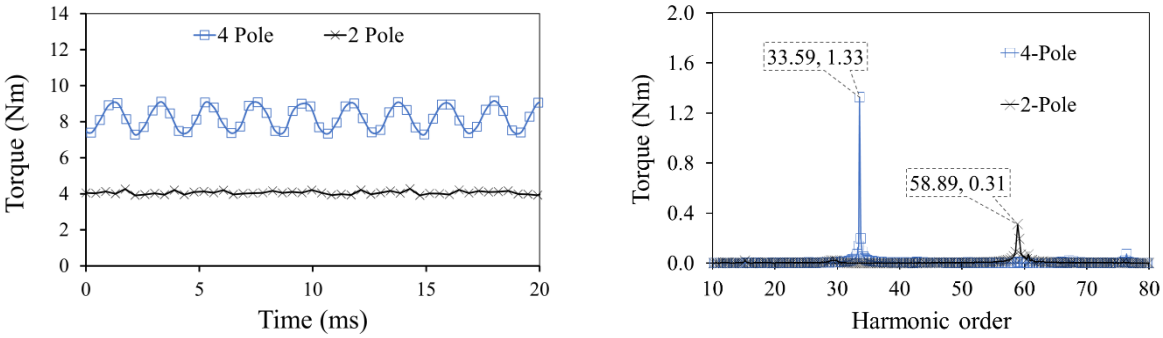

(a) Torque waveform (b) Harmonic spectrum of AC components of the torque

Fig. 5.13 Steady-state torque of 6-phase 120° pole-changing winding configurations at 600rpm and rated current of 1.5A with 4-pole and 2-pole operation.

The torque ripple is also higher for the 4-pole operation as seen from the harmonic spectrum. The frequencies of the harmonics of torque are dependent on the rotor slip, the number of stator and rotor slots and the winding distribution [HIC90]. Two components contribute to torque pulsations. The first component of torque pulsations is due to the time harmonics of the current supplied by the inverter. The torque pulsations arise from the interaction of air-gap MMF components that have the same pole numbers but will be rotating at different speeds. The magnitudes of these pulsations depend on the magnitudes of the two interacting fields and the frequency on the difference between the speeds determines the frequency of the pulsation [WIL01]. The second source of the torque is due to the geometry of the stator and rotor slot geometry and the slip [YLI13]. While analytically determining the magnitude of this torque ripple is a non-linear problem, an index that quantifies the space harmonic interactions between the stator and rotor which cause torque pulsations can be defined for a squirrel cage rotor [ALB12]. The shift of the dominant torque ripple frequency with slip is shown in Fig. 5.14(a) and Fig. 5.14(b) for 4-pole and 2-pole operation. The torque pulsations due to space harmonic interactions can be compared between the 4-pole and 2-pole operations using the space-harmonic interaction index defined as shown in (5.17):

$$S_{hi} = \frac{\sum_{v=1}^{\infty} \frac{k_{wsv} k_{wrv}}{v}}{\frac{k_{wsp} k_{wrp}}{p}} \tag{5.17}$$

where k_{wsv}, k_{wrv}, k_{wsp}, k_{wrp}, v and p are the stator winding factor for the v^{th} harmonic, the rotor winding factor for the v^{th} harmonic, the stator winding factor for the fundamental, the rotor winding factor for the fundamental, the harmonic order and the number of pole pairs respectively. S_{hi} for the 4-pole winding configuration is 3.26 and 1.922 for the 2-pole configuration. The lower torque, as well as the torque ripple, is due to the lower winding factor of the 2-pole winding.

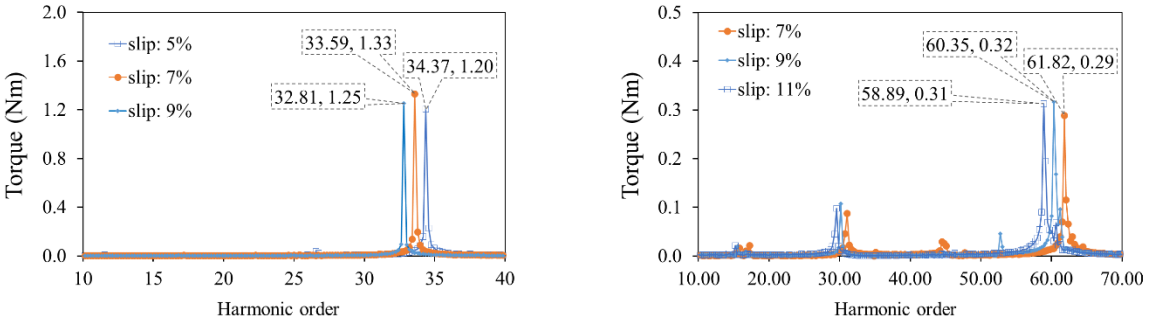

(a) 4-pole operation (b) 2-pole operation

Fig. 5.14 Harmonic spectra of AC components of torque showing variation with slip.

5.3.2 Torque and Power Capability Curves

Using a combination of analytical modelling and the model shown in Fig. 5.12, the torque and power capability at different speeds are calculated using the method described in detail in [GUA14]. At each speed, the slip required to achieve MTPA is determined and the torque and power at this slip for rated rms phase current of 1.5A are determined as shown in Fig. 5.15(a) and Fig. 5.15(b), respectively. The corner speed of the 4-pole excitation is half that of the 2-pole operation and the extended power capability of the 2-pole machine can be seen from Fig. 5.15(b). The variations of slip and the d-axis and q-axis currents with 4-pole and 2-pole excitations are shown in Fig. 5.15(c) and Fig. 5.15(d). It can be observed that the slip during the 4-pole operation is lower in the constant torque region compared to the 2-pole operation while the reverse is true in the flux weakening region. The slip under field-oriented conditions is proportional to the ratio of the q-axis to d-axis current and due to the corner speed of the 2-pole excited machine being higher than that during the 4-pole operation, the d-axis current must be reduced at a lower speed with 4-pole excitation to be within the DC bus voltage limit. As seen in Fig. 5.15(d), the d-axis current with 4-pole excitation begins to reduce at 800rpm and the slip begins to increase from that speed. While the increased torque and power capability due to pole changing is seen from Fig. 5.15(a). The benefit appears to be limited in efficiency due to the limitation of the maximum speed permissible by the experimental setup. The improvement in the power capability increases as the speed range is improved as seen for the higher power rating machine at speed of 10000rpm shown in Fig, 3.7(a) and Fig. 3.7(b).

5.3.3 Optimal 3rd Harmonic Current

The power capability of the inverter is limited by the voltage and current rating of the device used. The injection of the 3rd harmonic currents can be implemented with a constant peak current or a constant RMS current [WAN15]. Both these methods have a different impact on the losses and torque. When the 3rd harmonic currents are injected, as discussed previously, torque capability is increased by two mechanisms. The 3rd harmonic current produces a synchronously rotating MMF and contributes to torque production while the increase in the fundamental component to maintain comparable magnetic loading produces additional torque. The ratio of the 3rd harmonic component to the fundamental component of current *a*, is defined for a given maximum current in (5.18):

$$i(\theta) = I_a(\sin(p\theta) + a\sin(3p\theta)) \tag{5.18}$$

where *p* is the number of pole pairs. The relationship between *a* for a constant peak current is given by (5.19) and (5.20).

$$I_{max} = (1-a)I_a, 0 < a \leq \frac{1}{9} \tag{5.19}$$

$$I_{max} = I_a 8a\left(\frac{1+3a}{12a}\right)^{\frac{3}{2}}, a > \frac{1}{9} \tag{5.20}$$

The value of *a* for constant rms current with the 3rd harmonic current injection is given by (5.21)

$$a = \sqrt{\left(\frac{I_{max}}{I_a}\right)^2 - 1} \tag{5.21}$$

The influence of this ratio *a*, on the torque production in the constant torque region is shown in Fig. 5.1016(a) when the peak current is held constant as the 3rd harmonic current is varied, following (5) and (6). When the peak current is kept constant, with increasing 3rd harmonic injection, the fundamental component increases resulting in higher peak torque. Assuming a linear induction machine, the total torque the contribution of torque increase due to the 3rd harmonic current is 7% while the increased fundamental current possible due to the 3rd harmonic current contributes to 33% increase in torque [LYR02]. Due to this disproportionate contribution to the torque increase, the torque is the highest when the fundamental current is the highest. From (5.16) and (5.17), this occurs when *a*=0.167 for constant peak current and the torque is also the highest for this value of *a*. This

variation of current is shown in Fig. 5.17(a). When the 3rd harmonic is further increased, the fundamental component is decreased due to which the peak torque reduces as seen in Fig. 5.16(a). The value of *a*, at which the peak torque occurs is higher than 0.167 for higher currents due to saturation. From Fig. 5.16(a), it is observed that for a peak phase current of 1.5A, the maximum torque occurs at a=0.2, for 1A it occurs at slightly lower than 0.2 and at 0.17 for the low current of 0.5A.

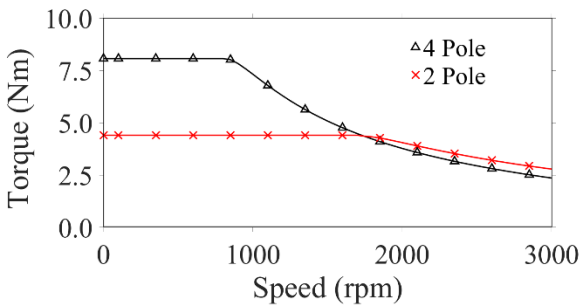

(a) Torque-speed characteristics

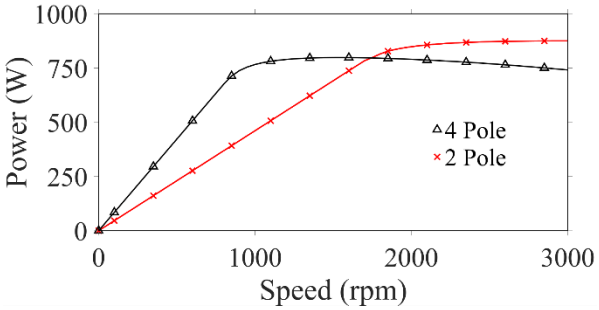

(b) Power-speed characteristics

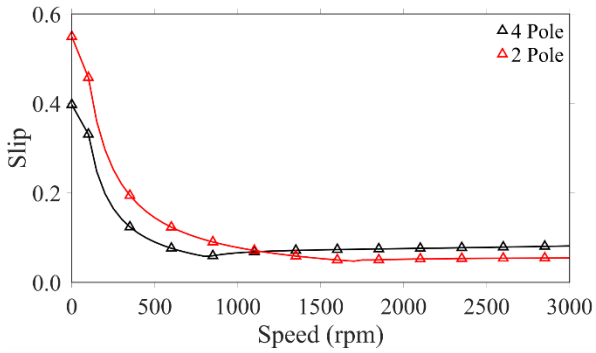

(c) Slip-speed characteristics

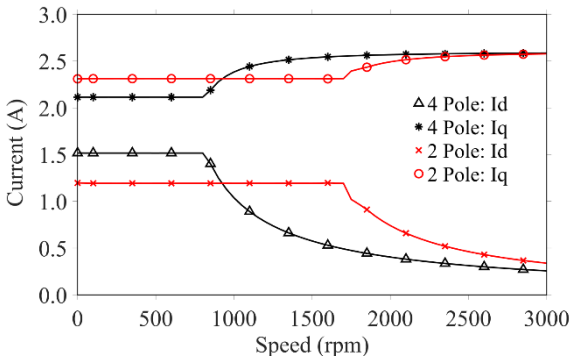

(d) d-axis, q-axis current vs speed characteristics.

Fig. 5.15 Simulated torque and power capability curves of 4-pole and 2-pole operation with a rated current of 1.5Arms over the operating speed range.

When the RMS current is kept constant with increasing the 3rd harmonic current, the torque does not increase significantly since the fundamental current has to be decreased with increasing 3rd harmonic current to keep the RMS current constant. This variation of the peak value of fundamental current is shown in Fig. 5.17(b). The variation of torque for constant RMS current when *a* is varied based on (7) is shown in Fig. 5.16(b). The variations of losses with the 3rd harmonic injection user the two conditions of keeping peak current and RMS current constant are shown in Fig. 5.17(c)-(f).

5.3.4 Torque Capability with 3rd Harmonic Current Injection

Peak torque capability of the induction machine is limited by the thermal limit which specifies the maximum current and the voltage limit imposed by the DC bus. With the neutral point of the

induction machine phases connected, there is a path for the 3rd harmonic currents to flow when the 3rd harmonic voltages are applied. However, additional voltage is required to supply the 3rd harmonic current and this results in the voltage limit being reached earlier than the case when no 3rd harmonic currents are injected as shown in Fig. 5.18(a). As such the corner speed of the machine is lower with the 3rd harmonic current injection. With the 3rd harmonic injection, the torque-speed curve can be divided into three distinct regions. In Phase I, for speeds below the corner speed, the voltage limit of the inverter is reached at a 1500rpm with the 3rd harmonic injection compared to the base speed of 1650 rpm when only fundamental current is used to produce torque.

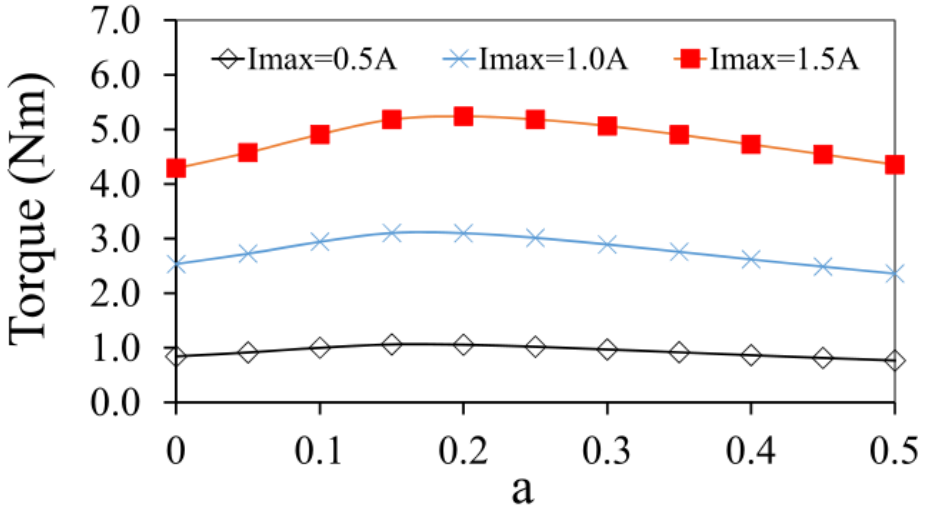

(a) Constant peak current/phase.

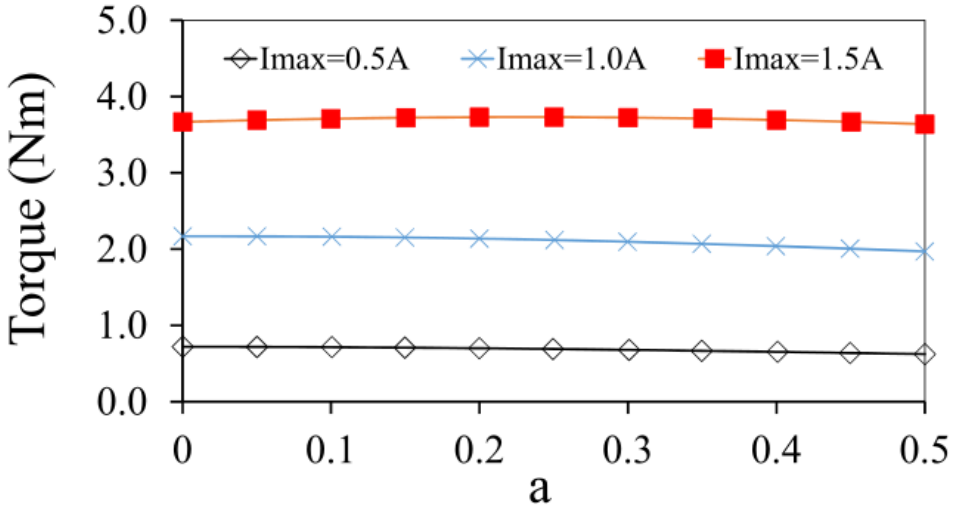

(b) Constant rms current/phase.

Fig. 5.16 Variation of torque with 3rd harmonic to fundamental current ratio at 500rpm.

Once the voltage limit is reached with the 3rd harmonic injection, the ratio of the 3rd harmonic current to the fundamental current is progressively reduced from the optimum value of 0.2 to 0 at the base speed of 1650rpm. This results in the torque reducing to the value achievable with only the fundamental current as shown in Fig. 5.18(b). The available shaft power follows a similar trend as shown in Fig. 5.18(c). The combined torque-speed and power-speed characteristics with 4-pole excitation and 2-pole excitation with and without the 3rd harmonic injection are shown in Fig. 5.19(a) and Fig. 5.19(b), respectively.

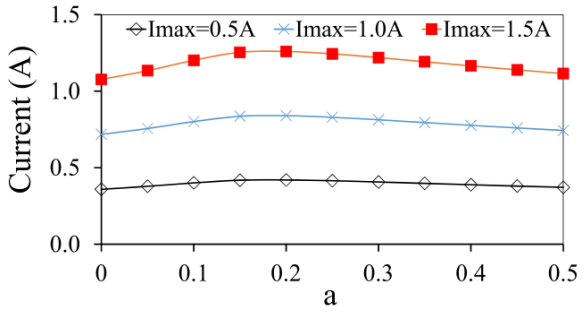

(a) Phase current variation with constant peak current.

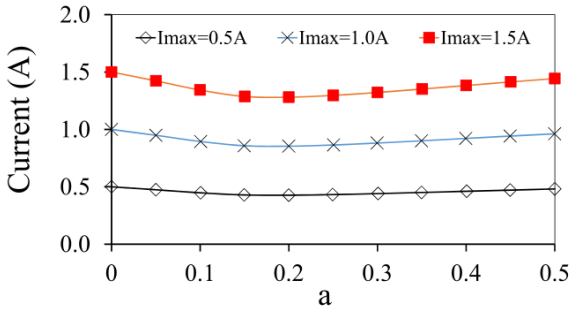

(b) Phase current variation with constant rms current.

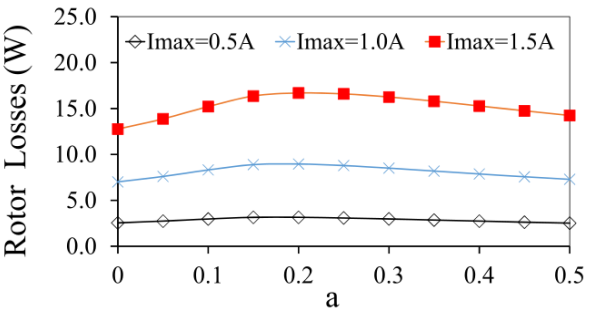

(c) Rotor loss variation with constant peak current.

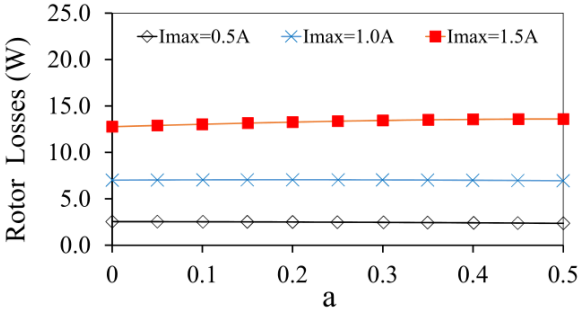

(d) Rotor loss variation with constant rms current.

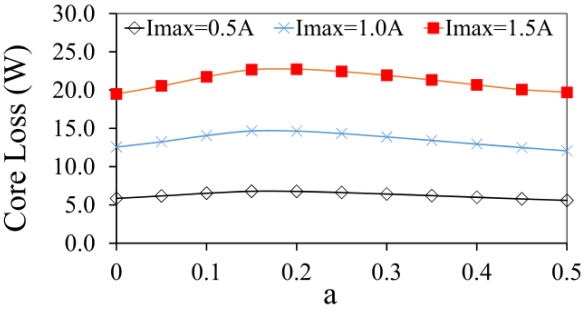

(e) Core loss variation with constant peak current.

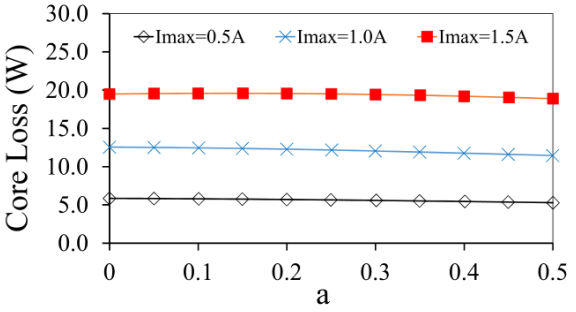

(f) Core loss variation with constant rms current.

Fig. 5.17 Variation of phase current and losses with 3rd harmonic to fundamental current ratio at 500rpm.

5.4 Experimental Validation

A six-phase induction machine with parameters detailed in Appendix II was prototyped. The stator is wound with terminals of all the individual coils brought out to a terminal box to allow for

the 4-pole and 2-pole connections according to TABLE 5.1. The machine is coupled to a dynamometer through a torque sensor for torque measurement. A quadrature encoder is mounted on the non-load end of the shaft for measuring the rotor speed. Five thermocouples on the stator winding in the slots, end windings and the frame are used to monitor the temperature of the machine during operation. The machine is supplied from a six-phase inverter for steady-state tests as shown in the layout of Fig. 5.20. The control algorithm and pulse generation for driving the six-phase inverter are implemented on a dSPACE1006 controller. The currents in the six phases are measured and the neutral current is determined by their sum. To reduce the number of current sensors, the neutral current can be directly measured using only five current sensors instead of six.

5.4.1 Test Methodology

To determine the steady-state performance characteristics and capability curves of the six-phase pole changing winding induction machine with MTPA control, indirect rotor field-oriented control (IRFOC) is implemented according to the block diagram shown in Fig 5.21. While the IRFOC in the d-q plane is identical for the abc and the xyz phases in as described in [SIN05], the control of the 3rd harmonic current is described as follows. The 3rd harmonic current is determined from the sum of the abc and xyz phase currents. The phase shift between the two sets of 3-phase windings in the 4-pole mode of operation is 60^{o} and neutral current is zero and no control of the 3rd harmonic current is needed when sine-PWM (SPWM) control is used. However, when the windings are connected for 2-pole excitation, the phase shift between the phase winding groups is 30^{o} and the neutral current flows between the phases. The neutral current appears as two waveforms shifted by 90^{o} in the 0-plane after dq0 transformation of the phase currents. To convert these to time-invariant quantities, a further $\alpha\beta$ to dq0 transform is performed with the appropriate angle, three times the fundamental flux angle as shown in Fig 5.21. The 3rd harmonic current in the d-axis current is controlled to a reference value and the corresponding q-axis current is controlled to 0 using PI controllers. To generate the capability curves of the induction machine, the dynamometer is configured to hold the shaft speed at a fixed value and the peak current value is applied as a reference. For this peak current value, initially, no 3rd harmonic current is injected and the q-axis current is progressively swept from 0 to the peak current. The d-axis current for each corresponding q-axis current is determined and the torque is observed at each step to determine the optimum current angle for maximizing torque. Once the optimum current angle is determined, the 3rd harmonic current to the fundamental current ratio is increased while keeping the peak current constant.

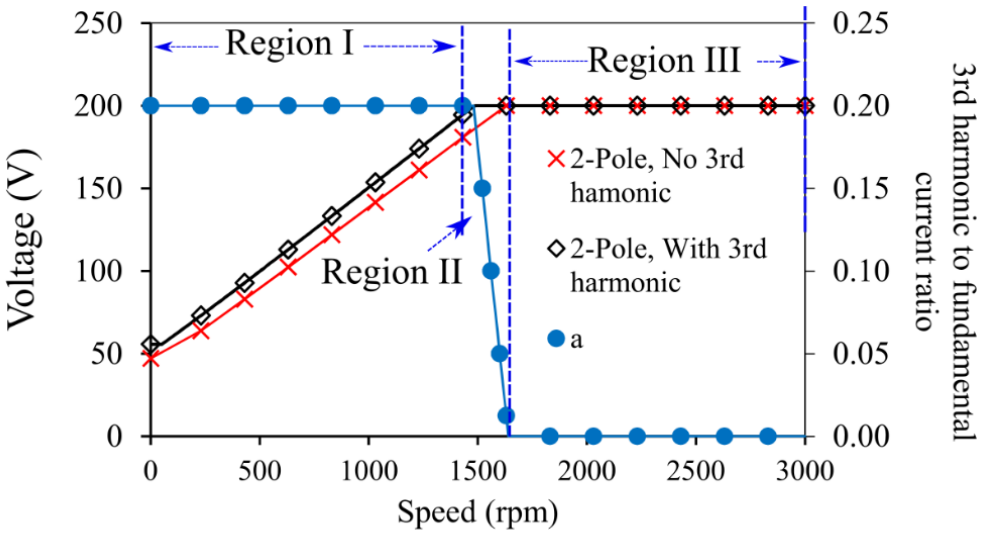

(a) Voltage-speed characteristics

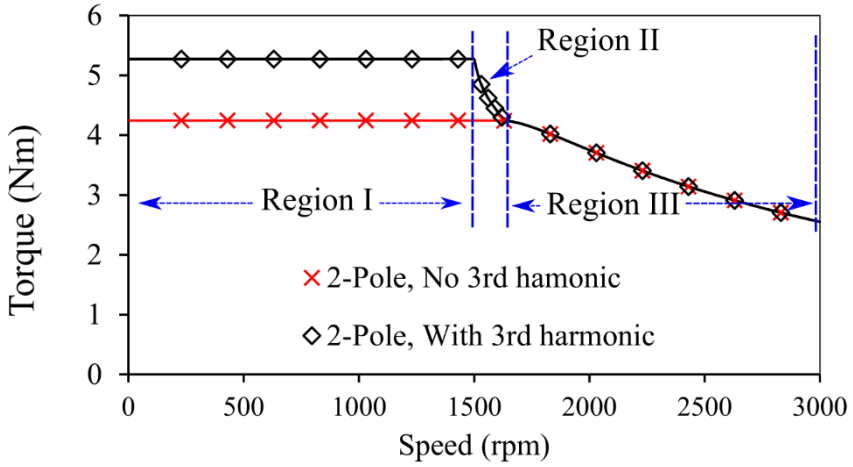

(b) Torque-speed characteristics

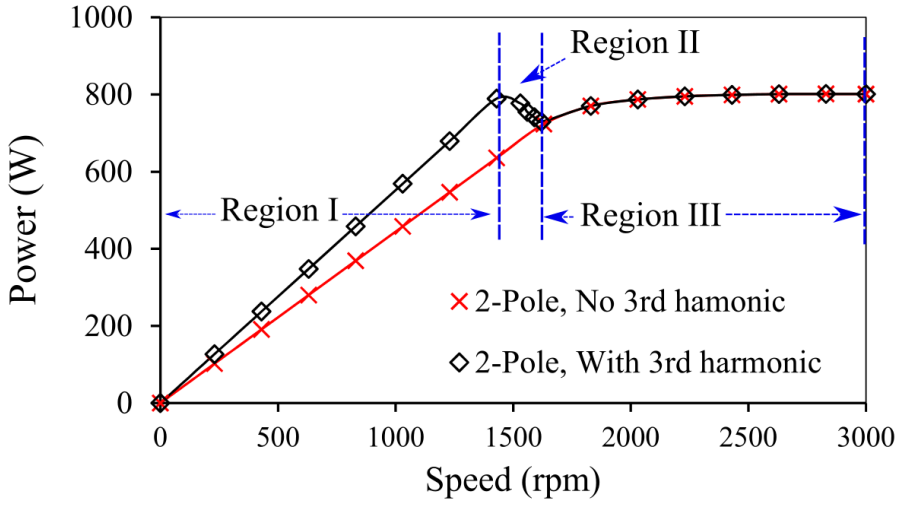

(c) Power-speed characteristics

Fig. 5.18 Influence of optimal 3rd harmonic current injection on the performance of the six-phase induction machine with 2-pole excitation.

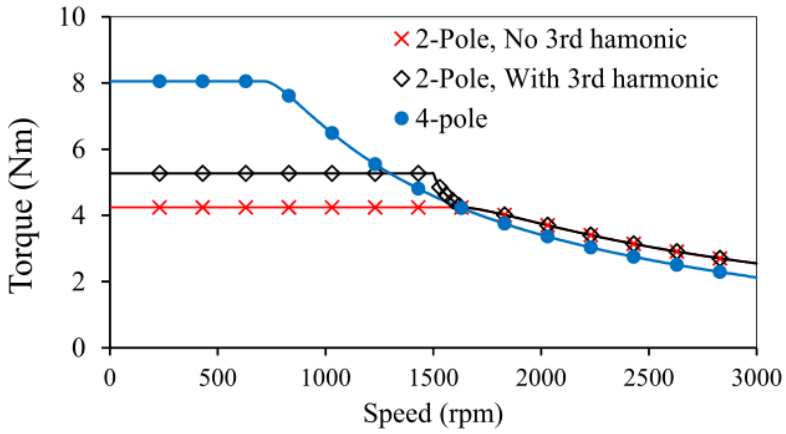

(a) Torque-speed characteristics.

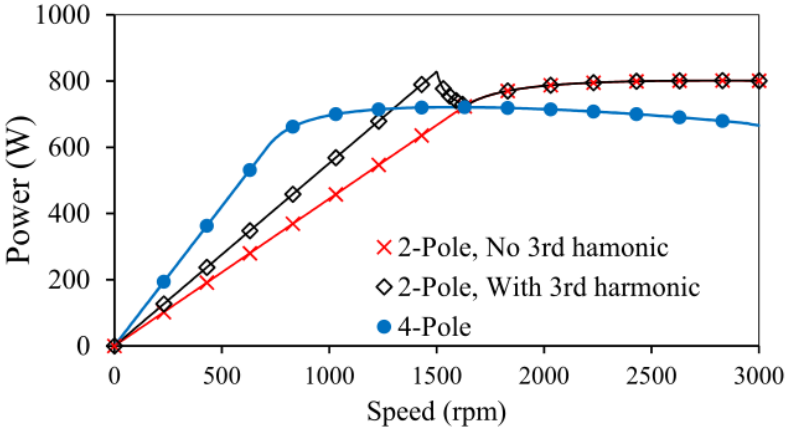

(b) Power-speed characteristics.

Fig. 5.19 Characteristics of 4/2-pole six-phase pole changing winding induction machine, with and without 3rd harmonic injection.

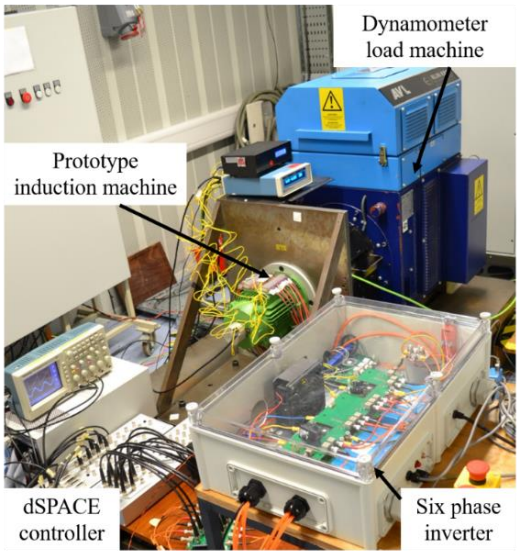

Fig. 5.20 Experimental setup showing prototype induction machine coupled to a dynamometer for performance measurement.

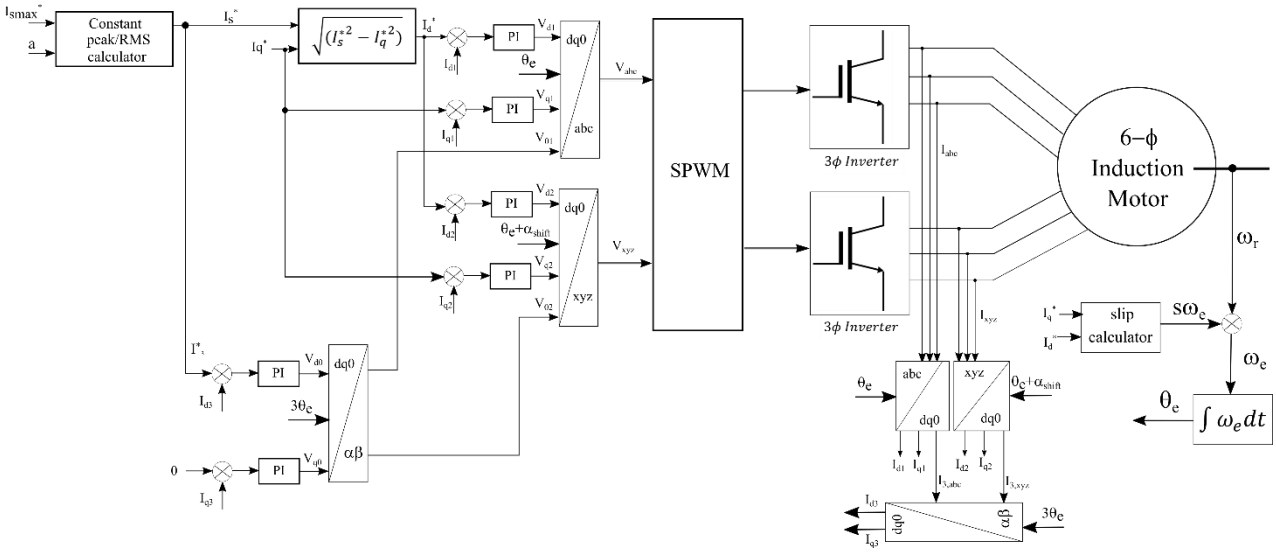

Fig 5.21 Control block diagram for field-oriented control of six-phase induction machine with 3rd harmonic injection.

The measured and simulated variations of the average torque are shown in Fig. 5.22 as the 3rd harmonic to the fundamental current ratio is increased for the rated current of 125A and a shaft speed of 500rpm. This process is repeated for different speeds and the capability curves are plotted.

5.4.2 Capability Curves

The measured torque-speed and power-speed curves of the six-phase induction machine for 4-pole operation are shown in Fig. 5.23(a) and Fig. 5.23(b), respectively. As expected, the peak torque for 4-pole operation is higher in the constant torque region by 15% which is in proportion to the winding factor for these winding configurations. The measured and simulated torque-speed and power-speed curves with 2-pole excitation with and without the 3rd harmonic injection are shown in Fig. 5.24(a) and Fig. 5.24(b). The experimental results and the simulated values are within 8% with the error being higher in the high-speed flux-weakening region due to the temperature variation when running with the maximum current for long durations. The measured and simulated torque-speed and power-speed curves with 4-pole and 2-pole operation including the 3rd harmonic injection are shown in Fig. 5.25(a) and Fig. 5.25(b). The extended power capability due to the pole changing and the 3rd harmonic injection is highlighted in the shaded region of Fig. 5.25(b). At 3000rpm, the peak power that the 2-pole winding can supply is 21% higher than with just the 4-pole winding excitation. Between 1300rpm and 1650rpm where the 2-pole winding is injected with the 3rd harmonic, the torque produced by the 2-pole winding configuration is higher than the 4-pole winding by 14%.

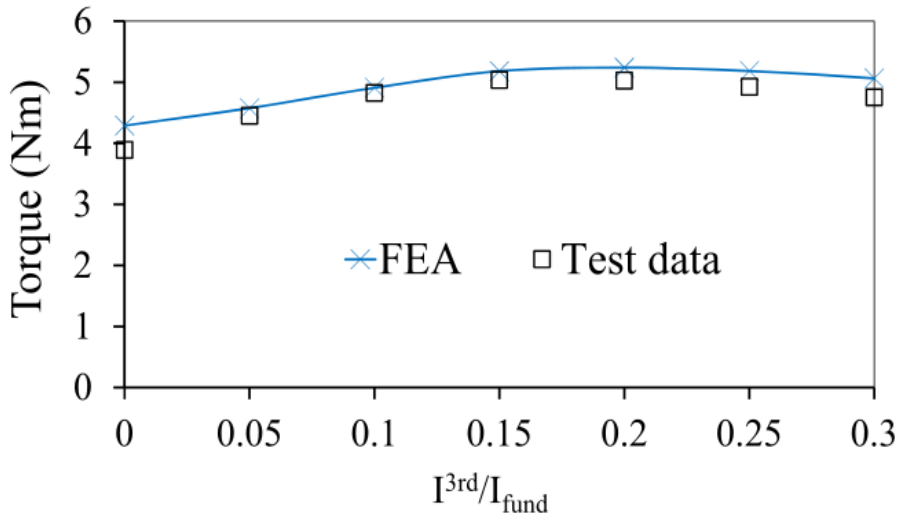

Fig. 5.22 Variation of measured torque with increasing 3rd harmonic current for a peak current of 1.25A at 500rpm.

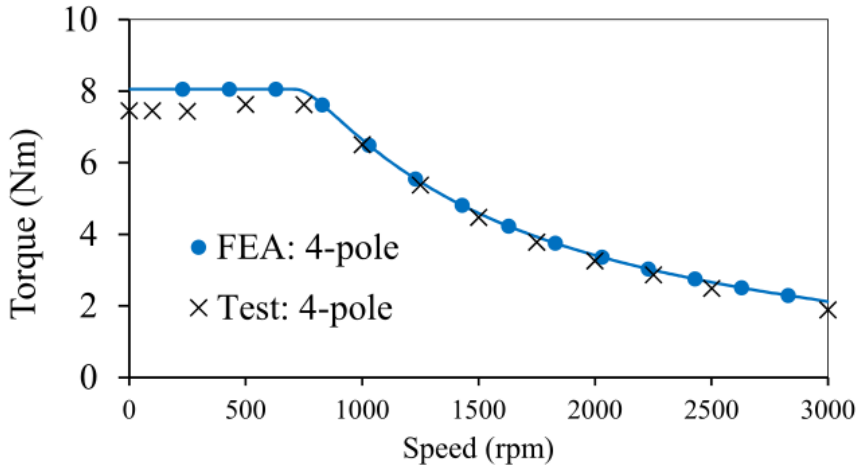

(a) Torque-speed characteristics.

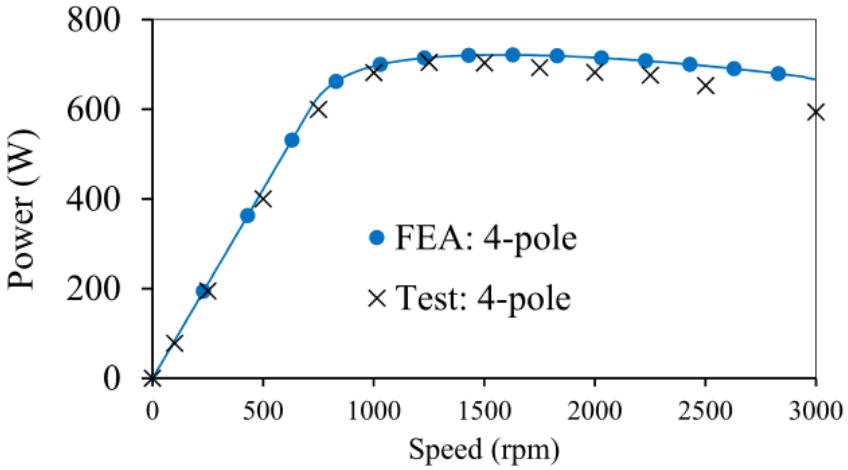

(b) Power-speed characteristics.

Fig. 5.23 Measured and simulated capability curves for 4-pole operation.

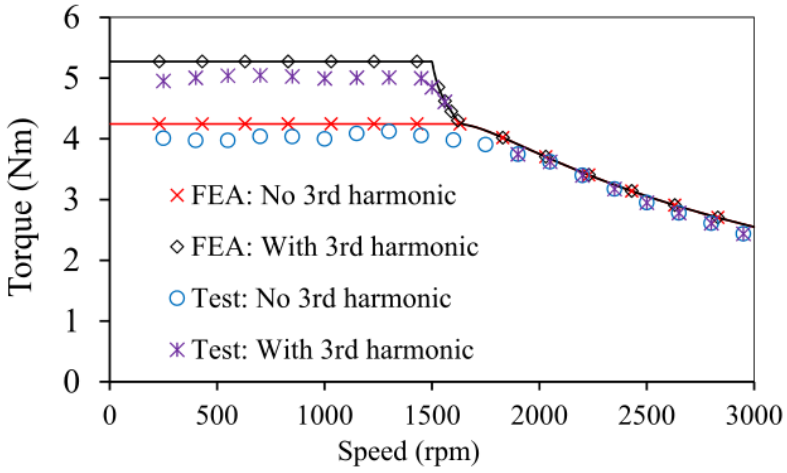

(a) Torque-speed characteristics.

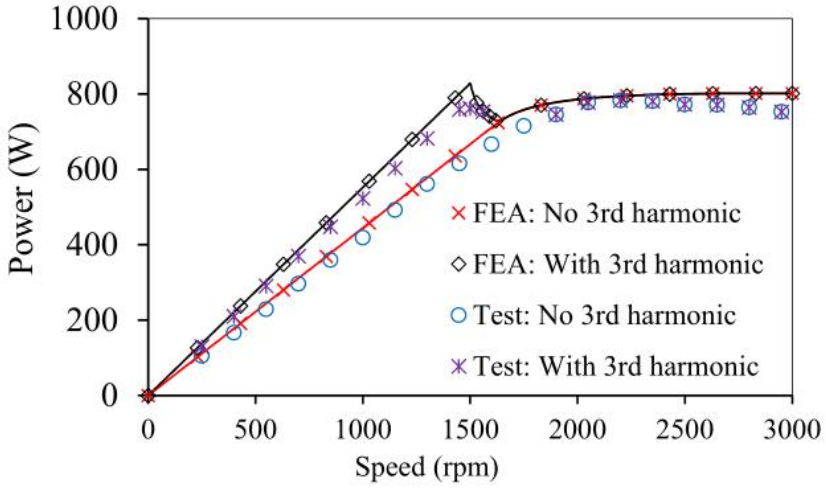

(b) Power-speed characteristics.

Fig. 5.24 Measured and simulated capability curves for 2-pole operation with and without 3rd harmonic injection.

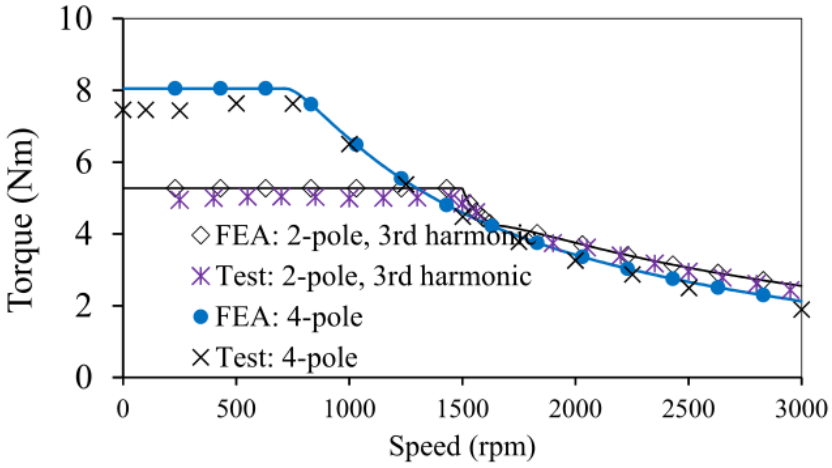

(a) Torque-speed characteristics.

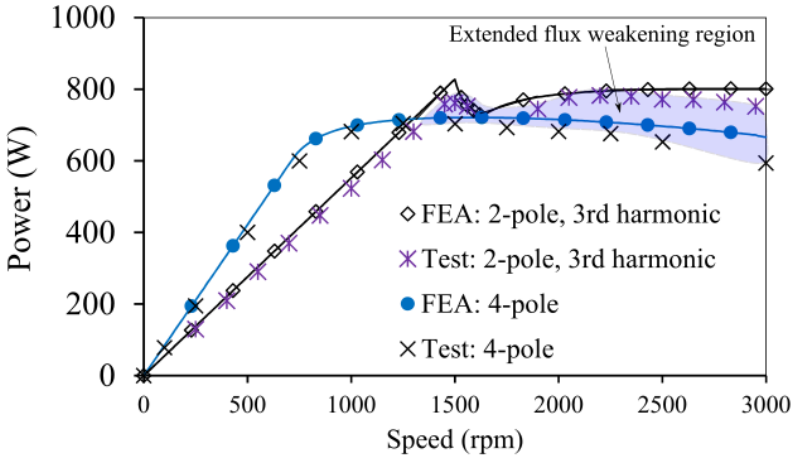

(b) Power-speed characteristics.

Fig. 5.25 Combined characteristics of pole changing winding machine with 4-pole and 2-pole excitation with 3rd harmonic injection.

5.5 Conclusions

Six-phase pole changing windings offer higher fundamental winding factor for the high pole number operation while still allowing for an extended flux-weakening region by reversing the current in half of the coil groups. The spatial angular separation between the two three-phase winding sets is reduced to 30^o with 2-pole excitation, which allows for the injection of the 3rd harmonic currents when the neutrals are connected.

TABLE 5-2 WINDING CONNECTION CONFIGURATION OF PROTOTYPE MACHINE

Machine Configuration	Peak Torque Capability	Flux Weakening Range
3 Phase 120^o phase belt 4-poles	Baseline	Baseline
3 Phase 120^o phase belt 2-poles	Baseline	Baseline
6 Phase 120^o phase belt 4-poles	15% higher	Similar to baseline
6 Phase 120^o phase belt 2-poles (3rd harmonic injection)	20% higher	21% higher above corner speed, 14% higher at corner speed

This produces additional torque in the constant torque region. The 3rd harmonic currents can be injected with the 2-pole winding configuration until a base speed at which voltage required for the additional 3rd harmonic currents over the fundamental is equal to the available DC bus voltage. The stator leakage reactance and the phase resistance have a significant impact on this speed. In the flux-weakening range, the 2-pole excitation can provide up to 21% additional power capability over the 2-pole operation with no 3rd harmonic injection and up to 14% additional power around the corner speed where the 3rd harmonic currents can provide additional power. The conclusions for comparing the 6 phase and 3 phase machines are summarised in Table 5.2.

Chapter 6

Dynamic Performance of Pole-changing Winding Induction Machine

Induction machines are subject to a range of dynamic conditions during operation. Induction machines started direct-on line see significantly different transients compared to transients experienced by induction machines that are fed from solid-state drives. Transient performance cannot be determined by the use of steady-state FEA models or steady-state equivalent circuits. While the steady-state performance might be satisfactory, the transient performance under dynamic conditions may not be acceptable. In addition to dynamics due to load or supply variation, in a pole changing winding induction machine, during the pole changing operation there is a transient experience by the machine where the magnetic field in the rotor corresponding to the existing pole number has to decay to zero and simultaneously, the rotor field corresponding to the new pole number needs to be established. While FEA can be used to study this transient behaviour of the magnetic fields, the accompanying mechanical transient in speed and shaft torque can be very computationally expensive with FEA model due to the difference in the mechanical and electrical time constants. Consequently, a pole changing winding induction machine transient model is necessary to study the behaviour during the pole changing operation. The dynamic model must be capable of replicating the physical behaviour of the machine with the highest level of fidelity. The parameters and their variation with different load conditions must be modelled to capture all transient phenomena. Of particular interest is the magnetising inductance of the induction machine which varies quite widely with the magnetising current. Dynamic models that can incorporate these variations are well documented to simulate the physical behaviours of the machine [SLE89]. Most dynamic models utilise the lumped parameters to represent the equivalent circuit of the induction machine. While direct models where the inductances of the machine are sinusoidally varying are well established by the use of Modified Winding Function Theory model (MWFT) [TOL91a], most models for dynamic control are based on orthogonal axes transformation [SLE89].

In this chapter, the parameters of the prototype machine as required for a *d-q* model of the induction machine are derived using FEA and compared with the experimentally obtained values. The dynamic model of the 3-phase induction machine with non-linear magnetising inductance is extended to pole changing winding machine as discussed in [OSA97]. Using this model, the transient performance of the 3-phase pole changing winding machine under full load in the constant

torque region and the flux weakening region are studied. A dynamic *d-q* model for the 6-phase pole changing winding is proposed and a similar analysis of transient performance under full load in the constant torque region and the flux weakening region are studied. For both machines, the transient performance is shown under open-loop or direct-on line control and with field-oriented control to compare the improvement of performance.

6.1 Dynamic Model of 3-phase Induction Machines

The dynamic equations of the induction machine in the rotating d-q-reference frame for a symmetrical 3-phase induction machine have been discussed in Appendix I. The equations are replicated in (6.1).

$$\begin{bmatrix} v_{qs}^e \\ v_{ds}^e \\ v_{qr}^e \\ v_{dr}^e \end{bmatrix} = \begin{bmatrix} R_s + sL_s & \omega_e L_s & sL_m & \omega_e L_m \\ -\omega_e L_s & R_s + sL_s & -\omega_e L_m & sL_m \\ sL_m & (\omega_e - \omega_r)L_s & R_r + sL_r & (\omega_e - \omega_r)L_r \\ -(\omega_e - \omega_r)L_m & sL_m & -(\omega_e - \omega_r)L_r & R_r + sL_r \end{bmatrix} \begin{bmatrix} i_{qs}^e \\ i_{ds}^e \\ i_{qr}^e \\ i_{dr}^e \end{bmatrix} \tag{6.1}$$

If the speed of the rotor ω_r is considered constant, similar to when the machine is connected to a dynamometer, knowing the input voltage and frequency, the unknown currents in (6.1) can be determined. If the rotor speed is not constant then the mechanical coupling equation in (6.2) can be solved to determine the rotor speed.

$$T_e = T_L + \frac{2}{P} J \frac{d}{dt} \omega_r \tag{6.2}$$

The electromagnetic torque is given by (6.3)-(6.6), all the equations producing identical values of torque [BOS01].

$$T_e = \frac{3}{2}\frac{P}{2}(\psi_{dm}^e i_{qs}^e - \psi_{qm}^e i_{ds}^e) \tag{6.3}$$

$$T_e = \frac{3}{2}\frac{P}{2}(\psi_{ds}^e i_{qs}^e - \psi_{qs}^e i_{ds}^e) \tag{6.4}$$

$$T_e = \frac{3}{2}\frac{P}{2}(\psi_{dr}^e i_{qr}^e - \psi_{qr}^e i_{dr}^e) \tag{6.5}$$

$$T_e = \frac{3}{2}\frac{P}{2} L_m (i_{qs}^e i_{dr}^e - i_{ds}^e i_{qr}^e) \tag{6.6}$$

The pole changing winding induction machine is composed of three phases that are divided into six-stator coil groups. The pole changing operation as discussed in Chapter 4, is obtained by

the reversal of current in one of the coil groups. For example, the first coil group of phase A, say A1 and its second coil group A2 are separated by 180^o electrical degrees. Similarly, for the phase B and phase C, the coil groups are shifted from each other by 180^o electrical degrees and each phase is shifted from the other by 120^o electrical degrees as is usual for a 3-phase symmetrical induction machine. For a 6-phase induction machine, on the other hand, the phases are separated by 60^o electrical degrees for a symmetrical 6-phase machine. For the lower pole operation of the 6-phase pole changing winding machine, the two sets of three phases are separated by 30^o electrical degrees. In this chapter, the prototype induction machine discussed in Chapter 4 will be used for discussion but the principles can be extended for a pole changing winding induction machine of any rating. The different winding configurations of the 3-phase and 6-phase pole changing winding machines are shown in TABLE 6-1.

TABLE 6-1 WINDING CONNECTION CONFIGURATIONS OF THE PROTOTYPE MACHINE

Phase-A Connection Diagram	Machine Configuration	Machine ID
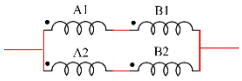	3 Phase 120^o phase belt 4-poles (A-B, X-Y, C-Z)	M3,4P (baseline)
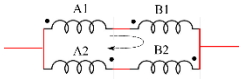	3 Phase 120^o phase belt 2-poles (A-B, X-Y, C-Z)	M3,2P (baseline)
	6 Phase 120^o phase belt 4-poles (A,Z, X,B,Y,C)	M6,4P
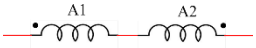	6 Phase 120^o phase belt 2-poles (A,Z, X,B,Y,C)	M6,2P

6.2 Dynamic Model of 3-phase Pole Changing Winding IM

The standard 3-phase d-q model cannot be directly applied to the 3-phase pole changing winding induction machine due to the six coil groups required for pole changing operation. While the Modified Winding Function Theory (MWFT) model can be used to model the dynamics of the machine, the sinusoidal varying nature of the stator to rotor mutual inductances result in large and computationally inefficient matrices that change at every time instant as the rotor rotates. The complexity is further increased when the non-linear magnetising inductance is introduced into the MWFT model as a time-varying air gap thickness. Vector space decomposition (VSD) can be used as an alternative to model the six independent coil group quantities into an orthogonal six-dimensional system [ZHA95] [OSA97]. The fundamental components of the MMF for the six coil

groups are given by (6.7)-(6.12). Assuming the currents fed into these coils have the same phase angles as the spatial distribution of the windings, a basis vector can be defined as shown in (6.13) where the spatial angle $\gamma = \frac{\pi}{3}$. The fundamental component of this basis vector with k=1 corresponds to the 2-pole components with $\omega t = 0$ & $\omega t = -\pi/3$, the first subspace that is spanned by this fundamental component and is represented by the two orthogonal vectors q_2 and d_2 is obtained as shown in (6.14) and (6.15).

$$N_{A1}(\phi_m) = N_{S1}\cos(\phi_m) \tag{6.7}$$

$$N_{A2}(\phi_m) = N_{S1}\cos(\phi_m - \pi) \tag{6.8}$$

$$N_{B1}(\phi_m) = N_{S1}\cos\left(\phi_m - \frac{\pi}{3}\right) \tag{6.9}$$

$$N_{B1}(\phi_m) = N_{S1}\cos\left(\phi_m - \frac{4\pi}{3}\right) \tag{6.10}$$

$$N_{C1}(\phi_m) = N_{S1}\cos\left(\phi_m - \frac{2\pi}{3}\right) \tag{6.11}$$

$$N_{C2}(\phi_m) = N_{S1}\cos\left(\phi_m + \frac{\pi}{3}\right) \tag{6.12}$$

$$S_k(\omega t) = [\cos(k\omega t)\ \ \cos(k(\omega t - 3\gamma))\ \ \cos\big(k(\omega t - \gamma)\big)\ \ \cos\big(k(\omega t - 4\gamma)\big)\ \ \cos\big(k(\omega - 2\gamma)\big)\ \ \cos(k(\omega t - 5\gamma))]^T \tag{6.13}$$

$$q_2 = \left[1\ \ -1\ \ \frac{1}{2}\ \ -\frac{1}{2}\ \ -\frac{1}{2}\ \ \frac{1}{2}\right]^T \tag{6.14}$$

$$d_2 = \left[0\ \ 0\ \ -\frac{\sqrt{3}}{2}\ \ \frac{\sqrt{3}}{2}\ \ -\frac{\sqrt{3}}{2}\ \ \frac{\sqrt{3}}{2}\right]^T \tag{6.15}$$

The second orthogonal sub-space is the surface that is spanned by the 4-pole component corresponding to the 2nd harmonics with k=2. The two orthogonal vector q_4 and d_4 are selected by assigning $2\omega t = 0$ & $-\frac{\pi}{2}$ respectively. The expressions for q_4 and d_4 are shown in (6.16) and (6.17) respectively.

$$q_4 = \left[1\ \ 1\ \ -\frac{1}{2}\ \ -\frac{1}{2}\ \ -\frac{1}{2}\ \ -\frac{1}{2}\right]^T \tag{6.16}$$

$$d_4 = \begin{bmatrix} 0 & 0 & -\frac{\sqrt{3}}{2} & -\frac{\sqrt{3}}{2} & \frac{\sqrt{3}}{2} & \frac{\sqrt{3}}{2} \end{bmatrix}^T \tag{6.17}$$

The other two zero vectors must be chosen to be orthogonal to the 2-pole and 4-pole d-q planes. The 3rd harmonic components corresponding to the 2-pole and 4-pole planes are zero-sequence components and are obtained by setting k=3. The two zero vectors with k=3 and $3\omega t = \pi/4$ are shown in (6.18) and (6.19) respectively.

$$\bar{0}_2 = \begin{bmatrix} \frac{1}{\sqrt{2}} & -\frac{1}{\sqrt{2}} & -\frac{1}{\sqrt{2}} & \frac{1}{\sqrt{2}} & \frac{1}{\sqrt{2}} & -\frac{1}{\sqrt{2}} \end{bmatrix}^T \tag{6.18}$$

$$\bar{0}_4 = \begin{bmatrix} \frac{1}{\sqrt{2}} & \frac{1}{\sqrt{2}} & \frac{1}{\sqrt{2}} & \frac{1}{\sqrt{2}} & \frac{1}{\sqrt{2}} & \frac{1}{\sqrt{2}} \end{bmatrix}^T \tag{6.19}$$

When ωt is varied between $0 \leq \omega t \leq 2\pi$ it can be seen that the surfaces corresponding to the harmonics k=1, 2, 3 are orthogonal to each other as shown in (6.20)

$$d_4^T \bullet d_2 = q_4^T \bullet q_2 = \bar{0}_4^T \bullet \bar{0}_2 = 0 \tag{6.20}$$

The stationary reference frame transformation matrix corresponding to these 6 basis vectors is given by (6.21).

$$\boldsymbol{T}(0) = \frac{1}{\sqrt{3}} \begin{bmatrix} 1 & 1 & -\frac{1}{2} & -\frac{1}{2} & -\frac{1}{2} & -\frac{1}{2} \\ 0 & 0 & -\frac{\sqrt{3}}{2} & -\frac{\sqrt{3}}{2} & \frac{\sqrt{3}}{2} & \frac{\sqrt{3}}{2} \\ 1 & -1 & \frac{1}{2} & -\frac{1}{2} & -\frac{1}{2} & \frac{1}{2} \\ 0 & 0 & -\frac{\sqrt{3}}{2} & \frac{\sqrt{3}}{2} & -\frac{\sqrt{3}}{2} & \frac{\sqrt{3}}{2} \\ \frac{1}{\sqrt{2}} & \frac{1}{\sqrt{2}} & \frac{1}{\sqrt{2}} & \frac{1}{\sqrt{2}} & \frac{1}{\sqrt{2}} & \frac{1}{\sqrt{2}} \\ \frac{1}{\sqrt{2}} & -\frac{1}{\sqrt{2}} & -\frac{1}{\sqrt{2}} & \frac{1}{\sqrt{2}} & \frac{1}{\sqrt{2}} & -\frac{1}{\sqrt{2}} \end{bmatrix} \tag{6.21}$$

A transformation matrix that transforms the machine variables to a reference frame rotating at an arbitrary speed is required to convert the time-variant inductances to constant values. The two-pole surface has the same electrical speed as the speed of the reference frame ($\omega_m = d\theta/dt$). The 4-pole planes are rotating at twice the speed, so q_4 and d_4 axes rotate at an electrical speed of $\omega_4 =$

$2\omega_2 = 2\omega_m$. The transformation matrix is then given by (6.22) which can be used for transforming the stator variables to the rotating reference frame as shown in (6.23). The rotor is rotating at a speed of $\omega_r = d\theta/dt$ and the rotating reference frame transform for rotor variables is modified as shown in (6.24). In the rotor transform the 4-pole angle θ_4 is replaced by $\theta_4 - 2\theta_r$ and the 2-pole angle θ_2 is replaced by $\theta_2 - \theta_r$.

$$T(\theta) = \frac{1}{\sqrt{3}}\begin{bmatrix} \cos(\theta_4) & \cos(\theta_4) & \cos\left(\theta_4 - \frac{2\pi}{3}\right) & \cos\left(\theta_4 - \frac{2\pi}{3}\right) & \cos\left(\theta_4 + \frac{2\pi}{3}\right) & \cos\left(\theta_4 + \frac{2\pi}{3}\right) \\ \sin(\theta_4) & \sin(\theta_4) & \sin\left(\theta_4 - \frac{2\pi}{3}\right) & \sin\left(\theta_4 - \frac{2\pi}{3}\right) & \sin\left(\theta_4 + \frac{2\pi}{3}\right) & \sin\left(\theta_4 + \frac{2\pi}{3}\right) \\ \cos(\theta_2) & -\cos(\theta_2) & -\cos\left(\theta_2 + \frac{2\pi}{3}\right) & \cos\left(\theta_2 + \frac{2\pi}{3}\right) & \cos\left(\theta_2 - \frac{2\pi}{3}\right) & -\cos\left(\theta_2 - \frac{2\pi}{3}\right) \\ \sin(\theta_2) & -\sin(\theta_2) & -\sin\left(\theta_2 + \frac{2\pi}{3}\right) & \sin\left(\theta_2 + \frac{2\pi}{3}\right) & \sin\left(\theta_2 - \frac{2\pi}{3}\right) & -\sin\left(\theta_2 - \frac{2\pi}{3}\right) \\ \frac{1}{\sqrt{2}} & \frac{1}{\sqrt{2}} & \frac{1}{\sqrt{2}} & \frac{1}{\sqrt{2}} & \frac{1}{\sqrt{2}} & \frac{1}{\sqrt{2}} \\ \frac{1}{\sqrt{2}} & -\frac{1}{\sqrt{2}} & -\frac{1}{\sqrt{2}} & \frac{1}{\sqrt{2}} & \frac{1}{\sqrt{2}} & -\frac{1}{\sqrt{2}} \end{bmatrix} \tag{6.22}$$

$$f_{d_4q_4d_2q_2\bar{0}_4\bar{0}_2s} = [T(\theta)][f_{stator}] \tag{6.23}$$

$$f_{d_4q_4d_2q_20_40_2r} = \left[T(\theta - \theta_r)\right][f_{rotor}] \tag{6.24}$$

This transformation can now be applied to the three-phase voltage equations of the induction machine. The stator voltage equations in the arbitrary reference frame using the transform T are shown in (6.25). The superscript *'e'* has been dropped for convenience form variables in a rotating reference frame.

$$\begin{aligned} v_{q4s} &= R_s i_{q4s} + \frac{d\psi_{q4s}}{dt} + \omega_4 \psi_{d4s} \\ v_{d4s} &= R_s i_{d4s} + \frac{d\psi_{d4s}}{dt} - \omega_4 \psi_{q4s} \\ v_{q2s} &= R_s i_{q2s} + \frac{d\psi_{q2s}}{dt} + \omega_2 \psi_{d2s} \\ v_{d2s} &= R_s i_{d2s} + \frac{d\psi_{d2s}}{dt} - \omega_2 \psi_{q2s} \end{aligned} \tag{6.25}$$

$$\upsilon_{\bar{0}4s} = R_s i_{\bar{0}4s} + \frac{d\psi_{\bar{0}4s}}{dt}$$

$$\upsilon_{\bar{0}2s} = R_s i_{\bar{0}2s} + \frac{d\psi_{\bar{0}2s}}{dt}$$

The stator and rotor flux linkages are also transformed from the phase reference frame to the same arbitrary rotating reference frame as the voltages and currents. The stator and rotor inductances are also transformed using the relationship shown in (6.26) and (6.27) respectively to transform the time-varying inductances to time-invariant quantities.

$$\left[L_{dqs}\right] = [T(\theta)]\left[L_{ss}\right][T(\theta)]^{-1} \tag{6.26}$$

$$\left[L_{dqr}\right] = [T(\theta)]\left[L_{sr}\right][T(\theta)]^{-1} \tag{6.27}$$

The stator and rotor fluxes in the transformed reference frame are shown in (6.28)

$$\begin{aligned}
\psi_{q4s} &= (L_{m4} + L_{ls})i_{q4s} + L_{m4}i_{q4r} \\
\psi_{d4s} &= (L_{m4} + L_{ls})i_{d4s} + L_{m4}i_{d4r} \\
\psi_{q2s} &= (L_{m2} + L_{ls})i_{q2s} + L_{m2}i_{q4r} \\
\psi_{d2s} &= (L_{m4} + L_{ls})i_{d2s} + L_{m2}i_{d2r} \\
\psi_{\bar{0}4s} &= L_{ls}i_{04s} \\
\psi_{\bar{0}2s} &= \left(L_{m\bar{0}} + L_{ls}\right)i_{\bar{0}2s} + L_{m\bar{0}}\cos(3\theta_r)\, i_{\bar{0}2r} \\
\psi_{q4r} &= L_{m4}(i_{q4s} + i_{q4r}) + L_{lr}i_{q4r} \\
\psi_{d4r} &= L_{m4}(i_{d4s} + i_{d4r}) + L_{lr}i_{d4r} \\
\psi_{q2r} &= L_{m2}(i_{q2s} + i_{q2r}) + L_{lr}i_{q2r} \\
\psi_{d2r} &= L_{m2}(i_{d2s} + i_{d2r}) + L_{lr}i_{d2r} \\
\psi_{d4m} &= L_{m4}(i_{d4s} + i_{d4r}) \\
\psi_{d2m} &= L_{m2}(i_{d2s} + i_{d2r})
\end{aligned} \tag{6.28}$$

The electromagnetic torque can then be determined as shown in (6.29)

$$T_e = \frac{3}{2}(2\left(\psi_{q4s} i_{q4s} - \psi_{q4s} i_{d4s}\right) + \left(\psi_{q2s} i_{q2s} - \psi_{q2s} i_{d2s}\right) \tag{6.29}$$

The magnetising inductance of the machine in the (6.24) is assumed to be constant at the unsaturated value. However, with high currents especially during the operation in the constant torque region of the torque-speed curve, the machine is usually saturated resulting in a significant decrease in the magnetising inductance.

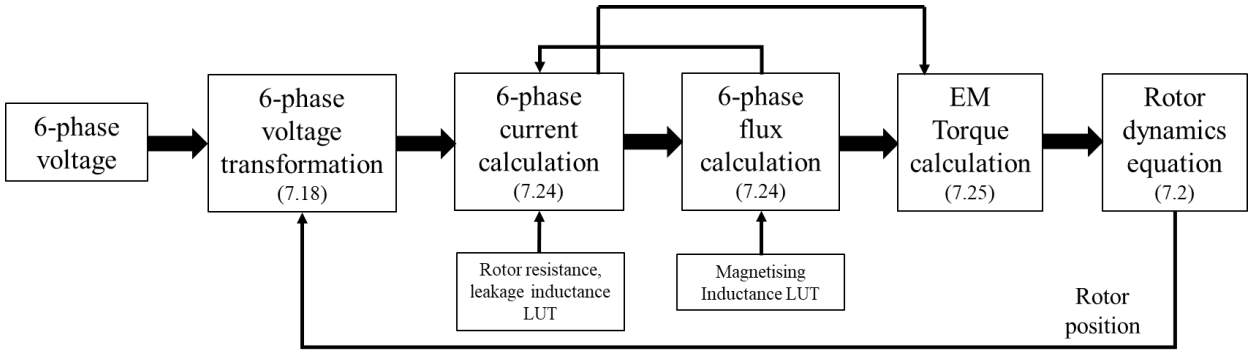

Fig. 6.1 Simulink model of dynamic equations of the 3-phase pole changing winding induction machine.

This results in the electromagnetic torque also reducing in value. To account for the reduction in the magnetic saturation, the magnetising inductance can be modelled as a function of the d-axis current. The magnetising inductance characteristics of the induction machine are derived from the FEA of the machine. The FEA is performed at the no-load condition with the rotor component being suppressed. The relationship between the magnetising current and the d-axis and q-axis current for the 4-pole and 2-pole operation are shown in (6.30) and (6.31) [GUA14].

$$i_{m4} = \frac{i_{d4s}}{\sqrt{2}} \sqrt{1 + \left(\frac{L_{lr} i_{q4s}}{(L_{lr} + L_{m4}) i_{d4s}}\right)^2} \tag{6.30}$$

$$i_{m2} = \frac{i_{d2s}}{\sqrt{2}} \sqrt{1 + \left(\frac{L_{lr} i_{q2s}}{(L_{lr} + L_{m2}) i_{d2s}}\right)^2} \tag{6.31}$$

This characteristic is incorporated as a lookup table in the block diagram of the simulated shown in Fig. 6.1

6.2.1 Parameters of Prototype Machine

Using the FEA model of the prototype machine, the different parameters required to model the dynamics of the machine can be extracted [CAR18] [CAR19]. The list of electrical parameters needed and the FEA method that is used to determine the parameters are shown in TABLE 6-2.

TABLE 6-2 PARAMETERS TO BE OBTAINED FOR THE DYNAMIC MODEL OF POLE CHANGING WINDING MACHINE

Parameter	Symbol	FEA Method
Stator resistance	R_s	No FEA required.
Rotor resistance (vs. *f*)	R_r	Time harmonic (2D)
Stator leakage inductance (vs. *f*)	L_{ls}	Time harmonic (2D)
Rotor leakage inductance (vs. *f*)	L_{lr}	Time harmonic (2D)
Magnetising inductance (vs i_m)	L_m	Magnetostatic (2D)

The stator resistance is analytically determined whereas the rotor resistance which varies with frequency is determined as a function of frequency using a time-harmonic model of the machine with appropriate mesh sizes being selected for the rotor bars. The rotor leakage reactance is similarly determined [ALB08].

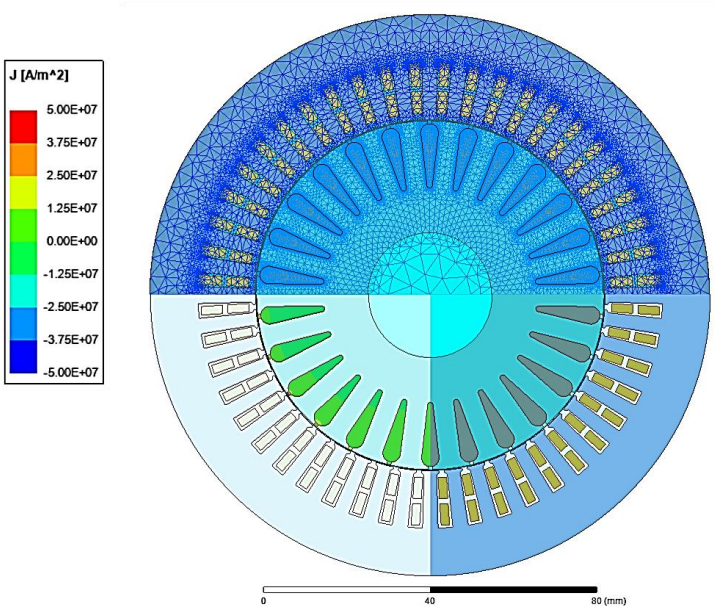

Fig. 7.2 FEA model of the pole changing M3, 4P machine showing mesh and rotor current density plot for at 200Hz and rated stator current of 4Apeak.

Two methods can be used to determine the stator leakage inductance in the active portion of the induction machine as discussed in [CHI08] and [ABD19]. To determine the stator leakage inductance using FEA, the useful flux that links the rotor due to currents flowing in the stator must

be neglected and the portion of the flux that does not contribute to torque production due to the imposed stator current must be determined. This condition can be achieved in FEA by replacing the region normally occupied by the rotor with air and exciting the stator with rated currents [BAN03]. Alternatively, to completely eliminate the useful flux linkage (this is required to determine the leakage flux) , the rotor surface may be replaced by a material of very low permeability or a zero vector potential boundary condition. In this case, the magnetic flux due to the current in the stator winding does not enter the rotor space and only the leakage flux remains. Both methods show agreement with each other and analytical methods [CHI08]. The leakage inductance is measured using an LCR meter. This, however, results in the rotor and stator leakage inductances being combined into a single measured value. The separation of the stator and leakage inductances is done by subtracting the stator leakage inductance obtained by simulation from the measured total leakage indutance. The magnetising inductance on the other hand is determined using a series of magnetostatic simulations. The stator is excited along the d-axis meaning $i_a = -i_b/2 = -i_c/2$. The rotor bars are not shorted by the end ring thus preventing any rotor current from flowing and the magnetic flux linking the stator winding for increasing values of currents is determined. This is the flux-linkage vs magnetising current curve. The referred-rotor resistance and the leakage inductances are measured using an LCR meter and compared with simulated results from FEA. The referred-rotor resistance and leakage inductance variation for the M3, 4P machine are shown in Fig. 6.3 and Fig. 6.4. The variation of the rotor leakage inductance over a frequency range is dependent on the machine parameters like rotor bar shape, bar depth, airgap thickness and lamination material etc. The variations of the inductances, as shown in Fig. 6.4, Fig. 6.6, Fig. 6.8 and Fig. 6.10 with frequency, can be explained by the influence of the induced eddy currents in the rotor bars with increasing frequency.

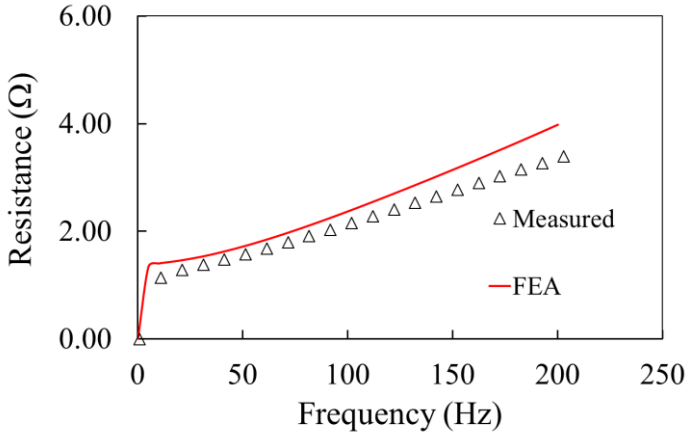

Fig. 6.3 Variation of rotor resistance referred to the stator of the M3, 4P machine with frequency.

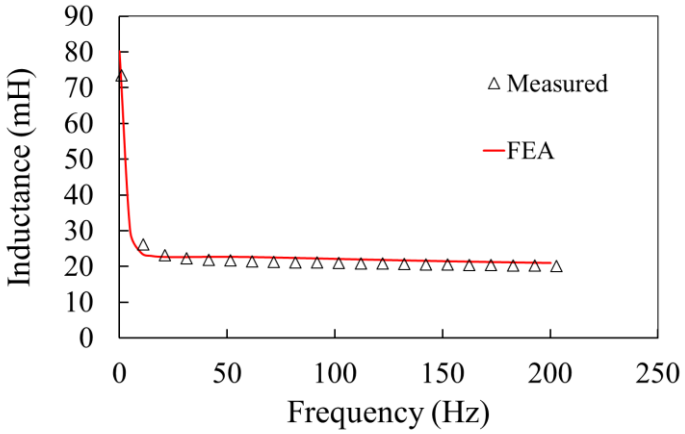

Fig. 6.4 Variation of rotor leakage inductance referred to the stator of the M3, 4P machine with frequency.

At lower frequencies, the depth of penetration of the flux is higher, and the flux linkage is higher than that at higher frequencies. At higher frequencies, eddy currents induced on the surface of the rotor bar shield the flux lines from penetrating and linking the interior of the rotor bars, resulting in a reduction of the inductance.

The referred-rotor resistance and referred-leakage inductance variation for the M3, 2P machine are shown in Fig. 6.5 and Fig. 6.6.

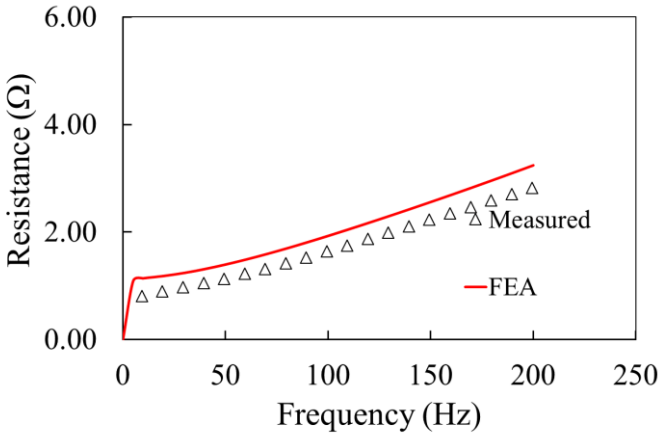

Fig. 6.5 Variation of rotor resistance referred to the stator of the M3, 2P machine with frequency.

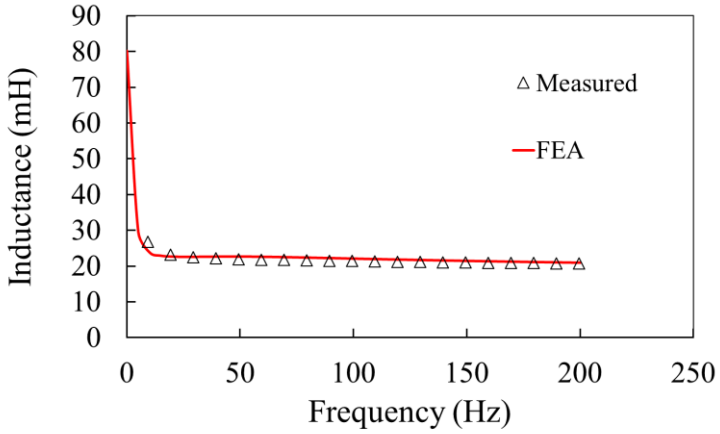

Fig. 6.6 Variation of rotor leakage inductance referred to the stator of the M3, 2P machine with frequency.

The referred-rotor resistance and referred-leakage inductance variation for the M6, 4P machine are shown in Fig. 6.7 and Fig. 6.8 respectively.

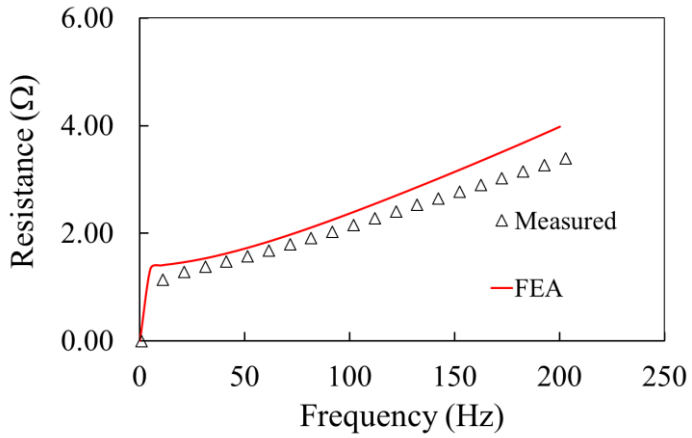

Fig. 6.7 Variation of rotor resistance referred to the stator of the M6, 4P machine with frequency.

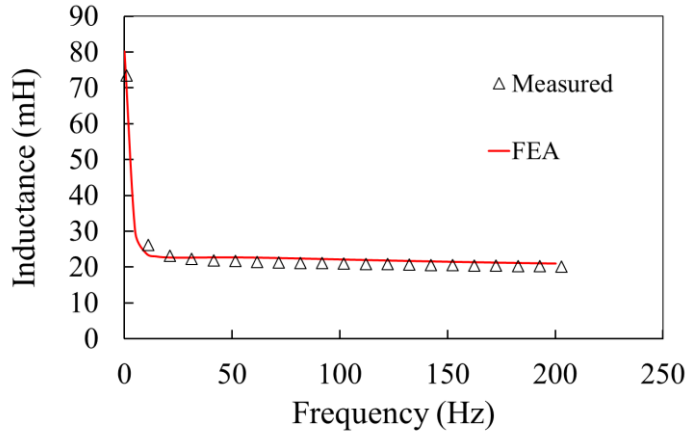

Fig. 6.8 Variation of rotor leakage inductance referred to the stator of the M6, 4P machine with frequency.

The referred-rotor resistance and referred-leakage inductance variation for the M6, 2P machine are shown in Fig. 6.9 and Fig. 6.10 respectively.

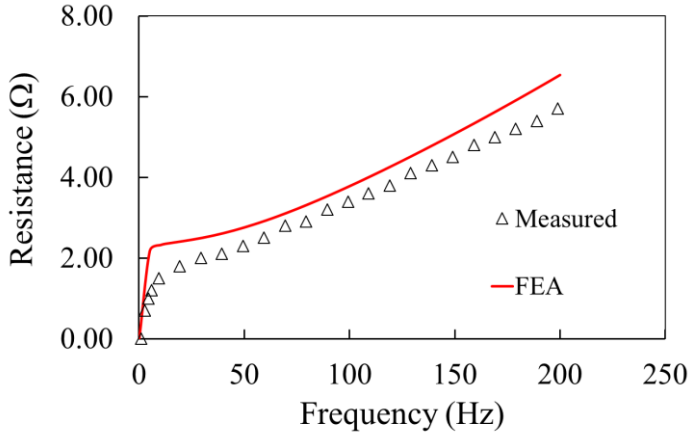

Fig. 6.9 Variation of rotor resistance referred to the stator of the M6, 2P machine with frequency.

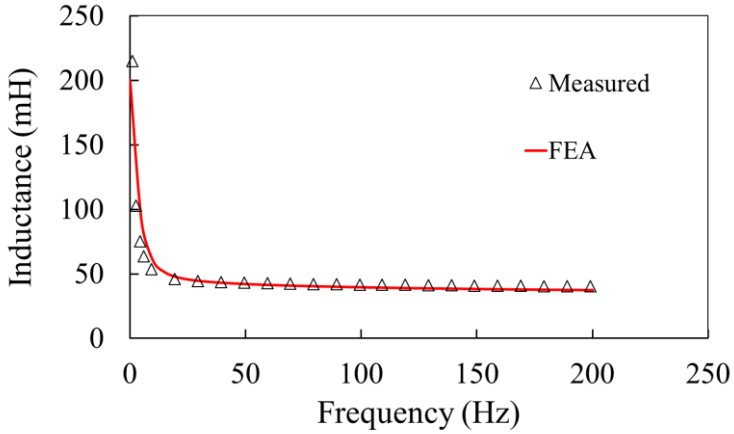

Fig. 6.10 Variation of rotor leakage inductance referred to the stator of the M6, 2P machine with frequency.

The comparison of the referred-rotor resistance and the rotor inductance variation of the 4 different machine configurations are shown in Fig. 6.11 and Fig. 6.12 respectively. The 2-pole machine referred -rotor resistances are lower than the corresponding resistances of the 4-pole machines. This is due to the winding factor being lower for the 2-pole windings as compared to the 4-pole machine. The rotor resistance is proportional to the square of the number of series turns per phase and the winding factor. The variation of the magnetising inductance with the no-load current is shown in Fig. 6.13 for all the 4 different machine configurations. The unsaturated magnetising inductance, which is the maximum value is shown in (6.32).

$$L_m = \frac{m\mu_o}{\pi g_{effective}} \left(\frac{k_w W}{p}\right)^2 D_{is} L_{stk} \tag{6.32}$$

The winding function of the 2-pole pole changing winding machine configuration is lower than that of the 4-pole configuration. In addition, though the number of poles is reduced by half and this reduction results in the increase of the magnetising inductance by 4 times and reduced in proportion to the square of the winding factor. For example the M3, 2P machine has a higher magnetising inductance than the M3, 4P. Similarly, the M6, 2P machine has a higher magnetising inductance than the M6, 4P machine. It is interesting to note that the corner magnetising current (which is the magnetising current at which the value of magnetising inductance begins to saturate) is lower for the 2-pole machine configurations. This implies that the magnetising inductance of the 2-pole machine begins to saturate with a lower value of magnetising current compared to the 4-pole machine. This means that at high torque low-speed regions of operation where the machine is fully saturated, the magnetising inductance is lower and hence the torque is lower for the 2-pole machine. On the flip-side, the higher unsaturated value of the 2-pole machines means that in the flux-weakening region where the magnetising current is low and the machine is unsaturated, the peak torque of the 2-pole machines is higher than the 4-pole machines. This results in the wider flux weakening region of the 2-pole machines but a lower peak torque.

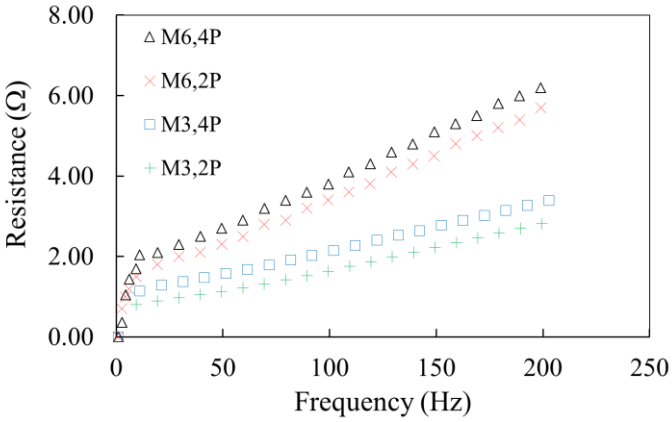

Fig. 6.11 Comparison of measured rotor resistance variation with frequency for different winding connections.

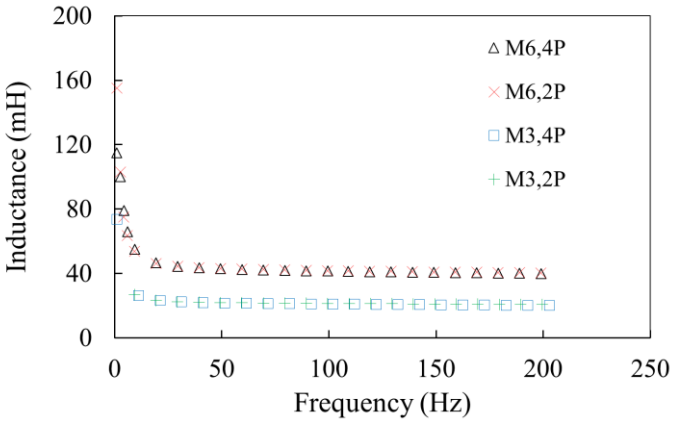

Fig. 6.12 Comparison of measured rotor inductance variation with frequency for different winding connections.

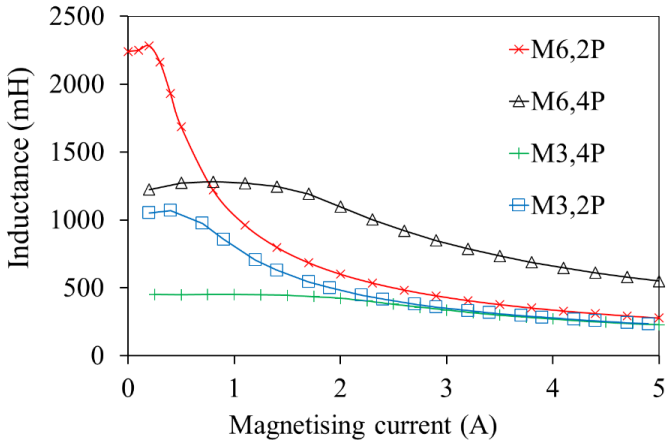

Fig. 6.13 Magnetising inductance variation with the magnetising current for different winding connections.

TABLE 6-3 NOMINAL INDUCTION MACHINE PARAMETERS FOR DIFFERENT MACHINE CONFIGURATIONS.

Parameter	**Symbol**	**M3, 4P**	**M3, 2P**	**M6, 4P**	**M6, 2P**
Stator resistance (Ω)	R_s	8.89	8.89	17.78	17.78
Rotor resistance (Ω)	R_r	1.71	1.39	2.93	2.3
Stator leakage (mH)	L_{ls}	32.04	16.06	15.96	8.27
Rotor leakage inductance (mH)	L_{lr}	40.6	21.5	40.6	21.5
(Unsat.)Magnetising inductance (mH)	L_m	451	1073	1272	2280

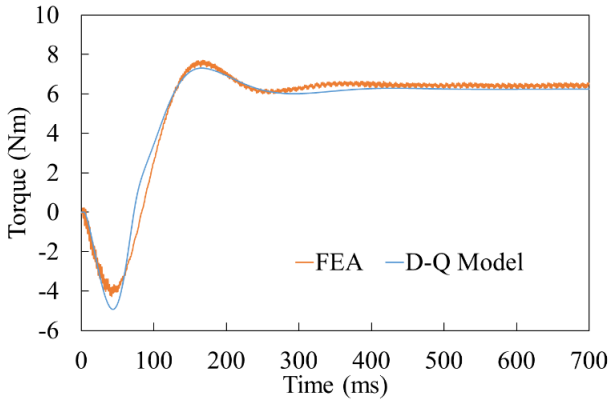

Fig. 6.14 Simulated torque from FEA and dynamic d-q model.

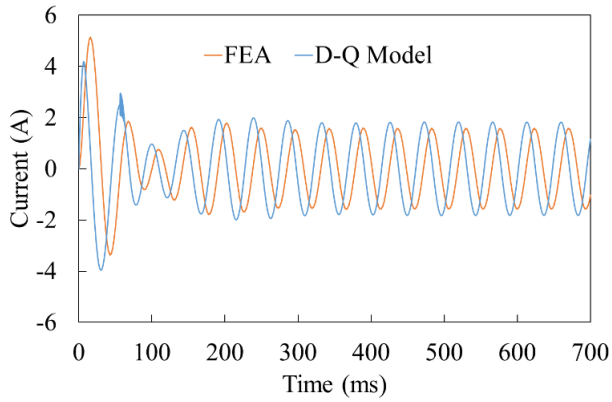

Fig. 6.15 Simulated A-phase current from FEA and dynamic d-q model.

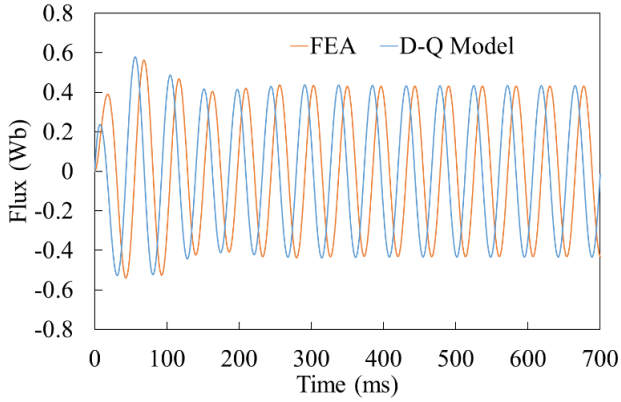

5

Fig. 6.16 Simulated A-phase flux linkage from FEA and dynamic d-q model.

The nominal parameter list for the different machine configurations are shown in TABLE 7-3. Using these parameters in the dynamic SIMULINK model, voltage fed, open-loop direct online starting is simulated and the same conditions are simulated in an FEA model to compare the torque current and flux-linkage waveforms from these simulations as shown in Fig. 6.14, Fig. 6.15 and Fig. 6.16 respectively. The models show a good correlation and the non-linear dynamic model can be

used as a replacement for the FEA model for studying the dynamic performance of the machine during the pole changing operation.

6.2.2 Comparison of Transient Operation of 3-phase Pole Changing Machine: Open-loop and Field Oriented Control

Using the parameters of the induction machine determined from the above analysis in the dynamic SIMULINK model, online open-loop pole changing can be performed. The pole changing operation can be performed under two conditions. In the first case, the induction machine is ramped up to the setpoint speed with the higher pole number and then the pole changing operation is performed resulting in a speed and torque transient. This operation can be performed under loaded or unloaded conditions. Alternatively, the pole changing operation can be performed when the induction machine is operated at a fixed speed simulating the condition where the machine is coupled to a dynamometer or an engine. In this case, the pole changing operation is performed at a fixed speed and the slip of the machine is adjusted (by controlling the stator frequency). The latter scenario is of greater interest for the target application where the induction machine is used as a starter-generator.

A. Principle of Field Oriented Control

Field oriented control, a brief overview of the principle of is presented here, can be used to control the machine in a closed-loop allowing for better transient performance. The objective of the field oriented control of the induction machine is to control the torque and flux of independently of one another similar to a DC motor. The torque equation of a DC motor is shown in (6.33) where k_T, ψ_f and i_a.are the motor torque constant, the flux due to PM or the field winding and the armature winding current respectively. Due to the independent nature of these windings in a DC machine, the torque and flux can be controlled separately. However, in an induction machine, since it is the stator or armature currents that create the rotor currents and the air gap field, there is a coupling between these quantities. The rotor currents from the torque expression of (6.6) can be rewritten in terms of stator currents and rotor flux. The expressions for the relationship between the rotor flux and rotor currents of the induction machine in the rotating reference frame are shown in (634) and (6.35). Substituting these values in (6.6) yields the torque equation shown in (6.36)

$$T_{DC} = k_T \psi_f i_a \tag{6.33}$$

$$i_{qr} = \frac{\psi_{qr}^{e} - L_m i_{qs}^{e}}{L_r} \tag{6.34}$$

$$i_{dr} = \frac{\psi_{dr}^{e} - L_m i_{ds}^{e}}{L_r} \tag{6.35}$$

$$T_e = \frac{3}{2}\frac{P}{2}\frac{L_m}{L_r}(i_{qs}^{e}\psi_{dr}^{e} - i_{ds}^{e}\psi_{qr}^{e}) \tag{6.36}$$

Decoupling the toque and flux is possible if $\psi_{qr}^{e} = 0$. Then the torque equation of the induction machine reduces to (6.37) which is comparable to that of the DC motor torque in (6.32)

$$T_e = \frac{3}{2}\frac{P}{2}\frac{L_m}{L_r}\, i_{qs}^{e}\psi_{dr}^{e} \tag{6.37}$$

When the rotor flux axis is oriented along the d-axis of the synchronously rotating reference frame this condition of $\psi_{qr}^{e} = 0$ is satisfied as shown in Fig. 6.17.

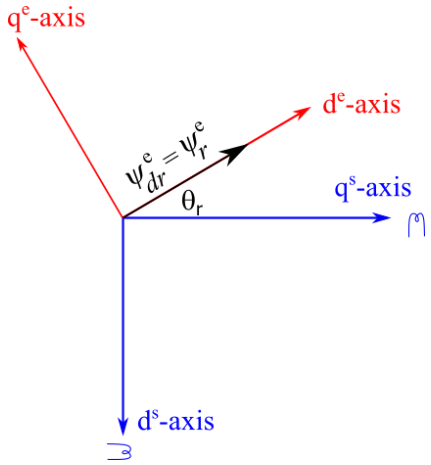

Fig. 6.17 Phasor diagram showing rotor flux alignment to the synchronously rotating reference frame for field oriented control.

The rotor voltage equations under the field orientation condition are shown in (6.38) and (6.39).

$$0 = R_r i_{qr}^{e} + (\omega_e - \omega_r)\psi_{dr}^{e} \tag{6.38}$$

$$0 = L_r i_{qr}^{e} + L_m i_{qs}^{e} \tag{6.39}$$

$$\omega_{sl} = (\omega_e - \omega_r) = \frac{L_m R_r}{\psi_{dr}^{e} L_r} i_{qs}^{e} \tag{6.40}$$

The unknown rotor current can be eliminated from (6.38) and the value of the rotor slip speed is calculated using (6.36). Once the slip speed is known, with an encoder on the shaft providing the rotor angular speed, the rotor flux axis which is rotating at the synchronous speed can be determined from (6.41).

$$\theta_r = \int_0^t (\omega_{rotor} + \omega_{sl})\, dt \tag{6.41}$$

This method of orienting the rotor flux vector along the d-axis of the rotating reference frame is called indirect rotor field oriented control (IRFOC) since the rotor flux orientation in the air gap is not directly determined from the flux measurement but rather indirectly by the use of the stator current measurements.

B. PI Controller Tuning for IRFOC

The linearized model of the induction machine can be used to design the PI controller parameters to achieve the desired transient performance. The linearized control block diagram of a DC motor with a speed controller and a current controller is shown in Fig. 6.18. The equivalent parameters for the induction machine are shown in (6.42) and (6.43).

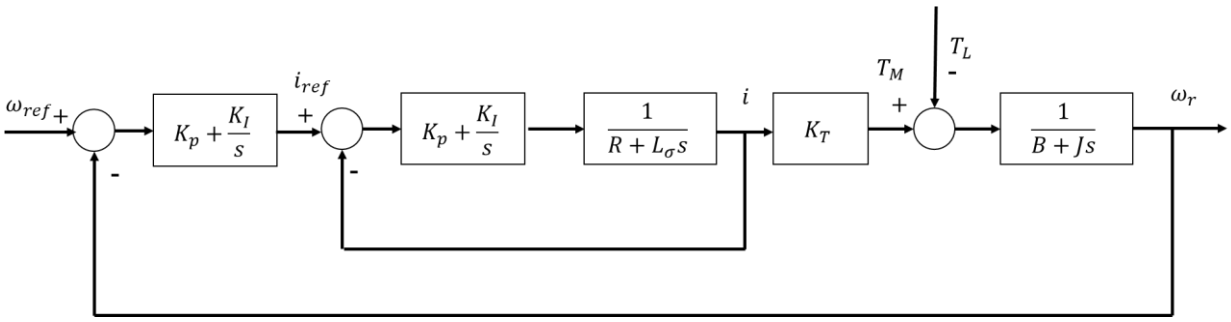

Fig. 6.18 Dynamic plant model of an induction machine with speed and current control

$$R = R_s + R_r \left(\frac{L_m}{L_r}\right)^2 \tag{6.42}$$

$$\sigma L_s = L_s - \frac{L_m^2}{L_r} \tag{6.43}$$

The open-loop transfer function in the current loop is given by (6.44). Using the PI controller as a pole-zero cancellation transfer function the ratio of the K_I to K_P value is given in (6.45). The PI values that cancel the zero of the open-loop transfer function is given by (6.46) and (6.47).

$$G_I(s) = \left(K_P + \frac{K_I}{s}\right)\left(\frac{1}{R_s + s\sigma L_s}\right) = \frac{K_P}{s}\left(s + \frac{K_I}{K_P}\right)\left(\frac{\frac{1}{s\sigma L_s}}{\frac{R}{s\sigma L_s} + s}\right) \tag{6.44}$$

$$\frac{K_I}{K_P} = \frac{R}{\sigma L_s s} \tag{6.45}$$

$$K_P = \omega_c \sigma L_s \tag{6.46}$$

$$K_I = \frac{R}{\sigma L_s} K_P \tag{6.47}$$

Similarly, for the speed loop PI controller parameters can be determined by assuming that the compared to the mechanical system, the current response of the electrical system is instantaneous, the open-loop transfer function is given by (6.48). The PI controller parameters are given by (6.50) and (6.51).

$$G_I(s) = \left(K_P + \frac{K_I}{s}\right)\left(\frac{1}{B + sJ}\right) = \frac{K_P}{s}\left(s + \frac{K_I}{K_P}\right)\left(\frac{\frac{1}{sJ}}{\frac{B}{sJ} + s}\right) \tag{6.48}$$

$$\frac{K_I}{K_P} = \frac{R}{Js} \tag{6.49}$$

$$K_P = \omega_c J \tag{6.50}$$

$$K_I = \frac{B}{J} K_P \tag{6.51}$$

C. Fixed Speed Pole Changing Transient Operation

In the first case, the speed of the rotor is fixed at 500rpm (in the constant torque region) and at, in the second case, 2600rpm (in the flux weakening region where the torque capability of the 4-pole machine is lower than that of the 2-pole machine) and the pole changing operation is performed at 1.5s. The torque transient, the A-phase and X-phase current transients, the q-axis and d-axis current transients are observed. The torque transient waveforms with the rated current of 4A peak current on the DC bus and at 500rpm with open-loop control and IRFOC are shown in Fig. 6.19 and Fig. 6.20 respectively. The transient performance is improved significantly with the IRFOC during pole changing and at start-up. With IRFOC, the negative torque transient that occurs during pole changing when open-loop control is used is reduced from -5Nm to 0Nm. The transient period is also

shortened with the closed-loop control. The A-phase and X-phase current waveform during start-up and pole-changing operation with open-loop control and closed-loop IRFOC are shown in Fig. 6.21 and Fig. 6.22 respectively. With the closed-loop IRFOC, the current transients are also reduced compared to the open-loop control. This can be explained by observing the q-axis and d-axis current transients during pole changing from the waveforms with open-loop control and closed-loop IRFOC shown in Fig. 6.23, Fig. 6.24 and Fig. 6.25, Fig. 6.26 respectively. When the pole changing operation is performed, the transient occurs for the duration in which the 4-pole flux in the rotor has to decay down to zero, while the two-pole field is established in the rotor. In open-loop control, the torque and flux are not decoupled as is the case in IRFOC and as a result, the transients in the d-axis and q-axis currents last for longer and result in a large torque and current transient. With closed-loop control, these currents can be independently controlled as shown in Fig. 6.24 and Fig. 6.26 and this results in better transient performance. Similarly, improved transient performance is observed in the flux weakening region. At 2600rpm the 4-pole and 2-pole machines are both in the flux weakening region of operation. The transient torque performance with open-loop control and IRFOC are shown in Fig. 6.27 and Fig. 6.28 respectively. Similar to the performance at low speed, the transient performance is improved with the closed-loop control. Similar improvement of the transient performance is seen by comparing the A-phase and the X-phase current waveforms shown in Fig. 6.29 and Fig. 6.30 respectively. The sharp spike of current in the q-axis and d-axis with the open-loop control as seen in Fig. 6.31 and Fig. 6.33 respectively is reduced significantly with IRFOC as seen from Fig. 6.32 and Fig. 6.34 respectively.

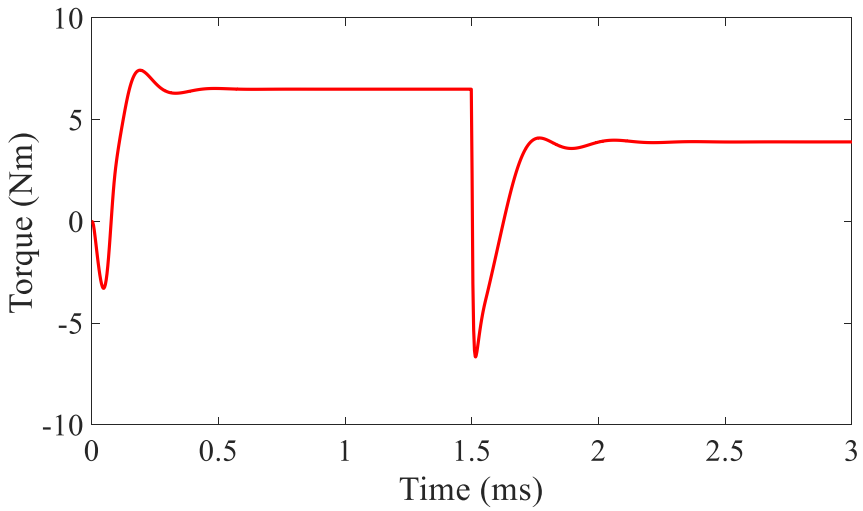

Fig. 6.19 Open-loop control torque transient with pole changing operation at 500rpm with rated current.

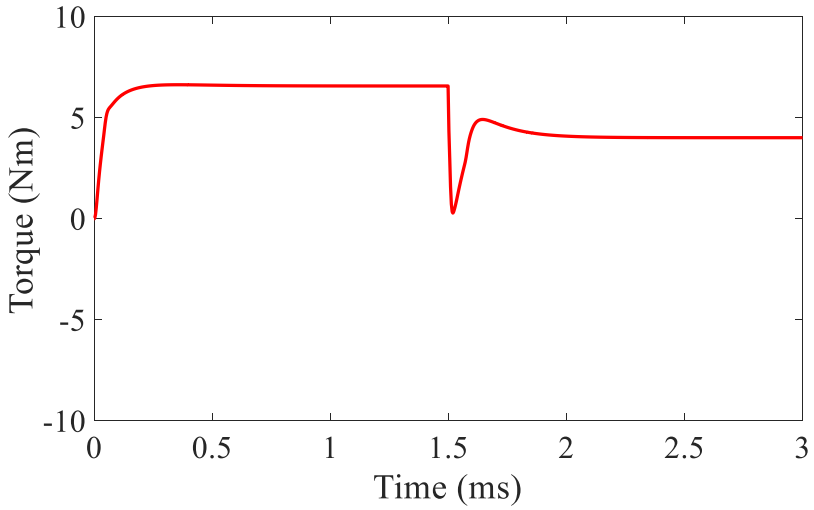

Fig. 6.20 IRFOC torque transient with pole changing operation at 500rpm with rated current

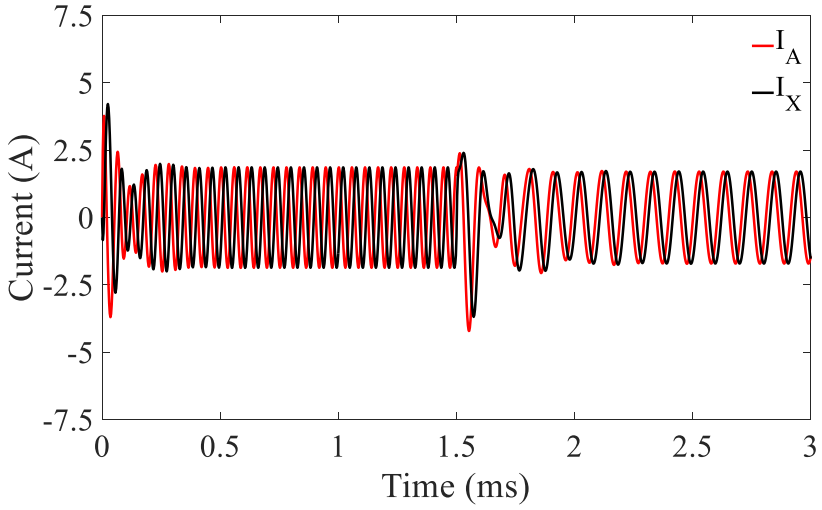

Fig. 6.21 Open-loop control A-phase and X-phase current with pole changing operation at 500rpm.

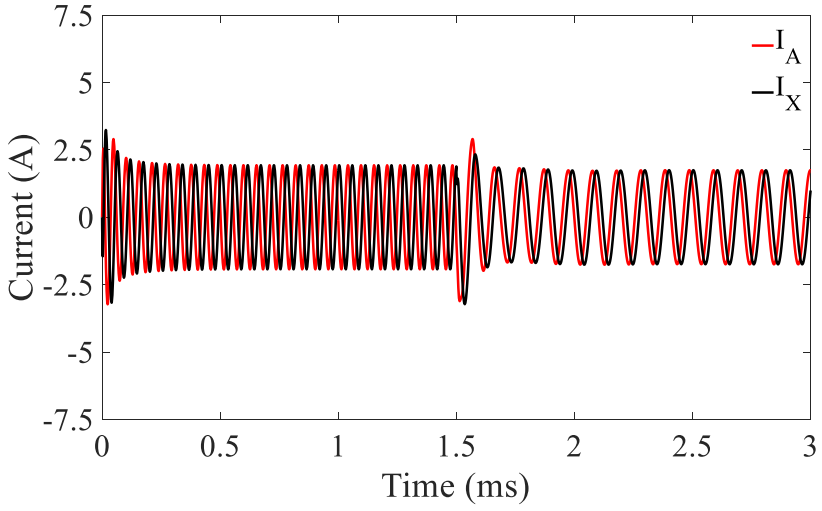

Fig. 6.22 IRFOC A-phase and X-phase current with pole changing operation at 500rpm.

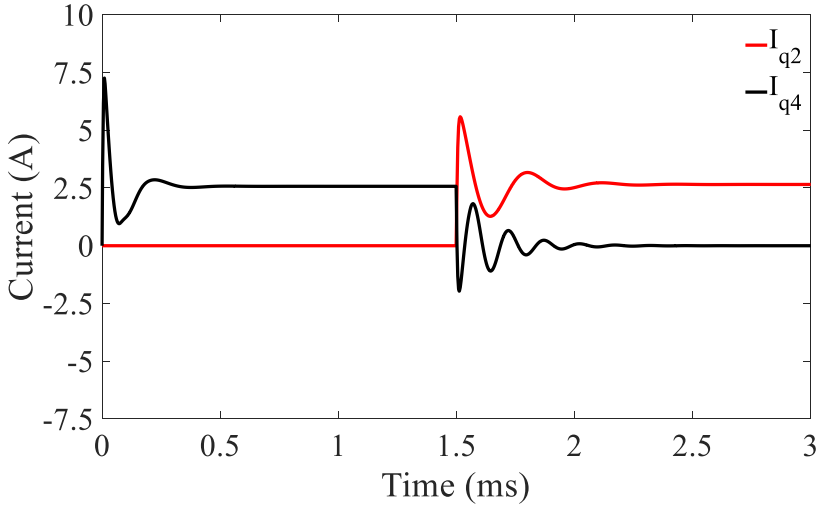

Fig. 6.23 Open-loop control q-axis current with pole changing operation at 500rpm.

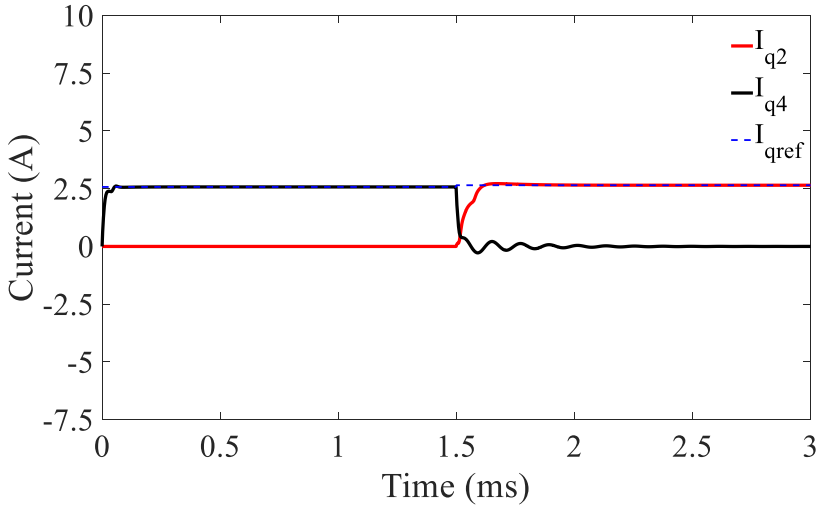

Fig. 6.24 IRFOC q-axis current with pole changing operation at 500rpm.

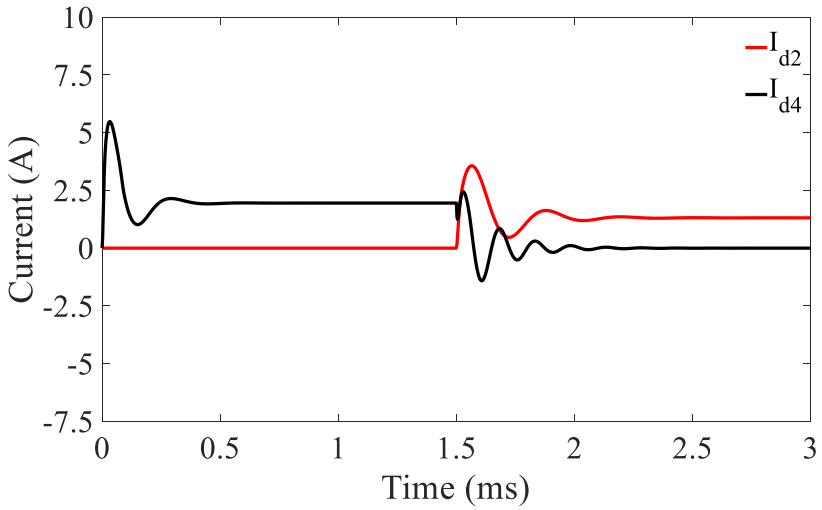

Fig. 6.25 Open-loop control d-axis current with pole changing operation at 500rpm.

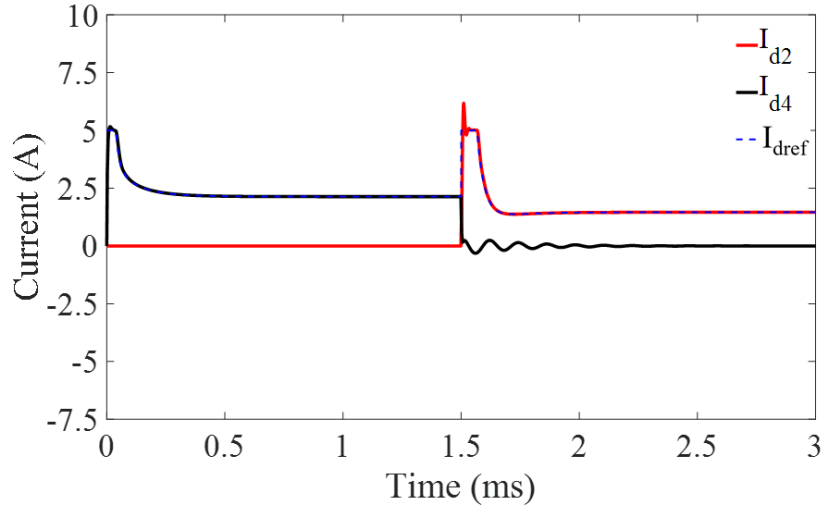

Fig. 6.26IRFOC d-axis current with pole changing operation at 500rpm.

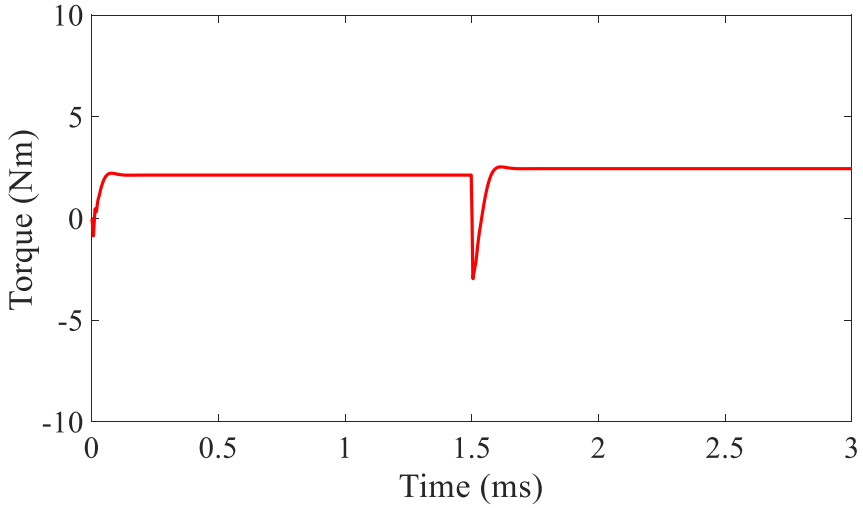

Fig. 6.27 Open-loop control torque transient with pole changing operation at 2600rpm with rated current.

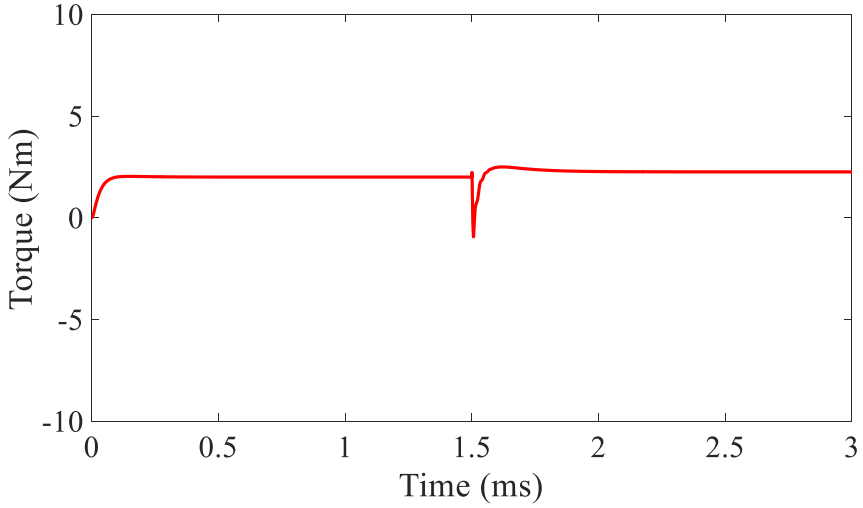

Fig. 6.28 IRFOC torque transient with pole changing operation at 2600rpm with rated current

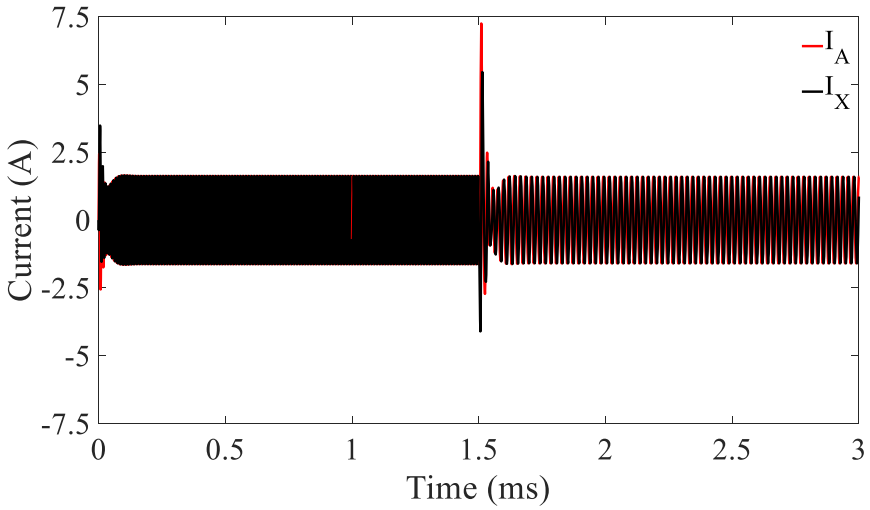

Fig. 6.29 Open-loop control A-phase and X-phase current with pole changing operation at 2600rpm.

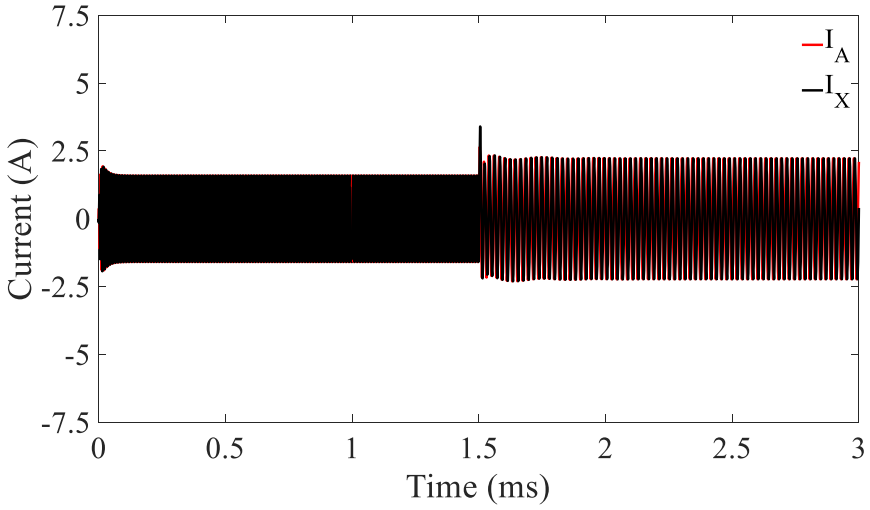

Fig. 6.30 IRFOC A-phase and X-phase current with pole changing operation at 2600rpm.

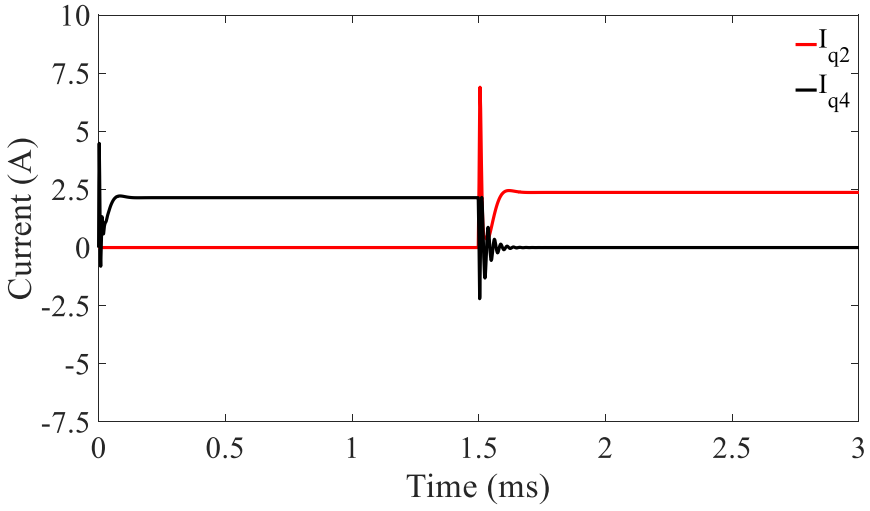

Fig. 6.31 Open-loop control q-axis current with pole changing operation at 2600rpm.

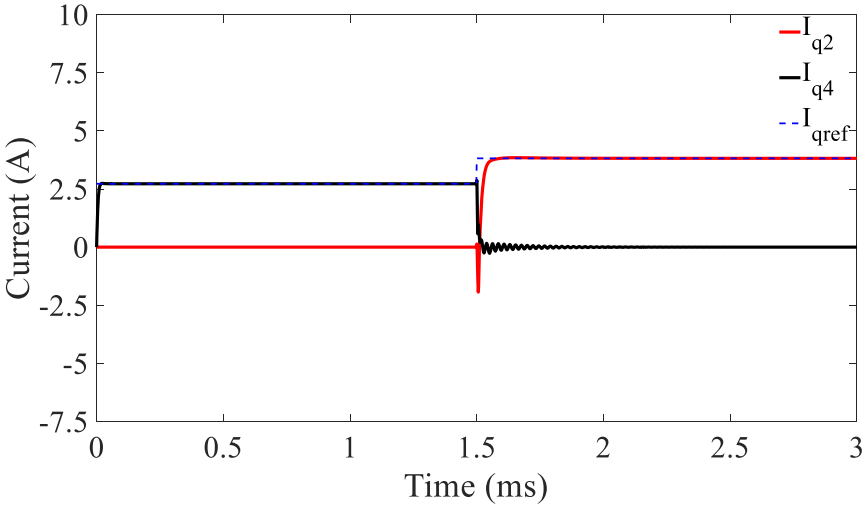

Fig. 6.32 IRFOC q-axis current with pole changing operation at 2600rpm.

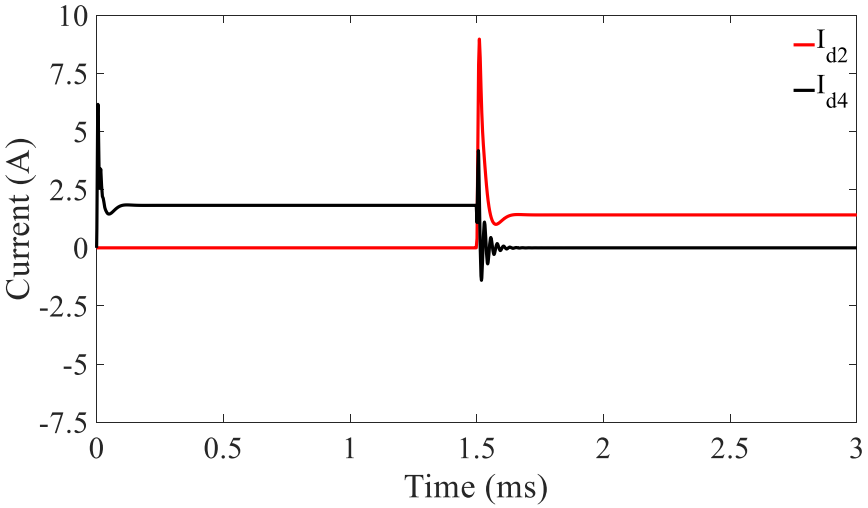

Fig. 6.33 Open-loop control d-axis current with pole changing operation at 2600rpm.

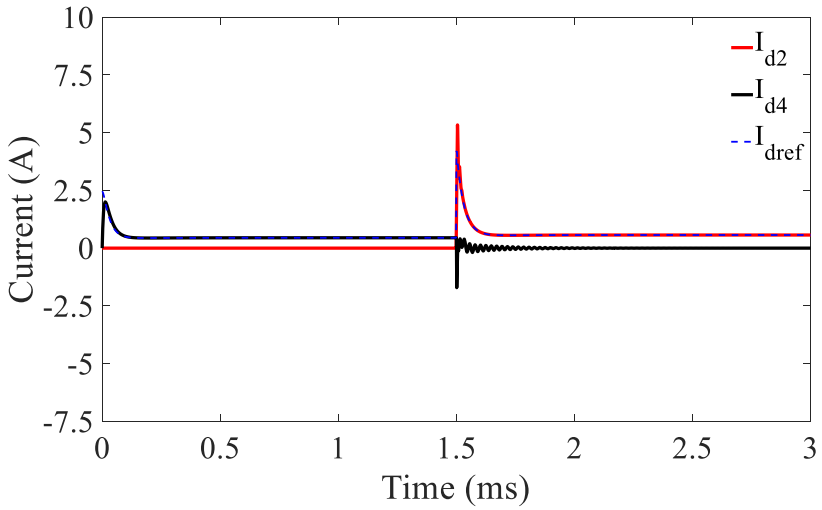

Fig. 6.34 IRFOC d-axis current with pole changing operation at 2600rpm.

D. Pole Changing Transient Operation during Start-up

In the second scenario, the voltage (amplitude and frequency) corresponding to the set-point of speed is applied to the machine and the rotor speed is allowed to ramp up to this value under no-load and loaded conditions with open-loop control. In the closed-loop IRFOC, the q-axis current is determined using a PI controller as explained in the previous section and the d-axis current in the flux weakening region is chosen to be equal to the vale that results in the rated flux in the machine. In the flux weakening region, the d-axis current is reduced in proportion to the speed beyond the corner speed of the induction machine. The duration of the start-up transient is determined by the rotor inertia and the starting torque capability of the simulated machine. The combined inertia of the rotor and shaft is $8.6 \times 10^{-3}\ kg\ m^2$.

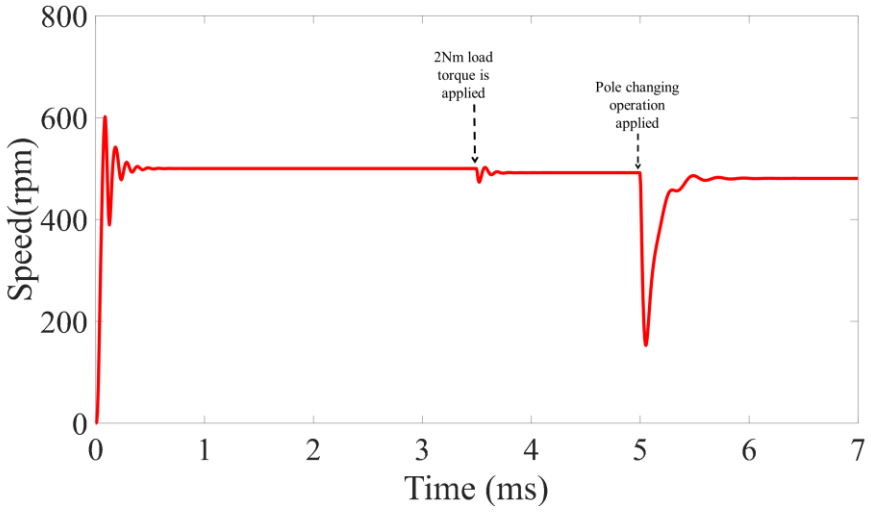

Fig. 6.35 Speed transient with open-loop control for a reference speed of 500rpm.

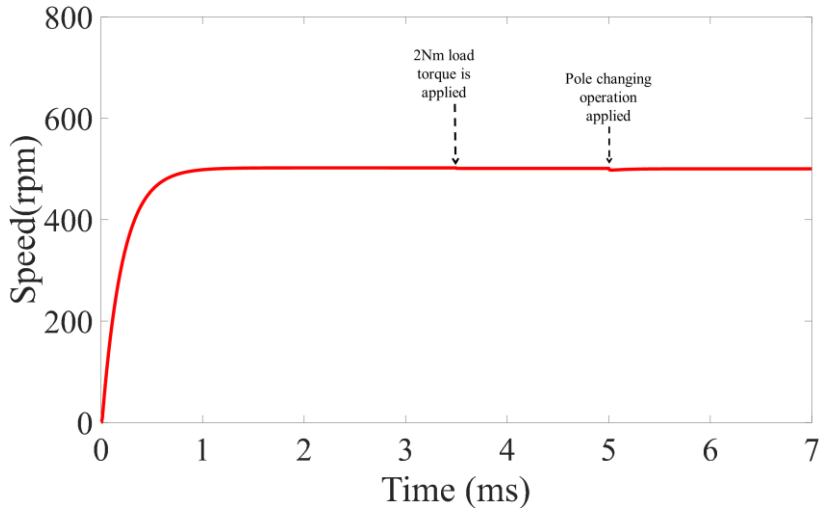

Fig. 6.36 Speed transient with IRFOC for a reference speed of 500rpm.

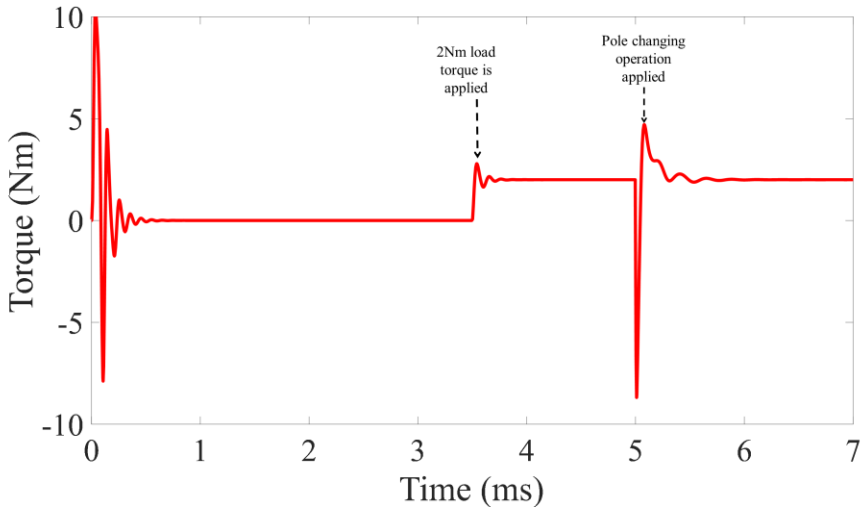

Fig. 6.37 Torque transient with open-loop control for a reference speed of 500rpm.

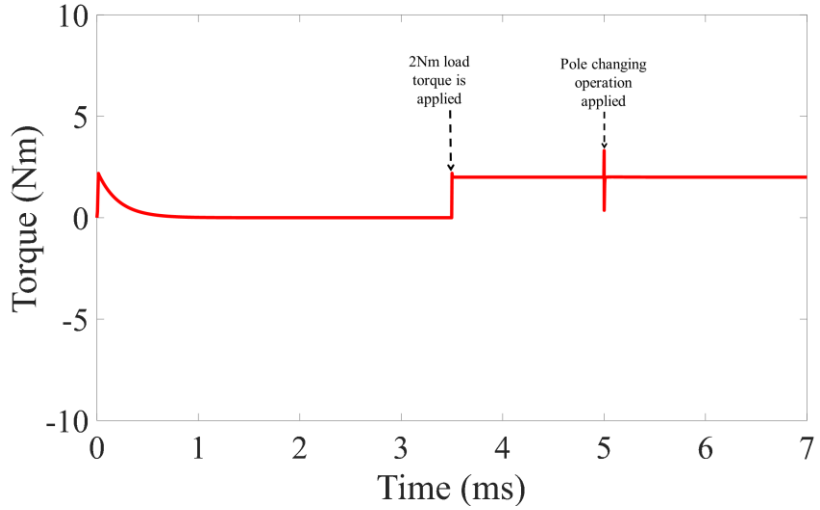

Fig. 6.38 Torque transient with IRFOC for a reference speed of 500rpm.

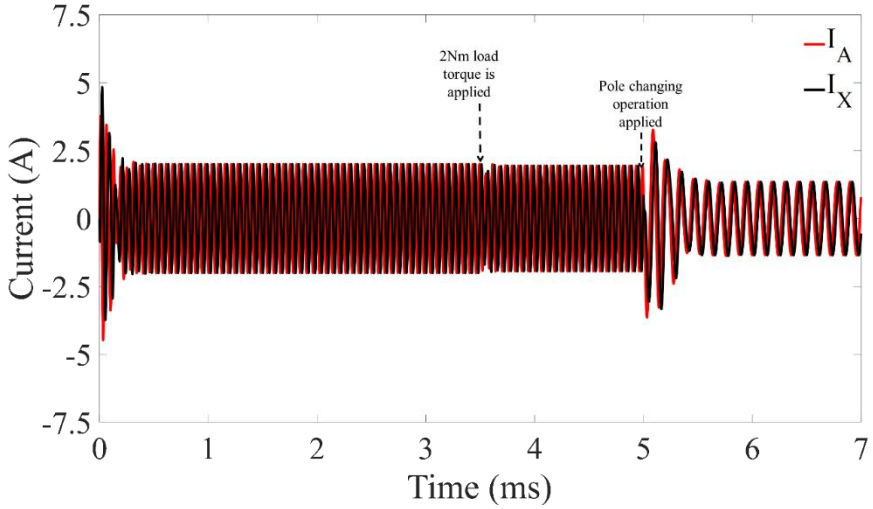

Fig. 6.39 A-phase and X-phase current transient with open-loop control for a reference speed of 500rpm.

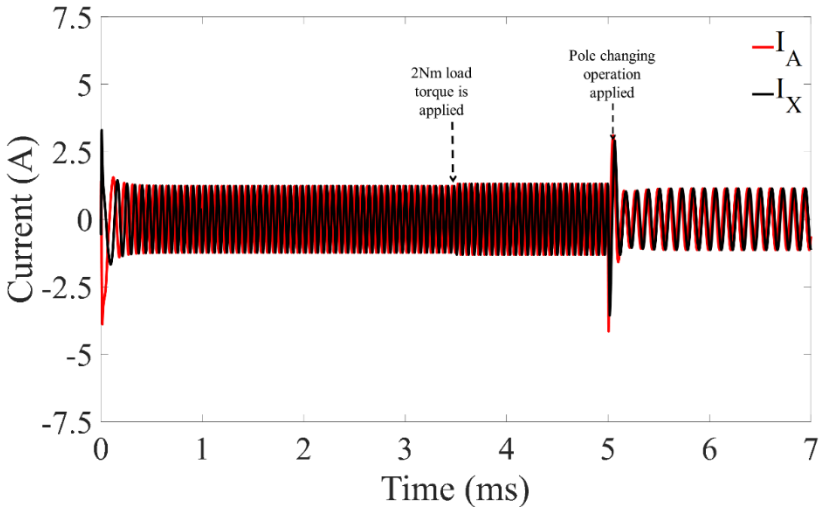

Fig. 6.40 A-phase and X-phase current transient with IRFOC for a reference speed of 500rpm.

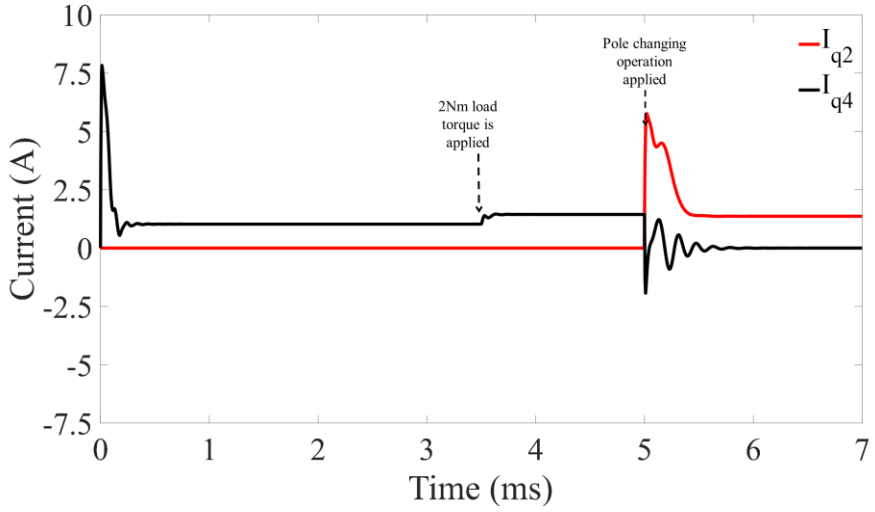

Fig. 6.41 q-axis current transient with open-loop control for a reference speed of 500rpm.

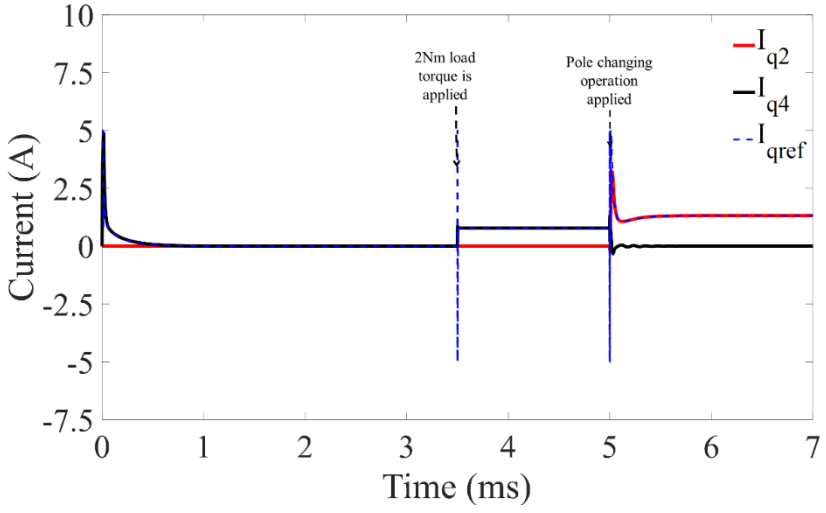

Fig. 6.42 q-axis current transient with IRFOC for a reference speed of 500rpm.

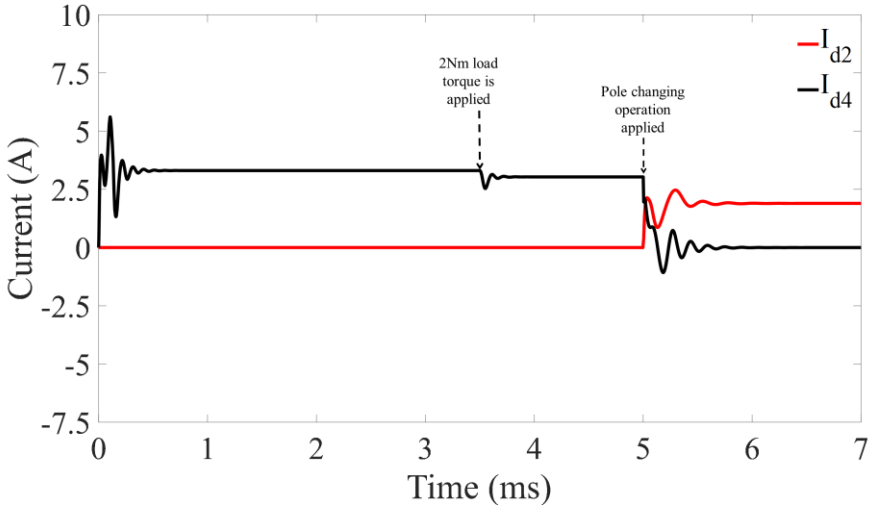

Fig. 6.43 d-axis current transient with open-loop control for a reference speed of 500rpm.

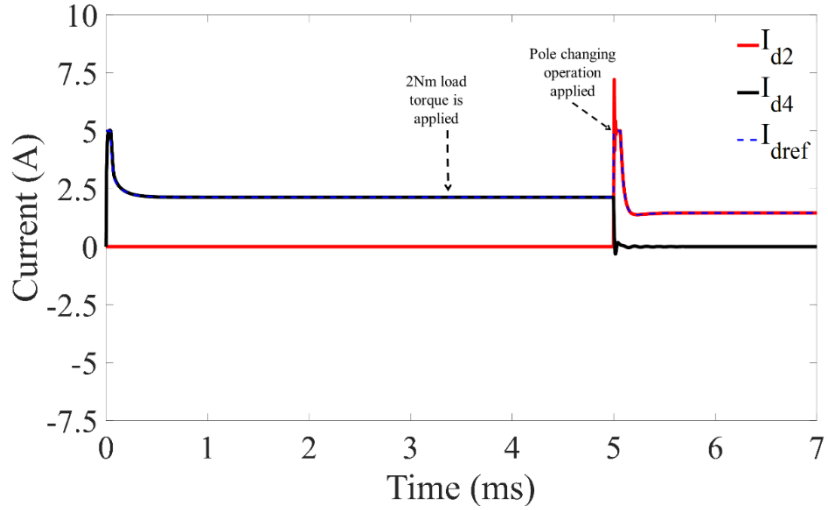

Fig. 6.44 d-axis current transient with IRFOC for a reference speed of 500rpm.

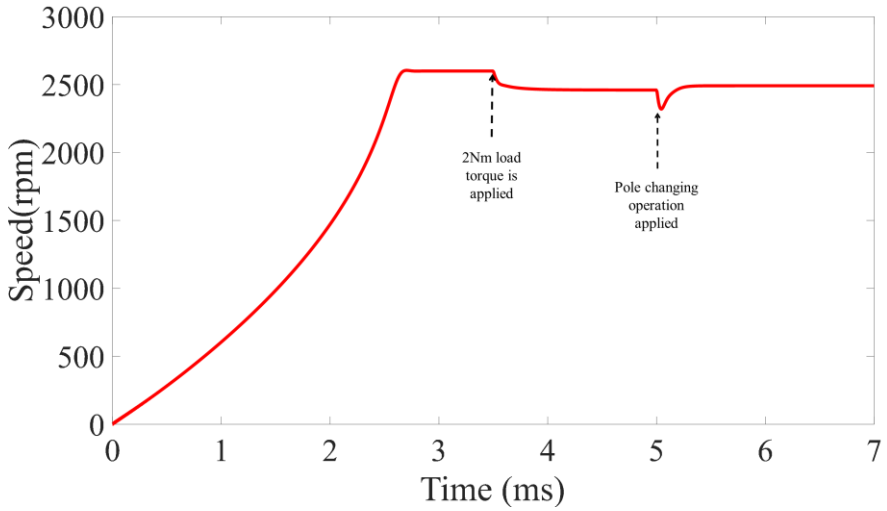

Fig. 6.45 Speed transient with open-loop control for a reference speed of 2600rpm

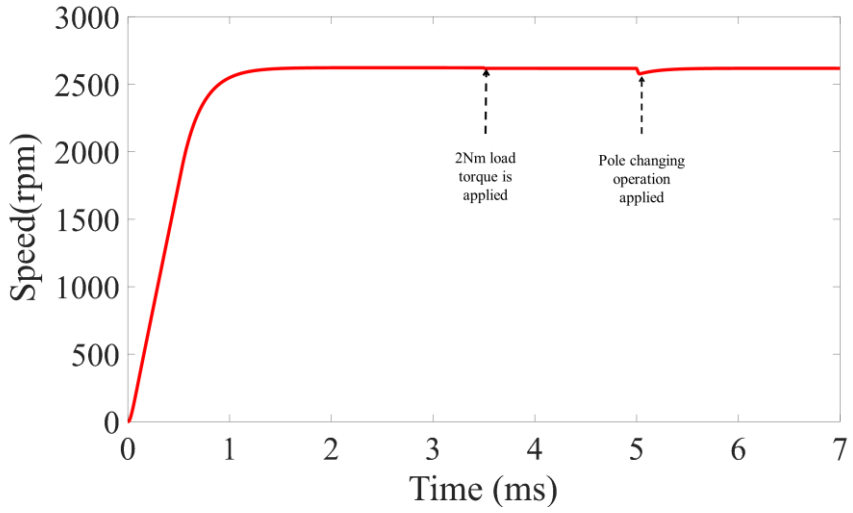

Fig. 6.46 Speed transient with IRFOC for a reference speed of 2600rpm.

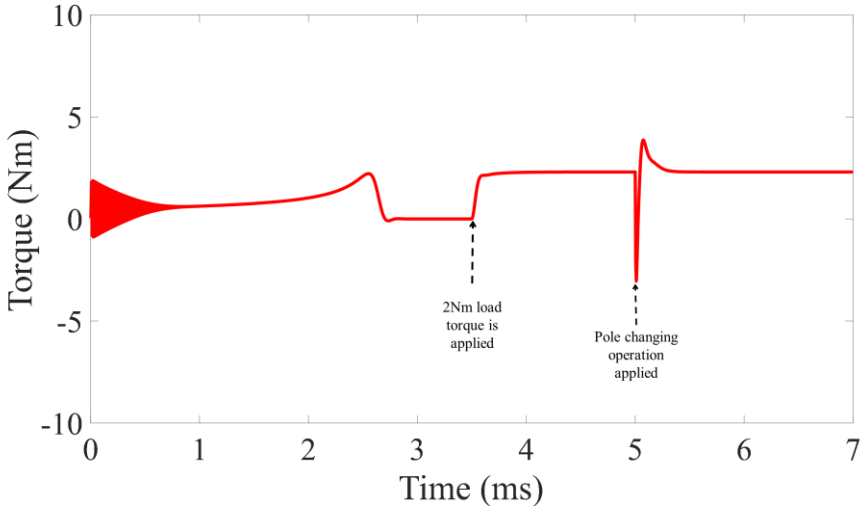

Fig. 6.47 Torque transient with open-loop control for a reference speed of 2600rpm.

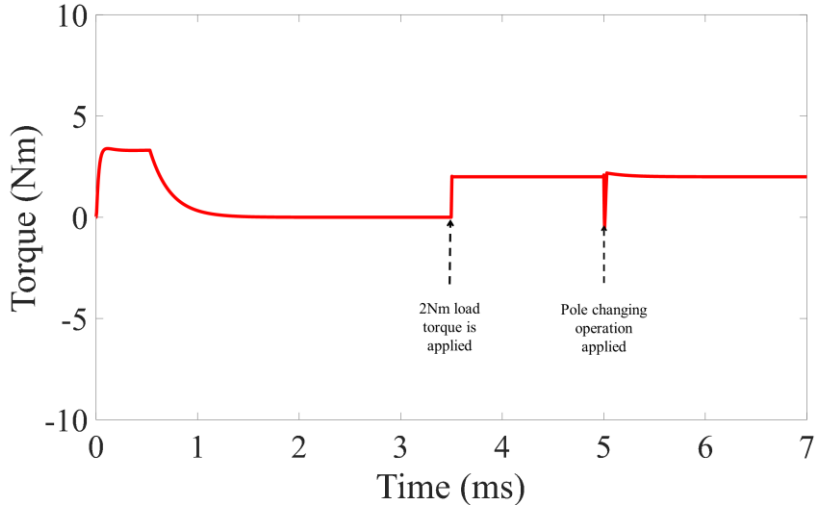

Fig. 6.48 Torque transient with IRFOC for a reference speed of 2600rpm.

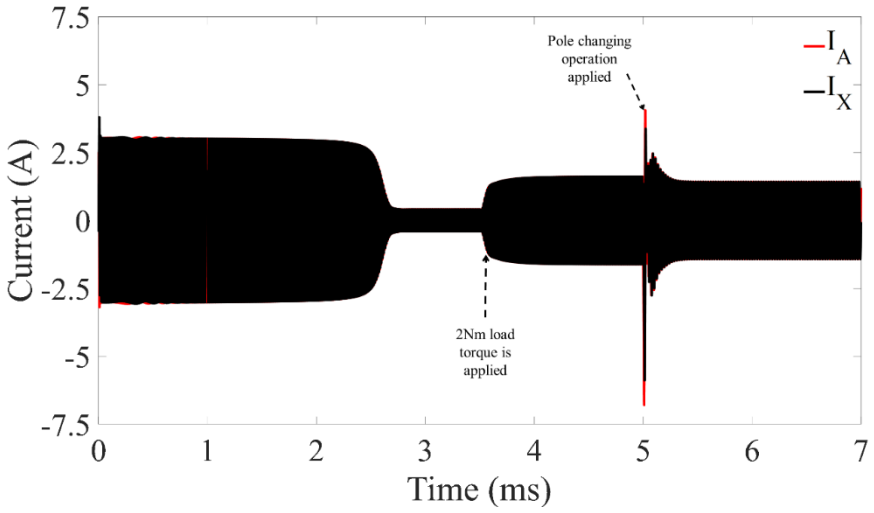

Fig. 6.49 A-phase and X-phase current transient with open-loop control for a reference speed of 2600rpm.

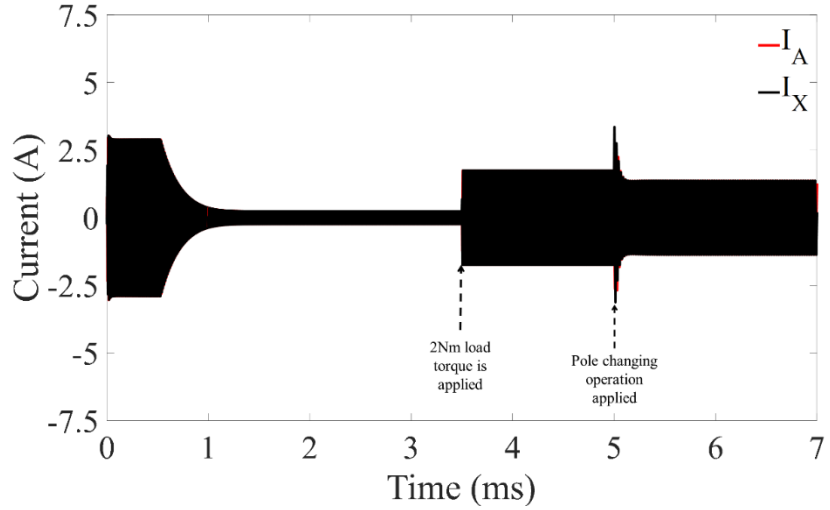

Fig. 6.50 A-phase and X-phase current transient with IRFOC for a reference of 2600rpm.

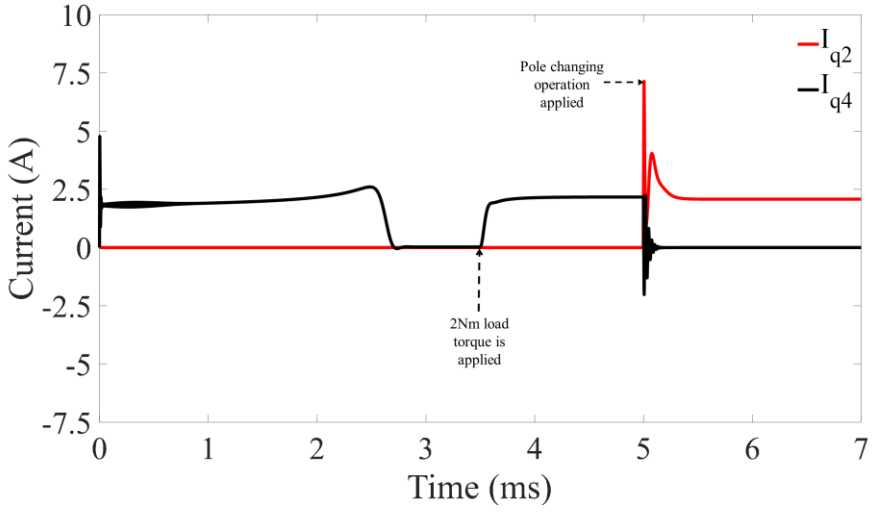

Fig. 6.51 q-axis current transient with open-loop control for a reference speed of 2600rpm.

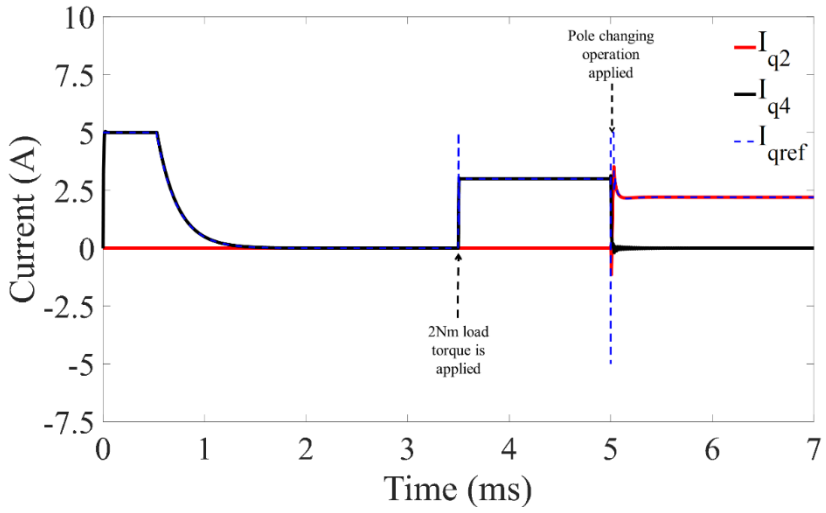

Fig. 6.52 q-axis current transient with IRFOC for a reference speed of 2600rpm.

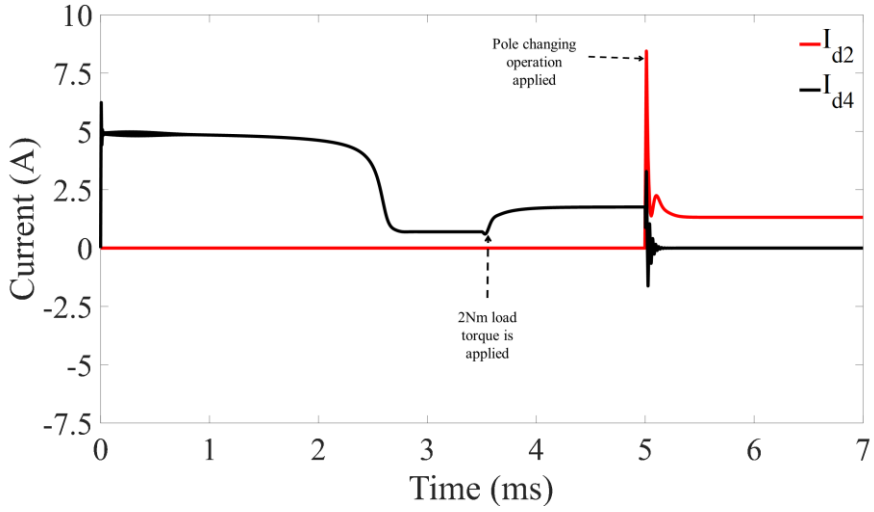

Fig. 6.53 d-axis current transient with open-loop control for a reference speed of 2600rpm.

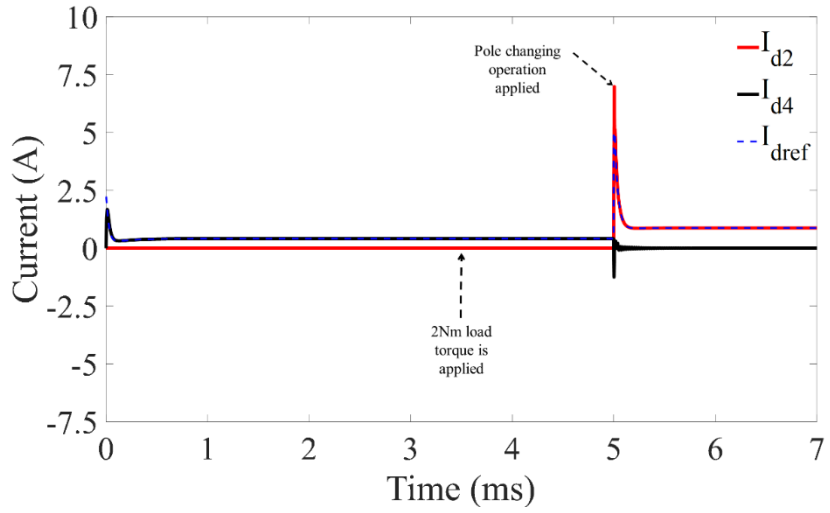

Fig. 6.54 d-axis current transient with IRFOC for a reference speed of 2600rpm.

6.3 Dynamic Model and FOC of 6-phase Pole Changing Winding IM

The spatial angle between the phases of the 6-phase pole changing winding induction machine is shown in Fig. 6.55. For enabling pole changing operation that requires the reversal of current in one-half of the phase coils in all six-phases of the machine, the phases are split into 2 coil groups A1, A2 for the A-phase, X1, X2 for the X-phase etc. Following the same method of vector space decomposition as for the 3-phase machine, for dynamic transient modelling, each phase is transformed onto reference 4-pole and 2-pole d-q axes.

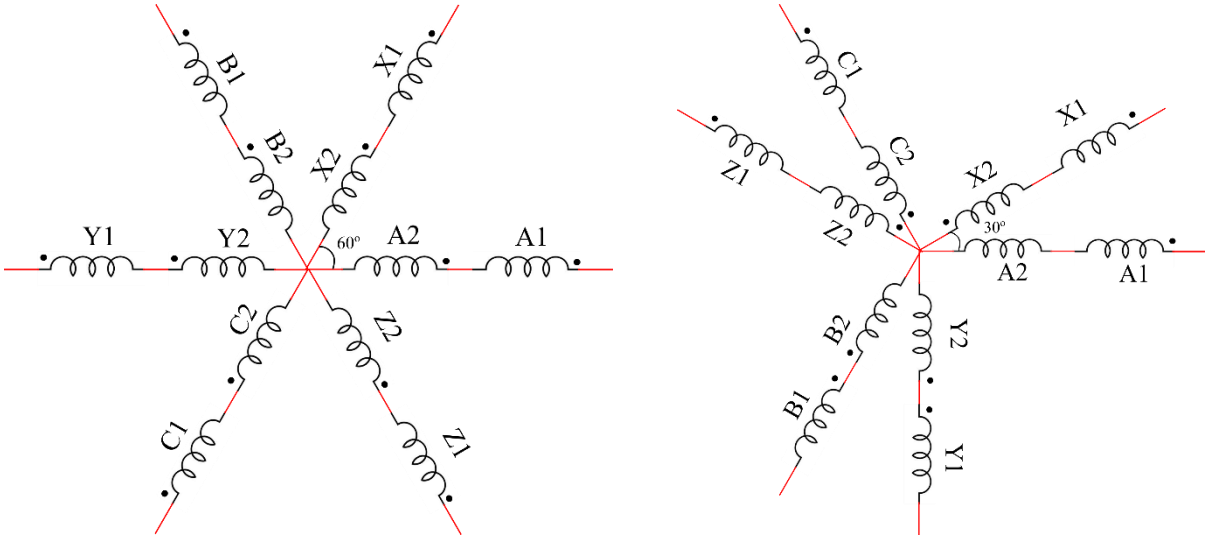

(a) 4-pole connection (b) 2-pole connection

Fig. 6.55 Stator winding phasor connection showing spatial angle for the 6-phase pole changing winding induction machine with a (a) 4-pole connection and (b) 2-pole connection.

Transient modelling of multiphase machines with an arbitrary displacement between the phases and for a 6-phase machine, in particular, have been well established in [NEL74] and [LIP80] respectively. In [SIN05] a simplified model for a 6-phase induction machine is presented. The model represents the two sets of 3-phases of the 6-phase machine onto d-q axes which are displaced with each other by the same angle as the angle between the two 3-phase sets. This model has been adapted here for the 6-phase pole changing winding induction machine. A phasor representation of the stator and the rotor windings of the 6-phase induction machine is shown in Fig. 6.56. The two sets of 3-phase windings are separated by an arbitrary angle of α. When the pole number is changed from 4-pole to 2-pole or vice versa, the dynamic model can then be easily adapted by changing this angle of separation between the phases. The 3-phase sets, *abc* and *xyz* each have a 120^o separation between their corresponding phases. The cage rotor winding can be assumed to be sinusoidally distributed

with a 120^o separation between the rotor phases as well. In this model, there is assumed to be no fault the 3-phase sets that will result in a fault current physically flowing between the phases. When 3rd harmonics are injected with the neutral connected between the phase in the 2-pole mode of operation, the torque due to this current can be independently computed and added to the electromagnetic torque due to the fundamental [ABD12a]. The equations of the 6-phase pole changing winding machine in the arbitrary reference frame are shown in (6.52).

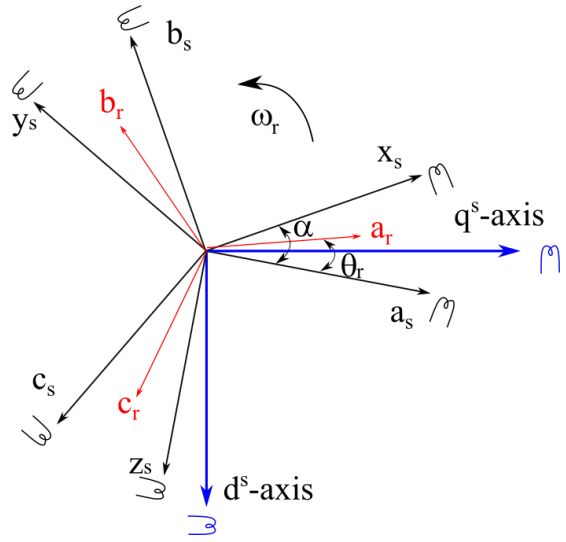

Fig. 6.56 Phasor diagram of the six-phase induction machine with a phase displacement of α between the two three-phase sets.

$$
\begin{aligned}
v_{q4s_1} &= R_s i_{q4s_1} + \frac{d\psi_{q4s_1}}{dt} + \omega_4 \psi_{d4s_1} \\
v_{d4s_1} &= R_s i_{d4s_1} + \frac{d\psi_{d4s_1}}{dt} - \omega_4 \psi_{q4s_1} \\
v_{q2s_1} &= R_s i_{q2s_1} + \frac{d\psi_{q2s_1}}{dt} + \omega_2 \psi_{d2s_1} \\
v_{d2s_1} &= R_s i_{d2s_1} + \frac{d\psi_{d2s_1}}{dt} - \omega_2 \psi_{q2s_1} \\
v_{q4s_2} &= R_s i_{q4s_2} + \frac{d\psi_{q4s_2}}{dt} + \omega_4 \psi_{d4s_2} \\
v_{d4s_2} &= R_s i_{d4s_2} + \frac{d\psi_{d4s_2}}{dt} - \omega_4 \psi_{q4s_2}
\end{aligned}
\tag{6.52}
$$

$$v_{q2s_2} = R_s i_{q2s_2} + \frac{d\psi_{q2s_2}}{dt} + \omega_2 \psi_{d2s_2}$$

$$v_{d2s_2} = R_s i_{d2s_2} + \frac{d\psi_{d2s_2}}{dt} - \omega_2 \psi_{q2s_2}$$

The stator and rotor flux linkage equations in the same reference frame are given in (6.53).

$$\begin{aligned}
\psi_{q4s_1} &= (L_{m4} + L_{ls}) i_{q4s_1} + L_{m4} i_{q4r} + L_{lm}(i_{q4s_1} + i_{q4s_2}) \\
\psi_{d4s_1} &= (L_{m4} + L_{ls}) i_{d4s_1} + L_{m4} i_{d4r} + L_{lm}(i_{d4s_1} + i_{d4s_2}) \\
\psi_{q2s_1} &= (L_{m2} + L_{ls}) i_{q2s_1} + L_{m2} i_{q2r} + L_{lm}(i_{q2s_1} + i_{q2s_2}) \\
\psi_{d2s_1} &= (L_{m4} + L_{ls}) i_{d2s_1} + L_{m2} i_{d2r} + L_{lm}(i_{d2s_1} + i_{d2s_2}) \\
\psi_{q4s_2} &= (L_{m4} + L_{ls}) i_{q4s_2} + L_{m4} i_{q4r} + L_{lm}(i_{q4s_1} + i_{q4s_2}) \\
\psi_{d4s_2} &= (L_{m4} + L_{ls}) i_{d4s_2} + L_{m4} i_{d4r} + L_{lm}(i_{d4s_1} + i_{d4s_2}) \\
\psi_{q2s_2} &= (L_{m2} + L_{ls}) i_{q2s_2} + L_{m2} i_{q2r} + L_{lm}(i_{q2s_1} + i_{q2s_2}) \\
\psi_{d2s_2} &= (L_{m4} + L_{ls}) i_{d2s_2} + L_{m2} i_{d2r} + L_{lm}(i_{d4s_1} + i_{d4s_2}) \\
\psi_{q4r} &= L_{m4}(i_{q4s_1} + i_{q4s_2} + i_{q4r}) + L_{lr} i_{q4r} \\
\psi_{d4r} &= L_{m4}(i_{d4s_1} + i_{d4s_2} + i_{d4r}) + L_{lr} i_{d4r} \\
\psi_{q2r} &= L_{m2}(i_{q2s_1} + i_{q2s_2} + i_{q2r}) + L_{lr} i_{q2r} \\
\psi_{d2r} &= L_{m2}(i_{d2s_1} + i_{d2s_2} + i_{d2r}) + L_{lr} i_{d2r}
\end{aligned} \tag{6.53}$$

The torque due to the 4-pole or 2-pole excitation can then be expressed as shown in (6.54) where x can be 4 or 2 depending on the pole number and excitation.

$$T_e = \frac{3}{2}\frac{x}{2}\frac{L_m}{L_r}\left[\left(i_{qx_{s1}} + i_{qx_{s2}}\right)\lambda_{dr} - \left(i_{dx_{s1}} + i_{dx_{s2}}\right)\lambda_{qr}\right] \tag{6.54}$$

Using the dynamic model equations and the previously discussed principle of IRFOC, the equations when the rotor flux vector is aligned with the d axis can be derived. From (6.30) and (6.31) the rotor currents can be expressed in terms of the stator currents as shown in (6.55) and (6.56). The

rotor slip that aligns the rotor flux with the d-axis is given by (6.57) and the resulting torque is shown in (6.58).

$$i_{qr} = -\left(\frac{L_m}{L_r}\right)(i_{q4_{s1}} + i_{q4_{s2}}) \tag{6.55}$$

$$i_{dr} = \left(\frac{\lambda_r}{L_r}\right) - \left(\frac{L_m}{L_r}\right)\left(i_{d4_{s1}} + i_{d4_{s2}}\right) \tag{6.56}$$

$$\omega_{sl} = (\omega_e - \omega_r) = \frac{L_m R_r}{\psi_{dr} L_r}\left(i_{q4_{s1}} + i_{q4_{s2}}\right) = \left(\frac{L_m}{\tau_r}\right)\frac{\left(i_{q4_{s1}} + i_{q4_{s2}}\right)}{\psi_{dr}} \tag{6.57}$$

$$T_e = \frac{3}{2}\frac{P}{2}\frac{L_m}{L_r}\left(i_{q4_{s1}} + i_{q4_{s2}}\right)\psi_{dr} \tag{6.58}$$

6.3.1 Comparison of Transient Operation of 6-phase Pole Changing Machine: Open-loop and Field Oriented Control

Similar to the cases investigated with the 3-phase pole changing winding induction machine, two control methods are compared with the 6-phase pole changing winding machine. Using the developed dynamic model, the torque, speed and current transients are simulated, in the first case at a fixed rotor speed and rated current. In the second case, the torque, speed and current transients are observed when the rotor dynamics are accounted for, for a given rotor reference speed.

A. Fixed Speed Pole Changing Transient Operation

In this case, the speed of the rotor is fixed at 500rpm (in the constant torque region) and in another case at 2600rpm (in the flux weakening region where the torque capability of the 4-pole machine is lower than that of the 2-pole machine) and the pole changing operation is performed at 2s. The torque transient waveforms with open-loop control and IRFOC control are shown in Fig. 6.57 and Fig. 6.58 respectively. As previously seen from the transient performance of the 3-phase machine, the torque transient is significantly reduced with IRFOC. The A-phase and X-phase current waveforms with open-loop control and IRFOC control are shown in Fig. 6.59 and Fig. 6.61 respectively. In Fig. 6.60 the A-and X-phase current is shown in the region during which the pole changing transient operation occurs. The change of phase shift between the two 3-phase sets from 60^o during the 4-pole operation to 30^o phase shift during 2-pole operation can be observed. The q-axis currents with open-loop control and IRFOC control are shown in Fig. 6.62 and Fig. 6.63 respectively. Similarly, the d-axis current transients are shown in Fig. 6.64 and Fig. 6.65 respectively.

The operation, to observe the pole changing transient operation in the flux weakening region at 2600rpm is repeated under the same condition of fixed speed and rated current. The torque transients with open-loop control and IRFOC control are shown in Fig. 6.66 and Fig. 6.67 respectively. The A-and X-phase current transients with open-loop control and IRFOC control are shown in Fig. 6.68 and Fig. 6.69 respectively. The q-axis current transients with open-loop control and IRFOC control are shown in Fig. 6.70 and Fig. 6.71 respectively. Similarly, the d-axis current transients with open-loop control and IRFOC control are shown in Fig. 6.72 and Fig. 6.73 respectively.

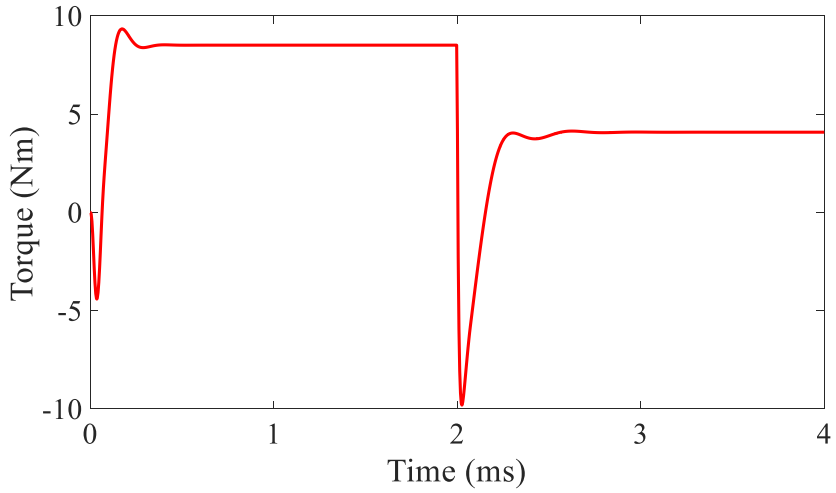

Fig. 6.57 Open-loop control torque transient with pole changing operation at 500rpm with rated current.

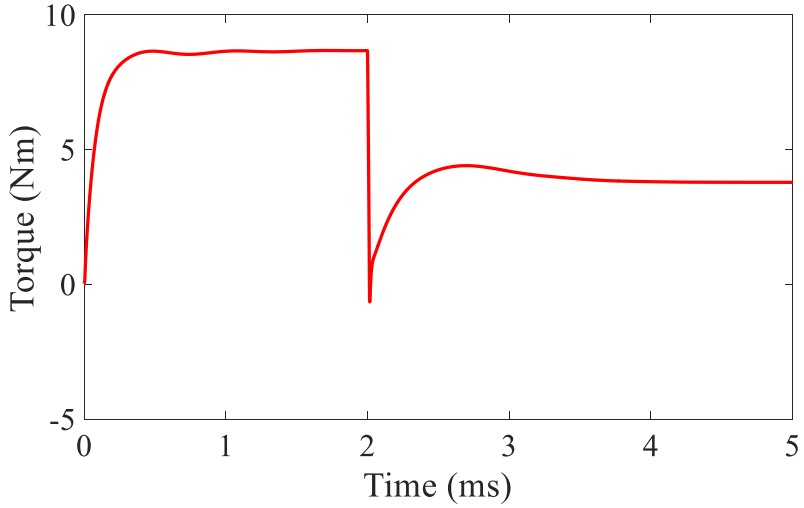

Fig. 6.58 IRFOC torque transient with pole changing operation at 500rpm with rated current

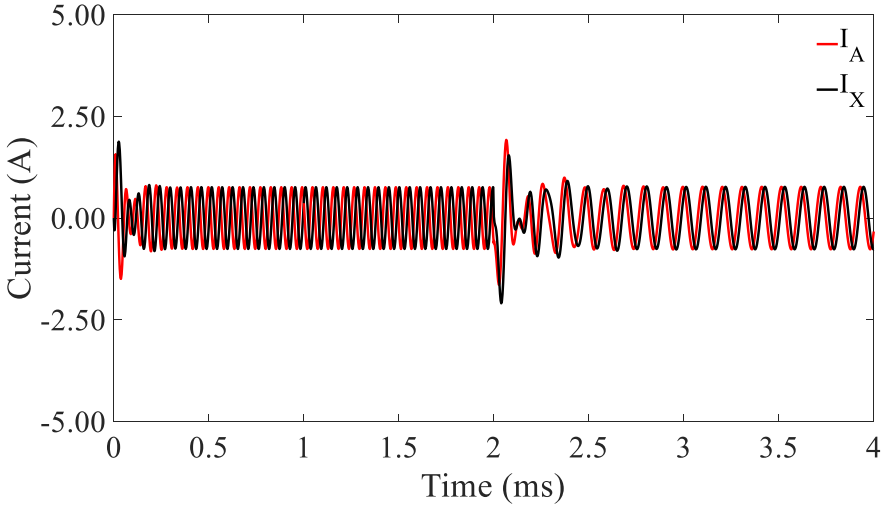

Fig. 6.59 Open-loop control A-phase and X-phase current with pole changing operation at 500rpm.

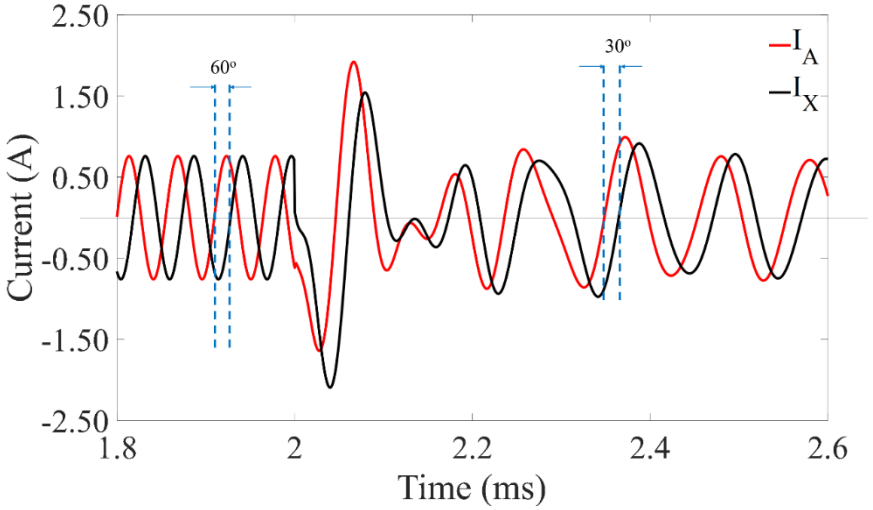

Fig. 6.60 A-phase and X-phase current showing phase shift change with pole changing operation at 500rpm.

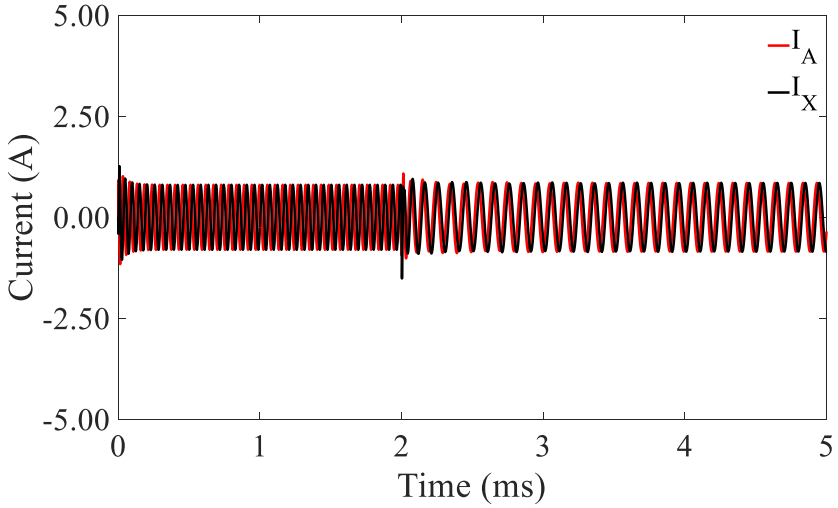

Fig. 6.61 IRFOC A-phase and X-phase current with pole changing operation at 500rpm.

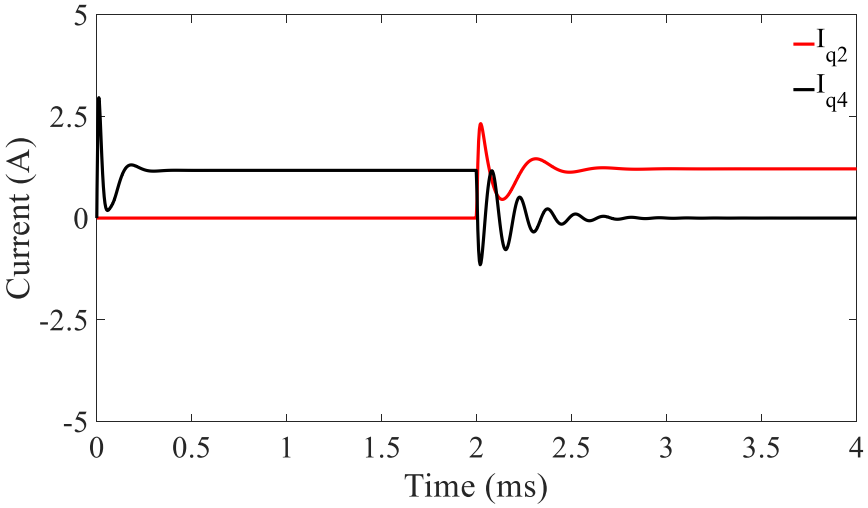

Fig. 6.62 Open-loop control q-axis current with pole changing operation at 500rpm.

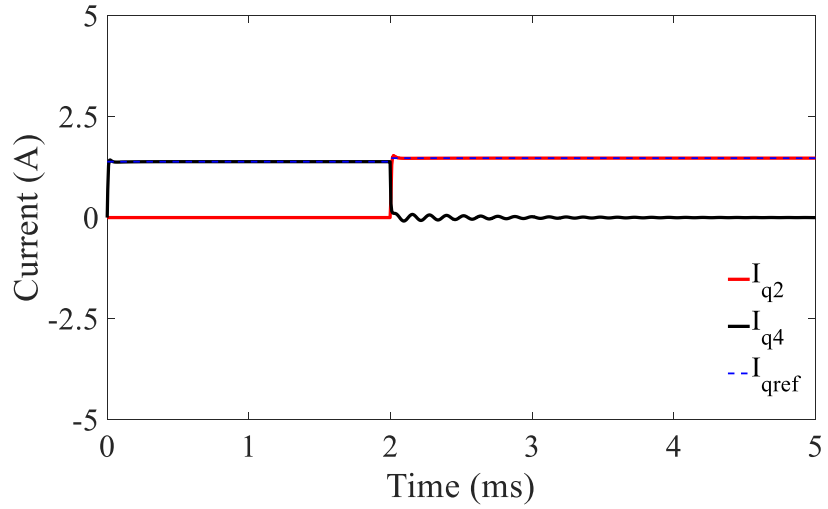

Fig. 6.63 IRFOC q-axis current with pole changing operation at 500rpm.

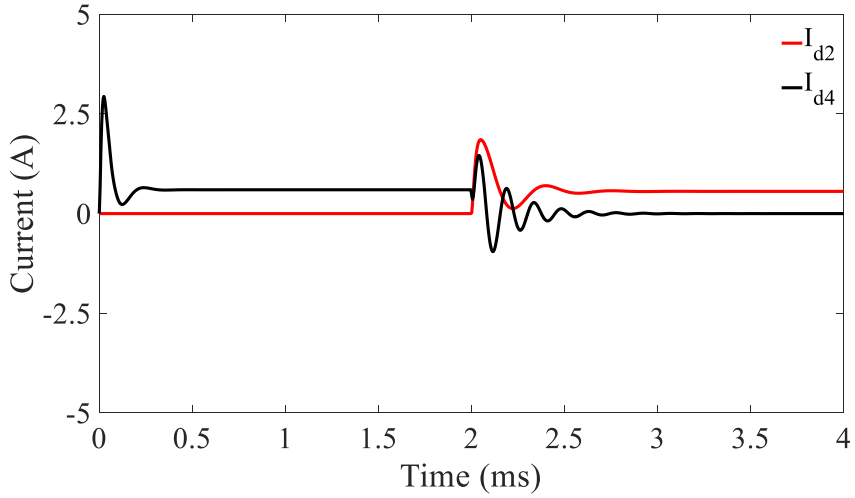

Fig. 6.64 Open-loop control d-axis current with pole changing operation at 500rpm.

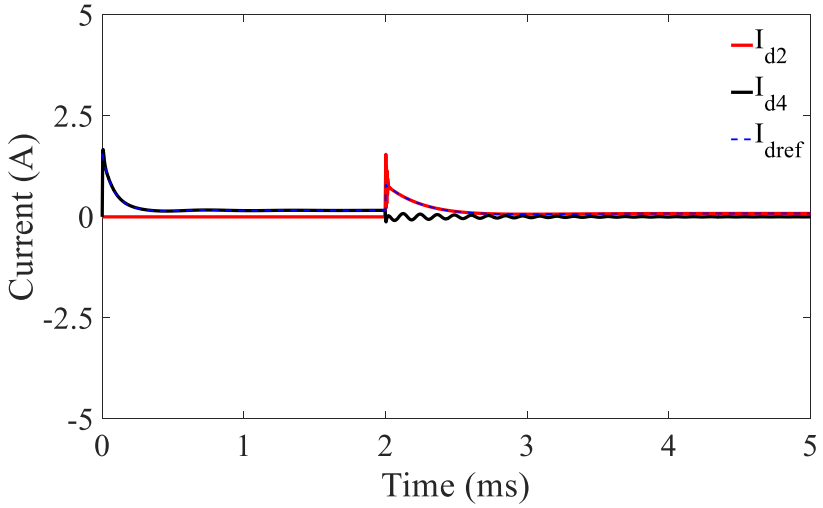

Fig. 6.65 IRFOC d-axis current with pole changing operation at 500rpm.

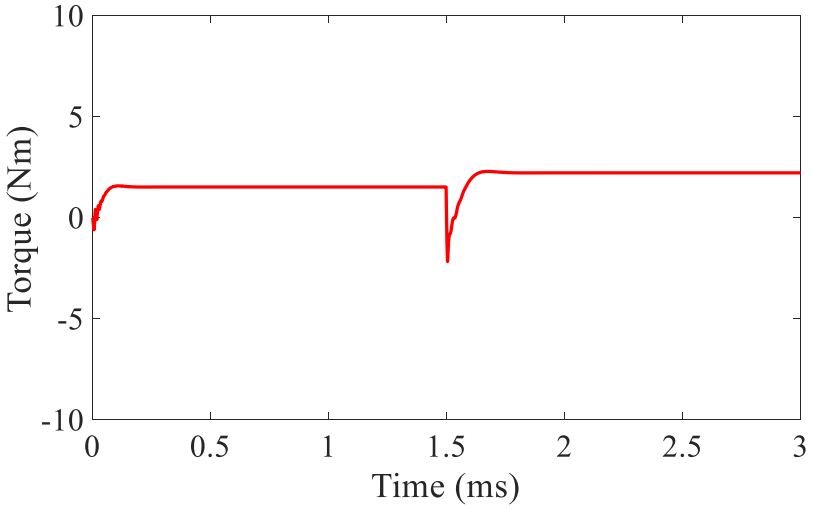

Fig. 6.66 Open-loop control torque transient with pole changing operation at 2600rpm with rated current.

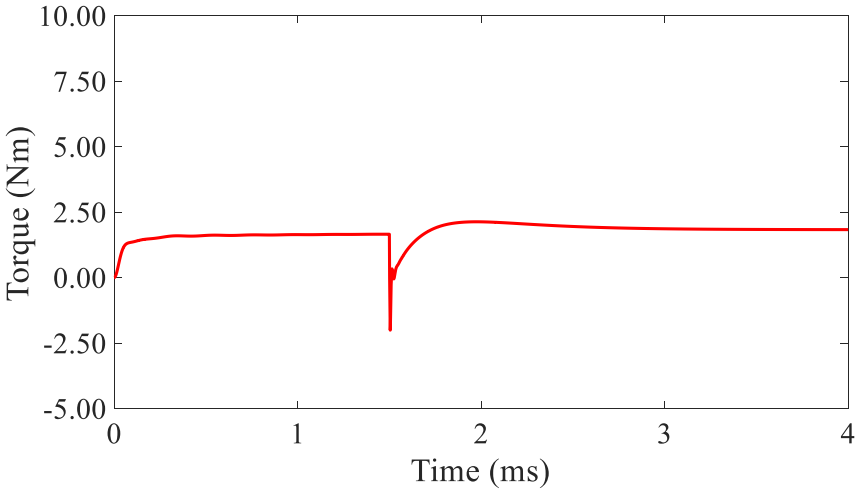

Fig. 6.67 IRFOC torque transient with pole changing operation at 2600rpm with rated current

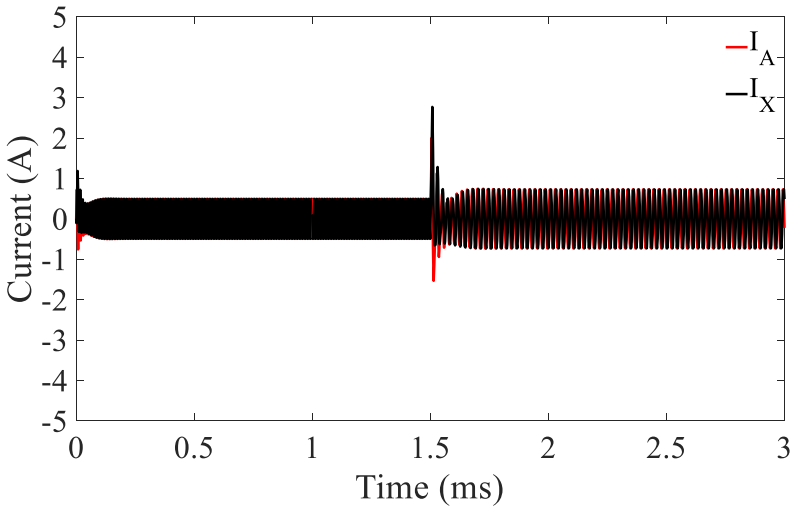

Fig. 6.68 Open-loop control A-phase and X-phase current with pole changing operation at 2600rpm.

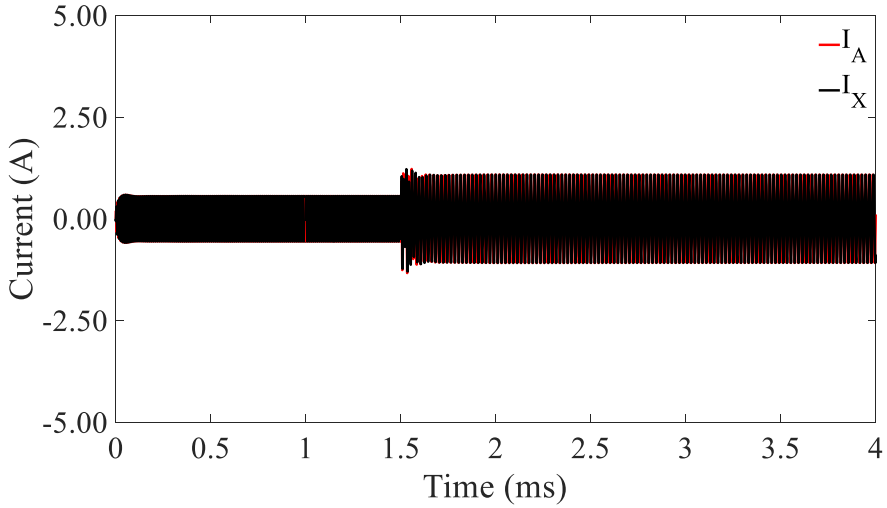

Fig. 6.69 IRFOC A-phase and X-phase current with pole changing operation at 2600rpm.

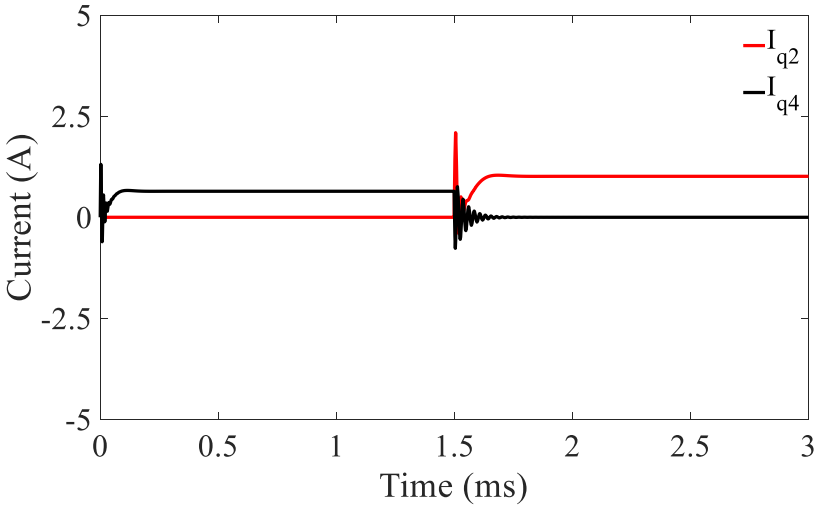

Fig. 6.70 Open-loop control q-axis current with pole changing operation at 2600rpm.

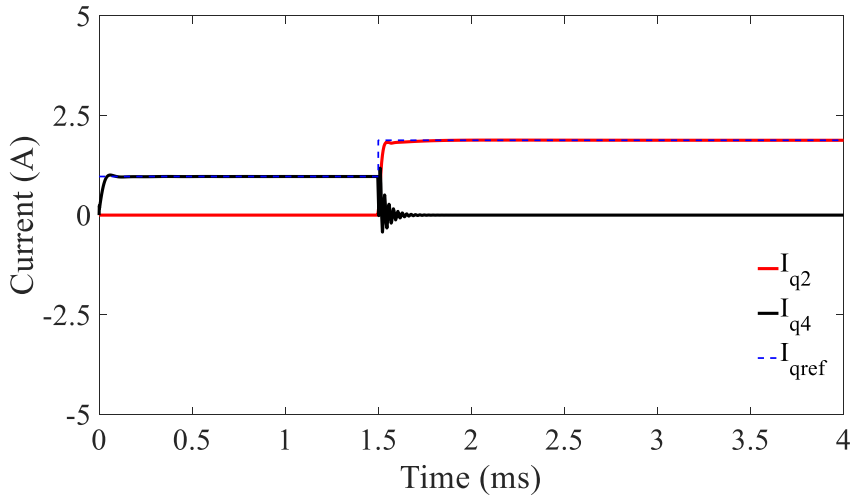

Fig. 6.71 IRFOC q-axis current with pole changing operation at 2600rpm.

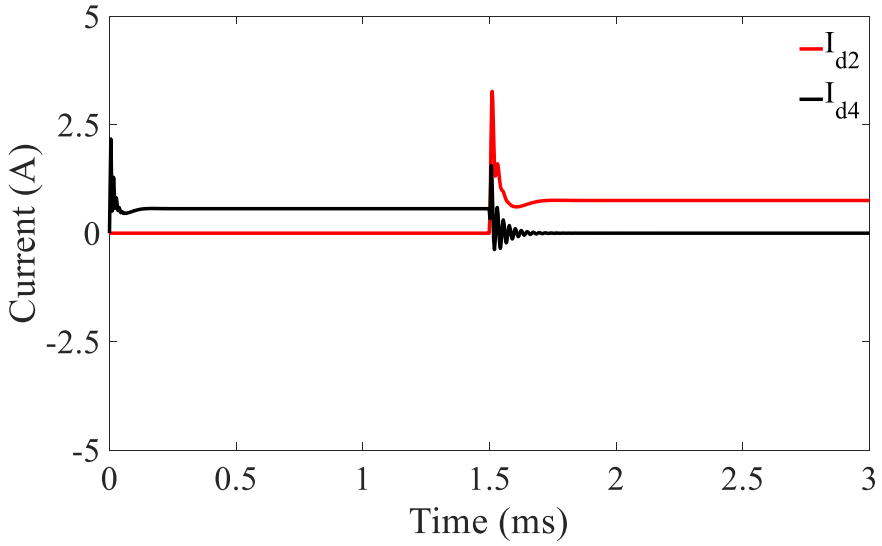

Fig. 6.72 Open-loop control d-axis current with pole changing operation at 2600rpm.

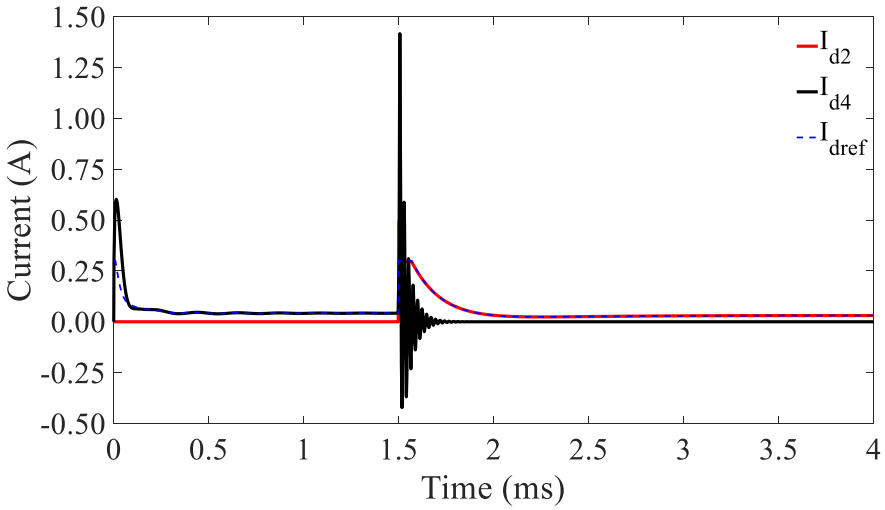

Fig. 6.73 IRFOC d-axis current with pole changing operation at 2600rpm.

B. Pole Changing Transient Operation during Start-up

In the second scenario, the voltage (amplitude and frequency) corresponding to the set-point of speed is applied to the machine and the rotor speed is allowed to ramp up to this value under no-load and loaded conditions with open-loop control. In the closed-loop IRFOC, the q-axis current is determined using a PI controller as explained in the previous section and the d-axis current in the flux weakening region is chosen to be equal to the value that results in the rated flux in the machine. In the flux weakening region, the d-axis current is reduced in proportion to the speed beyond the corner speed of the induction machine. The benefit of the IRFOC on the dynamic performance of the induction machine during the pole changing operation can be observed from Fig. 6.74 and Fig. 6.75. With open loop control at 500rpm, the start-up transient is as expected from Direct Online Starting of an induction machine and this transient is improved with IRFOC. The reference speed is reached with no oscillations or overshoot at start-up with IRFOC. The speed transient is also supressed with IRFOC when a load torque of 2Nm is applied at 2.5s. The most dramatic improvement is observed during pole changing operation at 4.5s. With IRFOC, as seen in Fig. 6.81, the d-axis and q-axis currents during transition from 4-pole to 2-pole have lower oscillations and a lower region of overlap between 4-pole and 2-pole operations when compared to Fig. 6.80. This is possible with IRFOC with which the d-axis and q-axis currents can be independently controlled.

The impact of IRFOC during start-up at 2500 rpm can be seen by comparing Fig.6.84 with Fig. 6.85. The start-up transient is reduced to less than 10^{th} due to the ability to control the q-axis and d-axis currents independently to reach a steady state control quicker than with open loop control

as seen from comparing the q-axis currents in Fig. 6.90 and Fig. 6.92 and the d-axis currents in Fig. 6.91 and Fig. 6.93 for the open loop and IRFOC cases, respectively.

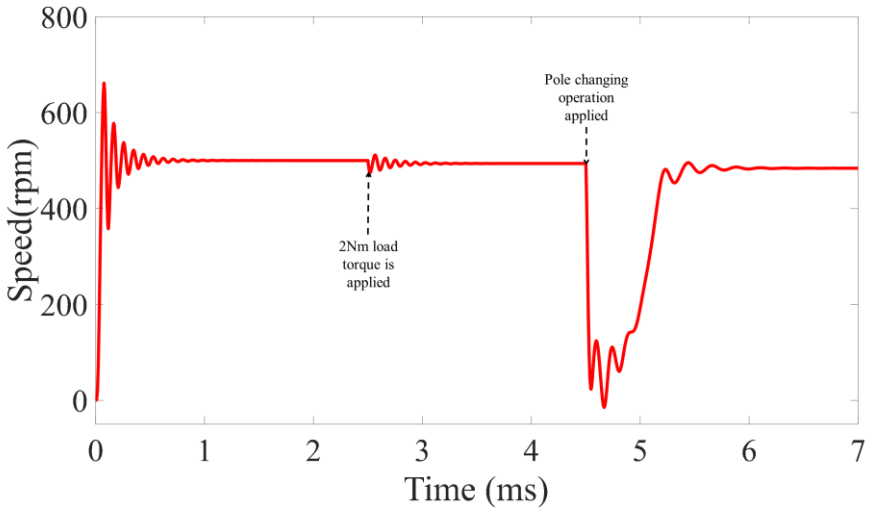

Fig. 6.74 Speed transient with open-loop control for a reference speed of 500rpm.

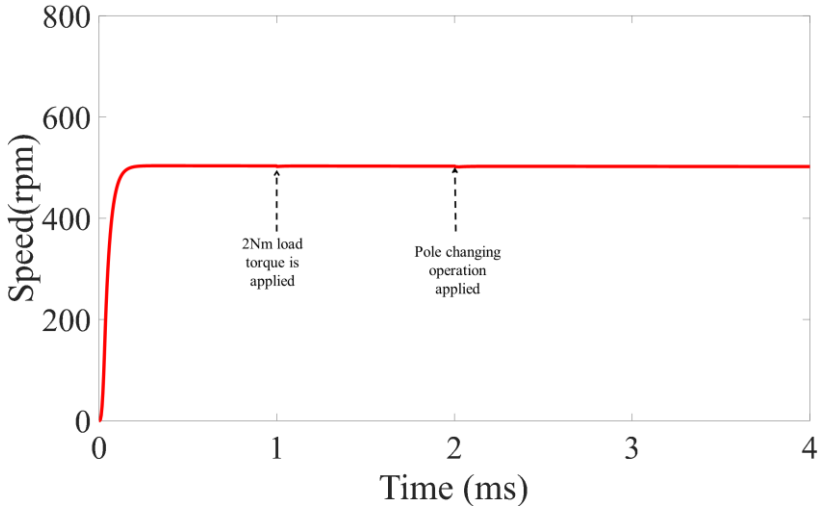

Fig. 6.75 Speed transient with IRFOC for a reference speed of 500rpm.

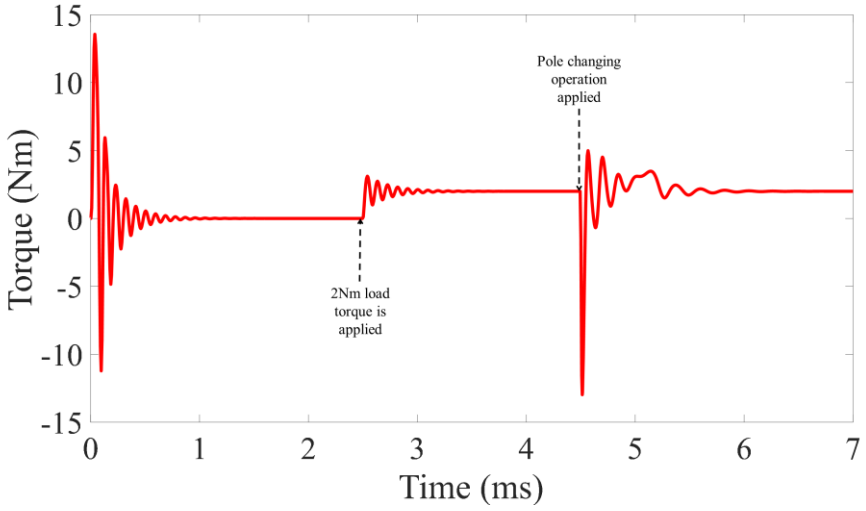

Fig. 6.76 Torque transient with open-loop control for a reference speed of 500rpm.

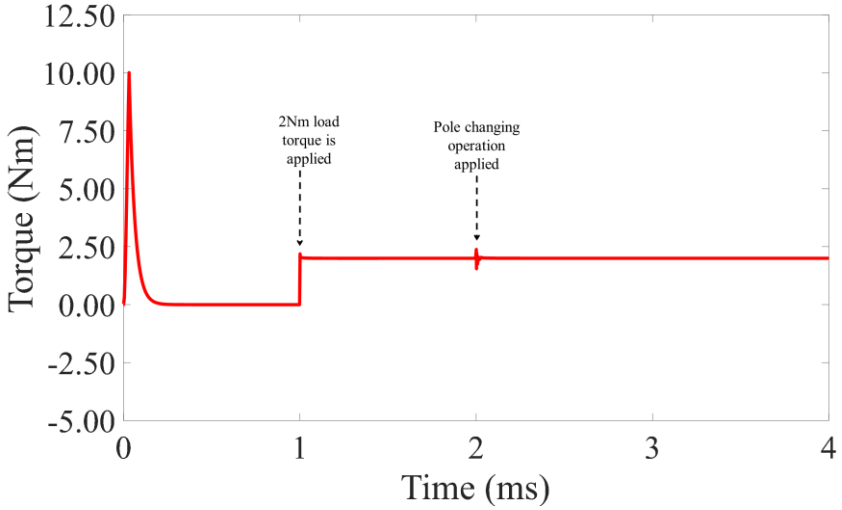

Fig. 6.77 Torque transient with IRFOC for a reference speed of 500rpm.

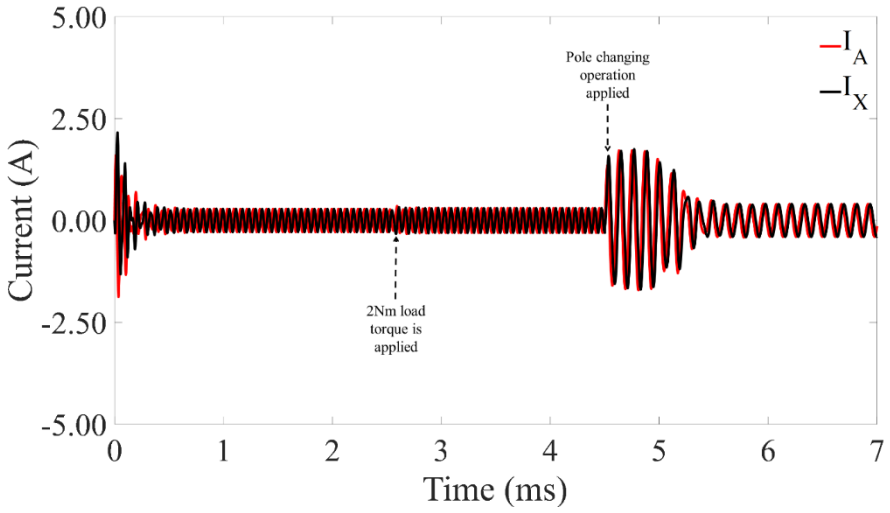

Fig. 6.78 A-phase and X-phase current transient with open-loop control for a reference speed of 500rpm.

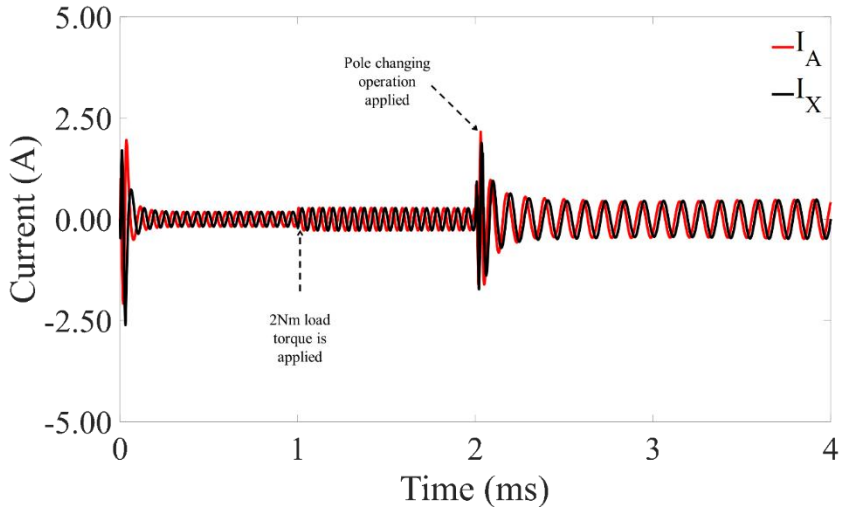

Fig. 6.79 A-phase and X-phase current transient with IRFOC for a reference speed of 500rpm.

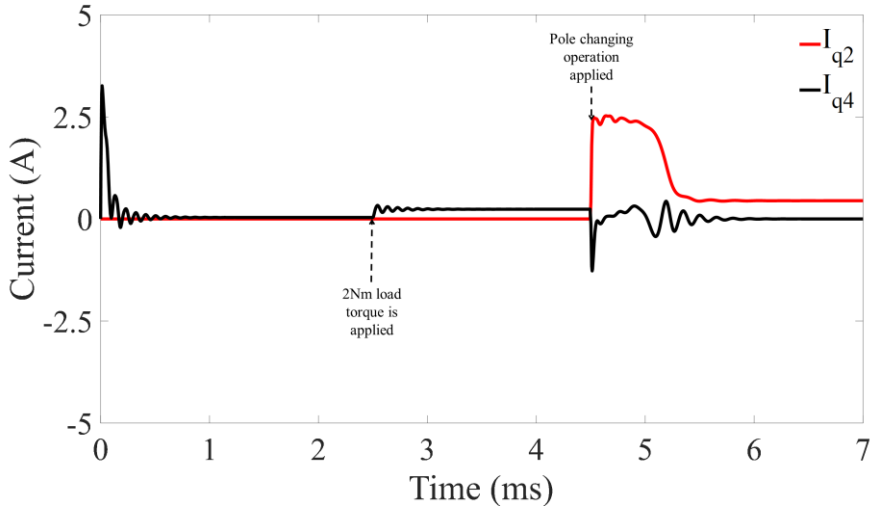

Fig. 6.80 q-axis current transient with open-loop control for a reference speed of 500rpm.

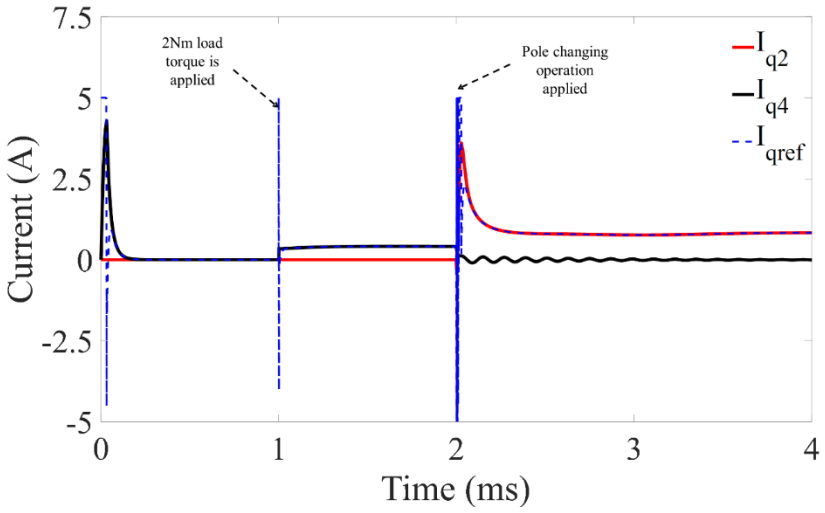

Fig. 6.81 q-axis current transient with IRFOC for a reference speed of 500rpm.

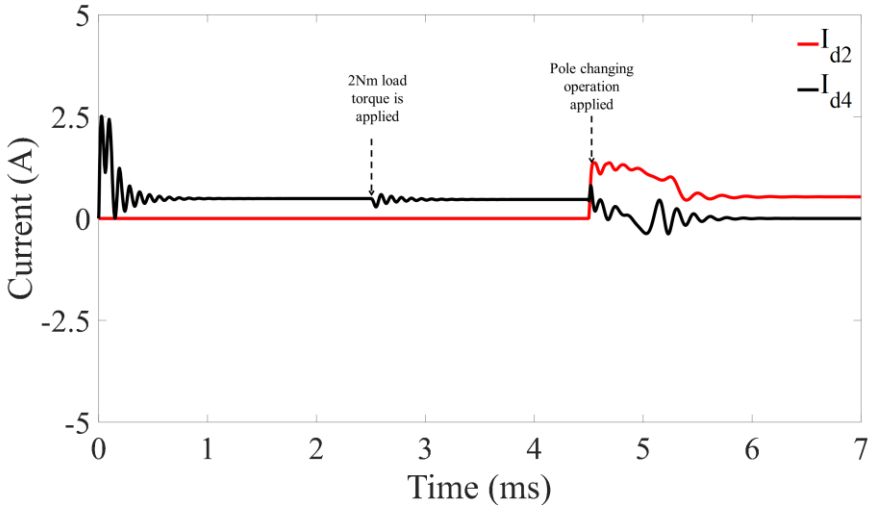

Fig. 6.82 d-axis current transient with open-loop control for a reference speed of 500rpm.

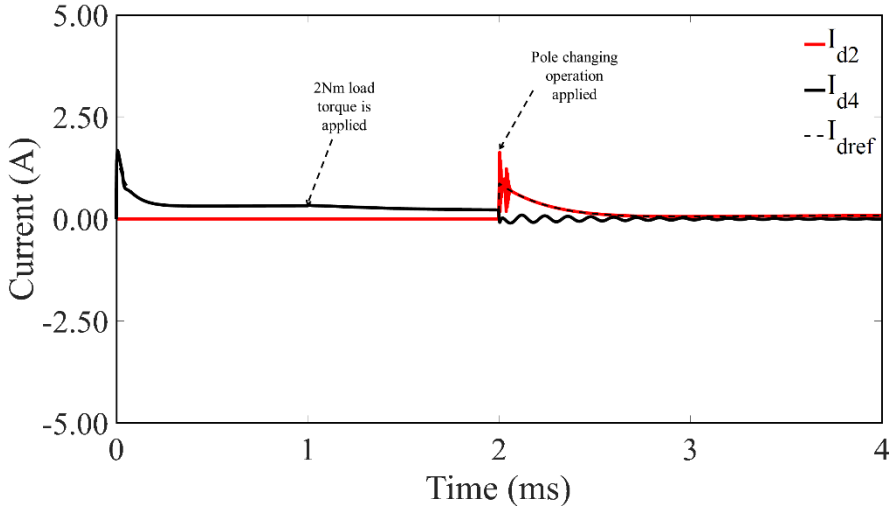

Fig. 6.83 d-axis current transient with IRFOC for a reference speed of 500rpm.

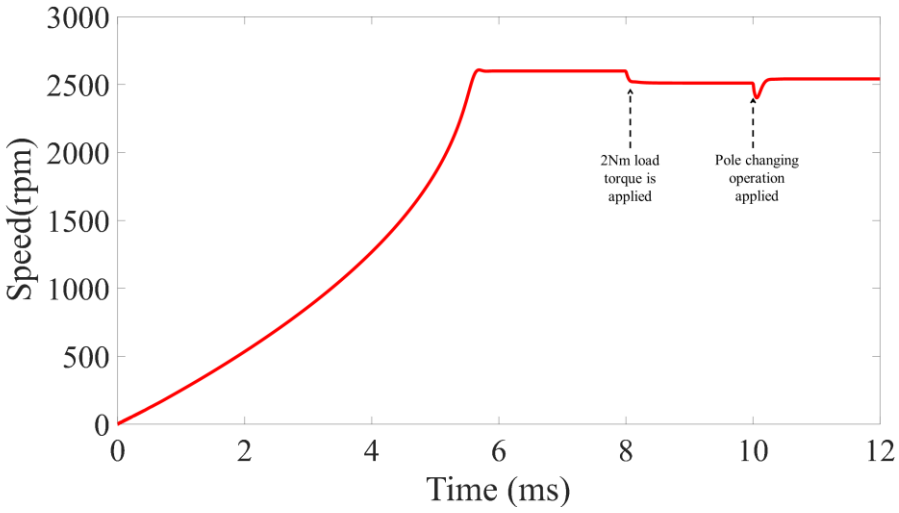

Fig. 6.84 Speed transient with open-loop control for a reference speed of 2600rpm

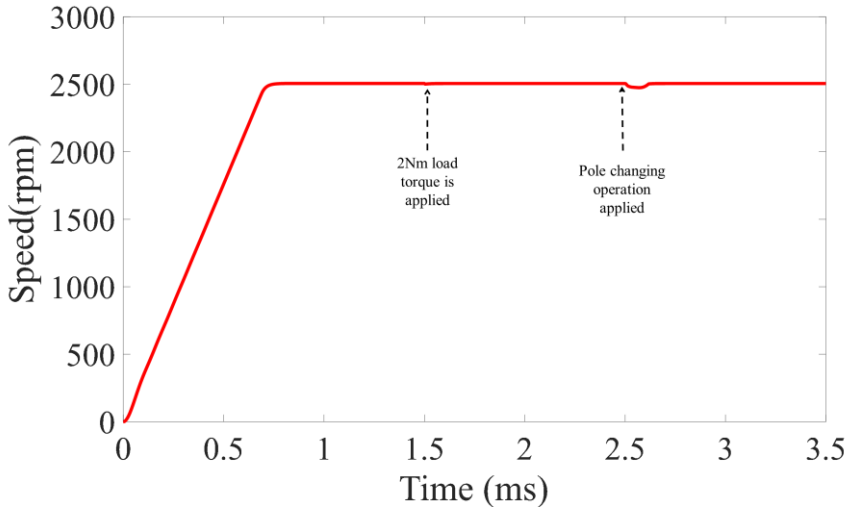

Fig. 6.85 Speed transient with IRFOC for a reference speed of 2600rpm.

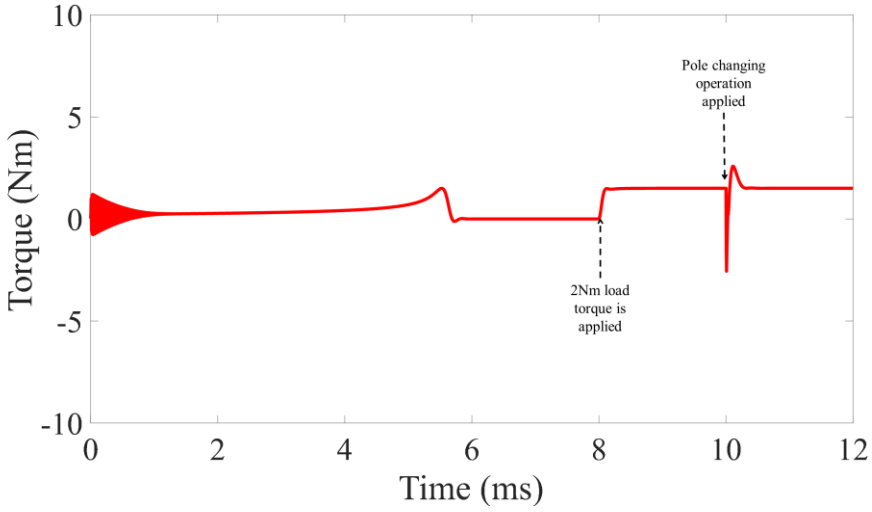

Fig. 6.86 Torque transient with open-loop control for a reference speed of 2600rpm.

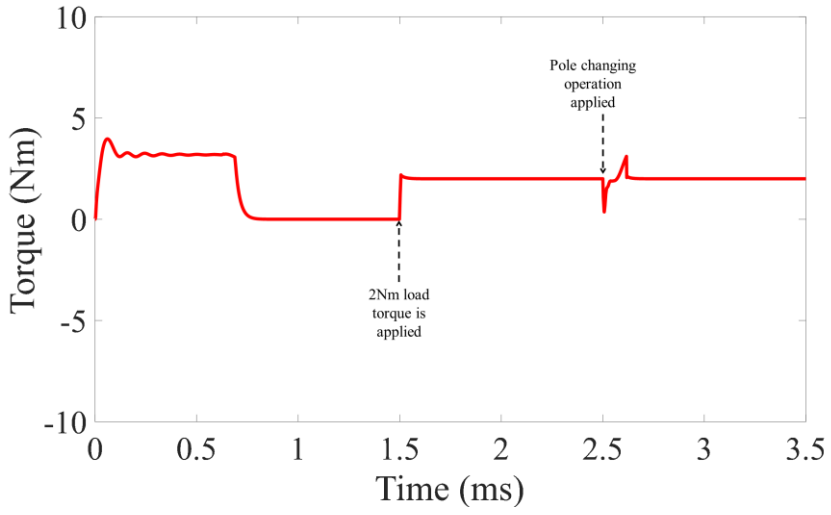

Fig. 6.87 Torque transient with IRFOC for a reference speed of 2600rpm.

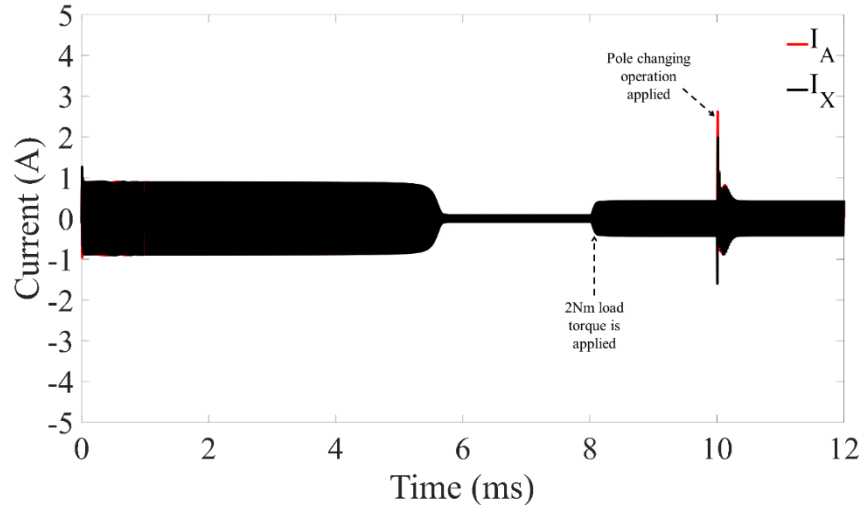

Fig. 6.88 A-phase and X-phase current transient with open-loop control for a reference speed of 2600rpm.

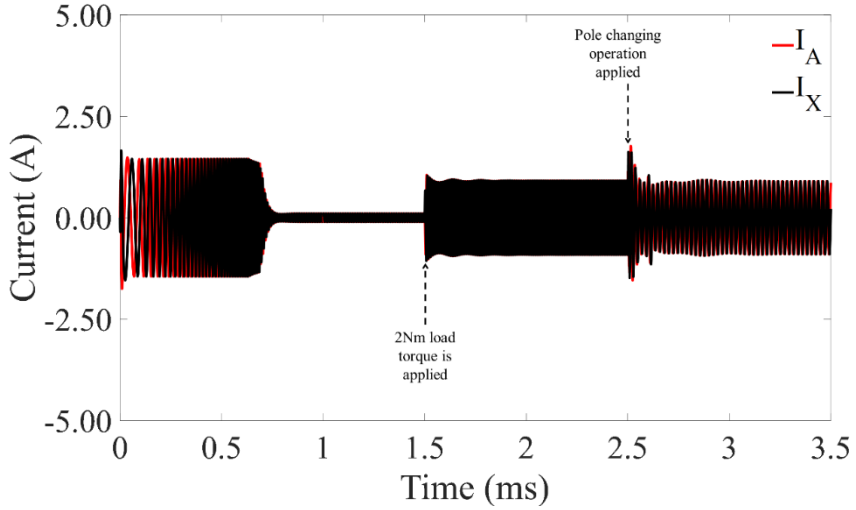

Fig. 6.89 A-phase and X-phase current transient with IRFOC for a reference of 2600rpm.

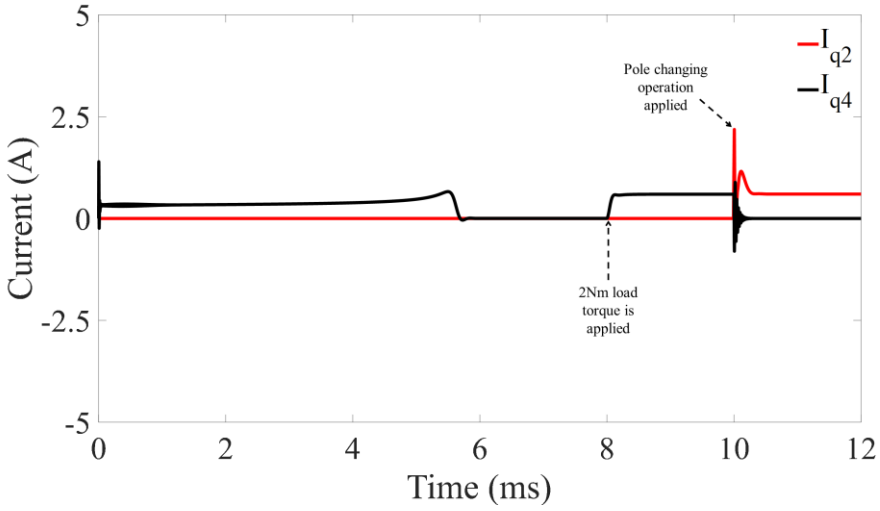

Fig. 6.90 q-axis current transient with open-loop control for a reference speed of 2600rpm.

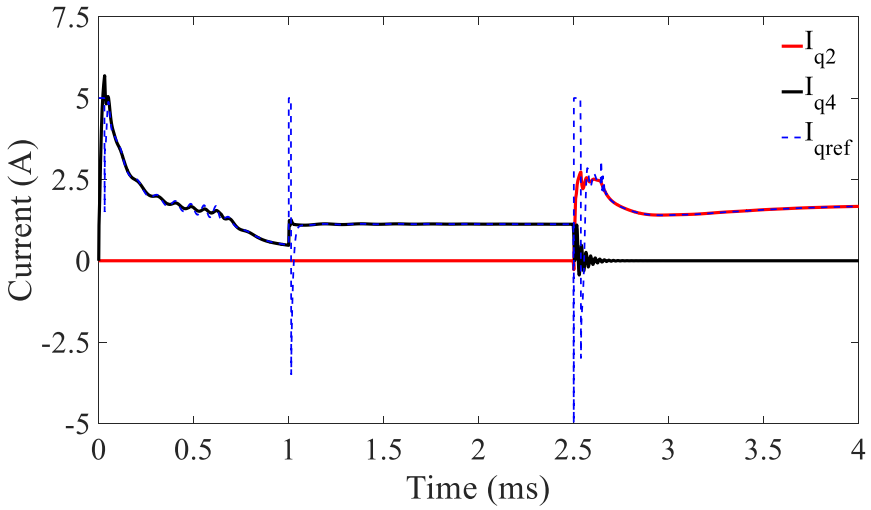

Fig. 6.91 q-axis current transient with open-loop control for a reference speed of 2600rpm.

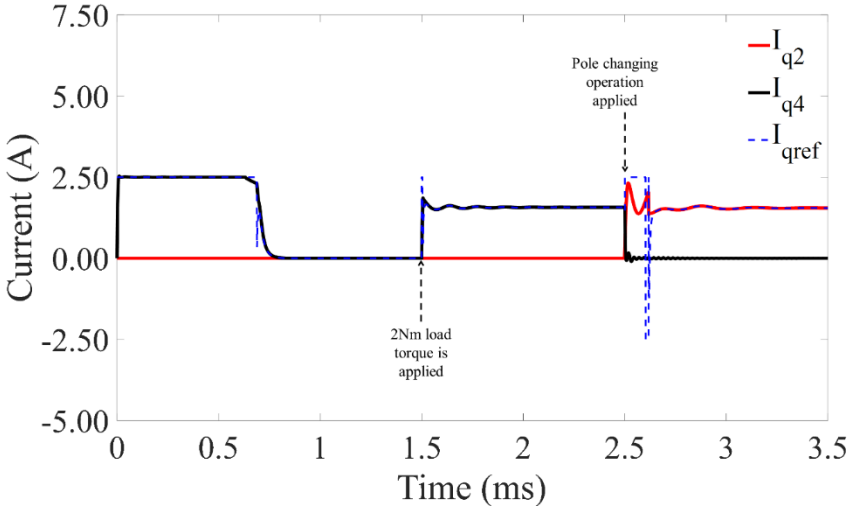

Fig. 6.92 q-axis current transient with IRFOC for a reference speed of 2600rpm.

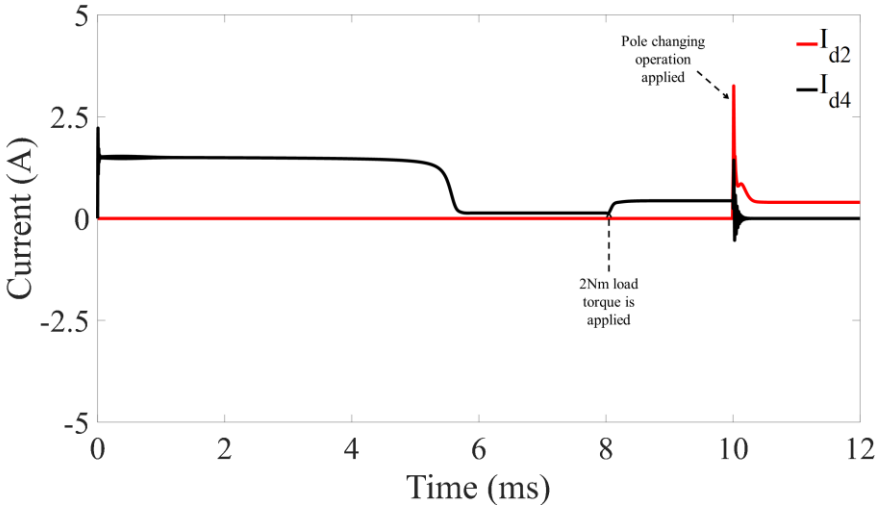

Fig. 6.93 d-axis current transient with open-loop control for a reference speed of 2600rpm.

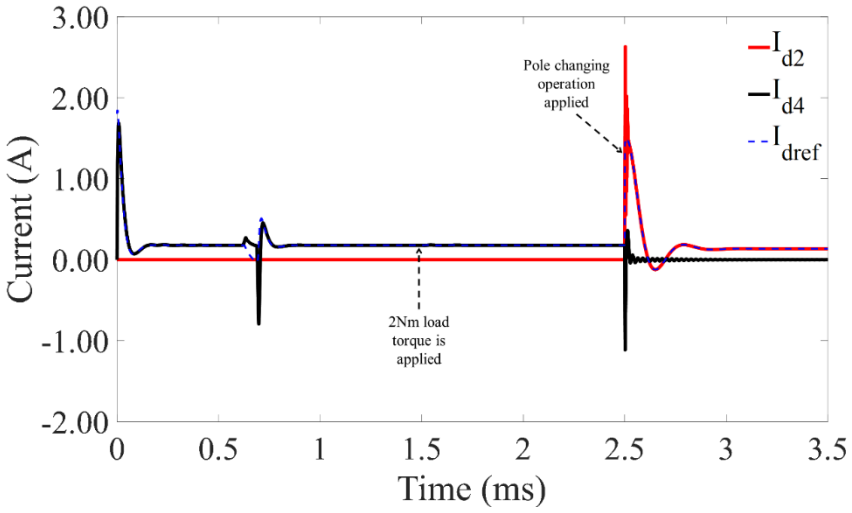

Fig. 6.94 d-axis current transient with IRFOC for a reference speed of 2600rpm.

6.4 Conclusions

In this chapter, the dynamic model of a 3-phase pole changing winding induction machine using the vector space decomposition method has been reviewed. Applying this model to study the transient behaviour reveals that the torque and current transients can be significantly reduced with IRFOC as compared to open-loop control. A dynamic model for multiphase induction machines with arbitrary phase displacement between the three-phase sets is used to model the 6-phase machine. Using this in conjunction with vector space decomposition, a dynamic model for the 6-phase pole changing winding has been developed. The transient performance of the 2-pole operation of the 6-phase and 3-phase machines are identical as expected. The peak torque of the 6-phase machine under 4-pole operation is higher than its 3-phase counterpart due to improved winding factor. The transient performance is improved with IRFOC for the 6-phase pole changing winding machine.

Chapter 7

General Conclusions and Future Work

7.1 Introduction

This thesis aimed to investigate the use of induction machines for extending the flux-weakening region of induction machines while preserving the peak torque capability in the constant torque region of operation making it a suitable candidate for starter-generator applications. Beginning with the relative comparison of various methods to extend the speed range and the peak torque of the induction machine, the electronic pole changing winding is identified as the most suitable candidate. The cause of the disadvantage of the poor fundamental winding factor of the state-of-art electronic pole changing winding three-phase induction machines are identified. A six-phase alternative winding is proposed to overcome this limitation and to improve the fundamental winding factor by 15% resulting in a winding factor comparable to a standard distributed winding with a 60^{o} phase spread. Additionally, the benefit of injecting an optimal 3^{rd} harmonic current for increasing the torque capability when operating with the lower pole number is determined. This results in the peak torque capability in the constant torque region improving proportionally by 15% for the same frame size as an equivalent three-phase pole changing winding induction machine. The injection of the 3^{rd} harmonic improves the torque capability in the constant torque region by 21% when operating with the lower number of poles. The transient performance of the three-phase and six-phase induction machines during the pole-changing operation is simulated and compared. The vector space decomposition method is used to develop a dynamic, *dq*- model for the six-phase pole changing winding induction machine. The transient performance with indirect rotor field oriented control is markedly improved compared to the operation with open-loop scalar control. This is due to the independent control of the torque and rotor flux of the induction machine with field orientation which enables the rotor flux corresponding to one pole number to be controlled to zero and the rotor flux corresponding to the other pole number to be established in the shorted possible time.

7.2 Conclusions

The conclusions from the different chapters of the thesis are categorised and discussed in this section. Beginning with the influence of the geometric parameters on the induction machine behaviour, the conclusions from the comparisons of the torque, power, power factor, efficiency and

transient performance of three-phase and six-phase pole changing winding induction machines are discussed.

7.2.1 Influence of Machine Parameters

The number of series turns per phase has a direct influence on the corner speed of the induction machine. As the number of series turns is increased for a given stack length and frame size, the peak torque in the constant torque region increases but the corner speed decreases. This reduces the torque in the flux weakening region. With low voltage 48V systems, the number of series turns per phase is limited by the DC bus voltage. For high power machines with a 48V DC bus, the current rating of the machine is relatively high (>250A per phase) and this results in the conductors are of large cross-section area to limit the current density. This limits in the number of conductors per slot to 2 or 4 conductors and hairpin windings make a suitable choice for such windings. Additionally, in an induction machine, the number of poles, the number of slots in the stator and rotor influence the torque density and torque ripple.

The influence of the number of stator slots and the number of poles is investigated under two scenarios. In the first case, the number of series turns per phases is held fixed at 12 to fix the corner speed and the number of conductors per slot is varied as the number of slots per pole per phase is changed. The influence of the slots per pole per phase and the number of poles for this scenario can be summarised as follows:

1. The 8-pole induction machine with an SPP of two has the highest torque below the base speed but the lowest torque in the flux weakening region.
2. The torque in the flux weakening increases with the SPP while the torque in the constant torque region decreases with SPP.
3. A compromise between high peak torque and a wide speed flux weakening region, the 8-pole induction machine with an SPP of 3 is the optimal machine.

In the second case, the number of conductors per slot is fixed at 2, which maximises the slot fill factor. The number of series turns per phase is allowed to vary with SPP. The influence of the slots per pole per phase and the number of poles for this scenario can be summarised as follows:

1. With increasing series turns per phase, the peak torque is increased in the constant torque region but the torque in the flux weakening region decreases at a given speed.
2. For an identical number of series turns per phase, the machines with higher pole numbers have better power factor due to the shorter end winding and consequent lower leakage inductances.

3. In this scenario as well, the machine with an SPP of 3 and 8 poles has the best compromise between the peak and the widest flux weakening region.

The number of rotor slots has a higher influence on the torque ripple and the torque in the flux weakening region compared to the torque in the constant torque region. The influence of the slots per pole per phase and the number of poles for this scenario can be summarised as follows:

1. When the number of rotor slots is an odd multiple of poles, then the torque ripple is higher.
2. Torque ripple is low for the cases when the difference in the number of stator and rotor slots is not an integer multiple of the number of pole pairs.
3. Increasing the number of rotor slots decreases the leakage inductance for all value of SPP and number of poles.
4. However, the increasing number of slots is limited by the manufacturable tooth width. Considering this behaviour, the optimal number of slots is determined to be $0.75N_S \leq N_R \leq 1.25N_S$, where N_S is the number of stator slots and N_R is the number rotor slots.

From the optimisation study, the parameters of the baseline induction machine that is best suited for the starter generator application can be summarised in Fig. 7.1. The number of series turns per phase and the number of poles and SPP are chosen to maximise the peak torque in the constant torque region and the flux weakening region while the number of rotor slots is chosen to minimise leakage inductance and torque ripple.

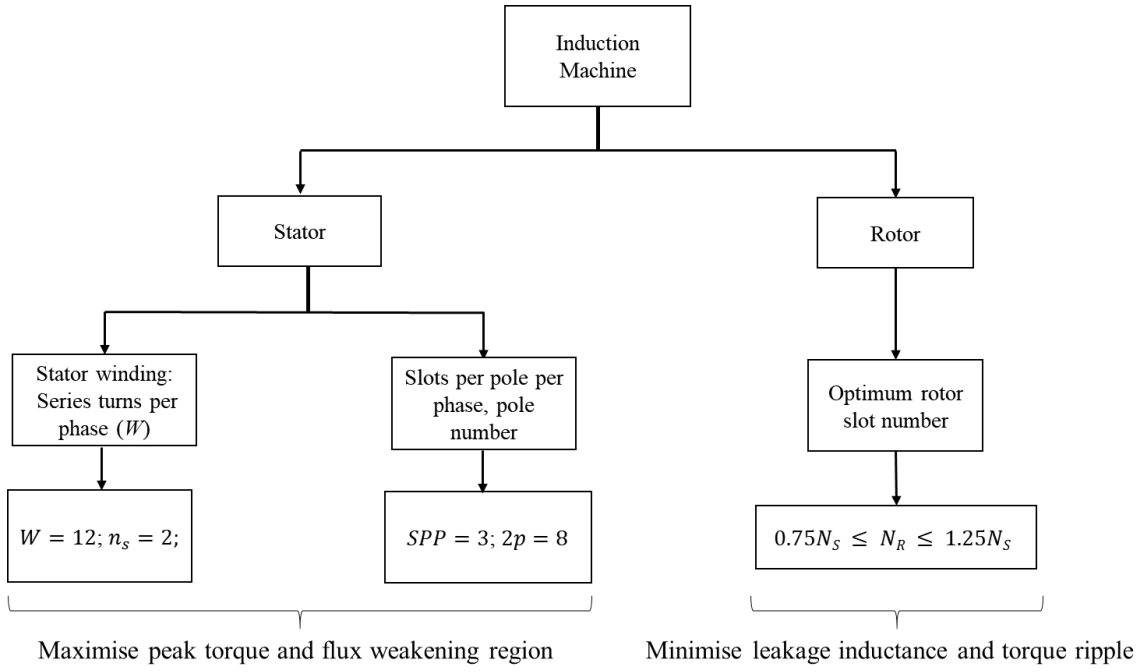

Fig. 7.1 Summary of optimisation of machine parameters for optimum peak torque and flux weakening region.

7.2.2 Pole Changing Windings and Influence of Phase Belt

Based on the slot and pole number combination determined from the optimisation study, a baseline 3-phase induction machine with 8 poles and an SPP of 3 is designed. A simple replacement of the fixed pole winding for the same stack length and series turns per phase, with an 8/4-pole 3-phase pole changing winding results in a 15% lower peak torque in the constant torque region due to a poor winding factor. For a starter generator operation where a peak torque capability for cranking is required at a lower speed, the torque at low speed can be increased and the stack length decreased. In chapter 3, it was shown that, for the specifications of the starter-generator application, the baseline machine with 12 series turns per phase can be replaced with a pole changing winding induction machine with 18 series turns per phase and a 20% reduction in active stack length. This comes at the expense of a drop in efficiency in the flux weakening region due to the higher copper losses as a result of the increased resistance. However, the peak efficiency in the flux weakening region above 6000rpm is improved by 3%. This is due to the increased number of conductors per slot (6 compared to 2) of the pole changing windings which reduces the conductor eddy current losses. The reduction in the winding factor is due to the 120^o phase belt that is required in 3-phase pole changing winding induction machines.

TABLE 7.1 COMPARISON OF FEATURES OF WINDINGS WITH DIFFERENT PHASES AND PHASE BELT

Feature	**Three-60^o phase belt**	**Three-phase 120^o phase belt**	**Six-phase 120^o phase belt**
Maximum fundamental winding factor	1	0.829	0.959
Pole changing winding	Inefficient due to MMF cancellation	Possible. No MMF cancellation	Efficient. No MMF cancellation
Magnetising inductance per phase	1 p.u	0.75 p.u	1.84 p.u

With a 120^o phase belt, the fundamental winding factor is below 0.83, compared to winding factors above 0.95 achievable with a 60^o phase belt windings. When a 60^o phase belt is used with pole changing windings, the portions of the windings where the current is reversed to change the number of poles cancel the MMF in the other sections of the windings where the current is not reversed. This MMF cancellation is inefficient since the currents in these windings do not produce

torque but crease copper losses. The comparison of winding factors, the ability for pole changing and magnetising inductance for different phase belt is shown in TABLE 7.1.

7.2.3 Performance of Six-Phase Pole Changing Windings

The poor winding factor of the three-phase pole changing windings due to the 120^o phase belt can be overcome by the use of a six-phase pole changing winding induction machine.

TABLE 7.2 COMPARISON OF FEATURES OF WINDINGS WITH DIFFERENT PHASES AND PHASE BELT

Feature	Three-phase pole changing winding	Six- phase pole changing winding
Torque and power capability (4-pole)	15% lower peak torque and power.	High peak torque and power.
Torque and power capability (2-pole)	Twice the flux weakening region compared to 4-pole operation.	Twice the flux weakening region compared to 4-pole operation. 3.7% improvement over three-phase pole changing winding.
Power factor (4-pole)	High at low speed, reduced at high speeds.	High at low speed, reduced at high speeds.
Power factor (2-pole)	Lower at low speeds and improved at high speeds.	Lower at low speeds and improved at high speeds
Efficiency (4-pole)	Low in constant torque region, higher in flux weakening region.	Low in constant torque region, higher in flux weakening region.
Efficiency (2-pole)	Low in constant torque region, higher in flux weakening region.	Low in constant torque region, higher in flux weakening region compared to three-phase pole changing winding.
Torque ripple (4-pole)	High	High
Torque ripple (2-pole)	Low	Low
3^{rd} harmonic injection	Not feasible	Feasible with the 2-pole operation. 21% increased torque capability in constant torque region and 14% increased power at corner speed

The six-phase induction machine can be wound with a 120^o phase belt which results in an improved winding factor while avoiding the MMF cancellation if such a phase belt were used in a three-phase pole changing winding machine. For comparison, in chapter 4, the fundamental winding factors of the three-phase and six-phase 120^o phase belt windings are shown to be 0.829 and 0.957 respectively. A summary of the comparison of the three-phase and six-phase pole changing winding machines are shown in TABLE 7.2. The individual performance metrics are discussed in the following sections.

A. Torque and Power Capability

Below the base speed, in the constant torque region, the starter-generator application requires a high peak torque for cranking operation and as such is operated with the higher 4-pole winding configuration. The peak torque in this region, for the six-phase pole changing winding machine, is increased by 15% as a direct result of the improved fundamental winding factor. During the 4-pole operation, due to the increased winding factor, the peak power capability of the six-phase pole changing winding machine is improved from zero speed to 1600rpm which is twice the corner speed. Above the base speed, in the flux weakening region, the number of poles is reduced to 2 poles and the corner speed of the machine increases. The fundamental winding factors during 2-pole operation for the three-phase and six-phase pole changing windings are 0.675 and 0.7 respectively which result in a marginal increase of 3.7% in torque and power capability. Due to the increase in the corner speed, the flux weakening region is extended in both the three-phase and six-phase winding machines.

B. Power Factor

The power factor variation of the three-phase and six-phase pole changing winding induction machines follow similar trends with speed. With the peak current, the total magnetising currents of the three-phase and six-phase windings are similar and the power factors are comparable. If the machine is operated with a 2-pole excitation below the base speed at peak current, the saturated magnetising inductance is significantly lower due to the lower winding factor. As a result, at low speeds, the power factor with a 2-pole excitation is lower. However, in the flux weakening region, the magnetising current is reduced and the machine is unsaturated. Due to the lower number of the poles, the magnetising inductance is higher and the power factor in the flux weakening region of the 2-pole operation is better than that during 4-pole operation in the flux weakening region. Additionally, due to the reduced frequency of operation with 2-pole compared to the 4-pole in the

flux weakening region, the leakage reactance of the 2-pole operation is lower than that of the 4-pole operation.

C. Efficiency

In the constant torque regions at high torque operation, the largest component of loss of is the stator copper loss. During 4-pole operation, the efficiency of the six-phase pole changing winding induction machine is higher than that of the three-phase pole changing winding induction machine for the same speed and torque capability. This is due to the winding factor being directly proportional to the torque capability and the higher winding factor of the six-phase pole changing winding induction machine results in a lower current requirement for developing the same torque as compared to the three-phase pole changing winding machine. The winding factors are similar for the three-phase and six-phase pole changing windings during the 2-pole mode of operation. As a result of the lower winding factor of both the three-phase and six-phase pole changing windings, the efficiency of the machine during the 2-pole operation at low currents is poorer than the efficiency during the 4-pole operation for the same speed. The benefit of improved efficiency during the 2-pole mode of operation is observed when operating at the peak value of current in the extended flux weakening region where the torque capability is better than during the 4-pole operation.

D. Third Harmonic Injection

In addition to a higher fundamental winding factor, the 3^{rd} harmonic currents can be injected to enhanced torque capability of the six-phase pole changing winding induction machine during the 2pole operation. The six-phase pole changing winding induction machine is wound with a symmetrical 4-pole winding with a 60^{o} electrical separation between the phases. When the number of poles is reduced to 2-pole using the inverter, the spatial separation of the windings remains physically the same, however, the electrical separation reduces to 30^{o}. This asymmetric angular separation enables the injected 3^{rd} harmonic currents to produce useful average torque. Utilising this phenomenon, the optimum ratio of the 3^{rd} harmonic current to fundamental current that maximises the peak torque for a fixed DC bus voltage and current rating is determined to be 0.2. The benefit of the 3^{rd} harmonic injection is limited at higher speeds in the flux weakening region due to the fixed DC bus voltage. However, at the corner speed of 1600rpm with the 2-pole operation, the power capability is increased by 14% with the 3^{rd} harmonic injection when compared to the operation without the 3^{rd} harmonic injection.

7.2.4 Transient Behaviour with Pole Changing Windings

The vector space decomposition method was applied to a six-phase pole changing winding induction machine and a dynamic model was implemented in SIMULINK. Using the dynamic model, the transient performances of the three-phase and six-phase pole changing winding induction machines under open-loop scalar control and closed-loop field oriented control are studied. Despite the torque being higher for the six-phase pole changing winding induction machine, the dynamic performances of the three-phase and six-phase machines are similar. With scalar control, the flux and the current control are not decoupled and this results in significant torque and current transients during pole changing operations.

With the rotor held at a fixed speed, with scalar control, when the pole changing operation is performed, a very high negative torque transient is observed. This negative torque transient is almost eliminated when field-oriented control is used. This also is reflected in a reduced current transient with field-oriented control during the pole changing operation.

TABLE 7.3 COMPARISON OF TRANSIENT PERFORMANCE DURING POLE CHANGING WINDING MACHINE

Feature	Scalar Control	Indirect Field Oriented Control
Speed transient	Negative speed transient	Negligible speed transient
Torque transient (with fixed speed)	Negative torque transient	Torque transient reduced by 50% compared to scalar control
Torque transient (with speed control)	Negative torque transient	Torque transient < 20% of rated torque
Current transient	3 times the peak value of steady-state current	<15% peak value of steady-state current

In the second scenario of simulations, the load torque is imposed on the rotor shaft and the speed controller maintains the shaft speed at the setpoint value. Under this condition, the field-oriented control is superior to the scalar control. With scalar control, when the number of poles is changed the rotor speed goes through a transient where the speed momentarily dips to zero and the electromagnetic torque sees a large negative torque transient. The speed transient is negligible under similar load and speed setpoint conditions when field-oriented control is used. Both the duration and the amplitude of the current are reduced with field-oriented control during pole changing operations. This is due to the decoupled nature of the field-oriented control where the d-axis current

can be independently controlled to decay the 4-pole flux and simultaneously build up the 2-pole flux when transitioning from a 4-pole to 2-pole operation. The transient performance during the pole changing operation for scalar and field-oriented control is compared in TABLE 7.3.

7.3 Limitations of Pole Changing Windings

The pole changing winding machines can double the flux weakening range of operation. Using the proposed six-phase pole changing winding, the MMF cancellation and poor winding factor of three-phase electronic pole changing windings can be avoided and a torque density improvement is possible. This advantage, however, is at the cost of using a higher number of switches for the inverter, driving the machine. The limitation of the six-phase pole changing windings are as follows:

1. The inverter to drive the electronic pole changing winding has doubled the number of legs as the number of phases of the machine. This implies that a 12 phase inverter is required to control a six-phase pole changing winding induction machine as opposed to the six-phase inverter required to run a three-phase pole changing winding induction machine. Despite the increased number of phases of the inverter, the VA rating of the inverter and the DC bus remains the same. This results in the ampere rating of the devices being lower. Device prices are dependent on the current rating of devices and this allows the inverter required to drive the pole changing winding machine to be cost-competitive.
2. The number of current sensors for an electronic pole changing winding induction machine is increased compared to a standard six-phase induction machine with a fixed number of poles. While five current sensors are sufficient for a fixed pole six-phase pole induction machine, eight current sensors are required for the six-phase pole changing winding machines. The number of current sensors is, however, lower than those required for a toroidally wound pole-phase modulated machine with a similar number of phases.
3. The inherent limitation of the electronic pole changing winding is the poor winding factor. Using the proposed six-phase pole changing winding improves the winding factor at the higher number of poles but does not improve the winding factor when operating with a lower number of poles.
4. Taking advantage of the asymmetric spatial distribution of the windings with the lower number of poles, the 3^{rd} harmonic currents can be injected to improve the torque capability of the machine. While theoretically, a torque improvement of 40% [LYR02] is possible, when the DC bus voltage and inverter current limit are factored into the operation, the improvement in the flux weakening region is limited to 14% close to the

corner speed since the voltage limit is exceeded if the 3rd harmonics are injected during operation well into the flux-weakening region.

7.4 Future Work

In this thesis, the relative advantages of different methods of pole changing have been investigated and the proposed six-phase electronic pole changing winding induction machine has been studied in detail. Tests on a prototype machine have been used to validate the hypothesis. There are, however, further opportunities to improve the performance of pole changing winding induction machines as discussed in the following.

1. A complete and detailed electric vehicle model is out of the scope of the thesis. Future work includes incorporating a pole changing winding induction machine into a detailed electric vehicle model to determine the impact of the proposed six-phase pole changing winding.
2. With the pole changing winding machine incorporated into the electric vehicle model, an algorithm to determine the most efficient way to switch between the two pole numbers needs to be developed to leverage the benefit of the machine.
3. The transient that occurs in the torque during the pole changing operation is largely due to the decaying of the flux of the outgoing pole number and the building up of the flux of the incoming pole number. Both of these fluxes decay and build up to the steady-state value depending on the rotor time constant of the corresponding pole numbers. The rotor time constant is defined as the ratio of the total rotor inductance (which is the sum of the leakage inductance and the magnetising inductance corresponding to the pole number) to the rotor resistance. Rotor design optimisation aimed at minimising the rotor time constant while preventing an increase in rotor copper losses can be studied.
4. Pole changing windings are most suitable for starter-generators applications where high peak torque and wide speed flux weakening region of operation are required. This is achieved by the increase in corner speeds by changing the number of poles. All of the pole changing windings for induction machines (with the exception of toroidal windings which have other disadvantages as discussed in Chapter 1) have distributed windings which increase the axial length of the machine. While tooth wound induction machines have a shorter end winding length, the high MMF harmonic content causes heating of the rotor and reduces efficiency. A combination of fractional slot windings with pole changing operation can be used to extend the flux weakening region while reducing the overall axial length of the machine.

5. Lastly, the concept of pole changing windings can be extended to permanent magnet machines. Induction machines are particularly suitable for pole changing windings due to the presence of a squirrel cage rotor that can take up any number of poles that the stator MMF excites. With PM machines, the number of rotor poles is determined by the rotor construction. However, using a combination of Alnico magnets and NdFeB magnets, the proposed pole changing winding can be used to change the stator number of poles and suitable current pulses in the *d*-axis to demagnetise and magnetise the Alnico magnets to change the number of poles can be explored [OST02].

Appendices

Appendix I

Design and Analysis of Induction Machines

Several methods for the analysis of an induction machine exist in literature. Depending on the level of accuracy needed, lumped equivalent circuit models, magnetic equivalent circuit (MEC) and finite element analysis (FEA) can be used to predict the performance of the induction machine with increasing levels of accuracy. For each of these methods, the geometric dimensions must be known. Sizing of the induction machine to meet a set of specifications results in a large number of possible designs. From an initial design an optimisation study, as discussed in Chapter 3, is performed to choose a machine design which best meets the specifications at the lowest cost, highest efficiency, highest torque or power density depending on the requirements of the application. In this chapter, a compilation of the equations used to arrive at the geometric dimensions of the machine is discussed. Using the geometric dimensions, the method of predicting the performance characteristics of the machine using analytical equations is discussed. An analytical dynamic model of a 3-phase induction machine that can be used to determine the transient performance (as opposed to the steady-state performance predicted by the lumped parameter, MEC or FEA) is also derived. Finally, the design process is used to dimension a baseline induction machine to meet the specifications of peak torque for a P0 induction machine.

AI.1 Specifications, Constraints and Constants

The specifications for a given induction machine are usually defined by the application that the machine is being designed for. For a starter generator application at the P0 location of a hybrid electric vehicle, an example is listed in TABLE AI.1. The outer diameter and the overall length of the machine are fixed, together with the terminal power conditions at the DC bus. If the outer diameter is not fixed, the induction machine designs with increasingly larger rotor dimensions can be investigated until the specifications are met [BOG12]. Alternatively, an empirical formulation that relates the air gap power density to the volume utilisation factor for various pole numbers, called the Esson's constant [BOL02], can be used to determine a starting point for the stator bore diameter. The outer diameter is calculated to accommodate sufficient ampere-turns in the slots that can meet the torque specifications [BOL02]. When the stator outer diameter is constrained by the specifications, the split ratio, which is defined as the ratio of the stator bore diameter to the stator

outer diameter, is used as the primary design factor that has the highest influence on the torque capability of the designed machine [ZHU01]. Some parameters are kept constant across designs due to geometric, thermal or mechanical constraints. The methods for selecting these constraints are shown in TABLE AI.1.

TABLE AI.1 P0 INDUCTION MACHINE SPECIFICATIONS

Peak Power Mode for 30s @85% Efficiency			
Power (kW)	Speed (rpm)	Environment	DC Bus Voltage (V)
10 (31Nm)	3000	80°C air and 105°C water	52
15 (23Nm)	6000	80°C air and 105°C water	52
Continuous Power Generation Mode			
Power (kW)	Speed (rpm)	Environment	DC Bus Voltage (V)
3.2	2400	120°C air and 105°C water	36, 42, 52
5	6000	120°C air and 105°C water	36, 42, 52
5	20000	120°C air and 105°C water	36, 42, 52
Cranking Mode (Duration of 500ms)			
Torque (N)	Speed (rpm)	Environment	DC Bus Voltage (V)
60 (4kW)	0	120°C air and 105°C water	36
60 (10kW)	1200	120°C air and 105°C water	36
12 (7.5kW)	6000	120°C air and 105°C water	36
Drive Specifications			
V_{DC}=48V $Iphase = 230Arms$ (6 Phase Cranking) $Iphase = 160Arms$ (6 Phase Generating)			
Packaging			
Stack Length +End Winding=100mm External Diameter=144mm			

The stator and rotor tooth flux densities are decided by the choice of the lamination steel materials' saturation flux density point. The stator current density is based on the method of cooling.

An upper limit of 30A/mm^2 is usually set for water-cooled machines. For a given stator bore diameter, the stack length can be selected based on empirical relationships between these quantities for a given pole number as shown in TABLE AI.2.

TABLE AI.2 INDUCTION MACHINE DESIGN CONSTRAINTS AND CONSTANTS

Material constants and constraints		
Parameter	Name	Reference/comment
B_{ts}, B_{ys}	Stator tooth and yoke flux densities	Limited to the saturation value of the steel material
B_{tr}, B_{yr}	Rotor tooth and yoke flux densities	Limited to the saturation value of the steel material
J_s, J_r	Stator and rotor current densities	The choice is based on the cooling system [SOO08][GIA19]
Geometric constants and constraints		
λ	Stator active stack length to bore diameter ratio	$0.95 < \lambda < 4.71$ $(2p = 2)$ $0.47 < \lambda < 2.31$ $(2p = 4)$ $0.32 < \lambda < 1.57$ $(2p = 6)$ $0.23 < \lambda < 1.17$ $(2p = 8)$ [BOL02] [PYR13]
D_{sh}	Shaft diameter	[OBE04]
$w_{ts_{min}}, w_{tr_{min}}$	Minimum stator and rotor minimum tooth width	[BOL02]
g	Air gap thickness	[BOL02] [PYR13]
K_{fill}	Slot fill factor	60%-85% for hairpin windings and up to 40% for round wire [GRO14]
K_{stack}	Stacking factor	$\approx$ 97% [BOL02] [PYR13]

The shaft dimensions are selected based on the torque transfer capability and the expression for keyed and non-keyed shafts are shown in (AI.1) and (AI.2) respectively. The motor rating P is in hp and the speed N is in rpm. Manufacturing limitations sets the minimum tooth width to 2mm. The air gap length is chosen to minimise the magnetising current while being feasible to manufacture. Too small an air gap increases the air gap permeance harmonics and also the surface eddy current losses. Empirical relationships for the air gap length are shown in (AI.3) [PYR13]. The lowest mechanically feasible air gap is 0.2mm. The smaller air gap results in high pulsating losses especially in stators with open slots.

$$D_{sh} = \sqrt[3]{\frac{60 \times P}{N}}\ in \tag{AI.1}$$

$$D_{sh} = \sqrt{\frac{105 \times P}{N}}\ in \tag{AI.2}$$

$$\begin{aligned} \delta &= \frac{0.2 + 0.01 \times P^{0.4}}{1000}\ m; \qquad if\ p = 1, \\ \delta &= \frac{0.18 + 0.006 \times P^{0.4}}{1000}\ m; \quad if\ p > 1. \end{aligned} \tag{AI.3}$$

For 48V machines, the number of turns is usually low and the slot currents are high. Hairpin windings are known to improve the slot fill factor significantly and subsequently improve the torque. The fill factor range for rectangular and round conductors are shown in TABLE AI.2.

AI.2 Basic Design Methodology

The design of the induction machine from a set of specifications subject to the constraints previously discussed is based on the iterative process shown in the flowchart of Fig. AI.1.

The steps are discussed below:

1. Given an outer stator diameter, the stator bore diameter can be chosen based on the empirical relationship between these quantities from the values shown in TABLE AI.3 [BOL02]. The number of poles can be chosen based on the top speed of the machine. Detailed optimisation for the choice of the number of poles is discussed in Chapter 2. Larger pole numbers result in a lower length of end windings as well as thinner yokes thus maximising the slot area available for accommodating windings. However, with rectangular conductors, the high frequency required for higher speeds with higher pole numbers can result in high AC losses in the windings and the stator surface. For a chosen split ratio, the stack length of the machine

can be determined from the stator active stack length to bore diameter ratio given in TABLE AI.2. The value λ is chosen based on the length limitations imposed by the specifications.

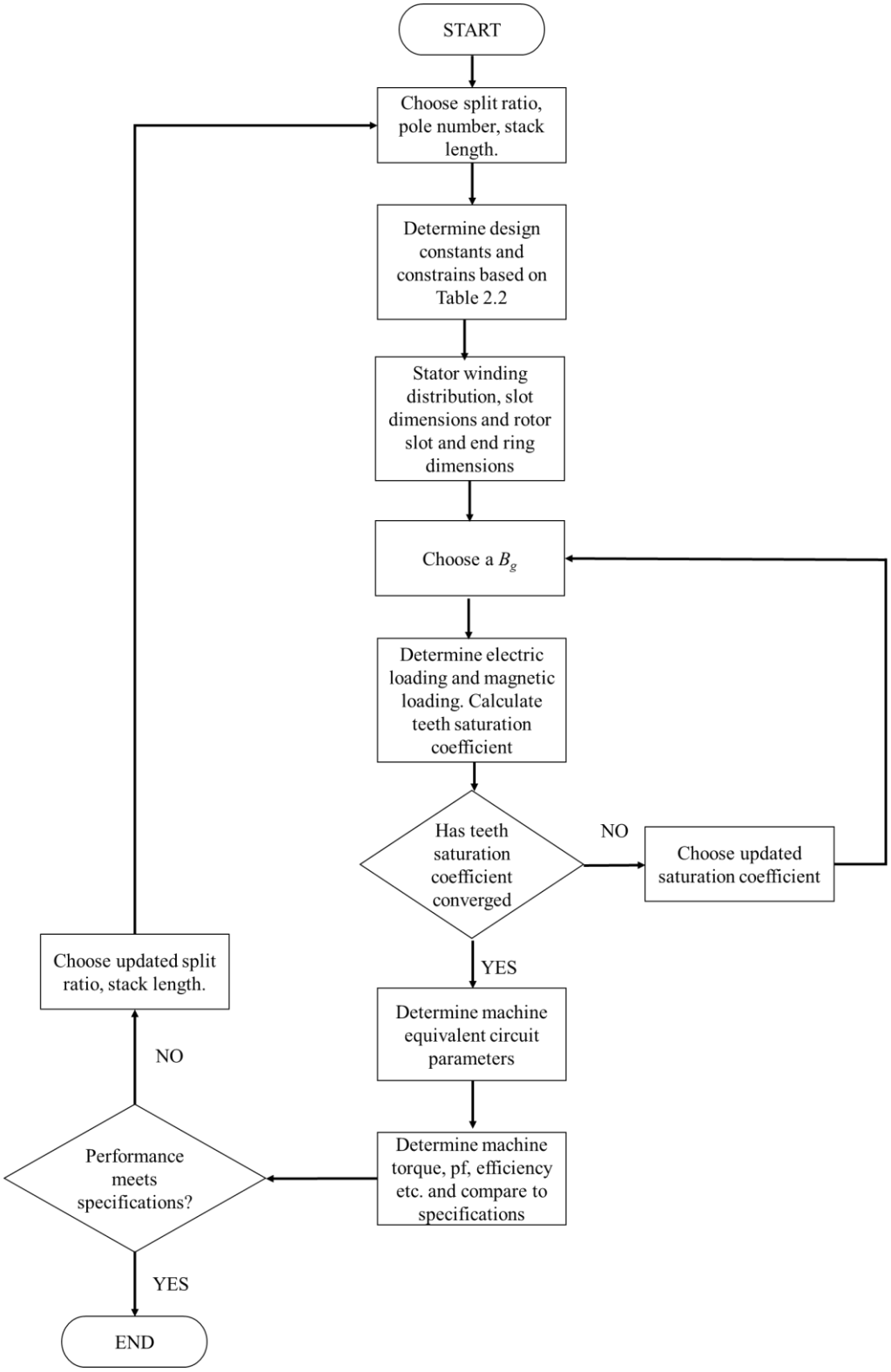

Fig. AI.1 Flowchart for the induction machine design algorithm.

TABLE AI.3 RANGE OF SPLIT RATIO FOR DIFFERENT POLE NUMBERS [BOL02]

Number of poles	2	4	6	8
$\frac{D_{is}}{D_{out}}$	0.54-0.58	0.61-0.63	0.63-0.68	0.68-0.73

2. From the constants in TABLE AI.2, the other parameters, namely, the air gap thickness, the flux density limits in the teeth based on lamination steel material, the current density for the stator and rotor based on the cooling technology to be adopted and the slot fill factor based on the winding methodology to be used, are selected [GOR14]. The choice of current density is a parameter that may have to be revisited after the thermal analysis is performed. This is especially true for high torque density water-cooled machines.
3. For a given pole number there is a wide choice of stator and rotor slot numbers available. Based on the stator slot number, the winding distribution is chosen to maximise the winding factor while minimising the MMF harmonics. The number of slots per pole per phase (SPP) impacts the differential leakage inductance of the stator winding. The differential leakage coefficient for SPP=1 is 10% and is too high to be practical. Higher values of SPP result in decreasing differential leakage coefficients. Higher values of SPP for a given pole and phase number result in a larger number of slots, more coils to be wound, and thinner slots. The mechanical limit and magnetic saturation of the teeth will limit the largest value of SPP that can be chosen. For a chosen number of stator slots, the fundamental winding factor can then be determined.
4. The iterative process begins at step 4 where an initial average air gap flux density, B_g is chosen and the flux per pole is calculated for a given tooth saturation factor.

A. Induced EMF and Saturation

Assuming a sinusoidal distribution of air gap flux in the machine, the equation for the main flux is given by (AI.4). $\hat{\phi}_m$, k_w, N and ω represent the maximum value of the air gap flux over a full-pitch winding, the fundamental winding factor, the number of turns per phase and the electrical frequency.

$$\phi_m(t) = \hat{\phi}_m \sin \omega t \tag{AI.4}$$

$$e_m = -\frac{d(N k_w \phi_m)}{dt} = -N k_w \omega \hat{\phi}_m \cos \omega t \tag{AI.5}$$

The induced EMF in the winding associated with this flux is given by (AI.5). The peak value of the air gap flux over one pole pitch for an assumed average air gap flux density is given by (AI.6).

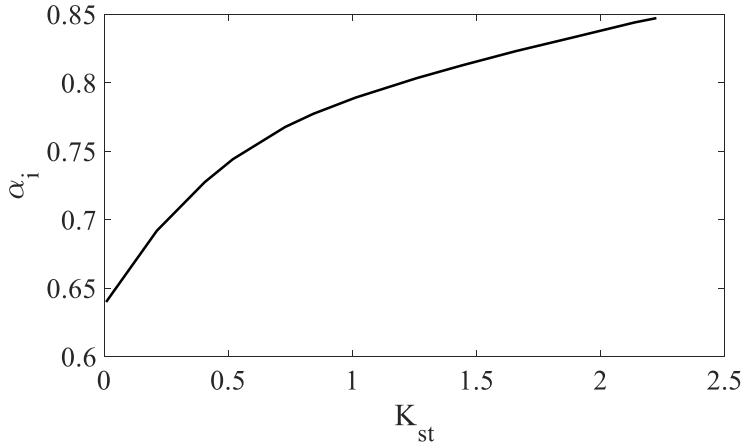

Fig. AI.2 Saturation factor vs flux density shape factor.

$$\hat{\phi}_m = \alpha_i B_g L_{stk} \frac{\pi D_{is}}{2p} \tag{AI.6}$$

In (AI.6), the flux density shape factor α_i depends on the initially chosen value of the tooth saturation factor. For a given tooth saturation factor, the value of the flux density shape factor is determined from the curve of Fig AI.2. The product $\alpha_i B_g$ represents the average of the flux density in the tangential direction. $\alpha_i = 2/\pi = 0.64$ for a sinusoidal flux density distribution. For best utilisation of the iron material in the stator, the dimensions of the stator teeth are chosen so that the machine is saturated at the peak value of the sinusoidal flux density. The resulting flux density distribution is a flat-topped waveform which results in α_i being greater than the ideal sinusoidal value of 0.64. The teeth experiencing this peak flux density are more saturated than the other teeth spatial located at other points of the flux density waveform. The value of the tooth saturation factor is to be iterated gradually until convergence is reached during the design process as shown in the flow chart of Fig. AI.1. The tooth saturation factor is defined as the ratio of the sum of stator MMF, F_{stator}, and rotor teeth MMF, $F_{rotor,}$ to the air gap MMF, $F_{airgap,}$ is shown in (AI.7).

$$K_{st} = \frac{(F_{stator} + F_{rotor})}{F_{airgap}} \tag{AI.7}$$

The number of series turns per phase, W can now be determined from (AI.8) and the number of conductors per slot for a chosen number of parallel paths a, and SPP of q is given in (AI.9).

$$W = \sqrt{2}\frac{E_m}{\omega k_w \alpha_i B_g L_{stk} \frac{\pi D_{is}}{2p}} \tag{AI.8}$$

$$n_s = \frac{aW}{pq} \tag{AI.9}$$

The number of conductors per slot should be an integer number and an even number for a double layer winding. With the number of conductors per phase rounded off, the number of series turns per phase and the air gap flux density have to be adjusted accordingly.

B. Stator and Rotor Slot Dimensioning

With the number of conductors determined and the assumed stator current density, the dimensions of the slot can be determined by calculating the area (A_{co}) and diameter (d_{co}) of the conductors in the slot from (AI.10) and (AI.11) respectively.

$$A_{co} = \frac{I_{rms}}{J_s a} \tag{AI.10}$$

$$d_{co} = \sqrt{\frac{4A_{co}}{\pi a_{strands}}} \tag{AI.11}$$

In (AI.10), I_{rms} is the maximum value of the rms current that can be supplied by the inverter. In (AI.11), $a_{strands}$ is the number of strands per conductor which are used for high current machines to limit large diameter wire cross-sections. While (AI.11) is suitable for round wires, for a rectangular cross-section, the dimensions of the wire can be determined based on the slot width and height. From the conductor area and slot fill factor, the area of the slot, A_{slot} that can accommodate the windings is given by (AI.12).

$$A_{slot} = \frac{A_{co} n_s}{K_{fill}} \tag{AI.12}$$

The stator tooth width can be determined by assuming that all the air gap flux passes through the stator teeth using the relationship in (AI.13).

$$B_g L_{stk} \frac{\pi D_{is}}{N_s} \approx B_{ts} b_{ts} L_{stk} K_{stack} \tag{AI.13}$$

The symbols for the slot dimensions for a flat and a round bottom stator slot are shown in Fig. AI.3. The other parameter used for optimisation is the stator tooth-width to slot pitch ratio which is defined as the ratio of tooth width to slot pitch. The slot dimensions now can be determined by these known parameters. The quadratic equation of (AI.15) is solved to determine the slot height h_s for a given height of slot opening and slot wedge for a round-bottomed slot.

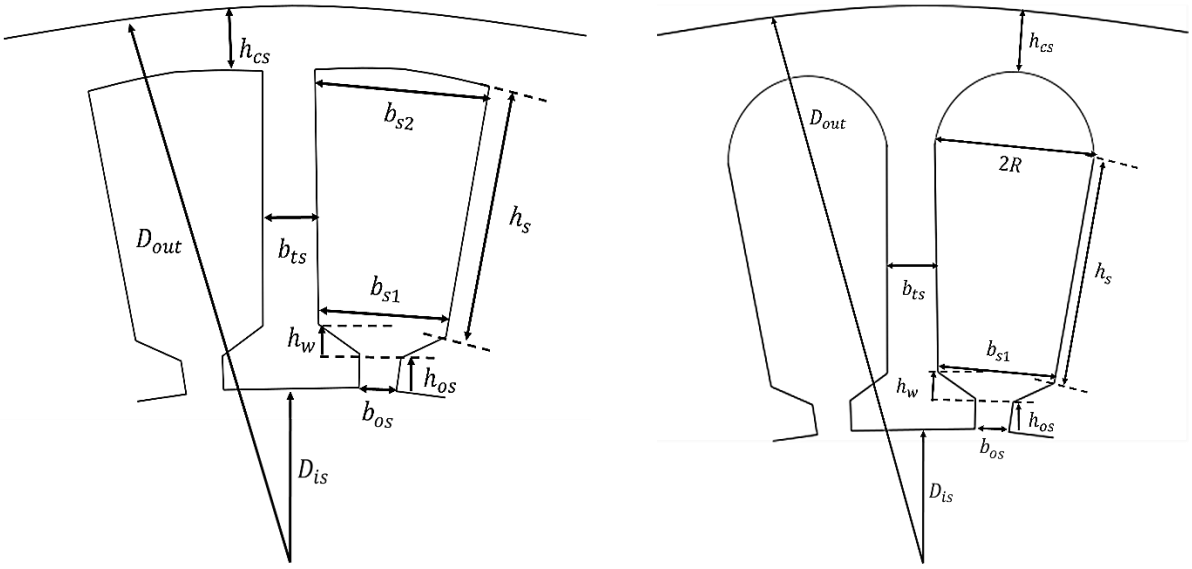

(a) Flat-bottomed slot (b) Round-bottomed slot

Fig. AI.3 Representative dimensions of stator slots.

$$\tau = \pi \left(D_{is} + \frac{2(h_{os} + h_w)}{N_s} \right) \tag{AI.14}$$

$$\left(\frac{\pi}{N_s} + \frac{\pi^3}{2N_s^2} \right) h_s^2 + \left(b_{s1} + \frac{\pi^2(\tau - b_{ts})}{2N_s} \right) h_s + \frac{\pi}{8}(\tau - b_{ts})^2 - A_{slot} = 0 \tag{AI.15}$$

$$R = \frac{b_{s2}}{2} = \left(\tau + \frac{2\pi h_s}{N_s} - b_{ts} \right) \frac{1}{2} \tag{AI.16}$$

For a flat-bottomed slot, the dimensions of the slot can be determined by solving the quadratic equation of (AI.17) in which the unknown dimension being calculated is the height of the slot h_s.

$$\left(\frac{2\pi}{N_s} \right) h_s^2 + \left(\pi \left(D_{is} + \frac{2(h_{os} + h_w)}{N_s} \right) + b_{s1} - b_{ts} \right) h_s - 2A_{slot} = 0 \tag{AI.17}$$

Once the slot height is determined, the yoke height can be calculated from AI.18.

$$h_{cs} = \frac{\left(D_{out} - \left(D_{is} + 2(h_{os} + h_w + h_s)\right)\right)}{2} \tag{AI.18}$$

The number of rotor slots is chosen based on considerations of torque ripple and leakage reactance. It is an optimisation parameter that also influences the torque capability in the flux weakening region of operation. Once a rotor slot number has been chosen the slot dimensions can be determined using a similar procedure as for the stator slot dimensions. The rotor bar current is given by (AI.19).

$$I_{bar} = \frac{2mW k_w}{N_r} I_{rms} \tag{AI.19}$$

The bar current and the rotor current density are used to determine the rotor slot area and based on the shape of the slot the dimension of the slot can be determined from (AI.14)-(AI.17).

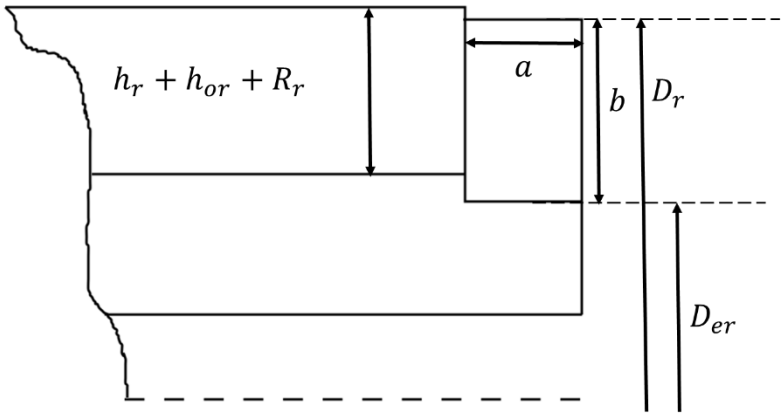

Fig. AI.4 End ring cross-section showing dimensions.

The cross-section of the end ring region is shown in Fig. AI.4. The end ring current is related to the bar current as shown in (AI.20). The end-ring current density is assumed to be 75%-80% of the bar current density. The rotor bars are in contact with the rotor laminations and can conduct the heat more effectively than the end rings, and therefore, a lower current density is assumed for the end-ring [BOL02]. The end ring area is given by (AI.21). The dimensions of the end ring are determined using the equations shown in (AI.22)-(AI.23).

$$I_{er} = \frac{I_{bar}}{2\sin\frac{\pi p}{N_R}} \tag{AI.20}$$

$$A_{er} = \frac{I_{er}}{J_{er}} \tag{AI.21}$$

$$b = (h_r + h_{or} + R_r) \tag{AI.22}$$

$$a = \frac{A_{er}}{b} \tag{AI.23}$$

5. With the slot dimensions calculated, the MMF drop across the stator tooth and the rotor tooth are determined and the tooth saturation factor is calculated and compared to the initially selected value. If these are different, the newly computed value is used to lookup an updated value of α_i from Fig. AI.2 and the air gap flux density is recalculated and steps 1 through 4 are repeated until convergence is reached.
6. In the next few steps, the machine performance is calculated by determining the equivalent circuit parameters from the geometric and winding parameters. Once the machine design is finalised and the steady-state performance is computed at the design point, the torque-speed characteristics can be determined using the method discussed in Section AI.3.
7. Using these machine parameters, the dynamic performance can also be determined using a d-q-axis dynamic model to be discussed in Section AI.4.

AI.3 Analysis of Electromagnetic Performance

The rated torque at the inverter current and voltage can be determined from the steady-state equivalent circuit of the induction machine. The equivalent circuit parameters of the machine can be calculated from the physical dimensions of the machine and the material properties of the machine like the grade of copper, aluminium and steel. In this section, the method of calculating these equivalent circuit parameters are discussed based on equations compiled from [BOL02] [PYR13] [BOL11a] [BOG11b].

AI.3.1 Equivalent Circuit Parameter Calculation

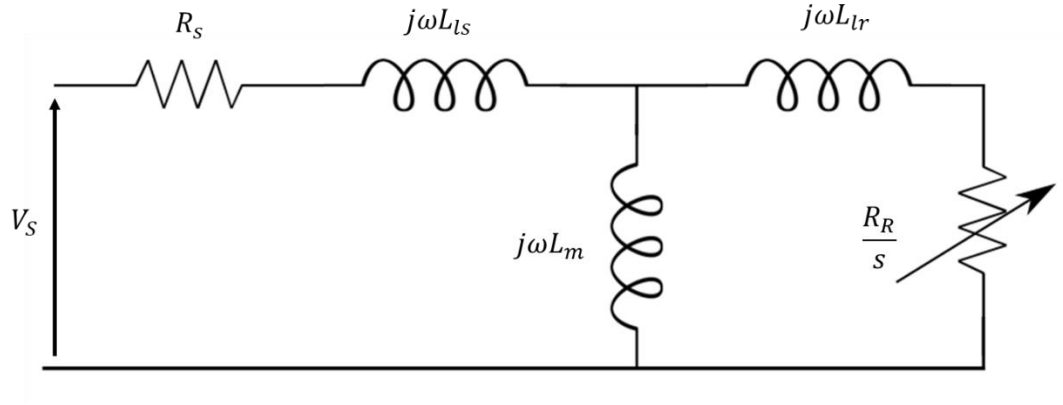

Fig. AI.5 Steady-state equivalent circuit of the induction machine.

A. Resistances

The stator phase resistance at any temperature can be calculated by taking into consideration the number of series turns per phase and the wire dimensions shown in (AI.24). y is the coil pitch expressed in the number of slots.

$$R_S = \frac{\rho_{Cu} L_{conductor} W}{A_{co} a}\left(1 + \frac{\Delta T}{273}\right) \tag{AI.24}$$

$$L_{conductor} = 2(L_{stack} + L_{end}) \tag{AI.25}$$

$$\begin{aligned} L_{end} &= 2y - 0.04\ m; \quad for\ p = 1 \\ L_{end} &= 2y - 0.02\ m; \quad for\ p = 2 \\ L_{end} &= \frac{\pi}{2} y + 0.018\ m; \quad for\ p = 3 \\ L_{end} &= 2.2y - 0.012\ m; \quad for\ p = 4 \end{aligned} \tag{AI.26}$$

The end winding length L_{end} is determined based on the empirical relationships of (AI.26). These are based on a circular shape of a distributed end winding coil [BOL02].

The relationship between the current in the rotor bars and the end rings can be determined by considering the current phasor diagram of the rotor cage shown in Fig. AI.6. The angular phase shift between the bars currents for the v^{th} harmonic is given by $\alpha v p = v\frac{2\pi p}{N_R}$. Based on the polygon of Fig. AI.6, the ring current is given by (AI.27).

$$I_{ring} = \frac{I_{bar}}{2\sin\frac{\pi p}{N_R}} \tag{AI.27}$$

The currents in the squirrel cage create a resistive loss in the rotor given by (AI.28). The rotor resistance is then given by (AI.29) where l_{er}.is the length of the end ring section given by (AI.30).

$$P_{cuR} = N_R\left(R_{bar}I_{bar}^2 + 2R_{ring}I_{ring}^2\right) = N_R I_{bar}^2(R_{bar} + \frac{R_{ring}}{2\sin^2\frac{\pi p}{N_R}} \tag{AI.28}$$

$$R_R = \rho_{Al}\left(\frac{L_{stack}}{A_{bar}}K_R + \frac{l_{er}}{2A_{er}\sin^2\frac{\pi p}{N_R}}\right)\left(1 + \frac{\Delta T}{273}\right) \tag{AI.29}$$

$$l_{er} = \frac{\pi(D_{er} - b)}{N_R} \tag{AI.30}$$

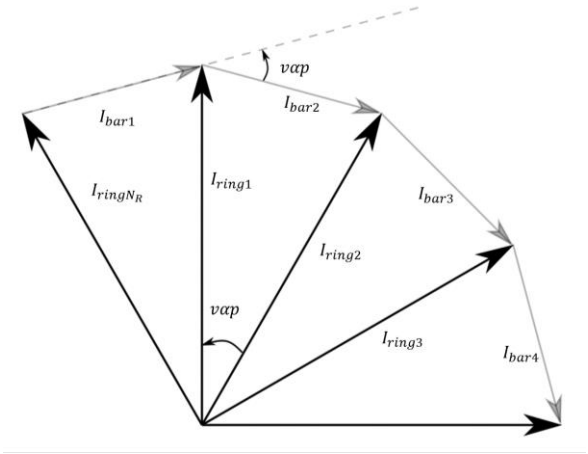

Fig. AI.6 Current distribution in cage bars and end ring sections.

The rotor bar is a solid conductor and is prone to skin effect induced losses. The factor K_R in (AI.29) accounts for these losses and is given by (AI.31) for a rectangular bar.

$$K_R = \zeta\frac{(\sinh 2\zeta + \sin 2\zeta)}{(\cosh 2\zeta - \cos 2\zeta)} \tag{AI.31}$$

$$\zeta = \sqrt{\frac{\omega\mu_o}{2\rho_{Al}}}h_R \tag{AI.31}$$

B. Leakage Inductances

The stator phase leakage inductance is a sum of the slot leakage inductance, the differential leakage inductance, and the end winding inductance and is given by (AI.33).

$$L_S = 2\mu_o L_{stk} \frac{W^2}{pq} (\lambda_s + \lambda_{ds} + \lambda_{ew}) \tag{AI.33}$$

Using the slot dimensions shown in Fig. AI.3, the slot leakage inductance coefficient (λ_s) is given by (AI.34). $\beta = y/\tau$ where y is the coil pitch in the number of slots and τ is the coil pitch for a full pitch winding in the number of slots.

$$\lambda_s = \left[\frac{2}{3}\frac{h_s}{b_{s1} + b_{s2}} + \frac{2h_w}{b_{os} + b_{s1}} + \frac{h_{os}}{b_{os}}\right] \left(\frac{1 + 3\beta}{4}\right) \tag{AI.34}$$

The differential leakage inductance is influenced by the effect of slotting which can be incorporated using Carter's coefficient. The stator and rotor slotting effects on Carter's coefficient are shown in (AI.35) and (AI.36) respectively [HEL77]. The total Carter's coefficient is given in (AI.37).

$$K_{cs} = \frac{\frac{\pi D_{is}}{N_S}}{\frac{\pi D_{is}}{N_S} - \frac{b_{os}^2}{5g + b_{os}}} \tag{AI.35}$$

$$K_{cr} = \frac{\frac{\pi D_r}{N_R}}{\frac{\pi D_r}{N_R} - \frac{b_{or}^2}{5g + b_{or}}} \tag{AI.36}$$

$$K_c = K_{cs} \times K_{cr} \tag{AI.37}$$

The differential leakage inductance coefficient [HEL77] is given by (AI.38).

$$\lambda_{ds} = \frac{0.9\frac{\pi D_{is}}{N_S} q^2 k_w^2 C_s \gamma_{ds}}{K_c g(1 + K_{st})} \tag{AI.38}$$

$$C_s = 1 - 0.033\frac{b_{os}^2}{g\frac{\pi D_{is}}{N_S}} \tag{AI.39}$$

$$
\begin{aligned}
\gamma_{ds} &= 9.5 \times 10^{-2} && ; q = 1 \\
\gamma_{ds} &= (0.25 \sin\phi + 2.6) \times 10^{-2} && ; q = 2 \\
\gamma_{ds} &= (0.18 \sin\phi + 1.24) \times 10^{-2} && ; q = 3 \\
\gamma_{ds} &= (0.14 \sin\phi + 0.76) \times 10^{-2} && ; q = 4 \\
\gamma_{ds} &= (0.11 \sin\phi + 0.41) \times 10^{-2} && ; q = 6 \\
\gamma_{ds} &= (0.11 \sin\phi + 0.28) \times 10^{-2} && ; q = 8 \\
\phi &= \pi(6\beta - 5.5)
\end{aligned}
\tag{AI.40}
$$

The end winding leakage inductance coefficient for a two-layer winding is shown in (AI.41) [BOL02].

$$\lambda_{ew} = 0.34 \frac{q}{L}(L_{end} - 0.64\ \beta\tau) \tag{AI.41}$$

The length of the end winding section is defined in (AI.25).

C. Magnetizing Inductance

The magnetising inductance of the induction machine is dependent on the magnetic characteristics of the material and the dimensions of the induction machine. The unsaturated value of the magnetising inductance can be determined by assuming a sinusoidal flux density distribution B_g over the pole pitch. The peak value of air gap flux $\hat{\phi}_m$ is the maximum flux that also produces the maximum flux linkage $\widehat{\psi_m}$ of a coil. These quantities are given in (AI.42) and (AI.43) respectively.

$$\hat{\phi}_m = \frac{2}{\pi}\frac{\pi D_{is}}{2p} L_{stk} B_g \tag{AI.42}$$

$$\hat{\psi}_m = k_w W \hat{\phi}_m = k_w W \frac{2}{\pi}\frac{\pi D_{is}}{2p} L_{stk} B_g \tag{AI.43}$$

The magnetic reluctance of the air gap is determined by the effective air gap length and the flux density is related to the current linkage of the stator phase winding as shown in (AI.44).

$$B_g = \frac{\mu_o \Theta_s}{g K_c} \tag{AI.44}$$

From (AI.42) and (AI.43) the flux linkage of a single phase is obtained in (AI.45).

$$\hat{\psi}_m = k_w W \hat{\phi}_m = k_w W \frac{2}{\pi} \frac{\pi D_{is}}{2p} L_{stk} \frac{\mu_o \Theta_s}{g K_c} \tag{AI.45}$$

The MMF of a single-phase winding is given by (AI.46).

$$\Theta_s = \frac{4}{\pi} \frac{k_w W}{2p} \sqrt{2} I_s \tag{AI.46}$$

Substituting (AI.46) in (AI.45) yields the expression for flux linkage of a single-phase in terms of the current flowing through the phase as shown in (AI.47).

$$\hat{\psi}_m = \frac{2}{\pi} \mu_o \frac{4}{\pi} \frac{\pi D_{is} L_{stk}}{g K_c} \left(\frac{k_w W}{2p} \right)^2 \sqrt{2} I_s \tag{AI.47}$$

From (AI.46), the magnetising inductance for a single-phase winding is determined by the ratio of the flux linkage and the current through that phase. In an *m-phase* machine, the flux is contributed by all the phases and the magnetising inductance is determined by the product of the single-phase inductance with *m/2* as shown in (AI.48).

$$L_m = \frac{4m}{\pi} \mu_o \frac{D_{is} L_{stk}}{g K_c} \left(\frac{k_w W}{2p} \right)^2 \tag{AI.48}$$

The magnetising inductance is a strong function of saturation. While analytical methods exist to determine this variation [GUA14] [BOL02] [BOG11a], these characteristics can be determined with a series of fast magnetostatic FEA simulations and result in a high accuracy model of the induction machine [ALB08]. This is discussed with numerical examples for 4 different induction machines in Chapter 7.

D. Magnetising Current

The complete magnetising inductance characteristic as a function of magnetising current is necessary only for the complete torque-speed characteristics of the machine. To determine the initial torque capability of the machine, the magnetising current under the single saturated operating point is sufficient. With the dimensions of the machine known, the magnetising current can be determined by calculating the magnetising MMF of the machine. The magnetising MMF is the sum of the MMF drop across the air gap, the stator tooth, the rotor tooth, and the stator and rotor back irons.

$$F_{1m} = 2\left(\frac{K_c g B_g}{\mu_o} + F_{mts} + F_{mtr} + F_{mcs} + F_{mcr}\right) \tag{AI.49}$$

From (AI.13), the tooth stator and rotor tooth flux densities are determined. For these flux densities in the iron regions, the corresponding flux intensity can be looked-up from the material BH characteristics to determine the MMF drop in the tooth regions of the stator and rotor (AI.50).

$$F_{mts} = H_{ts}(h_s + h_{os} + h_w) \tag{AI.50}$$

$$F_{mtr} = H_{tr}(h_r + h_{or} + h_{wr}) \tag{AI.51}$$

The MMFs in the stator and rotor back irons are calculated based on the flux intensity due to the flux density in the back iron. The flux densities in the back iron of the stator and rotor are determined based on (AI.53) and (AI.55).

$$h_{cs} = \frac{D_{out} - (D_{is} + 2(h_{or} + h_r + h_{wr}))}{2} \tag{AI.52}$$

$$B_{cs} = \frac{\hat{\phi}_m}{2L_{stk}h_{cs}} \tag{AI.53}$$

$$h_{cr} = \frac{D_{ir} - 2(h_{or} + h_r + h_{wr}) - D_{sh}}{2} \tag{AI.54}$$

$$B_{cr} = \frac{\hat{\phi}_m}{2L_{stk}h_{cr}} \tag{AI.55}$$

The back iron MMFs of the stator and rotor are shown in (AI.56) and (AI.57).

$$F_{mcs} = C_{cs}\frac{\pi(D_{out} - h_{cs})}{2p}H_{cs}(B_{cs}) \tag{AI.56}$$

$$F_{mcr} = C_{cr}\frac{\pi(D_{sh} + h_{cr})}{2p}H_{cr}(B_{cr}) \tag{AI.57}$$

The coefficients C_{cs}, C_{cr} are empirical coefficients that represent the length of the flux path in the back core and are defined in (AI.58) [BOL02].

$$C_{cs,r} \approx 0.88e^{-0.4B_{cs,r}^2} \tag{AI.58}$$

The magnetising current is then defined as shown in (AI.59).

$$I_m = \frac{\pi p F_{1m}}{6\sqrt{2} W k_w} \tag{AI.59}$$

AI.3.2 Performance Characteristics from Equivalent Circuit

The equivalent circuit of Fig. AI.5 can be simplified to a Thevenin equivalent circuit of Fig. AI.7.

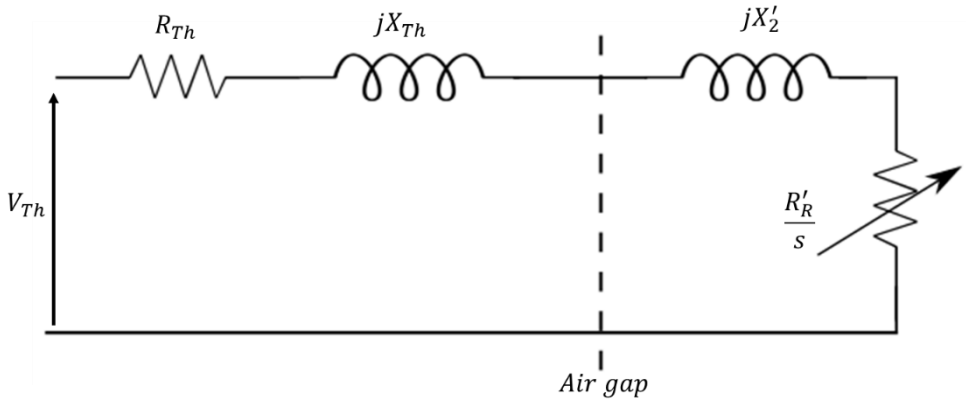

Fig. AI.7 Thevenin equivalent circuit of the induction machine.

The Thevenin voltage of the equivalent circuit is given by (AI.59).

$$V_{Th} = \frac{X_m}{\left[R_s^2 + (X_s + X_m)^2\right]^{\frac{1}{2}}} V_s \tag{AI.59}$$

The Thevenin equivalent circuit impedance is given in (AI.60).

$$Z_{Th} = R_{Th} + jX_{Th} = \frac{jX_m(R_s + jX_s)}{R_s + j(X_s + X_m)} \tag{AI.60}$$

The mechanical torque can now be calculated as a function of slip for an applied phase voltage as shown in (AI.61)

$$T_e = \frac{1}{\omega_s} \frac{V_{Th}^2}{\left(R_{Th} + \frac{R_r'}{s}\right)^2 + \left(X_{Th} + X_r'\right)^2} \frac{R_r'}{s} \tag{AI.61}$$

The stator current for an applied phase voltage is given by (AI.62).

$$I_s = \frac{V_s}{R_s + jX_s + \dfrac{jX_m\left(\dfrac{R'_r}{s} + jX'_r\right)}{\dfrac{R'_r}{s} + j\left(X_m + X'_r\right)}} \tag{AI.62}$$

Using the current equation of (AI.62), the variation of stator current with slip is plotted and the slip corresponding to the rated current can be determined. Substituting this slip in (AI.61), the rated torque is determined.

AI.4 Dynamic Modelling of Induction Machine

The standard per phase equivalent circuit of the induction machine is only valid for determining the steady-state performance of the machine. This is due to the absence of velocity-dependent flux terms in the equivalent circuit. However, to determine the transient performance of the induction machine and to couple the electromagnetic behaviour of the machine to a mechanical model, a dynamic model of the induction machine is required. In addition, the induction machine dynamic model must be capable of modelling the nonlinear behaviour of the induction machine. The stator and rotor coupling of the induction machines is characterised by the magnetising inductance which is a nonlinear quantity and is dependent on the magnetising current. The complexity of modelling the dynamic behaviour of the induction machine arises from the rotor dependent nature of the inductance of the stator and rotor windings. The induction machine can be modelled in the so-called natural reference frame where the physical variables are modelled as position-dependent variables. An extension of this proposed in [TOL91a] [TOL91b], known as the Modified Winding Function Theory (MWFT) model, is especially useful where the windings of the machine are non-sinusoidally distributed and all the corresponding effects of the harmonics are required to be captured by the model. Such models are also advantageous in cases where mechanical non-linearity like non-uniform air gaps, rotor eccentricities, broken rotor bars, stator turn-faults and other asymmetric faults are present [JOK00] [FAI02]. The non-linearity of the magnetising inductance can be incorporated in the MWFT model by assuming that the effect of saturation is to increase the effective air gap of the induction machine. The extent of this modification of the air gap is dependent on the flux level in the machine [BIS01] [NAN03] [NAN04]. This model is however computationally intensive since a new non-sparse matrix inversion is required at every time step.

Induction machines considered in this thesis have sinusoidally distributed stator windings and for sinusoidally distributed windings, the dynamic d-q model of the induction machines can be used [KRA02]. In this section, a brief outline of the d-q model of induction machines is discussed. In

Chapter 6, this model is extended with appropriate transforms for 3-phase and 6-phase symmetrical and asymmetric induction machines, as well as pole-changing winding induction machines. The motivation for developing the dynamic d-q model was to reduce the complexity of the induction machine model with time-varying parameters that results in a computationally intensive model. The induction machine can be considered as a rotating transformer with the primary and secondary corresponding to the stator and the rotor winding respectively. The phasor diagram of the stationary stator winding and the rotating rotor windings of a 3-phase induction machine is shown in Fig. AI.8.

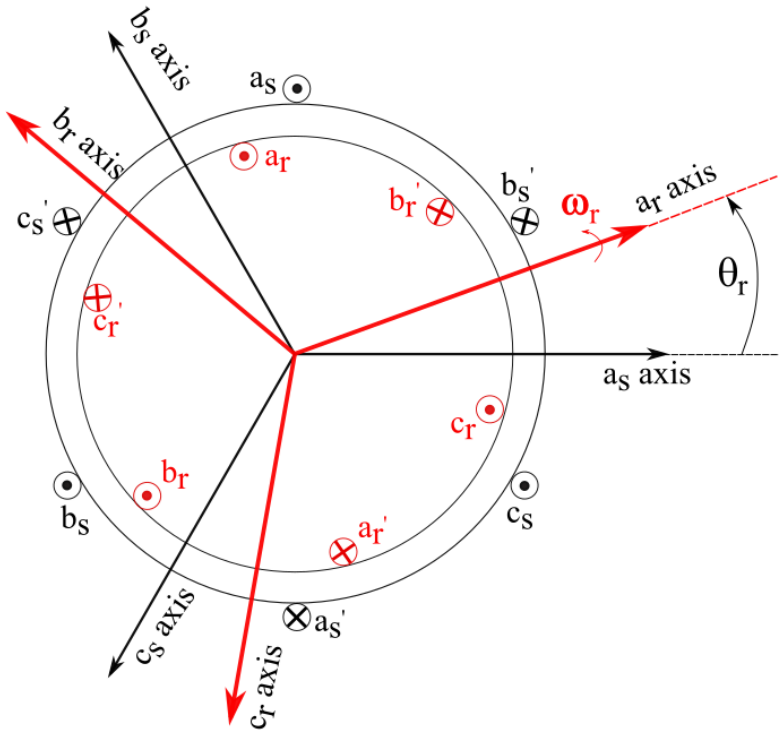

Fig. AI.8 Phasor diagram of stator and rotor of a 3-phase induction machine.

Each phase of the stator and the rotor are characterised by a resistance and inductance. The mutual inductance between the stator and rotor windings vary with rotor position. The transformation from of a stationary 3-phase voltage vector set to a stationary 2-phase system shifted at an angle θ from the 3-phase voltage vector is shown in Fig. AI.9(a). The corresponding transformation matrix is shown in (AI.63).

$$\begin{bmatrix} v_{qs}^{s} \\ v_{ds}^{s} \\ v_{os}^{s} \end{bmatrix} = \frac{2}{3}\begin{bmatrix} cos\theta & \cos(\theta - 120^{o}) & cos(\theta + 120^{o}) \\ sin\theta & sin(\theta - 120^{o}) & sin(\theta + 120^{o}) \\ 0.5 & 0.5 & 0.5 \end{bmatrix}\begin{bmatrix} v_{as} \\ v_{bs} \\ v_{cs} \end{bmatrix} \tag{AI.63}$$

The position-dependent inductances are not converted to position-invariant inductances using this transformation. To convert the inductance to constant position-invariant quantities can be achieved by transforming the d^s-q^s reference frame to a synchronously rotating d^e-q^e reference frame.

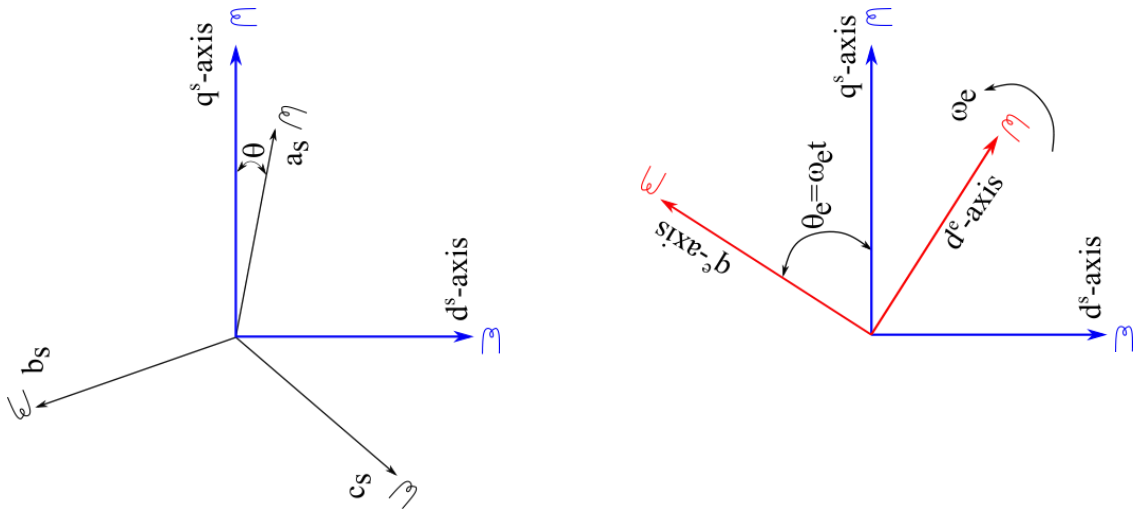

(a) Stationary three-phase to stationary 2-phase transformation

(b) Stationary two-phase to rotating 2-phase transformation

Fig. AI.9 Phasor diagram showing the transformation from stationary 3-phase axes to a stationary and rotating 2-phase d-q axis.

The corresponding phasor diagrams are shown in Fig. AI.9(b). The transformation matrix to perform this operation is shown in (AI.64).

$$\begin{bmatrix} v_{qs}^{s} \\ v_{ds}^{s} \end{bmatrix} = \begin{bmatrix} \cos(\theta_e) & sin(\theta_e) \\ -sin(\theta_e) & cos(\theta_e) \end{bmatrix} \begin{bmatrix} v_{qs}^{e} \\ v_{ds}^{e} \end{bmatrix} \tag{AI.64}$$

Applying this transformation, the voltage equation of the induction machine in the synchronously rotating reference frame is shown in (AI.65)-(AI.68).

$$v_{qs}^{e} = R_s i_{qs}^{e} + \frac{d}{dt}\psi_{qs}^{e} + \omega_e \psi_{ds}^{e} \tag{AI.65}$$

$$v_{ds}^{e} = R_s i_{ds}^{e} + \frac{d}{dt}\psi_{qs}^{e} - \omega_e \psi_{qs}^{e} \tag{AI.66}$$

$$v_{qr}^{e} = R_r i_{qr}^{e} + \frac{d}{dt}\psi_{qr}^{e} + (\omega_e - \omega_r)\psi_{dr}^{e} \tag{AI.67}$$

$$v_{dr}^{e} = R_r i_{dr}^{e} + \frac{d}{dt}\psi_{dr}^{e} - (\omega_e - \omega_r)\psi_{qr}^{e} \tag{AI.68}$$

The flux linkage values in the voltage expressions are functions of the current and inductances and are shown in (AI.69)-(AI.74).

$$\psi_{qs}^{e} = L_{ls} i_{qs}^{e} + L_m\left(i_{qs}^{e} + i_{qr}^{e}\right) \tag{AI.69}$$

$$\psi_{qr}^{e} = L_{lr} i_{qr}^{e} + L_m\left(i_{qs}^{e} + i_{qr}^{e}\right) \tag{AI.70}$$

$$\psi_{qm}^{e} = L_m\left(i_{qs}^{e} + i_{qr}^{e}\right) \tag{AI.71}$$

$$\psi_{ds}^{e} = L_{ls} i_{ds}^{e} + L_m(i_{ds}^{e} + i_{dr}^{e}) \tag{AI.72}$$

$$\psi_{dr}^{e} = L_{lr} i_{dr}^{e} + L_m(i_{ds}^{e} + i_{dr}^{e}) \tag{AI.73}$$

$$\psi_{dm}^{e} = L_m(i_{ds}^{e} + i_{dr}^{e}) \tag{AI.74}$$

Combining equations from (AI.65)-(AI.74) the electrical transient model can be expressed in a matrix form as shown in (AI.75).

$$\begin{bmatrix} v_{qs}^{e} \\ v_{ds}^{e} \\ v_{qr}^{e} \\ v_{dr}^{e} \end{bmatrix} = \begin{bmatrix} R_s + sL_s & \omega_e L_s & sL_m & \omega_e L_m \\ -\omega_e L_s & R_s + sL_s & -\omega_e L_m & sL_m \\ sL_m & (\omega_e - \omega_r)L_s & R_r + sL_r & (\omega_e - \omega_r)L_r \\ -(\omega_e - \omega_r)L_m & sL_m & -(\omega_e - \omega_r)L_r & R_r + sL_r \end{bmatrix} \begin{bmatrix} i_{qs}^{e} \\ i_{ds}^{e} \\ i_{qr}^{e} \\ i_{dr}^{e} \end{bmatrix} \tag{AI.75}$$

If the speed of the rotor ω_r is considered constant, like when the machine is connected to a dynamometer, given the input voltage and frequency, the currents in (AI.75) can be solved. If the rotor speed is not constant then the mechanical coupling equation in (AI.76) can be solved to determine the rotor speed.

$$T_e = T_L + \frac{2}{P} J \frac{d}{dt}\omega_r \tag{AI.76}$$

The electromagnetic torque is given by (AI.77)-(AI.80), all the equations being similar.

$$T_e = \frac{3}{2}\frac{P}{2}(\psi_{dm}^e i_{qs}^e - \psi_{qm}^e i_{ds}^e) \quad \text{(AI.77)}$$

$$T_e = \frac{3}{2}\frac{P}{2}(\psi_{ds}^e i_{qs}^e - \psi_{qs}^e i_{ds}^e) \quad \text{(AI.78)}$$

$$T_e = \frac{3}{2}\frac{P}{2}(\psi_{dr}^e i_{qr}^e - \psi_{qr}^e i_{dr}^e) \quad \text{(AI.79)}$$

$$T_e = \frac{3}{2}\frac{P}{2}L_m(i_{qs}^e i_{dr}^e - i_{ds}^e i_{qr}^e) \quad \text{(AI.80)}$$

The dynamic equations can be extended to multi-phase induction machines to determine the dynamic performance of these machines. In Chapter 7, the dynamic model discussed here is extended to pole changing 3-phase and 6-phase induction machines. Field oriented control is also discussed concerning these machines.

AI.5 48V Induction Machine Design

The steps discussed in the flow chart of Fig. AI.1 are applied to design an induction machine for the specifications of TABLE AI.1.

TABLE AI.4 CONSTANTS AND CONSTRAINTS OF INDUCTION MACHINE DESIGN

Parameters	***Value***
B_{ts}, B_{tr}	1.6T
B_{ys}, B_{yr}	1.2T
J_s	20 A/mm^2
J_r	20 A/mm^2
D_{sh}	25mm
$w_{ts_{min}}, w_{tr_{min}}$	1.5mm
g	0.3mm
K_{fill}	0.64

K_{stack}	0.97
D_{sh}	25mm

1. The outer diameter is fixed at $D_{ext} = 144\ mm$. With 8-poles, a starting split ratio of 0.67 is chosen resulting in a stator bore diameter of $D_{is} = 96.5\ mm$. For the number of poles and stator bore diameter, the stack length to bore diameter ratio (λ) of 0.68 is chosen from TABLE AI.2 resulting in a stack length of 66mm.
2. The rotor bars are cast from aluminium and the stator iron material is M-19 steel. The following constants are chosen for the designs based on TABLE AI.2.
3. The stator windings are designed to be accommodated in $N_s = 72$ slot with an SPP $q = 3$. A stator winding with a one slot short pitch is designed resulting in a winding factor of 0.9452. The stator slot width to slot pitch ratio of 0.55 is chosen for the stator and rotor laminations.

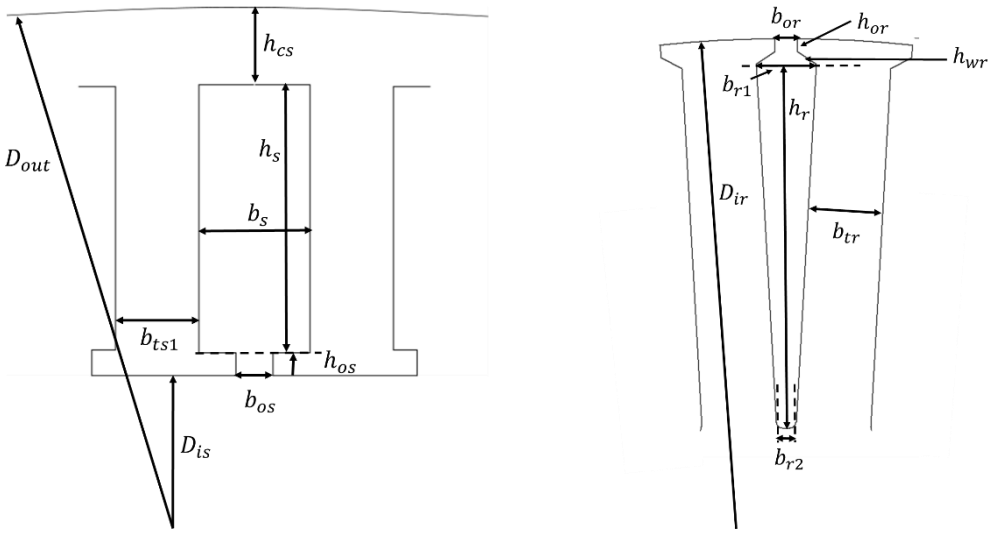

(a) Stator slot

(b) Rotor slot

Fig. AI.10 Slot dimensions of induction motor design.

An initial B_g of 1T is chosen and a saturation factor $K_{st} = 0.65$ is chosen. The flux and series number of turns is determined to be 2.943mWb and 12 turns per phase respectively with 2 conductors per slot. The conductors per slot are rectangular in cross-section and for the given current density, the slot area and the slot dimensions are determined. The value of the saturation factor is iterated until the MMF drops across the stator and rotor are approximately equal and their sum is equal to the MMF of drop across the air gap.

TABLE AI.5 STATOR AND ROTOR DIMENSIONS OF INDUCTION MACHINE DESIGN

Stator Parameters	Value (mm)	Rotor Parameters	Value (mm)
D_{out}	144	D_{ir}	95.85
D_{is}	96.5	b_{or}	0.9
b_{os}	1.0	b_{r1}	2.37
b_s	1.95	b_{r2}	0.85
b_{ts1}	2.36	h_r	13.5
h_s	13.2	a	4
h_{cs}	9.56	b	16.8

TABLE AI.6 INDUCTION MACHINE EQUIVALENT CIRCUIT PARAMETERS

Parameters	Value	Parameters	Value
Stator Resistance	$2.07m\Omega$	Rotor Leakage Reactance	$8.75m\Omega$
Stator Leakage Reactance	$8.43m\Omega$	Magnetising Reactance	$126.3m\Omega$
Referred Rotor Resistance	$1.43m\Omega$	Rated slip	0.173

TABLE AI.7 INDUCTION MACHINE PERFORMANCE CHARACTERISTICS AT CORNER SPEED

Parameters	Value	Parameters	Value
Torque	$60Nm$	Power Factor	0.81
Speed	$1900rpm$	Efficiency	64.5%
Current	$450A$	Total Loss	$6530W$

To accommodate the rectangular conductors, a rectangular stator slot is chosen with dimensions as shown in Fig. AI.10 (a). A parallel tooth slot shape is chosen for the 56 rotor slots and the dimensions are marked in Fig. AI.10 (b). The numerical values of the slots are shown in

TABLE AI.5. The slot opening height and the wedge height of both the stator and rotor are chosen to be 0.5mm. The dimensions of the stator and rotor being fixed, the equivalent circuit parameters of the machine are determined. These are listed in TABLE AI.6. The performance at the corner speed of the torque-speed curve where the rated inverter current and rated voltage are applied are shown in TABLE AI.7.

AI.6 Lamination Drawing and Material Properties

The radial cross-section of the baseline induction machine is shown in Fig. AI.11. The axial drawing of the induction machine is shown in Fig. AI.12. The rotor and slot sections are shown in Fig. AI.13.

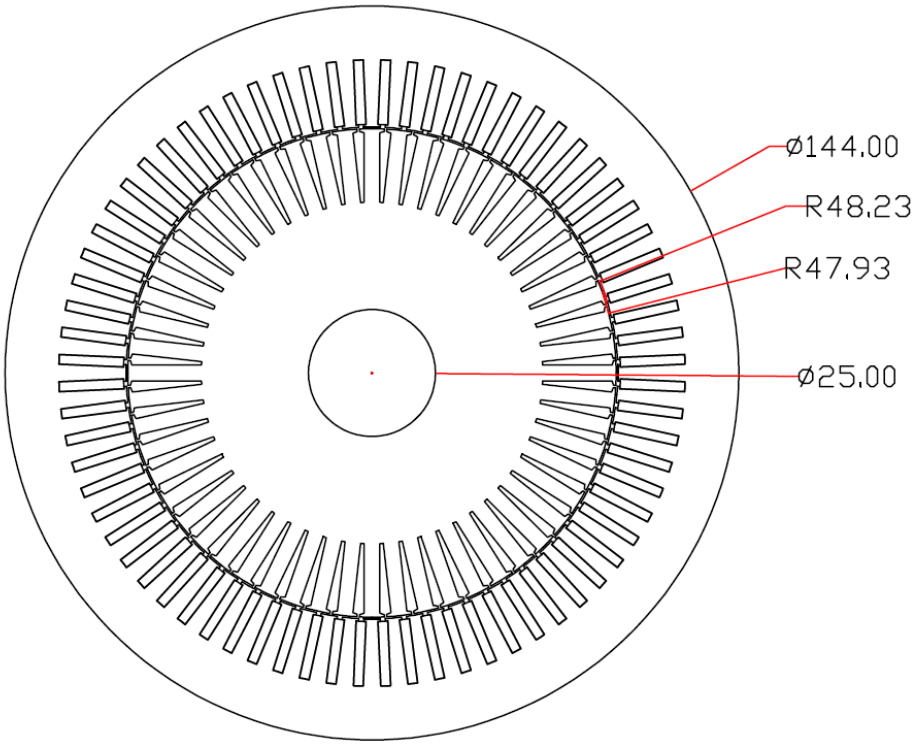

Fig. AI.11 Radial drawing of baseline induction machine lamination.

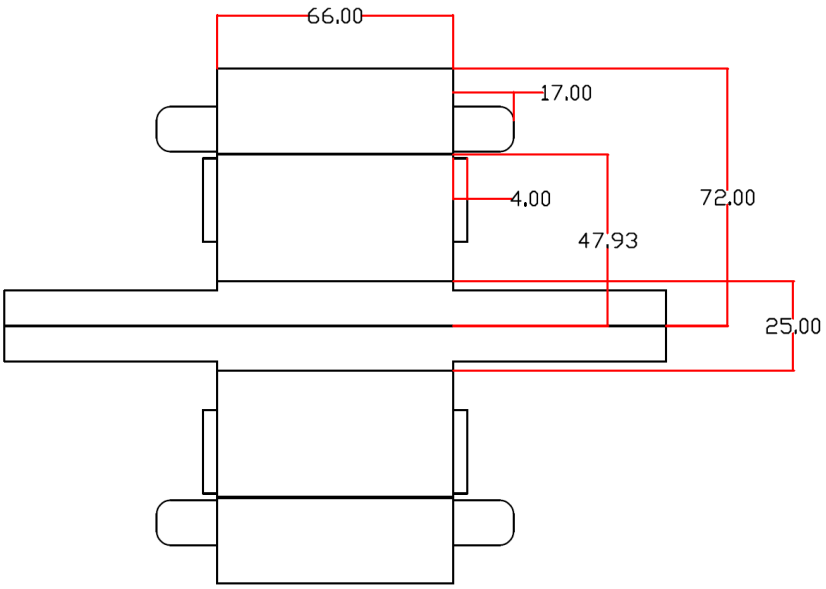

Fig AI.12 Axial drawing of baseline induction machine lamination.

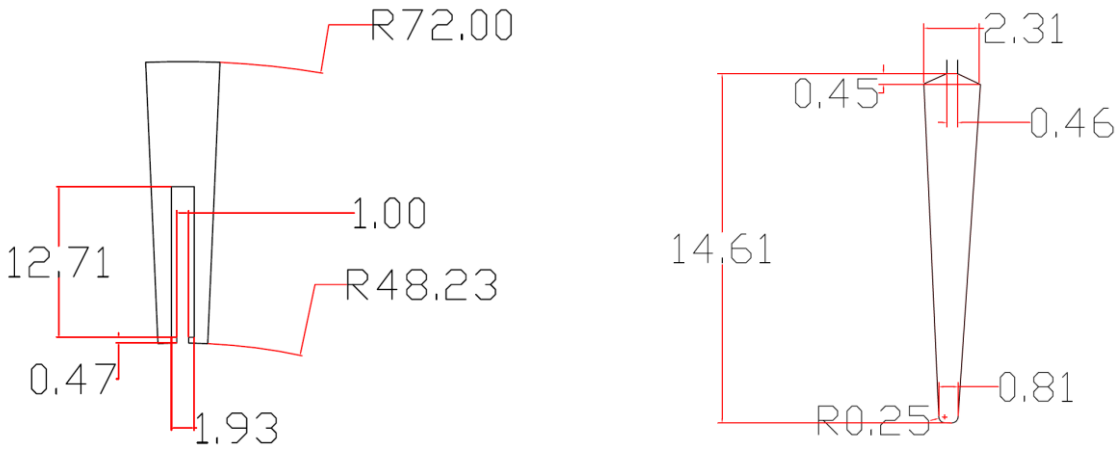

(a) Stator slot dimensions

(b) Rotor slot dimensions

Fig AI.13 Drawing of baseline induction machine stator and rotor slot dimension.

The BH curve of the lamination material, M19 24G, used in the simulation is shown in Fig. AI.14 and the iron loss variation of the steel with frequency and flux density is shown in Fig. AI.15. The same material is used for the prototype machine that is fabricated. The details of the prototype machine are discussed in Appendix II.

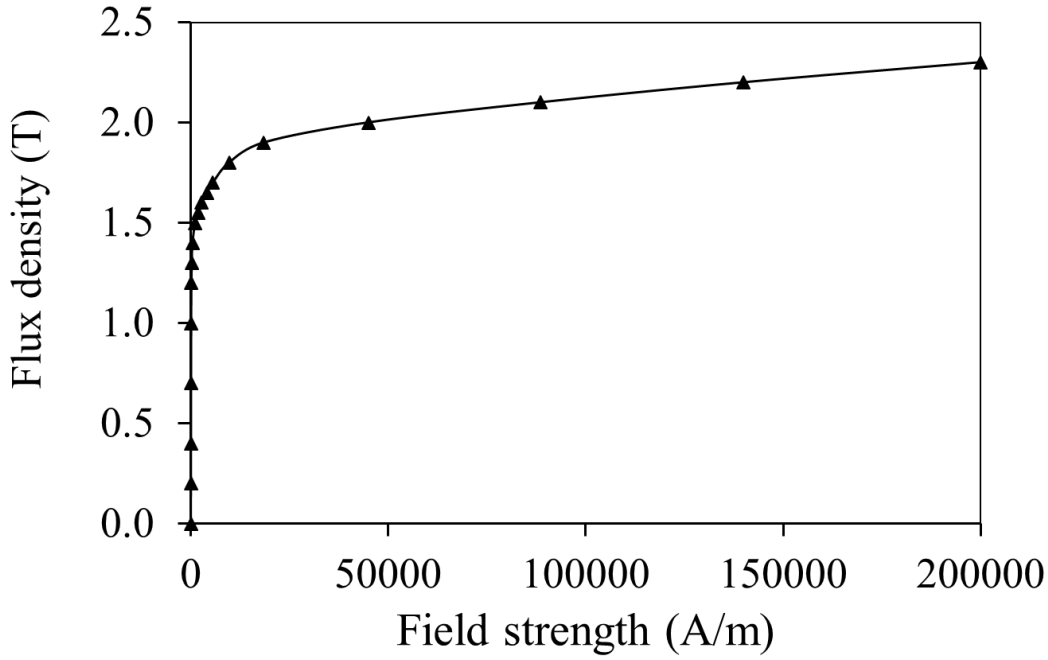

Fig. AI.14 Lamination BH-properties of the baseline induction machine.

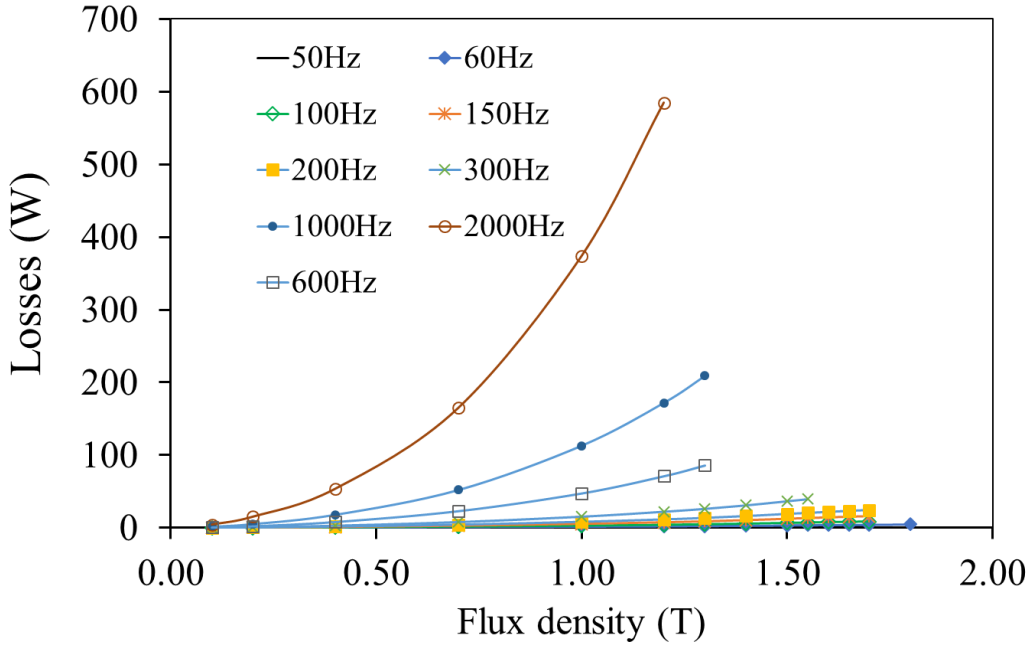

Fig. AI.15 Lamination (M19-24G) loss properties of the baseline induction machine.

AI.7 Conclusions

The design process of induction machines involves a combination of analytical equations and empirical relationships. Being a machine that is usually operating under saturated conditions, the non-linear characteristics of the materials need to be incorporated into the design process for accurate prediction of the performance of the designed machine. These analytical formulation

compiled from various resources in literature have been presented in this chapter. The design methodology is an iterative process that makes it suitable to use for optimisation. This is used in Chapter 3 for determining the optimal number of slots and poles for maximising torque capability while meeting the specifications. A dynamic model that uses the analytically computed parameters to predict transient performance has also been discussed. This model is extended in Chapter 7 to multiphase and pole changing winding induction machines.

Appendix II

Design and Fabrication of Prototype Induction Machine

AII. 1 Introduction

The process of fabrication of the prototype machine and the winding arrangement is described in this appendix. Following this, the dynamometer test setup to characterize the performance of the machine is described and the inverter layout to control the machine is discussed.

AII.2 Prototype Machine Fabrication & Winding Layout

The induction machine prototype is made of wire cut laminations that are stacked together into which the windings are inserted. The lamination material is M19 26Ga and the laminations are tig-welded together in a hydraulic press as shown in Fig. AII.1(a). The lamination stack is shrunk fit into a NEMA 90 size frame with air-cooled fins. The machine is wound with the individual coil terminals brought out to the terminal box. The advantage of this method is the ability to externally configure the machine for any number of phases and phase belts. The individual coils corresponding to each of the phases under each pole-pair are wound on a former externally and inserted into slots that are lined with mylar insulation. The non-terminal section of 8 such coils is shown in Fig. AII.1(b).The end winding sections are tied and held in place together and wrapped with mylar insulation before vacuum impregnation as shown in Fig. AII.1(b) and Fig. AII.1(c). The rotor from a NEMA 90 frame is used to test the performance of the prototype machine as shown in Fig. AII.1(d).

(a) Wire cut lamination stack

(b) Inserted coils

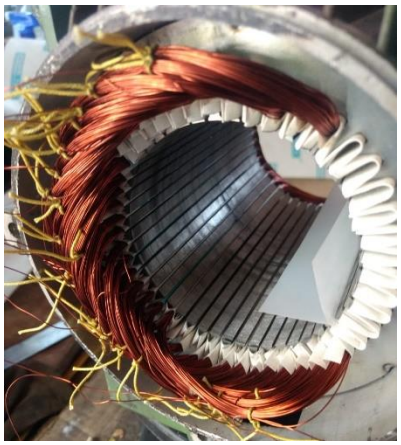

(c) Tied end of individual coils

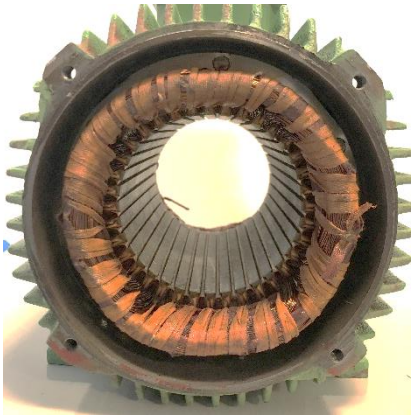

(d)

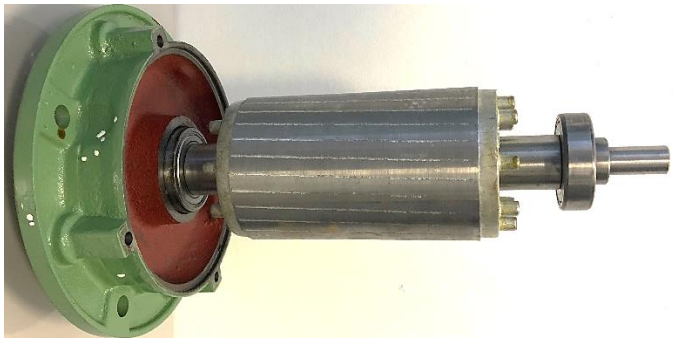

(e)

Fig AII.1 Lamination, coil insertion and rotor of the prototype machine.

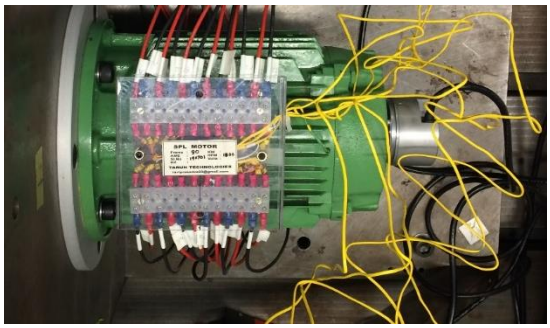

(a) Terminal box on the machine frame

(b) Configurable terminal box

Fig. AII. 2 Terminal box of the induction machine showing individual phase coil terminals

Poles	N												S											
Slot N^o	**1**	**2**	**3**	**4**	**5**	**6**	**7**	**8**	**9**	**10**	**11**	**12**	**13**	**14**	**15**	**16**	**17**	**18**	**19**	**20**	**21**	**22**	**23**	**24**
Layer 1	**A1**	**A1**	**A1**	**A1**	**A1**	**A1**	**A1**	**A1**	c1	c1	c1	c1	c1	c1	c1	c1	B1	B1	B1	B1	B1	B1	B1	B1
Layer 2	c2	c2	c2	c2	B2	B2	B2	B2	B2	B2	B2	B2	**a1**	**a1**	**a1**	**a1**	**a1**	**a1**	**a1**	**a1**	C1	C1	C1	C1

Poles	S												N											
Slot N^o	**25**	**26**	**27**	**28**	**29**	**30**	**31**	**32**	**33**	**34**	**35**	**36**	**37**	**38**	**39**	**40**	**41**	**42**	**43**	**44**	**45**	**46**	**47**	**48**
Layer 1	**a2**	**a2**	**a2**	**a2**	**a2**	**a2**	**a2**	**a2**	C2	C2	C2	C2	C2	C2	C2	C2	b2	b2	b2	b2	b2	b2	b2	b2
Layer 2	C1	C1	C1	C1	b1	b1	b1	b1	b1	b1	b1	b1	**A2**	**A2**	**A2**	**A2**	**A2**	**A2**	**A2**	**A2**	c2	c2	c2	c2

Fig. AII.3 Winding layout showing the coils for the six-phase windings brought out to the terminal box.

The dimensions of the stator and rotor lamination are shown in Fig. AII.4 and Fig. AII.5 respectively.

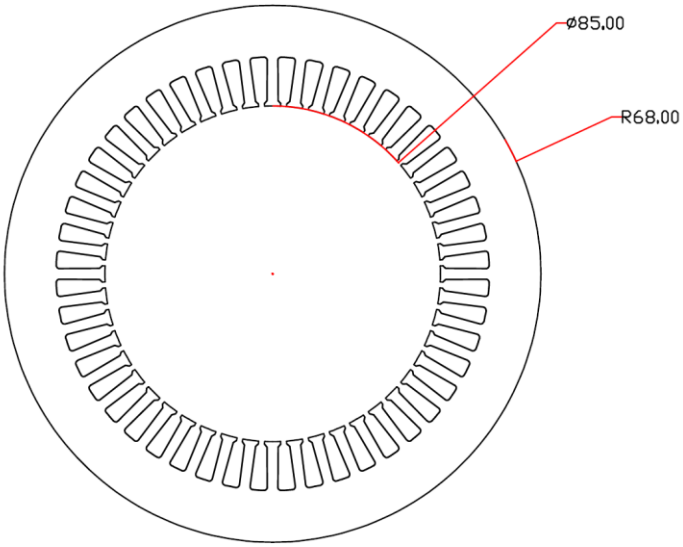

Fig. AII.4 Stator lamination dimensions of the prototype machine.

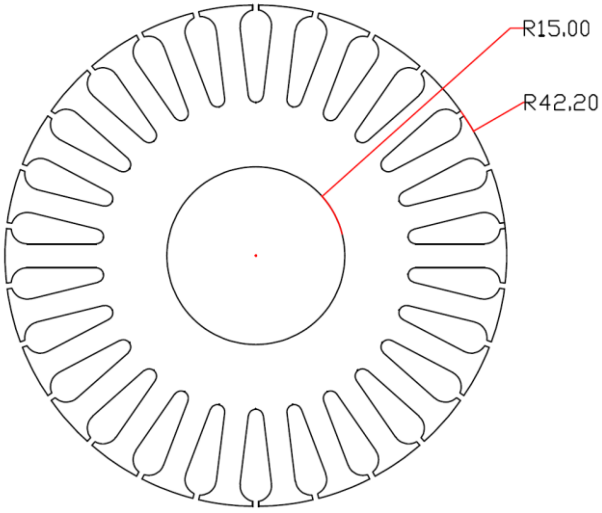

Fig. AII.5 Rotor lamination dimensions of the prototype machine.

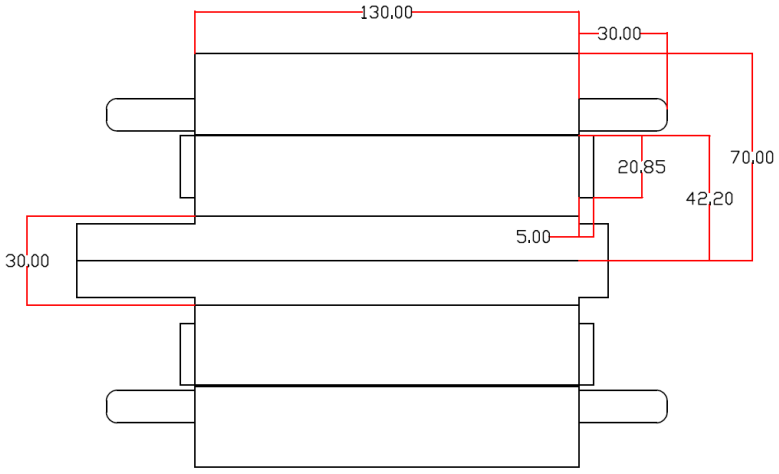

Fig. AII.6 Axial dimensions of the prototype machine.

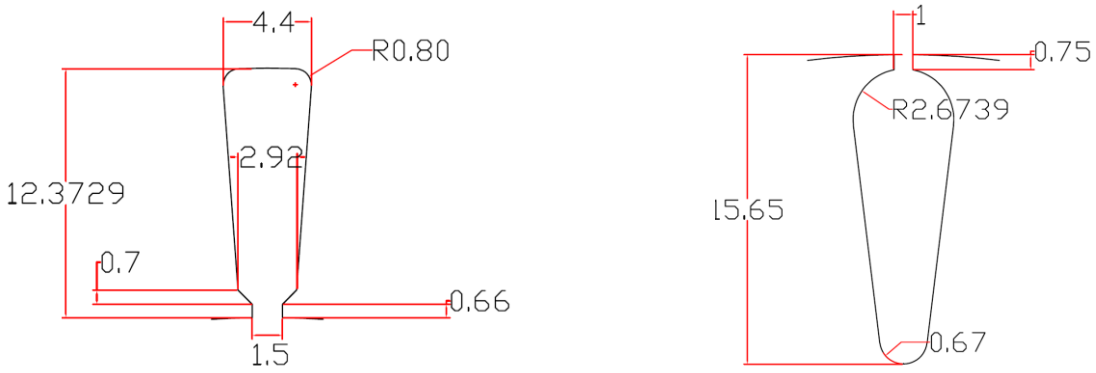

(a) Stator slot dimensions.

(b) Rotor slot dimensions.

Fig. AII.7 Stator and rotor slot section dimensioning.

Each coil that is inserted is tied to hold the bundle of wires together as shown in Fig. AII.1(c) to allow for the end windings to be held in place. The terminal box showing individual terminals of the machine coils being brought out is shown in Fig. AII.2(a) and Fig. AII.2(b). The coils are divided into the six phases and the two terminals of each of the windings of the phases A1, A2, B1, B2, C1, C2, X1, X2, Y1, Y2, Z1 and Z2 as shown in Fig. AII.3 are individually brought out to the terminal box. The rotor is a standard off the shelf rotor from a NEMA 90 frame induction machine. The axial section of the lamination is shown in Fig. AII.6. The stator and rotor slot sections are shown in Fig. AII.7.

AII.3 Dynamometer Test Setup

The prototype induction machine is loaded using an AVL dynamometer. The dynamometer is a 4-quadrant drive with the ability to regenerate and supply power back to the grid as well as provide motoring torque to run the machine under test as a generator provided the DC bus supplying the inverter that is driving the test machine has the ability to push power back into the grid. The dynamometer consists of the prototype machine under test mounted with an encoder at the non-load end of the machine. The machine is mounted on a frame and coupled with flex couplings to a Magtrol torque transducer. The torque transducer is coupled to the dynamometer load machine mounted on a frame and in line with the prototype machine. The entire assembly is mounted on a frame resting on vibration resistant pads.

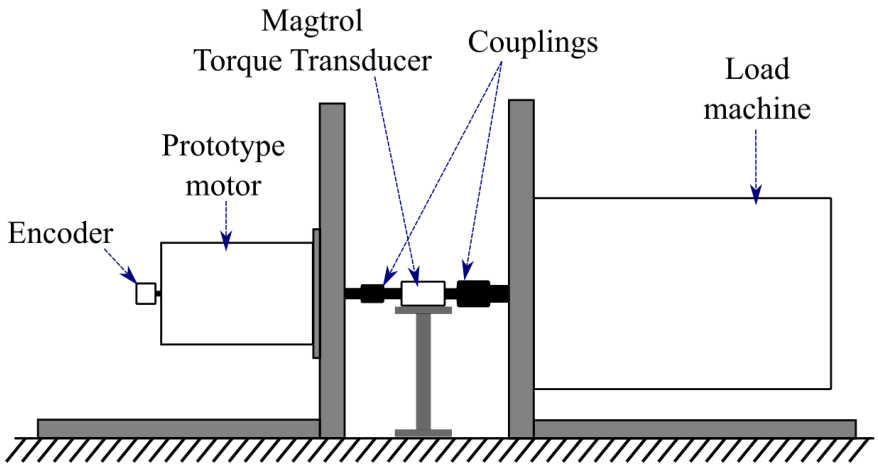

Fig. AII.8 AVL dynamometer setup.

The machine is a six-phase machine and two three-phase inverters are used to control the machine. With two three-phase inverters, online pole changing operation of the three-phase machine is possible and steady-state operation of the six-phase machine with 4-pole and 2-pole operation is possible.

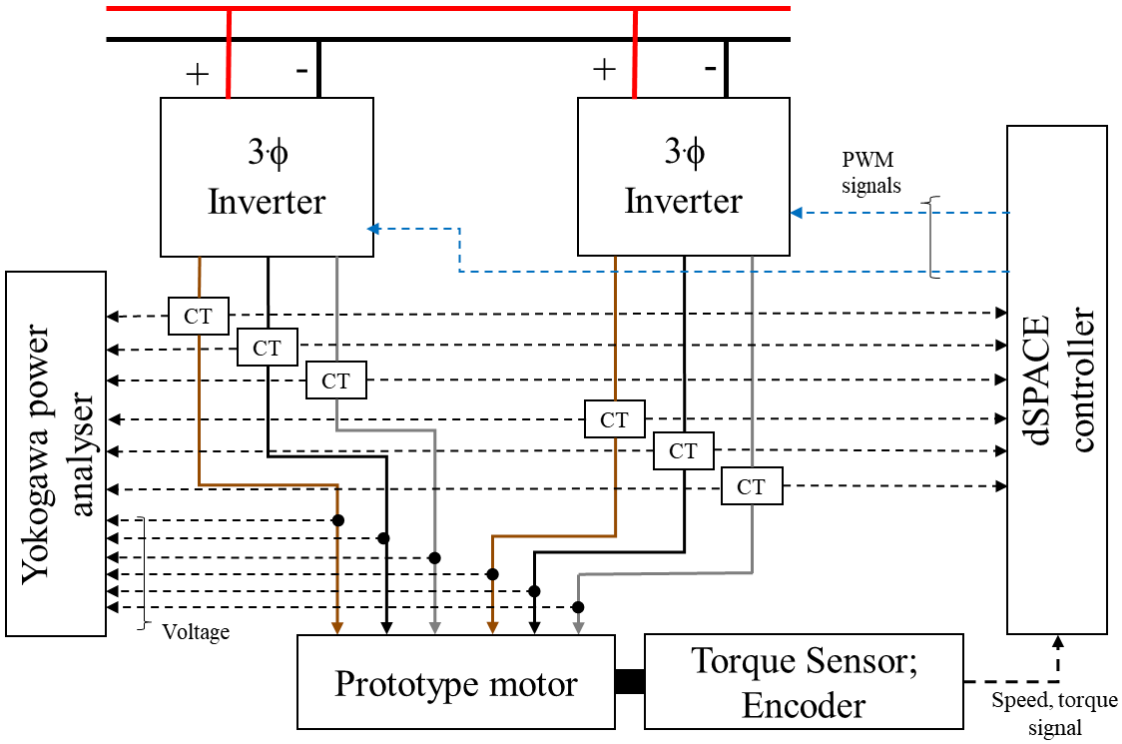

Fig. AII.9 Control line diagram of the inverter for testing the prototype machine.

TABLE AII.1 PROTOTYPE TEST EQUIPMENT MODEL AND MAKE

Equipment	Make and Model Number
Power analyser	Yokogawa WT3000 [YOK20]
Three-phase inverter	Infineon, Evaluation Hybrid Kit for HyperPak-1. 600V/400A IGBT & Diode chipset [INF20]
Motor controller	dSPACE 1006 [DSP20]
Current sensor	LEM LA25-NP 8, 12, 25 ARMS nominal. Multi-range, Fixed gain and offset [LEM20]
Torque transducer	Magtrol TM308 [MAG20]
Dynamometer	AVL, 250kW dynamometer [AVL20]
DC bus power supply	Regatron, ACS.350.528.504 [REG20]
Encoder	Hengstler ICURO RI64 [HEN20]

As explained in chapter 3 and chapter 4. For on-line pole changing of the six-phase machine, four three-phase inverters with 12 inverter legs are required. The control system for testing the machine consists of two Infineon HybridPack-1three-phase inverters fed from a common DC bus. The DC power supply is fed from a 4-quadrant Regatron DC power supply. The two three-phase inverters are connected to the prototype induction machine through six LEM current sensors. The current sensor's output is connected to the Yokogawa power analyser as well as the dSPACE controller. Voltage measurements on the phases of the inverter are also connected to the Yokogawa power analyser for power measurement. The dSPACE controller runs the control algorithms to drive the induction machine and provides the necessary PWM signals to drive the two three-phase inverters. The details of the various equipment used in the system are listed in TABLE AII.1.

References

[ABD11] A. S. Abdel-Khalik, S. Mostafa Gadoue, M. I. Masoud, and B. W. Wiliams, "Optimum flux distribution with harmonic injection for a multiphase induction machine using genetic algorithms," *IEEE Trans. on Energy Conversion*, vol. 26 no. 2, pp.501-512, June 2011.

[ABD12] A. S. Abdel-Khalik, S. Ahmed, "Performance evaluation of a five- phase modular winding induction machine," *IEEE Trans. on Industrial Electronics*, Vol. 59, No. 6, pp. 2654 – 2669, June 2012.

[ABD19] B. S. Abdel-Mageed, S. Mohamed S.A., K. F. Ali and M. A. Morsy, "Coupled Finite Element-Circuit Modelling and Parameter Estimation Of Six-Phase Induction Motor," *Proc. IEEE 21st International Middle East Power Systems Conference (MEPCON)*, Cairo, Egypt, pp. 645-649, 2019

[ABD12a] A. S. Abdel-Khalik, M. I. Masoud and B. W. Williams, "Improved flux pattern with third harmonic injection for multiphase induction machines," *IEEE Trans. on Power Electronics*, vol. 27, no. 3, pp. 1563-1578, March 2012.

[AKI94] Y. Akiyama and K. Takaku, "A study of the most suitable design of inverter-driven induction motors," *Proc.* PCIM, pp. 38-44, June 1994.

[ALB08] L. Alberti, N. Bianchi, and S. Bolognani, "A very rapid prediction of IM performance combining analytical and finite-element analysis," *IEEE Trans. on Industrial Applications*, vol. 44, no. 5, pp. 1505–1512, 2008.

[ALB12] L. Alberti and N. Bianchi, "Design and tests on a fractional-slot induction machine," *Proc. IEEE Energy Convers. Congress Expo. ECCE 2012*, vol. 2, no. 3, pp. 166–172, 2012.

[ALG51] P.L. Alger, "The nature of polyphase induction machines", Wiley, 2/e, 1951

[AOU14] S. Aouaouda and M. Boukhnifer, "Observer-based fault tolerant controller design for Induction Motor drive in EV," *Proc. IEEE International Conference on Control Application*, pp. 1190–1195, 2014.

[ARN15] P. Arnoux, P. Caillard, and F. Gillon, "Modelling finite-element constraint to run an electrical machine design optimization using machine learning," *IEEE Trans. Magnetics.*, vol. 51, no. 3, 2015.

[AVL20] AVL.com, "AVLe-drive testing dynamometers", 2020. Available: https://www.avl.com/dynamometers1

[BAC15] J. P. Bacher, A. Mütze, "Comparison of an induction machine with both conventionally distributed and fractional-slot concentrated stator windings," E*&I, Elektrotechnik und Informationstechnik*, vol. 132, no. 1, pp. 39-45, Feb. 2015.

[BAN03] D. Ban, D. Zarko, I. Mandic, "Turbogenerator end winding leakage inductance calculation using a 3-D analytical approach based on the solution of Neumann integrals," *Proc. IEEE International Electric Machines and Drives Conference*, Capos 2003., vol. 3, 1-4, pp. 1576-1582, June 2003.

[BES09] J. Le Besnerais, V. Lanfranchi, M. Hecquet, R. Romary, and P. Brochet, "Optimal slot opening width for magnetic noise reduction in induction motors," *IEEE Trans. Energy Conversion*, vol. 24, no. 4, pp. 869–874, 2009.

[BES09a] J. Le Besnerais, V. Lanfranchi, M. Hecquet, and P. Brochet, "Optimal slot numbers for magnetic noise reduction in variable-speed induction motors," *IEEE Trans. on Magnetics*, vol. 45, no. 8, pp. 3131–3136, Aug. 2009.

[BGE10] B. Ge, D. Sun, W. Wu, Y. Liu and D. Bi, "Uniform modeling for pole-phase modulation induction motors," *Proc. IEEE International Conference. Electrical Machines and Systems*, pp. 1401-1406, Oct.-1013.

[BGE13] B. Ge, D. Sun, W. Wu and F. Z. Peng, "Winding Design, Modeling, and control for pole-phase modulation induction motors," *IEEE Trans. on Magnetics*, vol. 49, no. 2, pp. 898-911, Feb. 2013.

[BIA12] L. Alberti and N. Bianchi, "Design and tests on a fractional-slot induction machine," *Proc. IEEE Energy Conversion Congress and Exposition (ECCE)*, Raleigh, NC, pp.166, 172, 15-20 Sept. 2012.

[BIA97] N. Bianchi and S. Bolognani, "Design procedure of a vector controlled induction motor for flux-weakening operations" *Proc. IEEE Industry Applications Society Annual. Meeting*, New Orleans, pp. 104–111, Oct. 1997.

[BIA97a] N. Bianchi and S. Bolognani, "Parameters and volt-ampere ratings of a field-oriented induction motor drive for flux-weakening applications," *Proc. IEEE Int. Conf. on Elect. Machines and Drives, (ICEM'97),* pp. 46-50, Cambridge UK, 1997.

[BIA98] N. Bianchi and S. Bolognani, "Unified approach to the analysis and design of an AC motor drive for flux-weakening operations," *Proc. IEEE Industrial Applications Conf. 33rd IAS Annual Meeting*, vol. 1, no. 4, pp. 95–102, 1998.

[BIS01] D. Bispo, L. Martins, Neto, J. T. de Resende and D. A. de Andrade, "A new strategy for induction machine modeling taking into account the magnetic saturation," *IEEE Trans. on Industry Applications*, vol. 37, no. 6, pp. 1710-1719, Nov.-Dec. 2001.

[BOG11a] A. Cavagnino, and M. Lazzari, "Computational algorithms for induction-motor equivalent circuit parameter determination-Part I: Resistances and leakage reactances," *IEEE Trans. on Industrial Electronics.*, vol. 58, no. 9, pp. 3723–3733, 2011.

[BOG11b] A. Boglietti, A. Cavagnino, and M. Lazzari, "Computational algorithms for induction motor equivalent circuit parameter determination-Part II: Skin effect and magnetizing characteristics," *IEEE Trans. on Industrial Electronics.*, vol. 58, no. 9, pp. 3734–3740, 2011.

[BOJ14a] R. Bojoi, A. Cavagnino, M. Cossale, A. Tenconi, and S. Vaschetto, "Design trade-off and experimental validation of multiphase starter generators for 48V mini-hybrid power train," *Proc. IEEE International Electric Vehicle Conference, Florence*, pp. 1–7, Dec. 2014.

[BOJ16] R. Bojoi, A. Cavagnino, M. Cossale, and A.Tenconi, "Multiphase starter generator for a 48V mini-hybrid powertrain: Design and testing," *IEEE Trans. on Industrial Applications*, vol. 52, no. 2, pp. 1750–1758, Mar.–Apr. 2016.

[BOJ16a] R. Bojoi, M. Cossale, A. Tenconi, and S. Vaschetto, "Prototyping experiences on 48V starter-alternators," *Proc. IEEE Internal Conference on Electrical Machines*, pp. 2009– 2014, Sept. 2016.

[BOL02] I. Boldea, S. A. Nasar, "The induction machine handbook," Boca Raton, FL, USA: CRC Press, 2002.

[BOS01] B. K. Bose, "Modern power electronics and ac drives," Englewood Cliffs, NJ: Prentice-Hall, 2001.

[BUY11] V. T. Buyukdegirmenci and P. T. Krein, "Control for high instantaneous torque from induction machines: Methods and limits," *Proc. IEEE International Conference on Electrical Machines and Drives*, Ontario, Canada, pp. 777–782, 2011.

[CAI04] W. Cai, "Comparison and review of electric machines for integrated starter alternator applications," *Proc. IEEE 39th Industry Applications Conference, IAS Annual Meeting.*, Seattle, WA, USA, 2004.

[CAI06] W. Cai, "Starting engines and powering electric loads with one machine," *Proc. IEEE Industry Applications Magazine*, vol. 12, no. 6, pp. 29-38, Nov.-Dec. 2006.

[CAI13] P. Caillard, F. Gillon, M. Hecquet and N. Janiaud, "Influence of machine control strategy on electric vehicle range," *Proc. IEEE 8th International Conference and Exhibition on Ecological Vehicles and Renewable Energies (EVER)*, Monte Carlo, 2013, pp. 1-6, 2013.

[CAR18] M. Carbonieri, N. Bianchi, and L. Alberti, "A fast and direct analysis of three-phase induction motors using finite element," *Proc. IEEE 8th International Conference on Electrical Machines (ICEM)*, Sep. 2018.

[CAR19] M. Carbonieri, N. Bianchi and L. Alberti, "Induction motor mapping using rotor field-oriented analysis technique," *Proc. IEEE Energy Conversion Congress and Exposition (ECCE)*, Baltimore, MD, USA, pp. 2321-2328, 2019.

[CAV14] A. Cavagnino, A. Tenconi, and S. Vaschetto, "Experimental characterization of a belt driven multi-phase induction machine for 48 V automotive applications: Losses and temperatures assessments," *Proc. IEEE Internal Conference on Electrical Machines*, pp.1165–1171, Sept. 2014.

[CAV16] A. Cavagnino, M. Cossale, A. Tenconi, and S. Vaschetto, "Prototyping experiences on 48V starter-alternators," *Proc. IEEE International Conference on Electrical Machines*, pp. 2009–2014, 2016.

[CAV16a] A. Cavagnino, A. Tenconi, and S. Vaschetto, "Experimental characterization of a belt driven multiphase induction machine for 48V automotive applications: Losses and temperatures assessments," *IEEE Trans. on Industrial Applications*, vol. 52, no. 2, pp. 1321–1330, Mar.–Apr. 2016.

[CHE01] S. Chen, B. Lequesne, R. R. Henry, Y. Xue, and J. J. Ronning, “Design and testing of a belt-driven induction starter-generator,” *Proc. IEEE International Electrical Machines and Drives Conf.(IEMDC)* , pp. 252–260, 2001.

[CHE02] S. Chen, B. Lequesne, R.R. Henry, Y. Xue, and J.J. Ronning, “Design and testing of a belt-driven induction starter-generator,” *IEEE Trans. On Indus. Appl.*, vol. 38, no. 6, pp. 1525–1533, Nov-Dec. 2002.

[CHI08] O. Chiver, E. Micu and C. Barz, "Stator winding leakage inductances determination using finite elements method," *Proc. IEEE 11th International Conference on Optimization of Electrical and Electronic Equipment*, Brasov, pp. 69-74, 2008.

[CHO01] D. Cho, H. Jung, and C. Lee, “Induction motor design for electric vehicle using a niching genetic algorithm,” *IEEE Trans. Indus. Appl.*, vol. 37, no. 4, pp. 994–999, Jul.-Aug. 2001.

[CPT16] R. Kelly, J. Spearman and H. Andreas, “Electric generator and/or motor for electric vehicle,” GB2536063A, Valeo Air Management UK Ltd, UK Patent 2016.

[DAH03] R. Dahlander and K. Lindstroem, “Device for varying the number of poles in alternate-current motors,” General Electric, US725415A, US Patent, 1903.

[DAJ11] G. Dajaku and D. Gerling, “A Novel 24-slots/10-poles winding topology for electric machines,” *Proc. IEEE International Electric Machines & Drives Conference*, Niagara Falls, ON, pp. 65-70, 2001.

[DAJ13] G. Dajaku and D. Gerling, “A novel tooth concentrated winding with low space harmonic contents,” *Proc. IEEE Intl. Electrical Machines and Drives Conf. (IEMDC)*, pp. 755–760, 2013.

[DAJ13a] G. Dajaku, “Electric Motor,” US8536754B2, 2013.

[DAJ14] G. Dajaku and D. Gerling, “Low costs and high efficiency asynchronous machine with stator cage winding,” *Proc. IEEE International Electrical Vehicle Conference*, Florence, pp. 1-6, 2014.

[DAJ14a] G. Dajaku, “Electric machine,” US20170047804A1, Volabo Gmbh, 2014.

[DAJ15] G. Dajaku, F. Bachheibl, A. Patzak, and D. Gerling, “Intelligent stator cage winding for automotive traction electric machines,” *Proc. IEEE 28th International Electric Vehicle Symposium*, Kintex, pp. 1-8, 2015.

[DAJ16] G. Dajaku, S. Spas, X. Dajaku and D. Gerling, “An improved fractional slot concentrated winding for low-poles induction machines,” *Proc. IEEE 22nd International Conference on Electrical Machines (ICEM)*, Lausanne, pp. 114-119, 2016.

[DAJ17] G. Dajaku, F. Bachheibl and D. Gerling, “Power supply unit and electric machine,” US9800194B2, Volabo Gmbh, 2017.

[DOR10] D. G. Dorrell, M. Popescu, L. Evans, D. A. Staton and A. M. Knight, “Comparison of permanent magnet drive motor with a cage induction motor

design for a hybrid electric vehicle," *Proc. IEEE International Power Electronics Conference,* Sapporo, pp. 1807-1813, 2010.

[DOR12] D. G. Dorrell, A. M. Knight, L. Evans, and M. Popescu, "Analysis and design techniques applied to hybrid vehicle drive machines-assessment of alternative IPM and induction motor topologies," *IEEE Trans. Industrial Electronics.*, vol. 59, no. 10, pp. 3690–3699, Oct. 2012.

[DOR15] D. G. Dorrell and Á. F. F. Filho, "Design of torque-dense induction motors for automotive drive applications," *Proc. IEEE 24th International Symposium on Industrial Electronics (ISIE)*, Buzios, pp. 1446-1451, Sept. 2015.

[DSP20] Dspace.com, "DS1006, Processor board, Computing power for complex real-time models", 2020.

Available: www.dspace.com/en/ltd/home/products/hw/phs_hardware/processor_boards/ds1006.cfm#143_23545

[EAS08] F. Eastham, T. Cox, P. Leonard, and J. Proverbs, "Linear induction motors with modular winding primaries and wound rotor secondaries," *IEEE Trans. Magnetics*, vol. 44, no. 11, pp. 4033–4036, Nov. 2008.

[EMA08] A. Emadi, Y. J. Lee, and K. Rajashekara, "Power electronics and motor drives in electric , hybrid electric , and plug-in hybrid electric vehicles," *IEEE Trans. Industrial Electronics*, vol. 55, no. 6, pp. 2237-2245, June 2008.

[EMA14] A. Emadi, "The 'Electrification Factor' in transportation," *IEEE Transportation Electrification. Newsletter*, Jan. 2014 [Online].

Available: http://electricvehicle. ieee.org/previous-newsletters/january-2014/. Retrieved on: Nov. 2014.

[FAI02] Faiz, J. and I. Tabatbaei, "Extension of winding function theory for non-uniform air gap in electric machinery," *IEEE Trans. on Magnetics*, vol. 38, no. 6, 2002.

[FEN19] J. Feng, L. Huang, Z. Q. Zhu, S. Guo and J. Shi, "Torque density enhancement of 6/4 variable flux reluctance machine with second-harmonic current injection," *IEEE Trans. on Energy Conversion*, vol. 34, no. 2, pp. 1135-1145, June 2019.

[FIR07] V. Fireteanu, T. Tudorache, and O. A. Turcanu, "Optimal design of rotor slot geometry of squirrel-cage type induction motors," *Proc. IEEE Int. Electric Machines & Drives Conf. (IEMDC'07),* Antala, pp. 537-542, 2007.

[GAI19] Y. Gai, M. Kimiabeigi, Y.C. Chong, J. D. Widmer, X. Deng, M. Popescu, J. Goss, D. Staton, and A. Steven, "Cooling of automotive traction motors: Schemes, examples, and computation methods," *IEEE Trans. Industrial Electronics.*, vol. 66, no. 3, pp. 1681–1692, 2019.

[GAN10] B. Ganji, A. Z. Kouzani and H. M. Trinh, "Drive cycle analysis of the performance of hybrid electric vehicles," *Lecture Notes*, Computer Science, pp. 434-444, Springer, Berlin, Heidelberg, 2010.

[GER15] D. Gerling, G. Dajaku, F. Bachheibl and A. Patzak, "Analytical calculation of the novel Stator Cage Machine," *Proc. IEEE 18th International Conference on*

Electrical Machines and Systems (ICEMS), Pattaya, Thailand, pp. 1346-1352, 2015.

[GIE07] Michael van der Giet, Kay Hameyer and Stephan Risse, "Induction motor with pole-changing winding for variable supply frequency," *Proc. IEEE Electric Machines & Drives Conference*, Antalya, Turkey, vol. 2, pp. 1484-1489, 2007.

[GOS13] J. Goss, M. Popescu and D. Staton, "A comparison of an interior permanent magnet and copper rotor induction motor in a hybrid electric vehicle application," *Proc. IEEE International Electric Machines & Drives Conference*, Chicago, IL, pp. 220-225, 2013.

[GRA17] P. Y. Grachev, E. V. Strizhakova and A. S. Tabachinskiy, "Starter-Generator design and analysis of start/stop processes for HEVs,"*Proc. IEEE International Conference on Industrial Engineering, Applications and Manufacturing (ICIEAM)*, St. Petersburg, pp. 1-4, 2017.

[GUA14a] Y. Guan, Z.Q. Zhu, J.C. Mipo, and I. Afinowi, "Calculation of torque-speed characteristic of induction machine for electrical vehicle application using analytical method," *Proc. IEEE 7th Intl. Electrical Machines and Drives Conf.*, Berlin, pp. 2715–2721, 2014.

[GUA14b] Y. Guan, Z. Q. Zhu, I. A. A. Afinowi, J. C. Mipo and P. Farah, "Comparison between induction machine and interior permanent magnet machine for electric vehicle application," *Proc. IEEE 17th Intl. Conf. on Electrical Machines and Systems (ICEMS)*, Hangzhou, pp. 144-150, 2014.

[GUA15] Y. Guan, Z.Q. Zhu, J.C. Mipo, and I. Afinowi, "Influence of machine design parameters on flux-weakening performance of induction machine for electrical vehicle application," *IET Electrical Systems in. Transportation*, vol. 5, no. 1, pp. 43–52, 2015.

[GUN14] T. Gundogdu, G. Komurgoz, B. Mantar, "Implementation of fractional slot concentrated windings to Induction Machines," *Proc. IEEE* 7th *International Conference on Power Electronics, Machines and Drives*, Manchester, UK, pp. 1-6, 08-10 April 2014.

[GUN16a] T. Gundogdu, Z. Q. Zhu, J. C. Mipo and P. Farah, "Influence of air-gap length on rotor bar current waveform of squirrel-cage induction motor," *Proc. IEEE* 19*th Intl. Conf. on Electrical Machines and Systems (ICEMS)*, China, pp. 1-6., 2016.

[GUN16b] T. Gundogdu, Z. Q. Zhu, J. C. Mipo and P. Farah, "Influence of magnetic saturation on rotor bar current waveform and performance in induction machines," *Proc. IEEE 23rd International Conference on Electrical Machines (ICEM)*, Lausanne, pp. 391-397, 2016.

[GUN16c] M. T. Güneşer, A. Dalcali, T. Öztürk, C. Ocak and M. Cernat, "An induction motor design for urban use electric vehicle," *Proc. IEEE International Power Electronics and Motion Control Conference (PEMC)*, Varna, pp. 261-266, 2016.

[GYF13] K. N. Gyftakis and J. Kappatou, "The impact of the rotor slot number on the behaviour of the induction motor," Advances in Power Electronics, vol. 2013, pp. 1-9, Jan 2013.

[HAO17a] H. Li and K. W. Klontz, "Rotor design to reduce secondary winding harmonic loss for induction motor in hybrid electric vehicle application," *Proc. IEEE Energy Conversion. Congress. Exposition*, pp. 1–6, 2017.

[HAO17b] H. Li and K. W. Klontz, "An investigation of current harmonic influence on induction motor in hybrid electric vehicle application," *Proc. IEEE International Conference on Electrical Machines and Drives*, Miami, May 2017.

[HAR95] A. Harson, P. H. Mellor, and D. Howe, "Design considerations for induction machines for electric vehicle drives," *Proc. IEE Int. Conf. Electrical Machines and Drives*, pp. 16–20, Sept. 11–13, 1995.

[HEL77] B. Heller, V. Hamata, "Harmonic Field Effects in Induction Machines;" Elsevier Science Ltd.: Amsterdam, The Netherlands, 1977.

[HEN20] Hengstler.de, "ICURO RI64 incremental encoder", 2020.Available: https://www.hengstler.de/en/s_c10030223/Rotary_encoders/Incremental_encoders/ICURO_RI64/

[HER09] J. Herbst, J. Hahne, H. Jordan, H. Liu, A. Gattozzi, and B. Wu, "Challenges in the design of a 100 kW induction motor for a PHEV application," *Proc. IEEE 5th Vehicular Power Propulssion Conference*, pp. 408–413, 2009.

[HIC90] J. Hickiewicz, M. Lukaniszyn, S. Szymaniec, and P. Wach, "On reducing the vibration and noise level of induction motors with integral and fractional slot windings," *Arch. für Elektrotechnik*, vol. 73, no. 3, pp. 163–171, 1990.

[HIR97] I. Hirotsuka, K. Tsuboi, and F. Ishibashi, "Effect of slot-combination on electromagnetic vibration of squirrel-cage induction motor under loaded condition," *Proc. Power Conversion Conf*., Nagaoka, Japan, pp. 843-848, 1997.

[HLI17a] H. Li and K. W. Klontz, "Rotor design to reduce secondary winding harmonic loss for induction motor in hybrid electric vehicle application," *Proc. IEEE Energy Conversion Congress and Exposition, (ECCE)*, pp. 1–6, 2017.

[HLI17b] H. Li and K. W. Klontz, "An investigation of current harmonic influence on induction motor in hybrid electric vehicle application," *Proc. IEEE Intl. Electric Machines & Drives Conf. IEMDC*, Miami, May 2017.

[INF20] Infineon.com, "Evaluation Kit including HybridPACK™ 1 power module, driverboard with coreless transformer isolated driver (1ED020I12- FA) and logic board", 2020, Available: https://www.infineon.com/cms/en/product/evaluation-boards/hybrid-kit1-plus/

[JOK00] M. G. Joksimovic, D. M. Durovic, J. Penman, and N. Arthur, "Dynamic simulation of dynamic eccentricity in induction machines-winding function approach," *IEEE Trans. on Energy Conversion*, vol. 15, no.2, 143–148, 2000.

[JUN15] M. Junaid Akhtar, R. K. Behera, and S. K. Parida, "Optimized rotor slot shape for squirrel cage induction motor in electric propulsion application," *Proc. IEEE, Int. Conference Power Electronics*, vol. 2015–May, no. 1, pp. 3–7, 2015.

[JUR12] S. Jurkovic, J. C. Morgante, K. M. Rahman, and P. J. Savagian, "Electric machine design and selection for general motors e-assist light electrification technology,"

Proc. IEEE Energy Conversion Congress and Exposition (ECCE), Raleigh, NC, pp. 906–913, Sept. 2012.

[JUR15] S. Jurkovic, K. M. Rahman, J. C. Morgante and P. J. Savagian, "Induction machine design and analysis for general motors e-assist electrification technology," *IEEE Trans. Industry Applications*, vol. 51, no. 1, pp. 631-639, Jan.-Feb. 2015.

[KAM13] K. Kamiev, J. Montonen, M. P. Ragavendra, J. Pyronen, J. A. Tapia and M. Niemela, "Design principles of permanent magnet synchronous machine for parallel hybrid or traction application," *IEEE Trans. Industrial Electronics*, vol. 60, no. 11, pp. 4881-4890, 2013.

[KIM20] B. Kim and D. Kang, "A study on the novel design to improve efficiency of wound field synchronous machine," *IEEE Trans. on Magnetics*, doi: 10.1109/TMAG.2020.3013260, 2020.

[KIM93] S. Kim, S. Sul and M. Park, "Maximum torque control of an induction machine in the field weakening region," *Proc. IEEE Industry Appl. Conf. 28th IAS Annual Meeting*, Toronto, Ontario, Canada, vol. 1, pp. 401-407, 1993

[KIM97] S.H. Kim, and S. K. Sul, 'Voltage control strategy for maximum torque operation of an induction machine in the field weakening region', *IEEE Trans. Industrial Electronics*, vol.44, no.4, pp. 512–518, 1997.

[KIM98] M. Kim, C. Lee, and H. Jung, "Multi-objective optimal design of three-phase induction motor using improved evolution strategy," *IEEE Trans. Magnetics*, vol. 34, no. 5, pp. 2980–2983, 1998.

[KIR07] J. L. Kirtley, J. G. Cowie, E. F. Brush, D. T. Peters, and R. Kimmich, "Improving induction motor efficiency with die-cast copper rotor cages," *Proc. IEEE Power Engineering Society General Meeting, PES*, Tampa, FL, pp. 1–6, 2007.

[KON16] W. Kong, R. Qu, J. Huang, and M. Kang, "Air-gap and yoke flux density optimization for multiphase induction motor based on novel harmonic current injection method," *Proc. IEEE 22nd International Conference on Electrical Machines*, vol. 1, no. 1, pp. 100–106, 2016.

[KRA02] P.C. Krause, O. Wasynczuk, and S. D. Sudhoff, "*Analysis of electric machinery and drive systems*", *IEEE Press*, Piscataway, NJ, 2002.

[KRO31] B. Y. G. Kron, "Rules to predetermine crawling, vibration, noise and hooks in the speed-torque curve induction motor slot combinations," *IEEE Trans. AIEE*, no. 1, pp. 757–767, 1931.

[LAM97] B. G. Lamme, "Induction Motor," US610067A, Westinghouse, US Patent, 1897.

[LEM20] Lem.com, "LTS 25-NP", 2020. Available: https://www.lem.com/en/lts-25np

[LEV07] E. Levi, R. Bojoi, F. Profumo, H. A. Toliyat and S. Williamson, "Multiphase induction motor drives - a technology status review," *IET Electric Power Applications*, vol. 1, no. 4, pp. 489-516, July 2007.

[LIA95] F. Liang, D. W. Novotny, R. Fei, and X. Xu, "Selection of the pole number of induction machines for variable speed applications," *IEEE Trans. Industry Applications*, vol. 31, no. 2, pp. 304–310, Mar-Apr. 1995.

[LIB04] F. Libert and J. Soulard, “Investigation on pole-slot combinations for permanent magnet machines with concentrated windings,” *Proc. IEEE Int. Conf.Electrical Machines*, Krakow, Poland, pp. 5–8, 2004

[LIP17] T.A. Lipo, “Introduction to AC machine design”, *IEEE Press Series on Power Engineering*, ch. 6, 2017.

[LIP80] T. A. Lipo, “A d-q model for six-phase induction machine,” *Proc. Int. Conf. Electrical Machines, ICEM’80*, Athens, Greece, pp. 860-867, Sep. 1980.

[LIW05] S. Liwei, D. Ying, C. Shumei and C. Shukang, “Constant-power operation performance improvement of the induction machine drives for hybrid electric vehicle applications,” *Proc. IEEE International Conference on Electrical Machines and Systems*, Nanjing, vol. 1, pp. 818-821, 2015.

[LOR90] R. D. Lorenz and D. W. Novotny, “Saturation effects in field-oriented induction machines,” *IEEE Trans. Industrial Applications*, vol. 26, no. 2, pp. 283–289, Mar.-Apr. 1990.

[LYR02] R. O. C. Lyra., and T.A Lipo, ‘Torque density improvement in a six-phase induction motor with third harmonic current injection’, *IEEE Trans. Ind. Appl.*, 38, (5), pp. 1351–1360, 2002

[MAG12] M. P. Magill and P. T. Krein, “Examination of design strategies for inverter-driven induction machines,” *Proc. IEEE Power Energy Conference, Illinois, Champaign, IL*, pp. 1-6, 2012.

[MAG15a] M. P. Magill and P. T. Krein, “A dynamic pole-phase modulation induction machine model,” *Proc. IEEE International Electric Machines & Drives Conference (IEMDC)*, Coeur d'Alene, ID, pp. 13-19, 2015.

[MAG15b] P. M. Magill, P. T. Krein, and H. S. Kiruba, “Equivalent circuit model for pole-phase modulation induction machines,” *Proc. IEEE International Electric Machines & Drives Conference (IEMDC)*, Coeur d'Alene, ID, pp. 293-299, 2015.

[MAG20] Magtrol.com, “TM Torque sensors”, 2020. Available: https://www.magtrol.com/product/torque-transducers/

[MAL04] K. Malte, “Application of 48 volt for mild hybrid vehicles and high power loads,” *SAE Technical Paper*, 2014-01-1790, Jan. 2014.

[MAL19] S. Mallampalli, Z. Q. Zhu, J. C. Mipo, and S. Personnaz, “48V starter-generator induction machine with pole changing windings,” *Proc. IEEE Energy Conversion Congress and Exposition (ECCE)*, Baltimore MD, USA, pp. 1609-1615, 2019.

[MAL20] S. Mallampalli, Z. Q. Zhu, J. Mipo and S. Personnaz, “Six-Phase pole-changing winding induction machines with improved performance,” *IEEE Trans. on Energy Conversion*, doi: 10.1109/TEC.2020.3009190, Jul 2020.

[MAR07] G. D. Martin, R. D. Moutoux, M. Myat, R. Tan, G. Sanders and F. Barnes., “An integrated starter-alternator system using induction machine winding reconfiguration,” *Proc. IEEE Vehicle Power and Propulsion Conference, Arlington, TX*, pp. 677–681, Sept. 2007.

[MEN14] A. L. Menn, W. R. Canders, and M. Henke, "Holistic analytical design of induction motors for automotive application," *Proc. IEEE 9th International Conference on. Ecological Vehicles and. Renewable Energies (EVER),* Monte-Carlo, pp. 1-7, 2014.

[MIL01] J. M. Miller and V. Stefanovic, V. Ostovic and J. Kelly, "Design consideration for an automotive integrated starter-generator with pole phase modulation," *Proc. IEEE IAS Annu. Meeting*, pp. 2366–2373, Oct. 2001.

[MIL99] J. M. Miller and V. Ostovic, "Pole-phase modulated toroidal winding for an induction machine," US5977679, Continental Automotive Systems Inc, Nov. 2, 1999.

[MOM16] F. Momen, K. Rahman, Y. Son, and P. Savagian, "Electrical propulsion system design of Chevrolet Bolt battery-electric vehicle," *Proc. IEEE Energy Conversion Congress and Exposition (ECCE 2016),* pp. 1-8, Milwaukee, WI, 2016.

[MOR13] O. Moros and D. Gerling, "New 30-Teeth /14-poles concentrated winding for use in induction machines," *HdT Elektrische Antriebstechnologie für Hybrid- und Elektrofahrzeuge*, Munich, Germany, 2013.

[MOR15] O. Moros, and D. Gerling, "New flexible harmonic cost effective concentrated winding topology," *Proc. Industrial Electronics Society, Yokohama*, pp. 427–432, Nov. 2015.

[MOR15a] O. Moros, G. Dajaku, C. Klusmann and D. Gerling, "New high voltage 2-pole concentrated winding and corresponding rotor design for induction machines," *Proc. IEEE Industrial Electronics Society*, Yokohama, Japan, November, 2015.

[NEE95] H. P. Nee, "Rotor slot design of inverter-fed induction motors," *Proc. IEEE 7th International Conference on Electrical Machines and Drives*, Durham, UK, pp. 52-56 no. 4, 1995.

[NEL74] R.H. Nelson, and P.C. Krause, "Induction machine analysis for arbitrary displacement between multiple winding sets", *IEEE Trans. Power Appar. Syst.*, vol. 93, no. 3, pp. 841 –848, 1974

[NET99] L. M. Neto, J. R. Camacho, C. H. Salerno and B. P. Alvarenga, "Analysis of a three-phase induction machine including time and space harmonic effects: the a, b, c reference frame," *IEEE Trans. on Energy Conversion*, vol. 14, no. 1, pp. 80-85, March 1999.

[OLD85] J. L. Oldenkamp and S. C. Peak, "Selection and design of an inverter-driven induction motor for a traction drive system," *IEEE Trans. Industry Applications*, vol. 21, no. 1, pp. 259–265, Jan-Feb. 1985.

[OSA00] M. Osama and T. A. Lipo, "Experimental and finite-element analysis of an electronic pole-change drive," *IEEE Trans. on Industrial Applications*, vol. 36, no. 6, pp. 1637–1644, 2000.

[OSA96] M. Osama and T. A. Lipo, "New inverter control scheme for induction requiring wide speed range," *IEEE Trans. on Industrial Applications*, vol. 32, no. 4, pp. 938–944, 1996.

[OSA97] M. Osama and T. A. Lipo, “Modeling and analysis of a wide-speed-range induction motor drive based on electronic pole changing,” *IEEE Trans. on Industrial Applications*, vol. 33, no. 5, pp. 1177–1184, 1997.

[OST02] V. Ostovic, “Pole-changing permanent-magnet machines,” *IEEE Transactions on Industry Applications*, vol. 38, no. 6, pp. 1493-1499, Nov.-Dec. 2002.

[PAT14] A. Patzak and D. Gerling, “Design of an automotive 48 V integrated starter-generator on the basis of an induction machine with concentrated windings,” *Proc. IEEE 17th Intl. Conf. on Electrical Machines and Systems (ICEMS)*, Hangzhou, pp. 2583-2589, 2014.

[PAT15] A. Patzak and D. Gerling, “Design of a multi-phase inverter for low voltage high power electric vehicles,” *Proc. IEEE International Electric Vehicle Conference (IEVC)*, Florence, 2015.

[PAT16] A. Patzak, F. Bachheibl, A. Baumgardt, G. Dajaku, O. Moros, and D. Gerling, “ISCAD - Electric high performance drive for individual mobility at extra-low voltages,” *SAE International Journal on Alternative Powertrains*, vol. 5, no. 1, pp. 148–156, 2016.

[PAT16a] A. Patzak, F. Bachheibl, A. Baumgardt, G. Dajaku, O. Moros, and D. Gerling, “Driving range evaluation of a multi-phase drive for low voltage high power electric vehicles,” *Proc. IEEE International Conference on Sustainable Mobility Applications, Renewables and Technology (SMART)*, Kuwait City, pp. 1-7, 2016.

[PEL12] G. Pellegrino, A. Vagati, B. Boazzo, and P. Guglielmi, “Comparison of induction and PM synchronous motor drives for EV application including design examples,” *IEEE Trans. Industry Applications.*, vol. 48, no. 6, pp. 2322–2332, Nov./Dec. 2012.

[PER12] L. A. Pereira, C. C. Scharlau, L. F. A. Pereira, and S. Haffner, “Influence of saturation on the air-gap induction waveform of five-phase induction machines,” *IEEE Trans. Energy Conversion*, vol. 27, no. 1, pp. 29–41, Mar. 2012.

[RAH15] K. M. Rahman, S. Jurkovic, C. Stancu, J. Morgante and P. J. Savagian, “Design and performance of electrical propulsion system of extended range electric vehicle (EREV) chevrolet volt,” *IEEE Trans. on Industry Applications*, vol. 51, no. 3, pp. 2479-2488, May-June 2015.

[RAH16] K. Rahman, S. Jurkovic, P. J. Savagian, N. Patel and R. Dawsey, “Retrospective of electric machines for EV and HEV traction applications at general motors,” *Proc. IEEE Energy Conversion Congress and Exposition (ECCE)*, Milwaukee, WI, pp. 1-8, 2016

[REF08] A.M. El-Refaie, M. R. Shah, “Comparison of induction machine performance with distributed and fractional-slot concentrated windings,” *Proc. IEEE Industry Applications Society Annual Meeting*, pp.1-8, 5-9 Oct. 2008.

[REG20] Regatron.com, “TC.ACS series 4-quadrant power supply”, 2020. Available: https://www.regatron.com/product/overview/programmable-bidirectional-ac-power-sources/tc-acs-series/#configurations”

[RIC07] D. Richard, Y. Dubel, “Valeo StARS Technology: A competitive solution for hybridization,” *Proc. IEEE Power Conversion Conference*, pp. 1601- 1605, Nagoya, 2007.

[SAB17] R. Sabarirajan, N. J. Singh, and N. Senthilnathan, “Finite element analysis of an integrated starter generator (ISG) for four-wheelers using an induction machine,” *Proc. IEEE, International Conference on Innovations in Information, Embedded and Communication Systems (ICIIECS), Coimbatore*, pp. 1–5, Mar. 2017.

[SAD11] Siavash Sadeghi, Leila Parsa, Hamid A. Toliyat, “Extending speed range of five-phase PM machines by changing the stator windings connections,” *Proc. IEEE International Electric Machines & Drives Conference (IEMDC),* Niagara Falls, ON, pp. 1540-1545, 2011.

[SAY70] M.G.Say, Performance and Design of AC Machines. London, U.K.: Pitman, 1970.

[SCH17] W Schöffmann, H. Sorger , M. Weissbäck , T. Pels, C. Kaup, M. Brunner, “The tailored powertrain for 48 V – options for the gasoline engine – chance for future Diesel engines,” *Proc. Internationaler Motorenkongress*, Springer Vieweg, Wiesbaden 2017.

[SCR05] S. Scridon, I. Boldea, L. Tutelea, F. Blaabjerg and A. E. Ritchie, “BEGA—a biaxial excitation generator for automobiles: comprehensive characterization and test results,” *IEEE Trans. on Industrial Application,* vol. 41, no. 4, pp.935-944, 2005.

[SIN05] G. K. Singh, K. Nam and S. K. Lim, “A simple indirect field-oriented control scheme for multiphase induction machine,” *IEEE Trans. on Industrial Electronics*, vol. 52, no. 4, pp. 1177-1184, Aug. 2005

[SLE89] G. R. Slemon, “Modelling of induction machines for electric drives,” *IEEE Trans. on Industry Applications*, vol. 25, no. 6, pp. 1126-1131, Nov.-Dec. 1989.

[SOZ16] F. A. A. R. Sozinho and K. Hatipoglu, “Comparison of IGBT modules focus on high power systems,” *Proc IEEE SoutheastCon 2016, Norfolk, VA*, pp. 1-6., 2016

[SPA13] C. M. Spargo, B. C. Mecrow, and J. D. Widmer, “Application of fractional slot concentrated windings to synchronous reluctance machines,” *Proc. IEEE International Electrical Machines and Drives Conference (IEMDC),* pp. 618–625, 2013.

[SPA16] S. Spas, D. Gerling, G. Dajaku and A. Greifelt, “Energy-based analytical inductance calculation of the novel Stator Cage Machine,” *Proc. IEEE International Conference on Power Electronics, Drives and Energy Systems (PEDES),* Trivandrum, pp. 1-6, 2016.

[SUN10] D. Sun, B. Ge and D. Bi, “Winding design for pole-phase modulation of induction machines,” *Proc. IEEE Energy Conversion Congress Exposition*, Atlanta, GA, pp. 278-283, Sep-2010.

[SUN16] V. M. Sundaram and H. A. Toliyat, “A Fractional Slot Concentrated Winding (FSCW) configuration for outer rotor squirrel cage induction motors,” *Proc. IEEE International Electrical Machines and Drives Conf.(IEMDC),* pp. 20–26, 2016.

[SUZ97] T. S. Suzuki, K. Tsubboi, I. Hirotsuka, and I. Matsuda, “Basic principle and maximum torque characteristics of a six phase pole changing induction machine for electric vehicles,” *Proc. IEEE Power Convers. Conf.*, Nagaoka, pp. 1–8, 1997.

[TES88] N. Tesla, “Electro-magnetic motor,” US382279A, US Patent, 1888.

[TIE05] T. Wang, P. Zheng, Q. Zhang and S. Cheng, “Design characteristics of the induction motor used for hybrid electric vehicle,” *IEEE Trans. on Magnetics*, vol. 41, no. 1, pp. 505-508, Jan 2005.

[TOL91a] H. A. Toliyat, T. A. Lipo, and J. Coleman White, “Analysis of a concentrated winding induction machine for adjustable speed drive applications, Part 1: Motor analysis,” *IEEE Trans. Energy Convers.*, vol. 6, no. 4, pp. 679–683, 1991.

[TOL91b] H. A. Toliyat, T. A. Lipo, and J. C. White, “Analysis of a concentrated winding induction machine for adjustable speed drive applications, Part II: Motor design and performance,” *IEEE Trans. Energy Convers.*, vol. 6, no. 4, pp. 684–692, 1991.

[VAR09] R. Vartanian and H. A. Toliyat, “Design and comparison of an optimized permanent magnet-assisted synchronous reluctance motor (PMa-SynRM) with an induction motor with identical NEMA Frame stators,” *Proc. IEEE Electric Ship Technologies Symposium*, Baltimore, MD, pp. 107-112, 2009.

[WAL04] J. E. Walters, R. J. Krefta, G. Gallegos-lopez, and G. T. Fattic, “Technology considerations for belt alternator starter systems,” *SAE World Cong.*, Detroit, Michigan, 8th-11th March, 2004.

[WAL93] I. T. Wallace, D. W. Novotny, R. D. Lorenz, and D. M. Divan, “Increasing the dynamic torque per ampere capability of induction machines,” *IEEE Trans. on Industrial Applications*, vol. 30, no. 1, pp. 146–153, Jan./Feb. 1993.

[WAL94] I. T. Wallace, D. W. Novotny, R. D. Lorenz and D. M. Divan, “Verification of enhanced dynamic torque per ampere capability in saturated induction machines,” *IEEE Trans. on Industry Appl.*, vol. 30, no. 5, pp. 1193-1201, Sept.-Oct. 1994.

[WAN05] T. Wang, P. Zheng, Q. Zhang, and S. Cheng, “Design characteristics of the induction motor used for hybrid electric vehicle,” *IEEE Trans. Magn*etics, vol. 41, no. 1, pp. 505–508, Jan. 2005.

[WAN15] K. Wang, Z. Q. Zhu, Y. Ren, and G. Ombach, “Torque improvement of dual three-phase permanent-magnet machine with third-harmonic current injection,” *IEEE Trans. on Industrial Electronics.*, vol. 62, no. 11, pp. 6833–6844, 2015.

[WEB16] https://www.continental.com/en/press/press-releases/2016-10-20-48v-hybrid-modular-system-99018

[WEI05] C. Wei, D. Fulton, and L. Christopher, “Multi-set rectangular copper hairpin windings for electric machines,” U S. Patent 0 206 265, Sep. 22, 2005.

[WIL01] S. Williamson and S. Smith, “Pulsating torque and losses in multiphase induction machines,” *Proc. IEEE Industry Applications Conference. 36th IAS Annual Meeting (Cat. No.01CH37248)*, Chicago, IL, USA, vol.2, pp. 1155-1162, 2001.

[WRO15] R. Wrobel, S.J. Williamson, J.D. Booker, and P. Mellor, “Characterising the performance of selected electrical machine insulation systems”, *Proc. IEEE Energy Conversion Congress and Exposition (ECCE 2015),* Montreal, Quebec, Canada, pp. 4857-4864, 20-24 September 2015.

[XIA08] X. Tu, L. A. Dessaint, R. Champagne, and K. Al-Haddad, “Transient modelling of squirrel-cage induction machine considering air-gap flux saturation harmonics,” *IEEE Trans. on Industrial Electronics.*, vol. 55, no. 7, pp. 2798–2809, 2008.

[YEP16] A. G. Yepes, F. Baneira, J. Malvar, A. Vidal, D. P. Estevez, O. Lopez and J. D. Gandoy, “Selection criteria of multiphase induction machines for speed-sensorless drives based on rotor slot harmonics,” *IEEE Trans. Industrial Electronics*, vol. 63, no. 8, pp. 4663–4673, Aug. 2016.

[YLI13] Y. Li, S. Li and B. Sarlioglu, “Analysis of pulsating torque in squirrel cage induction machines by investigating stator slot and rotor bar dimensions for traction applications,” *Proc. IEEE Energy Conversion Congress and Exposition*, Denver, CO, pp. 246-253, 2013.

[YOK20] Yokogawa.com, “WT3000, Precision Power Analyzer data sheet”, 2020 Available: https://tmi.yokogawa.com/uk/solutions/products/power-analyzers/wt3000-precision-power-analyzer/

[ZAR10] L. Zarri, M. Marano, M. Bonavoglia and D. Casadei, “Power losses of multiphase inverters,” *Proc IEEE Conf. on Electrical Systems for Aircraft, Railway and Ship Propulsion*, Bologna, pp. 1-6, 2010.

[ZHA00] Z. M. Zhao, S. Meng, C. C. Chan and E. W. C. Lo, “A novel induction machine design suitable for inverter-driven variable speed systems,” *IEEE Trans. Energy Conversion, .*, vol. 15, no. 4, pp. 413–420, Dec. 2000.

[ZHA19] Y. Zhao, D. Li, T. Pei and R. Qu, “Overview of the rectangular wire windings AC electrical machine,” *CES Trans. on Electrical Machines and Systems*, vol. 3, no. 2, pp. 160-169, June 2019.

[ZHA95] Y. Zhao and T. A. Lipo, “Space vector PWM control of dual three-phase induction machine using vector space decomposition,” *IEEE Trans. on Industrial Applications*, vol. 31, no. 5, pp. 1100–1109, 1995.

[ZHU07] Z. Q. Zhu and D. Howe, “Electrical machines and drives for electric, hybrid, and fuel cell vehicles,” *Proc. of the IEEE*, vol. 95, no. 4, pp. 746-765, April 2007.

[ZHU17] Z. Q. Zhu, B. Lee, L.R. Huang and W.Q. Chu, “Contribution of current harmonics to average torque and torque ripple in switched reluctance machines,” *IEEE Trans. on Magnetics*, vol. 53, no. 3, Mar. 2017.